



**INDIRECT THREE DIMENSIONAL
PRINTING OF APATITE-
WOLLASTONITE STRUCTURES FOR
BIOMEDICAL APPLICATIONS**

A thesis submitted to the Faculty of Science,
Agriculture and Engineering for the Degree of
Doctor of Philosophy

By
Naif Hamdan Alharbi

School of Mechanical and Systems Engineering
Newcastle University

June 2016

Abstract

The main goal of the current study was to investigate the capabilities of the indirect three-dimensional printing (3DP) process when used in combination with bioceramic Apatite-Wollastonite (A-W) powders and to evaluate the mechanical properties of the printed parts. A-W glass ceramic is a bioactive material that is used clinically for bone substitutes due to its suitable mechanical properties. Additive manufacturing approaches, especially 3DP, have been shown to produce 3D complex structures *via* computer aided design.

A-W with weight % of 4.6 MgO, 44.7 CaO, 34 SiO₂, 16.2 P₂O₅ and 0.5 CaF₂ was used in the present study. The approach taken to indirect 3DP was: (i) blending of the A-W with maltodextrin (MD) powder; (ii) using a Z Corp Z310plus 3D printer to selectively print binder into sequentially deposited thin layers of the blended powders in order to build up a 3D structure; (iii) heat treating the 3D printed parts to 1150°C to burn off the MD and sinter the A-W to create a consolidated 3D structure. Phosphate glass infiltration was used to fill the porosities and increase the mechanical strength of the sintered parts. Bioactive phosphate glass with weight % of 6.22 Na₂O, 71.29 P₂O₅, and 22.49 CaO was used because it can dissolve faster than A-W.

The flexural strength, Young's modulus, porosity and shrinkage were measured on various samples printed from the seven powder blends (PBs). PBs with 30% MD and zb®60 binder were required for the parts to develop sufficient strength. PBs 1, 4, and 5 develop the highest strength after sintering. PB1 contains A-W particle sizes in the range of 53-90 μm, PB4 contains A-W particle sizes in the range of 0-53 μm and PB5 contains mixed particle size ranges (78.5% in the range of 53-90 μm with 21.5% in the range of 0-53 μm). Average flexural strengths of 23.65 MPa, 35.64 MPa, and 25.68 MPa were achieved for PB1, PB4, and PB5, respectively. The average strength of PB5 increased to 31.34 MPa after glass infiltration.

In all cases, the increase in strength is a result of the increased consolidation during sintering, as indicated by the observed reduced porosity. Indirect 3D printing of A-W structures can be used to create strong, highly porous structures, but care must be taken to appropriately select binder and processing parameters. Moreover, this is a promising approach for fabrication in bone tissue engineering.

Author's Declaration

I hereby declare that this thesis is of my own composition and has not been accepted in any previous application for a degree. All sources of information have been specifically acknowledged by means of referencing. All data were collected and analysed by the author.

Signed:



Date: 1st June 2016

Naif Hamdan Alharbi

Student Number: A69118625

School of Mechanical and System Engineering

Newcastle University, UK

Dedication

To my Father & Brothers

To my Wife Neha

To my Daughter Layan & Son Thamer

Acknowledgments

I should be most grateful to Allah who generously enabled me to carry on and graciously provided me the real power to complete this work; without his precious help this work would not have been successful.

It would be my great pleasure to express my deepest gratitude to my supervisors Prof. Kenneth Dalgarno and Dr. Oana Bretcanu, School of Mechanical & Systems Engineering at Newcastle University. Many thanks to them, as they helped me learn to discover, and taught me to achieve new goals in a fantastic way. I am most grateful to them not only for their immense understanding, patience, support and encouragement when I needed it, but also for giving me the opportunity to spend time performing research on this project.

I am most grateful to all other researchers and staff at Newcastle University for their suggestions, wishes, and help during my studies; I am sincerely indebted to all of them.

I also owe my special thanks to all of the technicians, Doctors, and assessors of my presentation project during my studies at the School of Mechanical & Systems Engineering at Newcastle University. I express my special gratitude to Dr. Matthew German and Mr. Andrew Yates (School of Dental Sciences) for their invaluable assistance.

Special thanks and respect must go to my family in the Kingdom of Saudi Arabia for their support and encouragement, with my great love to my father, sisters, and brothers, and with very warm respect for all colleagues.

Finally, many thanks to the government of Kingdom of Saudi Arabia, namely the Saudi Interior Ministry and Border Guards, for giving me this opportunity and for sponsorship of my studies.

List of Abbreviations and Clarifications

3D	Three dimensional
3DP	3D Printing/Printer
ALM	Additive Layer Manufacturing
AM	Additive Manufacturing
ASTM	American Society for Testing and Materials
A-W	Apatite-wollastonite
AW-GC	Apatite-wollastonite glass-ceramic
CAD	Computer Aided Design
CT	Computer tomography
DW	distilled Water
ECM	Extracellular matrix
FDM	Fused Deposition Modeling
HA	Hydroxyapatite
LM	Layer Manufacturing
MD	Maltodextrin
PLA	Poly lactide
PLGA	Poly-lactide-co-glycolide
RM	Rapid Manufacturing
RP	Rapid Prototyping
RT	Room Temperature
SFFF	Solid Free Form Fabrication
SLA	Stereolithography
SLS	Selective Laser Sintering
STL	Stereolithographic file format language
UV	Ultraviolet

List of Contents

Chapter 1	1
1.1 Background	1
1.2 Research Aim and Objectives	2
1.2.1 Aim.....	2
1.2.2 Objectives.....	3
1.3 Thesis outline	3
Chapter 2	4
2.1 Bone Structure and Composition	4
2.1.1 Cortical Bone	5
2.1.2 Trabecular Bone	6
2.1.3 Subchondral Bone	8
2.2 Forming and repair of bone.....	9
2.3 Tissue engineering	11
2.4 Essential Requirements for Bone Scaffolds.....	12
2.4.1 Porosity and Interconnectivity	14
2.5 Materials Used to fabricate Bone Scaffolds.....	14
2.6 Fabrication Techniques for Bone Scaffolds.....	19
2.6.1 Conventional Techniques for Bone Scaffolds.....	19

2.6.2	Additive Manufacturing Techniques for Bone Scaffolds	21
2.6.2.1	Additive Manufacturing Processes	22
2.6.2.1.1	Stereolithography (SLA)	22
2.6.2.1.2	Fused Deposition Modelling (FDM).....	23
2.6.2.1.3	Selective Laser Sintering (SLS)	24
2.6.2.1.4	Three-Dimensional Printing (3DP)	24
2.6.2.2	Advantages and Disadvantages of RM Processes for Bone Manufacture	31
2.7	Summary	34
Chapter 3	35
3.1	Materials.....	37
3.1.1	Apatite-wollastonite powders	37
3.1.1.1	EDX and XRD evaluation of A-W powder and sintered A-W	37
3.1.2	Maltodextrin Powders	40
3.1.3	Polymers.....	40
3.1.4	Phosphate glass powder	40
3.1.5	Zb [®] 60 binder	40
3.1.6	Distilled Water and Glycerol binder (DW).....	41
3.2	Powder Preparation	41
3.3	Manufacture of Scaffolds.....	45

3.3.1	Preparing the 3D printer	45
3.3.2	Post-processing	48
3.3.2.1	Sintering	49
3.3.2.2	Infiltration	50
3.3.3	PLA Discs Printing Processes	51
3.4	Testing.....	51
3.4.1	Physical properties of DW and zb@60 binder solution	51
3.4.1.1	Viscosity.....	51
3.4.1.2	Surface Tension and Contact Angle.....	51
3.4.2	Accuracy and Shrinkage	52
3.4.3	Specimen density and porosity	53
3.4.3.1	Density of A-W Powder.....	53
3.4.3.2	Apparent density	54
3.4.3.3	Open Porosity.....	55
3.4.3.4	Total Porosity.....	55
3.4.4	Mechanical Properties Analysis.....	56
3.4.4.1	Flexural strength.....	56
3.4.4.2	Sample stiffness determined using Young’s modulus	57

3.4.5	Scanning Electronic Microscopy (SEM)	57
3.4.6	Microscopy.....	58
3.4.7	Micro-Computed Tomography (micro-CT).....	58
3.4.8	Data Analysis and Statistical Test.....	58
3.4.9	Bioactivity.....	58
3.4.9.1	<i>In vitro</i> cell-compatibility assessment.....	59
3.4.9.2	<i>In vitro</i> osteogenic differentiation.....	59
3.4.9.3	<i>In vivo</i> evaluation of A-W and AW/PLA discs for non-load-bearing applications.	59
3.4.10	Summary of the samples manufactured and post processes	59
Chapter 4	62
4.1	Process Characterisation	62
4.1.1	Powder characterisation	62
4.1.2	Printing and handling characteristics	63
4.1.3	Effect of build orientation on bending strength	68
4.1.4	Effect of heat treatment and powder setting on bending strength and shrinkage	70
4.1.5	Effects of different particle sizes of A-W on density of powder	72
4.2	Mechanical Properties Development	73

List of Contents

4.2.1	Green Parts	74
4.2.2	Sintered Parts	76
4.2.3	Shrinkage and Accuracy	77
4.2.4	Interconnectivity and Porosity	83
4.2.5	Effect of Phosphate glass Infiltration on the bending strength	90
Chapter 5	93
5.1	Manufacturing of Parts with Internal Channels	93
5.2	Implantable Devices.....	95
5.2.1	Accuracy of Printed Parts.....	98
5.2.2	Interconnectivity and porosity.....	103
5.2.2.1	Printed and sintered 8 mm (diameter) by 2 mm (height) discs of PB1 105	
5.2.2.2	Printed and sintered 8 mm (diameter) by 2 mm (height) discs of PB5 106	
5.2.2.3	Printed and sintered 8 mm (diameter) by 2 mm (height) disc with four pockets of PB1	106
5.2.2.4	Printed and sintered 6 mm (diameter) by 7 mm (height) plugs of PB5 108	
5.2.2.5	Printed and sintered 6 mm (diameter) by 7 mm (height) plugs with two through holes of PB5.....	110

5.2.2.6	Plugs with two through holes and one pocket hole of PB5	112
5.2.2.7	Hollow Cylinders	114
5.2.3	Bioactivity	116
5.2.3.1	<i>In vitro</i> cell-compatibility assessment.....	116
5.2.3.2	<i>In vitro</i> osteogenic differentiation.....	118
5.2.3.3	<i>In vivo</i> evaluation of A-W and AW/PLA discs for non-load-bearing applications.	119
5.2.4	Ex Vivo Case Study	122
5.2.4.1	Introduction	122
5.2.4.2	Experimental procedures.....	122
5.2.4.3	Results	124
Chapter 6	126
6.1	Introduction	126
6.2	Process Development	126
6.2.1	Powder Particle Size Range	126
6.2.2	Binder Optimisation	128
6.3	Device Design Rules	128
6.3.1	Possible Geometries	128
6.3.2	Accuracy and Repeatability	129

List of Contents

6.4	Potential for Scale Up and Application.....	130
6.4.1	Lead Time	130
6.4.2	Material Utilization and Productivity.....	130
6.4.3	Quality.....	131
6.4.3.1	Mechanical properties	131
6.4.3.2	Porosity	133
6.5	Achievement of Objectives	133
6.6	Novelty and Originality.....	135
Chapter 7	136
7.1	Conclusion	136
7.2	Limitations of the current study	137
7.3	Suggestion for future work.....	137
References	139
Appendix	158

List of Tables

Table 2.1 Typical features of biomaterials.....	15
Table 2.2 The chemical composition of AW-GC	18
Table 2.3 Mechanical properties of natural bone and ceramics.....	18
Table 2.4 Apatite formation on the surface of bioactive ceramics incubated in simulated body fluid (SBF) at 36.5 °C.....	18
Table 2.5 Conventional techniques for the fabrication of scaffolds	20
Table 2.6 Advantages and disadvantages of RM methods	32
Table 2.7 Mechanical properties of printed parts using rapid manufacturing (AM) approach.....	33
Table 3.1 Chemical composition (wt %) of A-W	37
Table 3.2 EDX results of the A-W powder and sintered A-W	38
Table 3.3 Chemical compounds based on XRD database.....	39
Table 3.4 Chemical composition (wt %) of phosphate glass.....	40
Table 3.5 The approximate composition as percent by weight (%) of binder zb®60	41
Table 3.6 Powder blends (PB) used for fabrication of green parts	44
Table 3.7 Powder and binder settings for the z 310 Plus printer	48
Table 3.8 Summary of the samples manufactured and post processes	60
Table 4.1 Printing and handling characteristics	64
Table 4.2 Measured contact angle and surface tension of DW and zb®60	65
Table 4.3 Three-point bending results of sintered parts produced using PB5 in a 0–0 build orientation	69
Table 4.4 Three-Point bending results of green parts produced using PB5 in a 0–90 build orientation	70
Table 4.5 Post-process heat treatments used on green parts	71

List of Tables

Table 4.6 3DP Powder settings	71
Table 4.7 Summary of average bending strength and average volume shrinkage of printed parts.....	71
Table 4.8 Density of A-W powder of three ranges of particle sizes using pycnometer method.....	72
Table 4.9 Mechanical properties of all powder blends	73
Table 4.10 Average volume shrinkage and the statistical analysis of all blends printed with DW	78
Table 4.11 Average volume shrinkage and the statistical analysis of all blends printed with zb@60.....	78
Table 4.12 Summary of properties of parts made using PB5 after phosphate glass infiltration.....	92
Table 4.13 Summary of average bending strength, young's modulus and total porosity after phosphate glass infiltration of PB5, PB6 and PB7 by Method B	92
Table 5.1 CAD model and indirect 3DP sintered specimens.....	96
Table 5.2 CAD model and dimension of devices	99
Table 5.3 Accuracy of devices	101
Table 5.4 Summary of average open porosity and apparent surface area and volume of devices.....	103
Table 5.5 Open porosity of PB1 disks	105
Table 5.6 Open porosity of PB1 discs with four pockets.....	107
Table 5.7 Open porosity of PB5 plugs	109
Table 5.8 Open porosity of PB5 plugs with two through holes.....	111
Table 5.9 Open porosity of PB5 plugs with two through holes and one pocket hole...	113
Table 5.10 Open porosity of PB5 cylinder device	115
Table 5.11 Accuracy of 6 mm (diameter) by 7 mm (height) plugs.....	125

List of Tables

Table 6.1 Lead time for producing 50 parts using 3DP	130
Table 6.2 Average bending strength of green parts (powder blends contain 70% by wt. of A-W mixed with 30% by wt. of MD).....	132
Table 6.3 Average bending strength, Young's modulus and porosity of porous parts printed from A-W (powder blends contain 70% by wt. of A-W mixed with 30% by wt. of MD) and natural bone	132
Table 6.4 Average total porosity and bending strength of infiltrated parts	133
Table 6.5 Average bending strength and Young's modulus of porous A-W printed parts using zb®60 binder solution	134

List of Figures

Figure 2.1 The hierarchical structure of bone	5
Figure 2.2 Microstructure of cortical bone	6
Figure 2.3 Microstructure of trabecular bone	7
Figure 2.4 Structure of subchondral bone	8
Figure 2.5 The general process of tissue engineering	12
Figure 2.6 The principle of RM	22
Figure 2.7 The process of stereolithography	23
Figure 2.8 The process of fused deposition modelling	23
Figure 2.9 The process of selective laser sintering	24
Figure 2.10 Three-dimensional printing processes	25
Figure 3.1 Overview of 3D Printing of AW Scaffolds	36
Figure 3.2 EDX results for A-W powder and sintered A-W.....	38
Figure 3.3 XRD pattern of the sintered AW	39
Figure 3.4 The ball mill used to grind the A-W and maltodextrin into powders.....	42
Figure 3.5 The sieve shaker used to give a range of particle sizes of AW and maltodextrin	42
Figure 3.6 The main working components of a commercial Z 310 Plus 3D printer (Z Corp, 2009)	46
Figure 3.7 Definition of shell and core (The black line of the diagram denotes the high saturation).....	47
Figure 3.8 The kit for cleaning printed structures.....	48
Figure 3.9 A-W Sintering cycle	49
Figure 3.10 chamber furnace used for sintering AW green Parts	50

List of Figures

Figure 3.11 Measuring the samples using microscope	52
Figure 3.12 Pycnometer bottle	54
Figure 3.13 Three-point bending testing machine used to calculate A-W flexural strength.....	56
Figure 3.14 Three-point bending testing.....	57
Figure 3.15 A-W and A-W/PLA composite discs (8mm diameter x 2 mm high)	59
Figure 4.1 SEM micrographs of A-W, MD and Powder blend	63
Figure 4.2 Shear viscosity of DW and zb®60 binder solution	65
Figure 4.3 The green part (50 X 6 X 4 mm) of PB5	66
Figure 4.4 SEM result of the green part of PB4 and PB5, at 100x magnification.....	67
Figure 4.5 Diagram displaying the strength characteristics in X, Y and Z direction	68
Figure 4.6 Diagram displaying 0–0 and 0–90 build orientation	69
Figure 4.7 SEM of a green part made using PB4 at 500x magnification.....	74
Figure 4.8 SEM of a green part made using PB5 at 100x magnification.....	74
Figure 4.9 Average flexural strength of green parts \pm SE.....	75
Figure 4.10 Average flexural strength of sintered parts \pm SE.....	76
Figure 4.11 Average young's modulus of sintered parts \pm SE	77
Figure 4.12 Average volume shrinkage of sintered parts \pm SE.....	77
Figure 4.13 Average linear shrinkage of green and sintered parts \pm SE for PB1/DW	79
Figure 4.14 Average linear shrinkage of green and sintered parts \pm SE for PB2/DW	79
Figure 4.15 Average linear shrinkage of green and sintered parts \pm SE for PB2/ zb®6080	
Figure 4.16 Average linear shrinkage of green and sintered parts \pm SE for PB3/DW	80
Figure 4.17 Average linear shrinkage of green and sintered parts \pm SE for PB3/ zb®6081	

List of Figures

Figure 4.18 Average linear shrinkage of green and sintered parts \pm SE for PB4/ zb®6081	
Figure 4.19 Average linear shrinkage of green and sintered parts \pm SE for PB5/ zb®6082	
Figure 4.20 Average linear shrinkage of green and sintered parts \pm SE for PB6/ zb®6082	
Figure 4.21 Average linear shrinkage of green and sintered parts \pm SE for PB7/ zb®6083	
Figure 4.22 Average total and open porosity of sintered parts \pm SE	84
Figure 4.23 3D micro-CT images of parts made using PB1 and zb®60	85
Figure 4.24 3D micro-CT images of parts made using PB2 and zb®60	85
Figure 4.25 3D micro-CT images of parts made using PB3 and zb®60	86
Figure 4.26 3D micro-CT images of parts made using PB4 and zb®60	86
Figure 4.27 3D micro-CT images of parts made using PB5 and zb®60	87
Figure 4.28 SEM of external surface of a sintered part made using PB4 at 100x magnification.....	88
Figure 4.29 SEM of external surface of a sintered part made using PB5 at 200x magnification.....	88
Figure 4.30 SEM of the fractured surface of a sintered part made using PB4 at 100x magnification.....	89
Figure 4.31 SEM of the fractured surface of a sintered part made using PB5 at 100x magnification.....	89
Figure 4.32 SEM of a sintered part made using PB5 after phosphate glass infiltration using Method A at 200x magnification.....	90
Figure 4.33 SEM of the fractured surface of a sintered part made using PB5 after phosphate glass infiltration using Method A at 100x magnification	91
Figure 4.34 3D micro-CT images of parts made using PB5 and phosphate glass Infiltration Method B; Voxel size: 14.9 μ m, Diameter of scanned volume is 10 mm....	91
Figure 5.1 CAD design (A), green (B) and sintered (C) A-W specimens with internal channels.....	94

List of Figures

Figure 5.2 Relationship between the possible channel diameter and the thickness of the green and sintered part	94
Figure 5.3 A-W Sintered specimens with internal channels made from PB1	95
Figure 5.4 Relationship between the average open porosity and surface area/ volume ratio	104
Figure 5.5 Printed and sintered discs of PB1	105
Figure 5.6 3D micro-CT images of PB5 discs	106
Figure 5.7 Printed and sintered discs with four pockets of PB1	107
Figure 5.8 3D micro-CT images of PB1 discs with four pockets	108
Figure 5.9 Printed and sintered plugs of PB5	109
Figure 5.10 3D micro-CT images of PB5 plug.....	110
Figure 5.11 Printed and sintered plugs with two through holes of PB5	111
Figure 5.12 3D micro-CT images of PB5 plugs with two through holes	112
Figure 5.13 Printed and sintered plugs with two through holes and one pocket hole of PB5.....	113
Figure 5.14 3D micro-CT images of PB5 plug two through holes and one pocket hole, Voxel size; 12.01 μm	114
Figure 5.15 Printed and sintered hollow cylinders of PB5	115
Figure 5.16 3D micro-CT images of PB5 cylinder device.....	116
Figure 5.17 Viability of rat BMSCs on A-W discs compared with plastic on Day 1 through Day 14.....	117
Figure 5.18 Growth of rat BMSCs on A-W compared with common biopolymers after 7 d in culture.....	117
Figure 5.19 Growth of rat COB on A-W compared with common biopolymers after 7 d in culture.....	118
Figure 5.20 Growth of rat COB on A-W compared with common biopolymers after 14 d in culture.....	118

List of Figures

Figure 5.21 Fold change in ALP activity compared with 24-h culture at 7 and 14 d...	119
Figure 5.22 Fold change in ALP activity on synthetic scaffold materials compared with common biopolymers at Day 7 of culture.....	119
Figure 5.23 Representative morphology of the calvarial defects treated with AW bioceramic discs,.....	120
Figure 5.24 Representative morphology of the calvarial defects treated with AW discs.	120
Figure 5.25 Representative morphology of the calvarial defects treated with the AW/PLA discs,	121
Figure 5.26 Representative morphology of the calvarial defects treated with the AW/PLA discs	121
Figure 5.27 A manual drill with 6 mm drill bit; drilling holes in hardwood	123
Figure 5.28 A-W scaffold fit into the 6 mm drilled hole	123
Figure 5.29 A-W scaffold fit in the 6mm drilled hole in pig mandible	123
Figure 5.30 A-W measuring the force necessary to install or remove the 3D-printed parts using an Instron 5567 testing machine	124
Figure 5.31 Force-distance curves of specimens	125
Figure 6.1 Effect of particle sizes on porosity: (a) powder blend with small particles (0-53 μm), (b) powder blend with large particles (53-90 μm), (c) mixed powder with small particles (0-53 μm) and large particles (53-90 μm)	127

Chapter 1

INTRODUCTION

1.1 Background

Tumours, diseases, and traumatic injuries cause the great majority of bone defects and skeletal failures (Bacon, 2002; Porter *et al.*, 2009; Castilho *et al.*, 2011). Melton *et al.* (1992) claim that 40–46% of Caucasian women and 13–22% of Caucasian men become subject to a lifetime risk of serious bone fractures at approximately the age of 50. In addition, Gullberg *et al.* (1997) believe that the total number of serious bone fractures actually rises annually. They expect that the incidence of serious bone fractures will reach around 4.5 million globally by 2050. Therefore, this topic has become a major healthcare concern worldwide.

Bone grafting has been found necessary for repair of bone defects of a critical size. A critical size defect can be defined as the smallest size of an intra-osseous defect that bones cannot heal without assistance (Schmitz and Hollinger, 1986; Hollinger and Kleinschmidt, 1990).

Three approaches have been suggested to support repair of bone defects, including:

1. Autografts,
2. Allografts, and
3. Xenografts.

The first approach refers to the use of bone segments that are extracted from the body of the patient. The second method refers to the use of bone segments that are extracted from humans other than the patient, normally cadavers. The third technique refers to the use of bone segments that are extracted from animals. However, for all of these approaches there is a high risk of chronic rejection, disease, lack of donor organs, cell morbidity, and infection. Accordingly, these risks have encouraged the adoption of synthetic bone tissue engineering scaffolds (Sachlos and Czernuszka, 2003).

Natural bone can self-generate and is a hierarchical structure. It includes a combination of proteins, organic collagen fibre, and inorganic hydroxyapatite. The perfect synthetic bone must have features resembling those of natural bone. Wang *et al.* (2010) define tissue engineering as *'the process of applying the principles of engineering and life sciences to developing techniques for generating or repairing tissue substitutes with the help of biological cells, scaffolds and growth factors'*. Yeong *et al.* (2004) argue that the main requirement for engineering bone tissues is a three-dimensional porous scaffold that mimics and undertakes the function of the natural extracellular bone matrix. Bone defects should be filled with biodegradable material containing interconnected pores of approximately 50-1000 μm in diameter to support the regeneration of bones (Bohner *et al.*, 2005).

Many methods for producing bone scaffolds have been researched however to date no technique has been widely adopted.

Rapid Manufacturing (RM) has become a popular method of processing biomaterials for fabrication of bone scaffolding. This manufacturing technique is based on an additive process that allows the layer-by-layer creation of complex parts supported by a computer-aided (CAD) design system. Hutmacher *et al.* (2004) noted that such a process requires no moulding or tooling.

A number of RM systems such as stereolithography (SLA), fused deposition modelling (FDM), selective laser sintering (SLS), and three-dimensional printing (3DP) have been used for tissue engineering applications (Peltola *et al.*, 2008). The 3DP process has been suitable for manufacturing 3D porous scaffolds that can be adapted to fill the various geometric shapes of bone defects. In this domain, it is essential to use biomaterials that achieve the essential requirements for bone scaffolding. Apatite-wollastonite glass-ceramic (A-W) is the biomaterial at the focus of this thesis due to its biocompatibility and good mechanical properties.

1.2 Research Aim and Objectives

1.2.1 Aim

The main aim of this study is to explore the processing of 3D powder printed bioceramic and its potential utility for tissue engineering of bone.

1.2.2 Objectives

Several objectives are defined as follows to achieve the above aim:

- To comprehend the capabilities of the indirect 3D printing process when used in combination with bioceramic powders, in terms of lead time, reproducibility, productivity, and quality;
- To produce an optimized binder system that results in high-quality interaction with the bioceramic particles for the 3D printing process;
- To realize the post-processing conditions needed for 3D printed bioceramic scaffolds (sintering conditions).
- To evaluate the mechanical properties of the 3D printed bioceramic scaffolds; and
- To supply batches of scaffolds for biological characterisation.

1.3 Thesis outline

The body of the thesis begins with Chapter 2, which presents the literature review. The literature review presents fundamental information concerning the structure and composition of human bones, the requirements for bone scaffolds, and fabrication methods. The third Chapter describes the materials and processing equipment used in this research. Chapter 4 covers process characterisation and mechanical properties development. In Chapter 5, the design and manufacture of scaffold devices are presented. In Chapter 6, a discussion of the results of the present research is presented, and in Chapter 7, conclusions and recommendations regarding future work are outlined.

Chapter 2

Literature Review

This chapter provides fundamental information regarding the structure of human bones, and the composition of and requirements for ideal scaffolds in terms of materials and fabrication methods.

2.1 Bone Structure and Composition

Bone is a major organ in the human body and its key functions include protection, support, movement, storage of minerals, and formation of blood cells (Porter *et al.*, 2009). Figure 2.1 shows the characteristics of bone, a material with high levels of hierarchical structure (Rho *et al.*, 1998). On a macro level, human bones can be generally categorized as cancellous or cortical. Cancellous bone is located inside the cortical tissue, inside the medullary cavities, which are located at the ends of the long bones and in the interior of short bones, such as the spinal vertebra. Cortical bone is found in the shaft of the long bones, as well as in the outer layer surrounding the trabecular bone, which is located at the ends of the bones and the vertebrae. Lamellae are the fundamental building blocks of trabeculae and osteons, the rod-shaped elements that provide mechanical support and the basic cylindrical unit of bone, respectively. On the nanostructural level, collagen fibrils and mineral crystals comprise a composite that strengthens the lamellae, which form channels through bone (Haghighi, 1989).

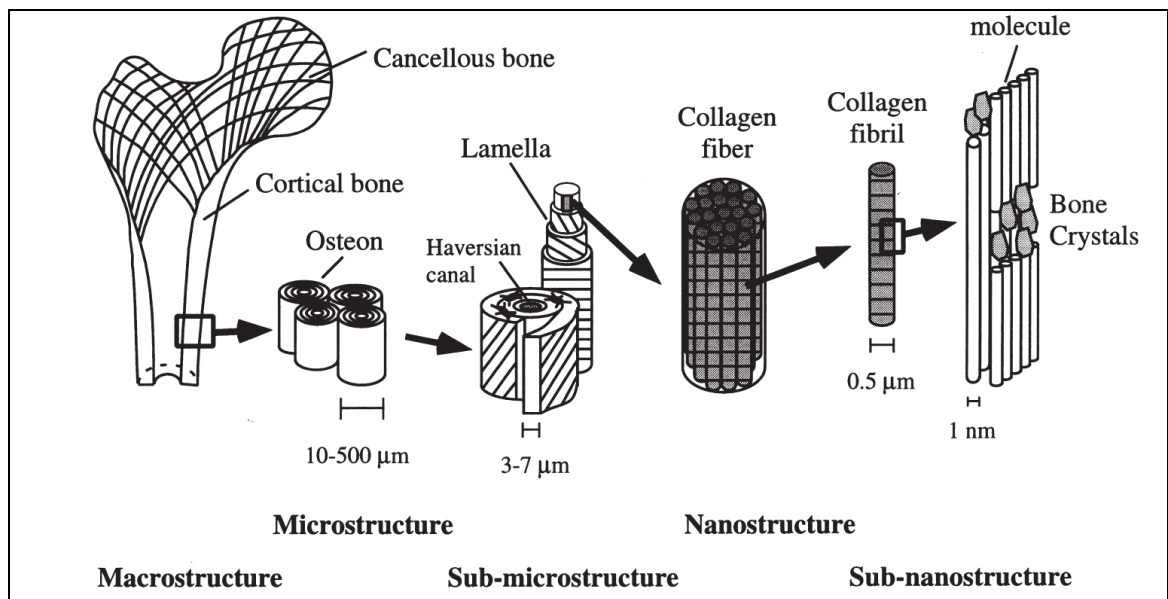


Figure 2.1 The hierarchical structure of bone (Rho *et al.*, 1998)

Buckwalter *et al.* (1996) stated that the adult skeleton normally includes 80% compact (cortical) bone and 20% cancellous (trabecular) bone.

2.1.1 Cortical Bone

Cortical bone is dense and solid, and comprises the shaft that surrounds the marrow cavity in the long bones, in addition to forming the external layer of some of other types bones (Athanasίου *et al.*, 2000). The degree of porosity in cortical bone is no more than 10% (Sikavitsas *et al.* (2001), which allows room for only a limited number of blood vessels and cells.

The primary unit of structure for cortical bones is formed from Haversian or cylindrical osteon systems (Ascenzi and Bonucci, 1968). The osteon is made up from bone matrix in concentric lamellae, which are principally fibres of collagen and these are distributed around the Haversian canal in the centre, through which minor blood vessels travel, as well as nerves. There are also canaliculi, or micro canals, and these facilitate diffusion of nutrients, (see Figure 2.2). Osteons position themselves in longitudinal alignment to the bone, and are therefore termed anisotropic. Figure 2.2 illustrates that the cement line forms the osteon's boundary (Morgan *et al.*, 2013). Lacunae are positioned between the osteon's lamellae, and hold osteocytes within them (Morgan *et al.*, 2013). The lacunae are interconnected via the canaliculi and also connected to the Haversian canal in the

same manner. These canaliculi host osteocyte processes as the cells use gap junctions for communication (Milovanovic *et al.*, 2013). Thereby, various materials such as hormones and nutrients are transferred from the blood vessels within the Haversian canal to reach the further osteocytes in a step by step journey. Bone can be deposited or resorbed via osteocyte activity (Schaffler & Kennedy, 2012).

The flexural strength is 50-160 MPa (Kim *et al.*, 2004), and the strength values reported in the longitudinal direction are 79–151 MPa and 131–224 MPa for tension and compression, respectively (Yaszemski *et al.*, 1996b). The elastic modulus for large cortical bone ranges from 13 to 17 GPa (Choi *et al.*, 1990).

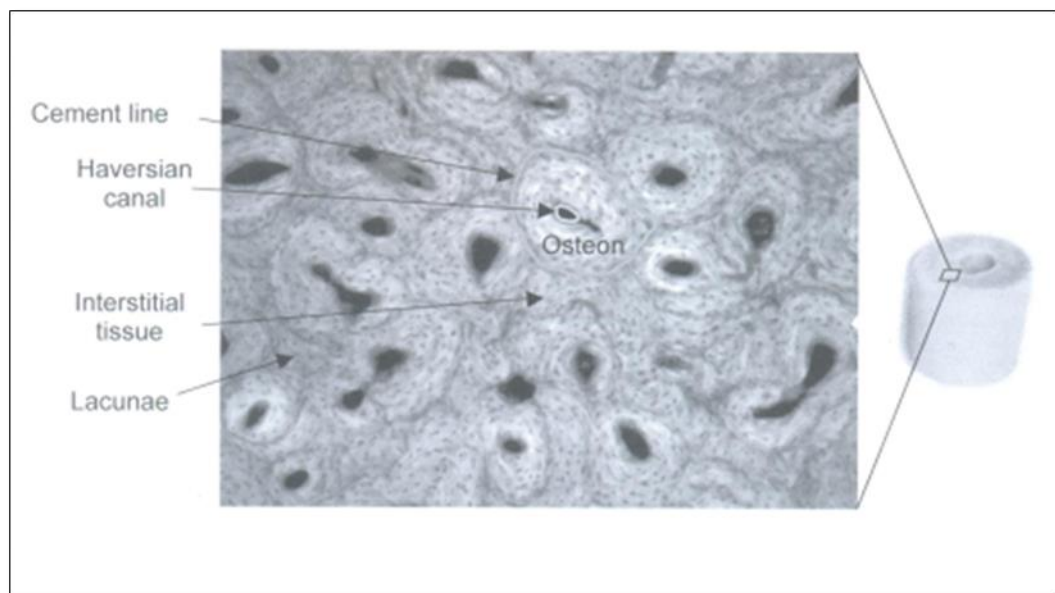


Figure 2.2 Microstructure of cortical bone (Wang *et al.*, 2010)

2.1.2 Trabecular Bone

The spine, ribs, and the ends of the long bones include porous, spongy trabecular bone (Athanasίου *et al.*, 2000). Trabecular bone, which can be 50–90% porous according to Sikavitsas *et al.* (2001). It is composed of an intertwined network of trabeculae, small rod-shaped structures composed largely of collagen that become aligned in the direction of the loading stress (Athanasίου *et al.*, 2000). The porous volume includes bone marrow and vasculature that offer little mechanical support in comparison with the cortical bone, as shown in Figure 2.3. The strength of the trabecular bone and its elastic moduli change according to the density of a particular bone (Mistry and Mikos, 2005),

and vary from 5 to 10 MPa and from 50 to 100 MPa for tension and compression, respectively (Navarro *et al.*, 2008, Athanasiou *et al.*, 2000, Yaszemski *et al.*, 1996a). Vainionpaa *et al.* (1987) reported that the flexural strength of cancellous bone is 10–20 MPa. Moreover, the the moduli ranges from 1 to 13 GPa (Choi *et al.*, 1990).

The distinctive mechanical characteristics of bone can, to a degree, be ascribed to the interaction of chemical components on a nanoscale (Taton, 2001). Bone is composed of approximately 10% water, 30% organic material, and 60% inorganic mineral (Athanasiou *et al.*, 2000). Crystals of calcium phosphate, principally hydroxyapatite (HA), make up the inorganic constituent, whereas the organic constituent is made up mainly of collagen. Molecules of collagen are aligned into triple helices, which are bundled into fibrils of 1.5–3.5 nm in diameter. Those fibrils, in turn, are bundled into fibres of collagen with diameters ranging from 50 to 70 nm (Rho *et al.*, 1998). HA crystals appear as small 2–3 nm thick plates that are 10s of nanometres in width and length that are precipitated onto the collagen fibres (Holmgren *et al.*, 1998), (Weiner and Traub, 1992). These rigid HA crystals increase the compressive strength of the composite, while the collagen fibres can dissipate energy and convey tensile strength to the bone (Thompson *et al.*, 2001). In addition, several other factors including the age or gender of the subject, and the anatomic location of bones play a significant role in the structure and composition of bone (Wang *et al.*, 2010).

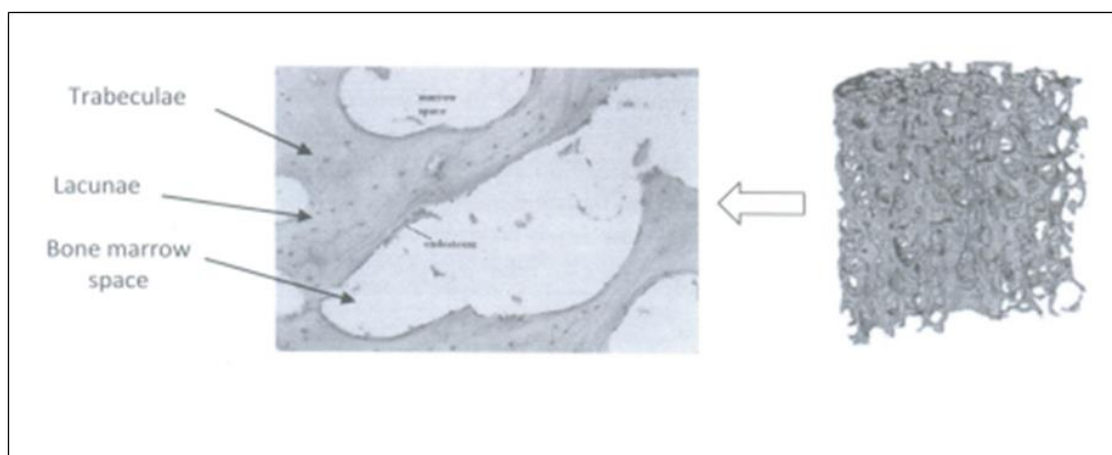


Figure 2.3 Microstructure of trabecular bone (Wang *et al.*, 2010)

2.1.3 Subchondral Bone

Subchondral bone can be defined as a zone that contains the calcified region of the articular cartilage and a layer of lamellar bone (Duncan *et al.*, 1987). Articular cartilage is specific form of connective covering of bone-endings at the sites of joints (Mow *et al.*, 1994). The main functions of this tissue include allowing loads to be transmitted without incurring high levels of friction and to ease articulation through its qualities of smoothness and lubrication (Poole, 1997). The articular cartilage is separated from the subchondral bone by two mineralized layers, as shown in Figure 2.4. Choi *et al.* (1990) reported that the moduli of subchondral bone ranges from 1 to 3 GPa.

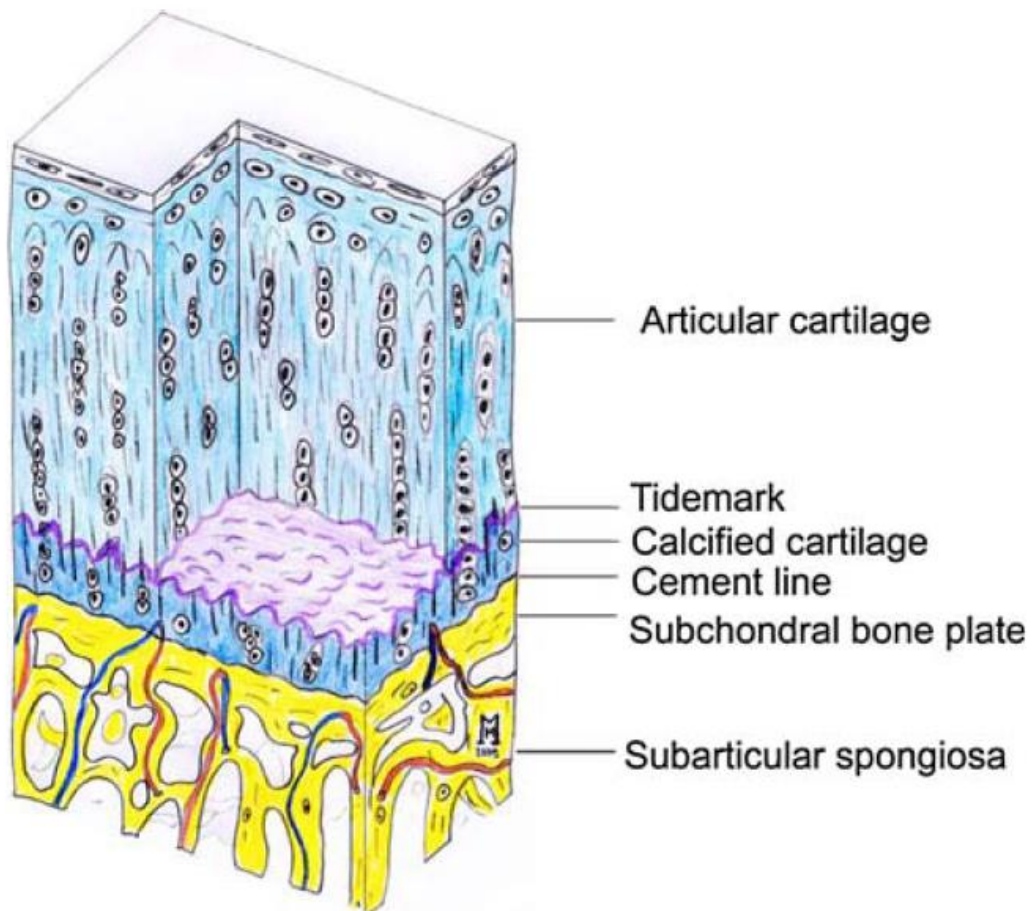


Figure 2.4 Structure of subchondral bone (Madry *et al.*, 2010)

2.2 Forming and repair of bone

Bone can be formed through either endochondral or intra-membrane routes (Nakashima & de Crombrughe, 2003). The intra-membranous route is known as direct formation, and utilises mediation from the inner periosteal osteogenic layer. Bone is formed in a way which does not utilise a cartilage stage as an intermediate. Instead, mesenchymal stromal cells differentiate to form pre-osteoblasts and then osteoblasts (Urist *et al.*, 1983). In the endochondral route, bone is synthesised onto a matrix of mineralized cartilage following elongation and shaping of the bone from physal and epiphyseal cartilage (Teti, 2011). These two types of bone formation also apply in the case of repair, with one factor in the method of formation being the bio-mechanical background in which this takes place (Shapiro, 2008).

Following bone fracture, the processes of healing allow the tissues to recover the mechanical and physical characteristics which were present prior to the break. This process is affected by various elements at a local and systemic level. There are three phases in healing: early inflammation; repair and; finally, remodelling (Dimitriou *et al.*, 2005; Phillips, 2005; Shapiro, 2008).

Early inflammation comes with the development of a haematoma at the location of the fracture, and this occurs over hours or several days. Cells involved in inflammation, including macrophages, lymphocytes, polymorphonuclear cells and monocytes, are mediated by prostaglandin to enter the bone tissue along with fibroblasts (Schindeler *et al.*, 2008; Shapiro, 2008). Granulation tissue forms, mesenchymal cells migrate and vascular tissue grows into the site (Giannoudis *et al.*, 2007; Marsell & Einhorn, 2011).

The phase which follows is devoted to repairing the fracture, with fibroblasts creating a stroma to enable blood vessels to grow into the area. As this is achieved, a matrix of collagen is formed, and secretions of osteoid are generated and then subject to mineralisation. This creates a soft callus which surrounds the area being repaired (Schindeler *et al.*, 2008; Shapiro, 2008), and ultimately ossifies to present a section of bone weaving together to link the broken parts of the fracture (Marsell & Einhorn, 2011).

The final stage of healing is that of remodelling, a process which returns the bone to its former structure, form and strength level (Schindeler *et al.*, 2008; Shapiro, 2008). Bone is remodelled across a long period which can encompass years, with sufficient strength for normal function generally regained at between 3 and 6 months after the fracture occurs (Giannoudis *et al.*, 2007; Marsell & Einhorn, 2011).

However, the process of healing may not succeed, as a result for example of the level of the initial damage or the introduction of infection, it becomes necessary to turn to grafting of bone or substitutes for this.

With bioactive requirements in mind, ideally the material utilised for grafting bone should be osteogenic, osteoinductive and osteoconductive, which should lead to osteointegration as the graft substance and the bone itself bond (Giannoudis *et al.*, 2005).

- i. Osteoconductive materials facilitate the adherence and proliferation of bone cells as well as generation of an extracellular matrix on surfaces and porous structure. New blood vessels are also able to grow into the site, while osteogenic precursors penetrate the area of the graft (Albrektsson & Johansson, 2001; Bose *et al.*, 2012; Calori *et al.*, 2011).
- ii. Osteoinductive materials can mechanically stimulate the tissue or stimulate it on a biomechanical level in order that new bone is formed. For this, progenitor cells are recruited and cells differentiate following managed phenotypes or specific lineage. For this ideally bone growth factors are either contained in the graft substance or this is supplemented (Albrektsson & Johansson, 2001; Bose *et al.*, 2012).
- iii. Osteogenicity is the capacity to perform as a store for mesenchymal cells or osteoblasts with the potential for derivation in osteoblastic lineages, due to the role of these cells in forming the extracellular matrix and then mineralising it (Albrektsson & Johansson, 2001; Calori *et al.*, 2011).
- iv. The graft material should have osteointegrity, which refers to the capacity for formation of good-strength bonding to the osseous tissue around it, which gives continuity of the material as well as suitable transfer loading (Albrektsson & Johansson, 2001; Bose *et al.*, 2012).

The requirements for properties described above are fulfilled by autologous bone grafts, and in addition, no immune response is triggered by these grafts, meaning that the

approach represents the gold standard for repairing and regenerating bone (Damien & Parsons, 1991; Triplett & Schow, 1996). Notwithstanding this, there are disadvantages linked with autologous bone grafts, including issues of chronic pain following operations to collect tissues for grafting (Damien & Parsons, 1991), morbidity and infections at the location where the tissue is taken (Kurz *et al.*, 1989; Younger & Chapman, 1989). In addition, cells may die during the transplant procedure, leading to the graft losing its potential for osteogenicity, and also there are limitations relating to constraints of supply in both children and individuals of advanced age, as well as those suffering from malignant conditions (Giannoudis *et al.*, 2005). Meanwhile, the availability of xenogeneic and allogeneic grafts is offset by the danger of immune response in such approaches (Pigott *et al.*, 2013), and while steps may be taken to minimise these responses, this has effects in terms of reduced bio-effectiveness (Oklund *et al.*, 1986). In response to the scarcity of naturally-occurring graft responses, research has presented various possible approaches. Some utilise naturally-occurring materials with biological activity, such as collagen or DBM, while others rely upon synthesised materials, which may be derived from metallic sources such as stainless steel, ceramics such as glass, alumina or calcium phosphate ceramics, polymers such as methyl methacrylate - PMMA or grafts using composites from these elements. Further alternatives include work to engineer tissue utilising various carriers in order to increase capability for regenerating tissue.

2.3 Tissue engineering

Tissue engineering is a field in which various disciplines interact. It combines knowledge of and technology for manipulating cells, as well as appropriate biochemical elements, with aspects of engineering for the generation of artificial tissues and organs, or the recreation of damaged tissues (Langer & Vacanti, 1993). Currently in the tissue-engineering field for bone, there are several approaches that are being used to seed cells onto structural templates known as scaffolds. One method consists of seeding cells on a biomaterial scaffold and directly implanting it into the body (Mendes *et al.*, 2002). The other approach involves seeding the cells onto a synthetic scaffold. This template is then incubated under artificial conditions (*in vitro*), then eventually implanted as a prosthesis into the body after maturation (Rabkin & Schoen, 2002). The process of regenerating the natural tissue takes place subsequently in the body. The structure becomes infiltrated

by blood vessels and the scaffold finally degrades, leaving a newly formed tissue in position. Figure 2.5 illustrates the process of tissue engineering.

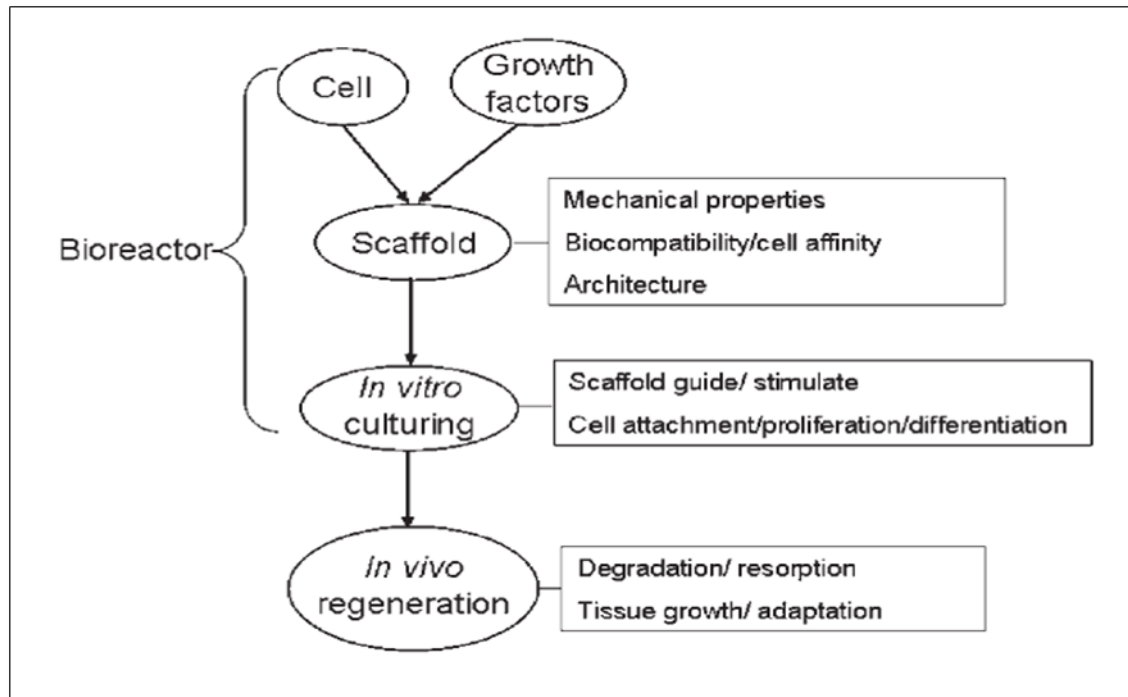


Figure 2.5 The general process of tissue engineering (Liu and Czernuszka, 2007)

2.4 Essential Requirements for Bone Scaffolds

The scaffold presents a framework that allows the cells to interact, proliferate, differentiate, and form an extracellular matrix (ECM) (Agrawal & Ray, 2001; Sachlos & Czernuszka, 2003), which provides structural integrity for the tissue. Moreover, the scaffold, in addition to acting as a support for the cells, also acts as a substrate through which growth factors and other bio-molecules can move or be transported.

It is necessary for the ideal scaffold to mimic the properties and structure of human bone, in order to control the macroscopic process of bone formation (Hutmacher, 2000). Based on this, it is essential that the scaffold should be stiff yet permeable, and offer mechanical resistance. Furthermore, it may be beneficial for a scaffold to be capable of degrading in a managed fashion post-implantation, as this will create voids into which new tissue can be generated.

These mechanical qualities in the scaffold are dependent upon the properties of the materials used as well as its structural porosity geometry, while the structure of the material controls the extent to which it is permeable. Stress shielding is avoided through

selecting materials for the scaffold which exhibit comparable mechanical qualities with the tissues for which it substitutes (Velasco *et al.*, 2015). Furthermore, the scaffold material must degrade at a similar speed to the pace at which tissue grows, in order to safeguard stability within the scaffold and tissue as the tissue regenerates (Bose *et al.*, 2012).

There is considerable complexity found in the biomechanics of regenerating bone, and varying designs for scaffolds are needed (Kolk *et al.*, 2012). Some major requirements which a design should fulfil are detailed below:

- I. The scaffold should be biofunctional, or function in the ways set out as required in the design process in substituting for normal tissue function in that area (Kolk *et al.*, 2012).
- II. The scaffold should be biocompatible, and allow the normal processes of cells to be continued, as with systems for molecular signalling for example. This should be maintained with no toxic impacts at either the location of the scaffold or in wider systems (Williams, 2008). Osteoconductivity should be achieved, with the scaffold capable of supporting the adherence and proliferation of bone cells as well as the formation of extracellular matrices on the surfaces and pore structure (Edalat *et al.*, 2012). Further, an important property of a scaffold is osteoinduction, facilitating bone to be formed by signals at the biomolecular level as well as recruitment of progenitor cells (Edalat *et al.*, 2012). Additionally, the scaffold should facilitate the creation of blood vessels within and/or around its structure in a time span of a small number of weeks post-implantation, as this is needed for active facilitation of transportation of waste, nutrients and oxygen (Giannitelli *et al.*, 2014).
- III. Bioresorption should be possible, or the scaffold should be biodegradable, giving the capability for degradation over time whether in vivo or in vitro. The speed of this should ideally be in line with the need for space to be created to accommodate new tissue growth (Lichte *et al.*, 2011). Thus, where cell proliferation takes place, the material of the scaffold should degrade at an analogous pace to create space, this is linked to the need for biocompatible materials which should not be toxic, and furthermore which the body should be able to metabolise and subsequently eliminate (Williams, 2008).

- IV. The scaffold must exhibit specific mechanical properties which match those of the tissue for which it is substituted. This includes matching of tensile strength, aselastic modulus, resistance to fracture, proportion of elongation and fatigue. This is to avoid osteopenia, losing bone tissue or stress shielding which can occur where bone is grafted (Lichte *et al.*, 2011). Bioresorption is also implicated here, as while the materials degrade, they should maintain mechanical properties at a level suitable to the stage of regeneration. The scaffold requires to be strong enough to maintain structural integrity adequate for the functions required of it, bearing loads and being as hard as the bone for which it substitutes (Olszta *et al.*, 2007; Woodard *et al.*, 2007).

2.4.1 Porosity and Interconnectivity

Porosity is the percentage of void space in a solid material, as defined by Karageorgiou and Kaplan (2005). There are two types of pores. The first type consists of pores that are connected to each other and to the surfaces of the solid, which are known as open pores. The second type consists of closed pores that are isolated and do not have any connectivity to the surfaces of the solid (Ishizaki, 1998). A porous scaffold is both a prerequisite for and acts to enhance bone ingrowth, or formation of bone tissue within the implant, *in vivo* (Ge *et al.*, 2008). However, porosity also tends weakens the implant. Therefore, recommended pore sizes are at least 300 μm in diameter, to facilitate the transportation of nutrients and waste for formation of the vascular system, and eventually osteogenesis (Karageorgiou & Kaplan, 2005). Interconnected pores are, in general, considered essential for promoting ingrowth of bone into a scaffold (Karageorgiou & Kaplan, 2005; Lu *et al.*, 1999). Pore shape is equally crucial, as it can influence the attachment and survival of cells deep inside the scaffold (Holy *et al.*, 1999; Burg *et al.*, 1999). Consequently, interconnectivity and pore size are critical factors for ideal design (Mastrogiacomo *et al.*, 2006).

2.5 Materials Used to fabricate Bone Scaffolds

Researchers have already established that scaffolds for bone growth must be created from materials with the capacity to promote both proliferation and differentiation of bone cells, to allow complete integration (Marquis *et al.*, 2009). Biomaterials that are

used for scaffolds should be biocompatible and have appropriate surface qualities that favour the attachment, differentiation, and proliferation of cells (Liu *et al.*, 2007).

A range of materials including ceramics, and synthetic or natural biodegradable polymers have been used to manufacture scaffolds that meet these requirements. Table 2.1 displays a brief outline of the most frequent biomaterials being used for bone tissue engineering (Marquis *et al.*, 2009).

Table 2.1 Typical features of biomaterials*

Materials	Main Advantage	Main Disadvantage	Types	References
Inorganic Materials	Biocompatible Osteoconduction Osteointegration Similar to bone Resorbable or non-resorbable	Osteoinduction Brittle Difficult to mould in 3D Exothermic	HAp**	(Koempel <i>et al.</i> , 1998; Jin <i>et al.</i> , 2000)
			TCP**	(Gao <i>et al.</i> , 1996)
			Porous coralline	(Gao <i>et al.</i> , 1996)
			Calcium phosphate cement	(Edwards <i>et al.</i> , 2004; Seeherman <i>et al.</i> , 2004)
			Octocalcium phosphate	(Seeherman <i>et al.</i> , 2004)
			Apatite-wollastonite	(Seeherman <i>et al.</i> , 2004)
			Bioactive glass	(Polak <i>et al.</i> , 2002)
			Ti	(Aparicio <i>et al.</i> , 2002; Spoerke and Stupp, 2003; de Oliveira and Nanci, 2004)
Natural Polymers	Biocompatible Osteoconduction Osteointegration Affinity for growth factors	Osteoinduction Pathogen agents transmission Difficult sterilization	Hyaluronic acid	(Seeherman <i>et al.</i> , 2004)
			Alginate	(Simmons <i>et al.</i> , 2004)
			Collagen	(Spira <i>et al.</i> , 2001; Geiger <i>et al.</i> , 2003)
			Starch	(Marques <i>et al.</i> , 2002)
			Chitosan	(Lee <i>et al.</i> , 2002)

Materials	Main Advantage	Main Disadvantage	Types	References
Synthetic Polymers	Osteoconduction Osteointegration Reproducible manufacture Readily tailored controlled-release properties Easy sterilization	Breakdown products Cell recognition Osteoinduction Possibility of protein denaturation by solvents or crosslinker	Oligo(PEG fumarate)	(Holland <i>et al.</i> , 2004)
			Poloxamer	(Clokie and Urist, 2000)
			Poly(alpha-hydroxy acids)	(Hollinger and Leong, 1996)
			PLA	(Zegzula <i>et al.</i> , 1997; Lee <i>et al.</i> , 2002)
			PGA	(Whang <i>et al.</i> , 1998)
			Poly(ortho ester)	(Daniels <i>et al.</i> , 1994)
			Polyanhydride	(Lucas <i>et al.</i> , 1990)
			Polyphosphazene	(Laurencin <i>et al.</i> , 1993)
			Polyphosphonate	(Richards <i>et al.</i> , 1991)
Composite Materials	A variety of materials	Complex manufacturing process	Collagen – Bioactive glass	(Eglin <i>et al.</i> , 2006; Bergeron <i>et al.</i> , 2007)
			Collagen – HAP – Alginate	(Sotome <i>et al.</i> , 2004)
			Starch – Bioactive glass	(Silva <i>et al.</i> , 2005)
			PLA – Chitosan	(Lee <i>et al.</i> , 2002)
			PLA – PEG – HAP	(Tamai <i>et al.</i> , 2005)
			PLA – PEG – <i>p</i> dioxanone	(Saito <i>et al.</i> , 2005; Kato <i>et al.</i> , 2006)
			PLGA	(Higuchi <i>et al.</i> , 1999)
			PLGA – Bioactive glass	(Lu <i>et al.</i> , 2003)
			PLGA – PEG	(Saito <i>et al.</i> , 2003)

*adapted from Marquis *et al.* (2009)

** HAp: hydroxyapatite, PEG: polyethylene glycol, PGA: polyglycolide, PLA: polylactide, PLGA: poly DL-lactide-co-glycolide, TCP: tricalcium phosphate.

Apatite-wollastonite glass-ceramic (AW-GC) scaffolds are the focus of this thesis. Ceramics have been used as substitutes for bone in two forms, either as granules or in bulk. Presently, bioactive glass-ceramics play a significant function in the regeneration of bone (Kokubo, 2008). Synthetic hydroxyapatite (HA), Ceravital®, Bioglass®, β -tricalcium phosphate (β -TCP), and apatite-wollastonite glass-ceramic (AW-GC) aid bone graft healing processes and are capable of forming a direct connection to living bone (Oonishi *et al.*, 1999; Oonishi *et al.*, 2000).

Bioglass®, Ceravital®, and β -TCP have not been used in the field of orthopaedic surgery, as their mechanical strength is not as great as that of human cortical bone (Kokubo, 2008). At present, synthetic hydroxyapatite (HA) is used extensively as a substitute for bone and as material for coating the joints of prostheses, as it is osteoconductive and bioactive (has the capability to form a direct union with the tissue of the living bone). However, in clinical practice, there is frequently a need for other similarly bioactive alternatives to HA with greater mechanical strength and the ability to form a stronger bond with bone during the early stages of implantation. This can allow patients to recover more rapidly, improving their ambulatory life. Consequently, AW-GC, which is both bioactive and stronger than HA, is used to manufacture a variety of spacers and prostheses that have been utilized in tumour and spinal surgeries (Kokubo, 2008).

AW-GC was developed by Kokubo and Yamamuro in 1982 (Kokubo *et al.*, 1982). Table 2.2 shows the chemical composition of this glass-ceramic product. Table 2.3 demonstrates that dense AW-GC has significantly higher compressive and bending strength than human cortical bone, whereas the bending strength of the cortical bone of a human is significantly higher than that of dense HA. With regard to bioactivity, after they are put in simulated body fluid (SBF) at body temperature, apatite formation usually takes ~7 d on AW-GC, whereas apatite formation takes 28 d on HA (as shown in Table 2.4) (Kokubo, 2008).

Table 2.2 The chemical composition of AW-GC*

Material	Weight %
MgO	4.6
CaO	44.7
SiO ₂	34.0
P ₂ O ₅	16.2
CaF ₂	0.5

*adapted from Kokubo (2008)

Table 2.3 Mechanical properties of natural bone and ceramics*

	Bending strength (MPa)	Compressive strength (MPa)	Elastic modulus (GPa)
Natural bone	30–190	90–230	3.8–17
Synthesized hydroxyapatite (HA)	110–170	500–900	35–120
A-W glass-ceramic	200–220	1000	120
Alumina polycrystal	300–400	2500–3000	350–380

*adapted from Kokubo (2008)

Table 2.4 Apatite formation on the surface of bioactive ceramics incubated in simulated body fluid (SBF) at 36.5 °C*

Ceramics	Apatite formation (d)
Bioglass	1
A-W-GC	5–7
TCP	14
HA	28

*adapted from Kokubo (2008)

2.6 Fabrication Techniques for Bone Scaffolds

Many techniques involving both conventional and advanced techniques have been proposed for scaffold fabrication.

2.6.1 Conventional Techniques for Bone Scaffolds

Conventional techniques for fabricating bone scaffolds include gas foaming (Mooney *et al.*, 1996), solvent casting particulate leaching (Mikos *et al.*, 1996), freeze drying (Hsu *et al.*, 1997), phase separation (Lo *et al.*, 1995), fibre bonding and fibre meshes (Cima *et al.*, 1991), emulsion freeze drying (Whang *et al.*, 1995), melt moulding (Thomson *et al.*, 1996), and solution casting (Schmitz & Hollinger, 1988). Unfortunately, each of these processing methods has a number of limitations. Researchers believe that it is impossible to precisely control pore interconnectivity, pore geometry, pore size, pore spatial distribution, and the construction of inner channels inside the scaffold using these techniques (Sachlos & Czernuszka, 2003; Yeong *et al.*, 2004). Additionally, many of these techniques require organic solvents such as methylene chloride or chloroform, which are not biocompatible, for dissolving synthetic polymers.

Organic solvent residues are a considerable problem for conventional techniques because of the carcinogens and toxins in the residual solvent to which the cells are exposed (Sachlos & Czernuszka, 2003). Table 2.5 outlines these conventional fabrication techniques, and explains the advantages and disadvantages of each method (Yang *et al.*, 2001).

Table 2.5 Conventional techniques for the fabrication of scaffolds*

Process	Material	Advantages	Disadvantages
Solvent casting and particulate leaching	- Polymers	<ul style="list-style-type: none"> - Large range of pore sizes - Independent control of porosity and pore size - Crystallinity can be tailored - Highly porous structures 	<ul style="list-style-type: none"> - Limited membrane thickness (3 mm) - Limited interconnectivity - Residual porogens - Poor control over internal architecture
Fibre bonding	- Polymers	<ul style="list-style-type: none"> - High porosity 	<ul style="list-style-type: none"> - Limited range of polymer - Residual solvents - Lack of mechanical strength
Phase separation	<ul style="list-style-type: none"> - Polymers - Ceramics 	<ul style="list-style-type: none"> - Highly porous structures - Permits incorporation of bioactive agents 	<ul style="list-style-type: none"> - Poor control over internal architecture - Limited range of pore size
Melt moulding	<ul style="list-style-type: none"> - Polymers - Ceramics 	<ul style="list-style-type: none"> - Independent control of porosity and pore size - Macro shape control 	<ul style="list-style-type: none"> - High temperature required for non-amorphous polymer - Residual porogens
Membrane lamination	- Polymers	<ul style="list-style-type: none"> - Independent control of porosity and pore size - Macro shape control 	<ul style="list-style-type: none"> - Lack of mechanical strength - Limited interconnectivity

Process	Material	Advantages	Disadvantages
Polymer/ceramic fibre composite foam	- Composite polymer and ceramic	- Independent control of porosity and pore size - Superior compressive strength	- Problems with residual solvent - Residual porogens
High-pressure processing	- Ceramics	- No organic solvents	- Non-porous external surface - Closed-pore structure
Freeze drying	- Polymers - Ceramics	- Highly porous structures - High pore interconnectivity	- Limited to small pore sizes

*adapted from Yang *et al.*, (2001)

2.6.2 Additive Manufacturing Techniques for Bone Scaffolds

With the goal of finding alternative methods for scaffold manufacture, a group of new techniques known as *Rapid Manufacturing* (RM) or *Additive Manufacturing* (AM) techniques has recently been presented to the field of tissue engineering. The RM technique depends on computer-aided designs (CAD). The CAD design saved as STL file format. STL file format is taken from the term for the oldest technology of rapid prototyping, stereolithography, and has since been accepted as the benchmark for the industry. The CAD data is transferred into a sequence of cross-sectional layers. Subsequently, various processes apply the computer-generated two-dimensional layers to create a solid model. From the bottom to the top, each layer is bonded or otherwise glued to the preceding one to produce a solid model of the item that is presented on the computer screen (Webb, 2000). The principle of RM is illustrated in Figure 2.6.

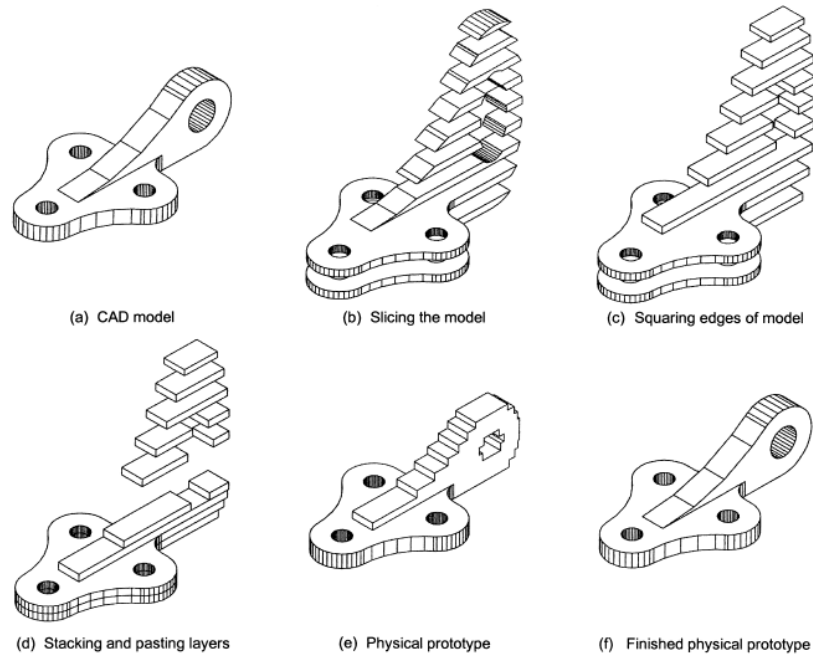


Figure 2.6 The principle of RM (Karunakaran *et al.*, 2000)

2.6.2.1 Additive Manufacturing Processes

2.6.2.1.1 Stereolithography (SLA)

Stereolithography, patented in 1986 (Nagarjan *et al.*, 2008), is considered the original rapid prototyping (RP) process. Figure 2.7 depicts the SLA technique used to construct a 3D part using an ultraviolet (UV) laser to solidify the cross-section of the model whilst maintaining the other areas in a state of liquidity. Subsequently, the level of the movable table drops by a sufficient amount to allow an additional liquid resin layer to cover the solid polymer (Sachlos & Czernuszka, 2003; Peltola *et al.*, 2008).

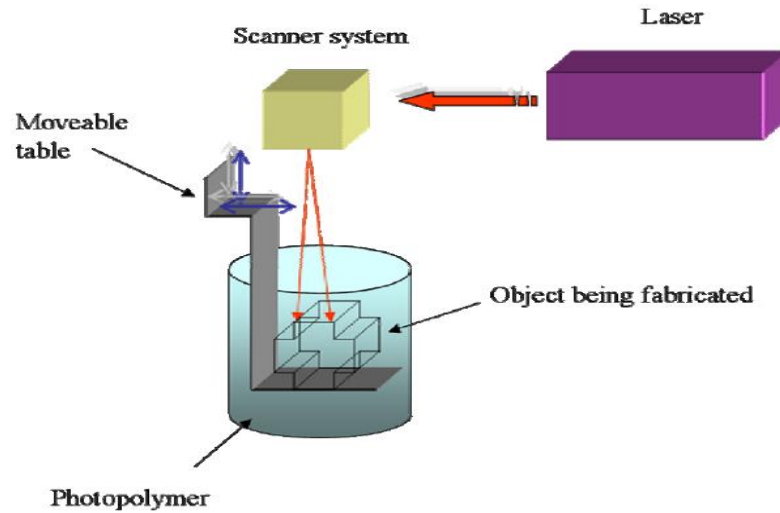


Figure 2.7 The process of stereolithography (Peltola *et al.*, 2008)

2.6.2.1.2 Fused Deposition Modelling (FDM)

Fused deposition modelling technology is used extensively in rapid prototyping. Figure 2.8 displays the FDM process. FDM employs a moving nozzle to extrude a polymeric fibre to build the physical model layer by layer (Sachlos & Czernuszka, 2003; Peltola *et al.*, 2008).

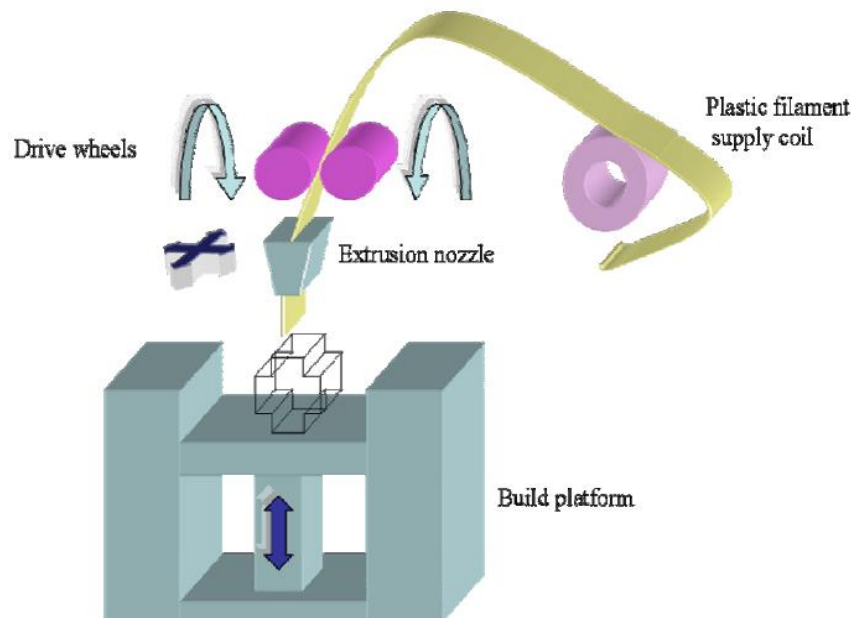


Figure 2.8 The process of fused deposition modelling (Peltola *et al.*, 2008)

2.6.2.1.3 Selective Laser Sintering (SLS)

As shown in Figure 2.9, a laser fuses powdered material by scanning cross-sections that are generated from the 3D digital description of the part onto the surface of the powder bed. Following the scanning of each cross-section, the powder bed drops by one layer of thickness, allowing one new coating of material to be added. The same process is reiterated until the desired part is completed (Sachlos & Czernuszka, 2003; Peltola *et al.*, 2008). SLS can be categorized into direct and indirect methods. In the indirect method the part depicted as a light green box in the upper right in Figure 2.9 is then sintered to improve its mechanical properties.

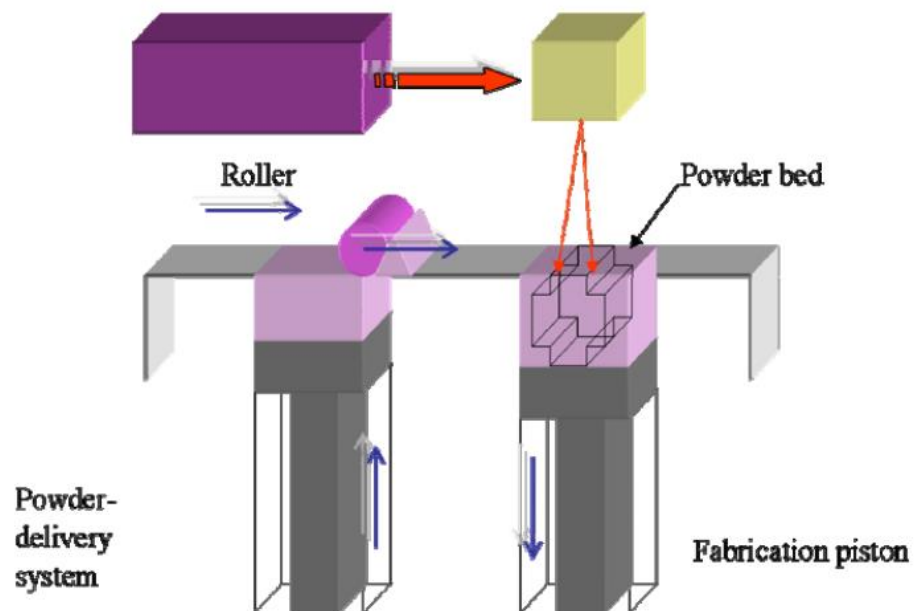


Figure 2.9 The process of selective laser sintering (Peltola *et al.*, 2008)

2.6.2.1.4 Three-Dimensional Printing (3DP)

There are two different technologies for 3DP currently found on the market. One approach uses technology for jet spraying of material, and the other uses a technology similar to ink-jet printing to allow printing onto powder materials. This process is schematically demonstrated in Figure 2.10. In steps 1 and 2, a rotating roller spreads a thin, homogeneous layer of powder and then slightly compresses it. Next, a liquid, as step 3 shows, is sprayed by the print head onto the top layer of the powder.

Subsequently, the liquid combines the powder particles together either through a reaction, phase change, or surface tension. At that time, the next layer is spread by the roller, as shown in step 4. The same steps are reiterated for each layer until the final layer is printed (Butscher *et al.*, 2011). When the 3D printing process is used *indirectly*, it makes what is known as a *green*, or unfinished, part that is then sintered, to fuse the powder into a solid yet porous structure.

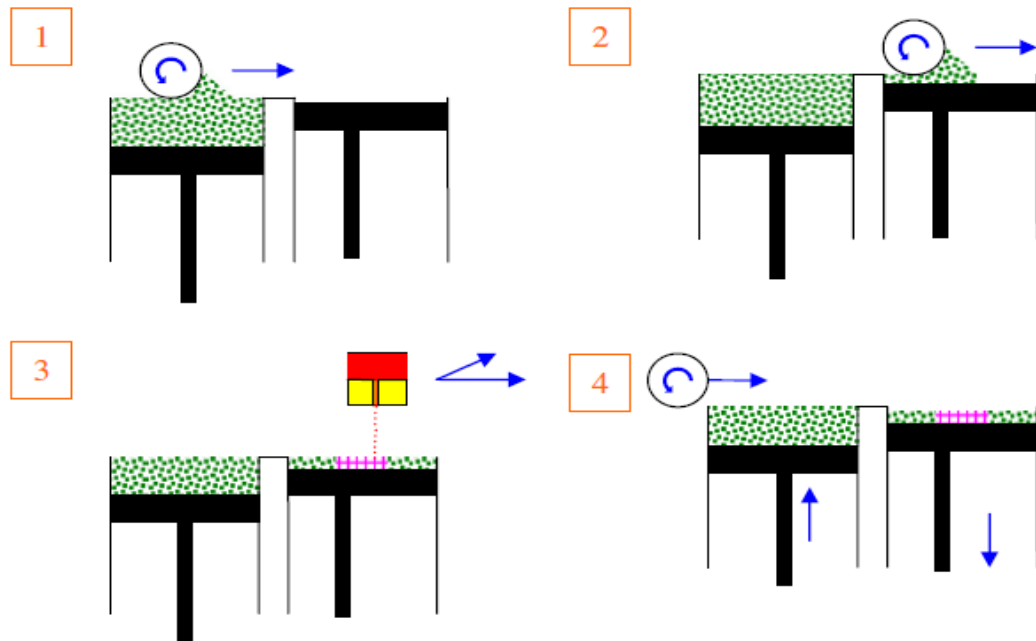


Figure 2.10 Three-dimensional printing processes (Butscher *et al.*, 2011)

2.6.2.1.4.1 3D Printing in comparison to different RM systems

3DP offers a flexible solution from a number of standpoints. First, in relation to materials, an extremely wide range of powders is suitable for the process when mixed with an appropriate binding agent. In theory, unlimited powder combinations might be bound into solid form with a range of binders. In order to provide an understanding of the possibilities which exist in 3DP, a comparison of this technique with others used in RP fabrication will be given.

3DP provides a comparable resolution to the majority of RM fabrication approaches (Bose *et al.*, 2013), with a lower limit for size of features at between 150-200 μm , dependent upon the combination of powder and binding agent (Lee & Wu, 2012). Stereolithographics (SLA) reach resolutions in the range of several microns only: however, this can only be achieved with certain initiators and polymers combined (Melchels *et al.*, 2010). It is possible to incorporate live cells into materials for this

technique, although free radical production on polymerisation may damage these (Melchels *et al.*, 2010). Among other approaches, Selective Laser Melting and Selective Laser Sintering and Selective Laser Melting offer a wider range of possible material in comparison with SLA as powders rather than liquid polymers are required (Yeong *et al.*, 2004; Utela, 2008). The laser offers a lower limit for spot size of approximately 60 μm , with the lower limit for size of features being greater. These methods do not offer the possibility to use live cells or organic elements, as the process involves strong heat levels being undergone (Bremen *et al.*, 2012).

Another approach, which uses a nozzle to deposit materials, is fused deposition modelling. For this, materials used are first prepared by melting or forming slurry suitable for spraying (Zein *et al.*, 2002; Yeong *et al.*, 2004). Therefore, temperatures for this technique may be the same as ambient or may be higher, with this flexibility giving the opportunity to incorporate various materials. Biologics have been used in this approach, both by spraying materials containing live cells and through seeding cells onto the pre-prepared structures (Yeong *et al.*, 2004). However, despite the varied advantages of these different methods, 3DP offers a more flexible solution than any other approach (Tsang & Bhatia, 2004).

3DP offers comparable or stronger resolutions than many RP systems, and has the added benefit of taking and developing advances in different areas, using powder processes comparable to those used previously before and after fabrication, but with the facility for creating more complex or previously unachievable forms (Lee & Wu, 2012). Ceramics and metal require analogous post-processes to those used in older techniques using powders, while avoiding the need for costly experiments. However, 3DP holds a disadvantage in that post-processes must be conducted and parts generally remain porous following the first temperature application, in comparison to the selective laser melting and sintering approaches which result in a sintered and less porous product not requiring post-processing (Sachlos & Czernuszka, 2003; Yeong *et al.*, 2004; Dimitrov *et al.*, 2006).

While powder processes are found in metals and ceramics, this is a less common approach for polymers, although it has a precedent in tissue engineering, which is adaptable for 3DP, and which allow it to modify rather than replace older processes for fabrication. Alternative RP approaches necessitate processes to be entirely replaced with new methods for new materials (Bose *et al.*, 2013).

2.6.2.1.4.2 3DP requirements

There is not presently a complete picture of the required properties of binding agents and powder materials for use in 3DP. This section provides a review of current understanding in this area.

The powder used must be able to flow in order that fine layers of material can be built up, as well as for removal purposes. Flow properties are determined by the form and size of particles in the powder (Irsen *et al.*, 2006). A good flow capacity means that fine, even layering is possible using a roller, allowing greater resolution levels in print solids, and this is necessary for the scaffold. Resolutions can usually be achieved at double the size of particles of powder (Butscher *et al.*, 2012) and therefore finer powders lead to greater resolutions. This is countered however by the tendency of finer and drier powders towards agglomeration, based on forces between particles becoming more influential than gravity and thus reducing flow (Zimmermann *et al.*, 2004; Castilho *et al.*, 2011). Depowdering processes also depend on flowability of the powder, with poor flows impeding the ability to remove particles from within the cavities and pores in the green print specimen, to the point where it may not be possible to completely depowder an item. A simple cavity must be 5 times larger in diameter than the mean particle size in the powder to facilitate depowdering (Butscher *et al.*, 2011). More complicated cavities and materials where cell structures are less regular may require a larger size difference.

The powder material must be stable to facilitate the spray and recoat process with the binding agent, Drops of approximately 30 μl of binding agent are sprayed at speeds of around 6 m s^{-1} (Arthur, 1996; Creagh & McDonald, 2003), creating a round pit with the drop in the centre.

While the recoat process is taking place, shear force impacts upon the upper powder layer, and this may cause displacement of fine print structures, with negative results for the end product's accuracy and integrity. In addition to powder being displaced laterally, it may also be displaced vertically as the forces of gravity cause compression (Lee *et al.*, 1995).

Powders suitable for 3DP should within certain wettability parameters to receive the droplets of binding agent, as this is essential for the structure's green strength and for accurate prints to be made (Uhland *et al.*, 2001). Where excessive wetting takes place,

the binding agent will spread and resolution will be poorer, while too little wetting with, for example, a highly viscous binding agent or too broad an angle of contact, reduces interdigitation of adjacent layers, impairing the mechanical strength in the green print object (Sachs *et al.*, 1992). The extent to which powders are wetted is affected by a range of factors. These include the angle of contact between binding agent and particles of powder, chemical interaction of binding agent and powder, how viscous the binder is and powder bed topography at its top level (Ming & Gibson, 2006). Therefore, the capacity for migration during flow is not simply reliant upon the characteristics of binding agents and powders, as it depends also on the rate at which the binders cure (Sachs *et al.*, 1992). However, there has been difficulty in achieving quantitative evidence on angle of contact in solid objects, with surface qualities impacting upon this (Madihally & Matthew, 1999; Hutmacher *et al.*, 2004). Powders present an even greater challenge in this regard, and research into particle-binding agent interactions has necessitated various techniques, including capillary rise, floating particle techniques and dynamical drop shape analysis (Chau, 2009). It is clear nevertheless that this area of study requires further development.

The reaction between binders and powders is of interest for 3DP due to strong reactivity impeding binder spread while minimal reactivity allows the binding agent to spread strongly (Bohner *et al.*, 2008). Therefore, the extent of and duration to the reaction are essential in creating accurate prints, as well as to strengthening the object through layering (Utela *et al.*, 2008). Further, where scaffolding created through 3DP are subject to sintering post-fabrication, where binding agent levels are excessive, this can lead to burning during this process. It is therefore important to keep binder levels to the minimum required for adequate mechanical strength to maintain a stable construction (Butscher *et al.*, 2011).

The strength of the structure on first printing but prior to being sintered or otherwise processed is known as green strength. This characteristic is central for print scaffolds (Lee *et al.*, 1995). Inadequate strength of the green structure can cause alterations in form and even structural failure. This strength can be affected by the weight of particles of powder which are not bound, and this can be an issue where scaffolds are not strong (Lee *et al.*, 1995). Green strength for printed parts is principally dependent upon: bond strength from particle to neighbouring particle; and bond strength from layer to layer (Uhland *et al.*, 2001; Yin *et al.*, 2008). The green body's mechanical characteristics

come from dual mechanisms for binding, which are mechanical interlocking and adsorption of binding agent (Butscher *et al.*, 2011).

2.6.2.1.4.3 Benefits and drawbacks of 3DP

3DP techniques offer an advantage in the range of powders which can be used, including ceramic materials, metal, composites and polymers (Stevens *et al.*, 2008; Utela *et al.*, 2008; Butscher *et al.*, 2011; Castilho *et al.*, 2011). In addition, the process is simple to customise and scale, and designs of considerable complexity may be fabricated without supporting structures being required (Hutmacher *et al.*, 2004) (Stevens *et al.*, 2008) Further, green parts can be fabricated without requiring high temperatures (Castilho *et al.*, 2011; Derby, 2012), while 3D design can be digitally managed, as can features on a macro-scale, including for instance connective channels embedded in the object (Hutmacher *et al.*, 2004; Stevens *et al.*, 2008). When considering particular uses for 3DP such as tissue scaffolds, the microporous nature of the product, which is caused by the way in which particles of powder are arranged, can be a great advantage (Madhally & Matthew, 1999; Hutmacher *et al.*, 2004).

Meanwhile, use of 3DP is also constrained by a number of disadvantages in its present state of development. Importantly, these disadvantages include the minimum size possible for features using 3DP based on powder, as dictated by the volume of drops of binding agent (Butscher *et al.*, 2011). A further issue is achieving the desired flow rate with powders flowability, the forces of compaction as applied to powder, and the possibility of the trapping of particles within cavities (Shanjani, 2011); (Hutmacher *et al.*, 2004; Butscher *et al.*, 2011; Derby, 2012). In general, the technique is not able to create features smaller than $500\mu\text{m}$ (Butscher *et al.*, 2011; Castilho *et al.*, 2011). Where conformal channels of high complexity are required, the inability to eradicate trapping of support materials from internal spaces becomes even more important.

In addition, 3DP fabricated parts need to be processed post-fabrication: possibly requiring to be sintered or densified under the application of heat, for example (Utela *et al.*, 2008). While a part is being sintered it is likely to shrink, and this may not occur uniformly, and thus may lead a part to crack: especially when producing scaffolds with high porosity. Further, in imitating bone, a difficulty arises in that the outer bone layers should be dense, and only approximately 10% porous, while the central area may be more than 50% porous, and the uneven shrinking which occurs while the part is

sintered creates major problems for such structures. During post-fabrication processes, a further issue is the need to remove powder which is loose within internal connecting pores, and this is especially problematic where pore sizes are less than 600 μm (Sachlos and Czernuszka, 2003). This loose powder can sinter with porous areas to reduce connectivity and decrease the size of pores.

Additional specifications becoming known for 3DP using powder include: the need to use a single uniform size and type of powder in fabrication; even and continuous forces of compaction while distributing layers of powder; use of a uniform thickness for each layer and across one part; and low controls on binder volume greyscale gradient in a layer (Venuvinod & Ma, 2013).

To summarise, the benefits of AM fabrication techniques are clear when creating low numbers of parts or one-off orders (Yeong *et al.*, 2004). Within AM, the versatility of 3DP has gained it popularity in use for scaffolding in engineered bone tissue, as it is capable of producing precisely-shaped scaffolding and managed and connected structures with specified porosity (Bose *et al.*, 2013). The features of the processes involved allow an extremely wide range of materials to be fabricated, but difficulty remains in appropriate choice of binding agent, and combinations will need to be optimised through a time-consuming process if fabrication of good quality parts is to come from this technique (Utela *et al.*, 2008). Considering binding agents, organic materials have been shown to be effective, but may have impact upon plastics in the 3DP machine when used over a long period. Binder residues can pose a challenge for removal in the sintering process, and this has particular implications when using biologics (Bourell *et al.*, 2011). Further, for accurate and high resolution 3DP, a specific gap is required from pore to pore reliant on the specifications of the structure and on powder properties. This affects the ability to produce scaffolds with high levels of porosity and a size of lower than 500 μm for sintered pores (Khalyfa *et al.*, 2007).

2.6.2.2 Advantages and Disadvantages of RM Processes for Bone Manufacture

Common RM systems such as stereolithography (SLA), fused deposition modelling (FDM), selective laser sintering (SLS), and three-dimensional printing (3DP) have been found suitable for manufacturing porous structures that can be used for tissue engineering. In this domain, it is important to be able to manufacture 3D scaffolds with different geometric shapes, to repair defects in or injuries to natural bone. Table 2.6 demonstrates the main features of the RM techniques that are currently used for fabrication of bone scaffolds. In addition, these RM fabrication techniques are feasible for the design and creation of bone implants specifically for a certain patient (Dean *et al.*, 2003). Table 2.7 illustrates the mechanical properties of printed parts using RM techniques.

Table 2.6 Advantages and disadvantages of RM methods

RM Technique	Advantages	Disadvantages	Reference
SLA	- easy to remove support material	- Limited choice of photopolymerizable and biocompatible liquid polymer materials	(Yang <i>et al.</i> , 2002)
	- Perfect small features		
FDM	- No material trapping within small features	- Requires support material for irregular structures	(Zein <i>et al.</i> , 2002)
	- Good mechanical strength	- Anisotropy between XY and Z direction	
	- Solvent free		
	- Low cost		
SLS	- Good mechanical strength	- High temperatures during process	(Tan <i>et al.</i> , 2003)
	- Wide range of material	- Trapped material is difficult to remove	
	- Solvent free		
3DP	- Wide range of material	- Trapped material is difficult to remove	(Lam <i>et al.</i> , 2002)
	- Low heat effect on raw material	- Weak bonding between powder particles	
	- Low cost	- Lack of mechanical strength	
	- Fast processing	- Rough surface	

Table 2.7 Mechanical properties of printed parts using rapid manufacturing (AM) approach

RM Method	Material (powder)	Sintering conditions	Total porosity (%)	Sintered Compression strength (MPa)	Sintered flexural strength (MPa)	Reference
3DP Zcorp (Z400)	Porous hydroxyapatite/Apatite-wollastonite (HA/AW)	1200°C, 3 h	51.49±1.21	-	21.01±0.09	(Suwanprateeb <i>et al.</i> , 2009)
		1300°C, 3 h	2.50±0.12	-	76.82±4.35	
3DP	Hydroxyapatite	1200°C, 2 h	-	21.2±2.2	-	(Seitz <i>et al.</i> , 2005)
3DP Zcorp (Z402)	Tetracalcium phosphate/ β -tricalcium phosphate (TTCP/ β -TCP)	1200°C, 6 h	36	1.3±0.1	-	(Khalyfa <i>et al.</i> , 2007)
3DP Zcorp (Spectrum Z510)	Calcium phosphate	134°C, 2 h	28-35	-	3.9-5.2	(Klammert <i>et al.</i> , 2010)
3DP Zcorp (Designmate CX)	β -tricalcium phosphate/45S5Henchglass [®] (β -TCP/BGH)	1000°C	-	-	14.9±3.6	(Bergmann <i>et al.</i> , 2010)
SLS	Apatite-wollastonite	779°C, 1 h & 1150°C, 1 h	40	-	65.97±5.4	(Xiao <i>et al.</i> , 2008)

2.7 Summary

Understanding human bone structure is very important for fabricating ideal artificial bone scaffolds. Scaffolds must mimic the structure and properties of human tissue. Interconnectivity, pore size, and suitable mechanical strength are critical factors for ideal scaffold design. In addition, biomaterials that are used for scaffolds should be biocompatible, biodegradable, and have appropriate surface qualities. Ceramic, glass ceramic, and polymers are the most common materials that have been used to manufacture bone scaffolds to date. Many manufacturing techniques have been used for scaffold fabrication, such as conventional techniques or additive manufacturing techniques. With conventional techniques, it is impossible to control pore interconnectivity and the average pore size of the scaffold. On the other hand, additive manufacturing techniques, which depend on computer-aided design to fabricate scaffolds, allow more control of the interconnectivity and porosity of fabricated structures.

Chapter 3

Materials and Methods

To date, various methods have been developed to fabricate porous scaffolds. In recent studies, apatite-wollastonite (A-W) glass ceramic powder has been used to produce porous scaffolds because it has good biocompatibility, bioactivity, chemical stability, and high mechanical strength properties (Cao *et al.*, 2008). In the present study, an indirect method of Additive Manufacturing (AM) known as 3D printing (3DP) was adapted for the manufacture of porous apatite-wollastonite scaffolds. The 3DP approach was chosen because it has a number of attractive features, such as the ability to manufacture complex shapes in different sizes and quantities with low cost. Figure 3.1 gives an overview of the final processes used to create A-W scaffolds using the ZPrinter 3D printing process (Z Corporation, Rock Hill, South Carolina, US) followed by infiltrating the A-W scaffolds with phosphate glass and PLA, and the sections that follow will describe these in more detail. A-W and maltodextrin (MD) powder mixtures were developed as the powder-binder system for the fabrication of green parts. The green parts were then sintered to generate functional parts. An initial study was performed to understand the processing conditions for this powder-binder system. The effectiveness of the printable binder system was demonstrated by printing various 3D parts for test specimens. A-W scaffolds with different concentrations of binder were characterised for shrinkage, density, porosity, and flexural strength. This chapter describes in detail the materials and equipment that were used in the present study.

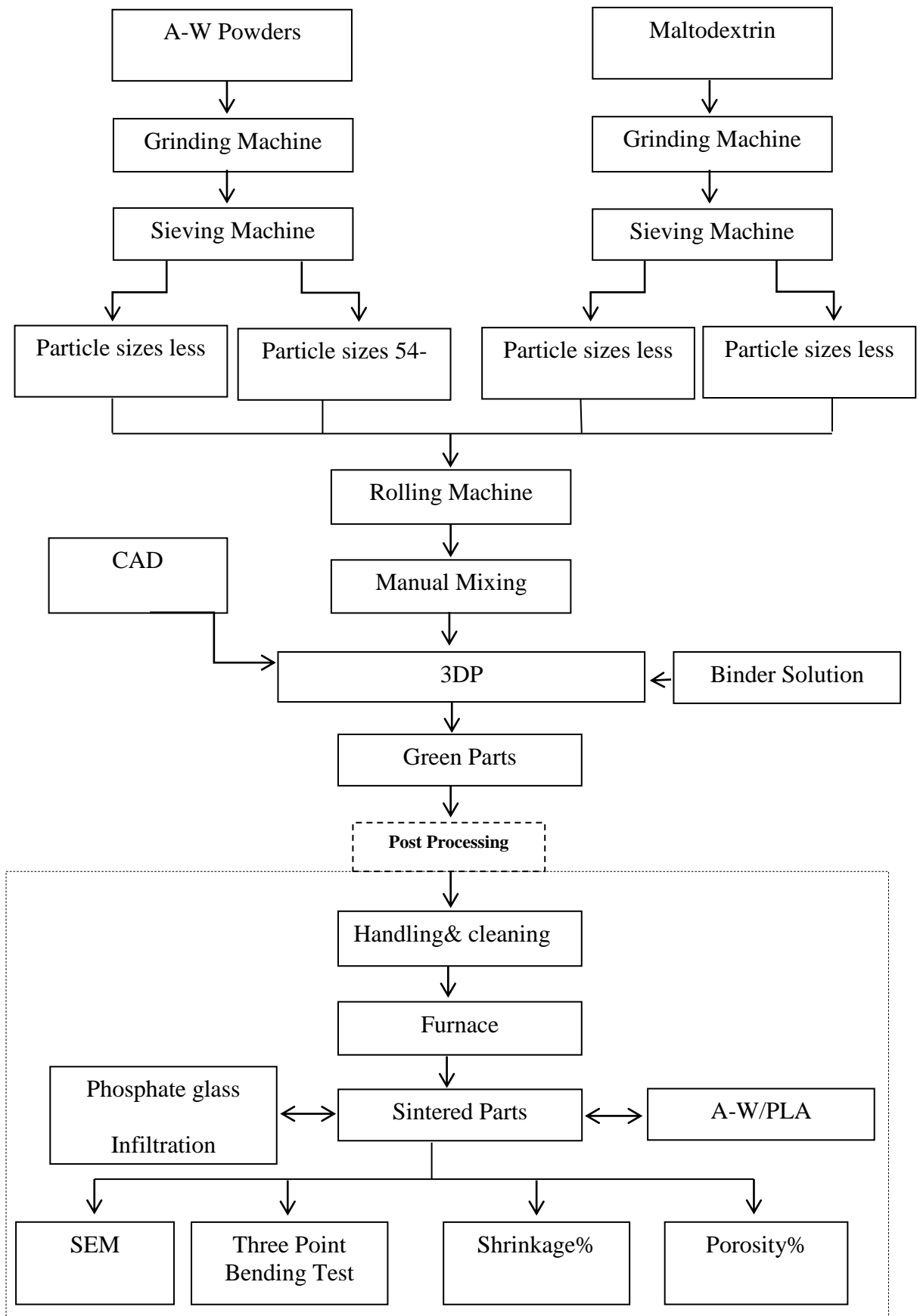


Figure 3.1 Overview of 3D Printing of AW Scaffolds

3.1 Materials

Several materials were used during the fabrication and infiltration processes of A-W scaffolds using 3DP.

3.1.1 Apatite-wollastonite powders

A-W frit and powders were supplied by GTS (Sheffield, UK). Table 3.1 displays the composition and weight ratio of A-W glass, as defined by Kokubo (Kokubo, 1991). The average particle size of A-W powders was approximately less than 100 μm , with a density of 3.078 g/cm^3 .

Table 3.1 Chemical composition (wt %) of A-W

Composition	Weight ratio (%)
MgO	4.6
CaO	44.7
SiO ₂	34
P ₂ O ₅	16.2
CaF ₂	0.5

3.1.1.1 EDX and XRD evaluation of A-W powder and sintered A-W

EDX analyses were conducted on the A-W powder and sintered samples fabricated using PB5 in order to ensure that the chemical composition is similar to Kokubo's formulation (Table 3.2 and Figure 3.2).

XRD analysis was done for sintered A-W samples and the phases was obtained are shown in Figure 3.3 and Table3.3.

Table 3.2 EDX results of the A-W powder and sintered A-W

Element	Norm. wt%	
	A-W powder	Sintered part of PB5
Calcium	33.35	31.16
Silicon	16.93	18.86
Phosphorus	5.33	6.46
Magnesium	3.00	4.09
Oxygen	41.39	39.43

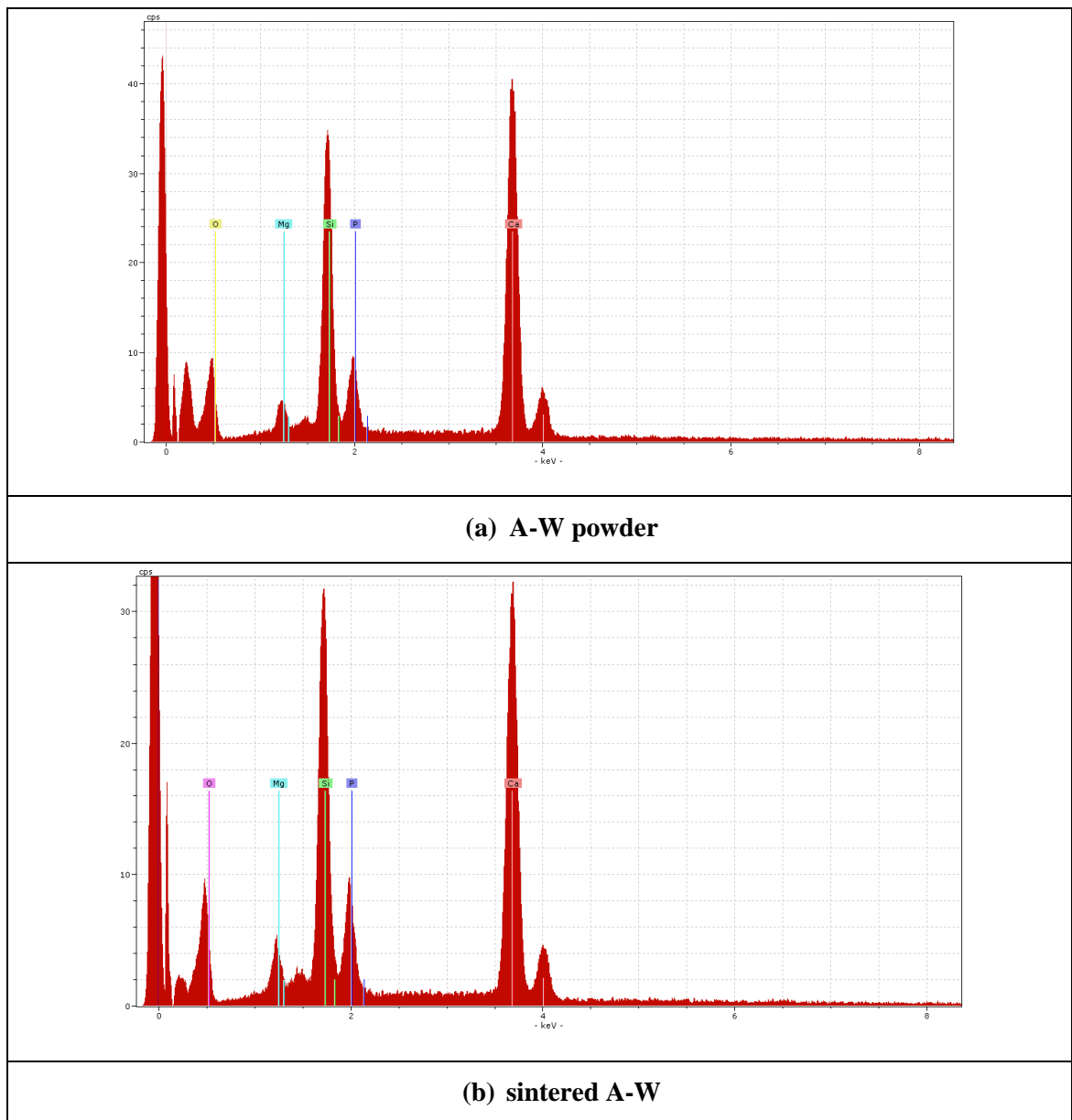


Figure 3.2 EDX results for A-W powder and sintered A-W

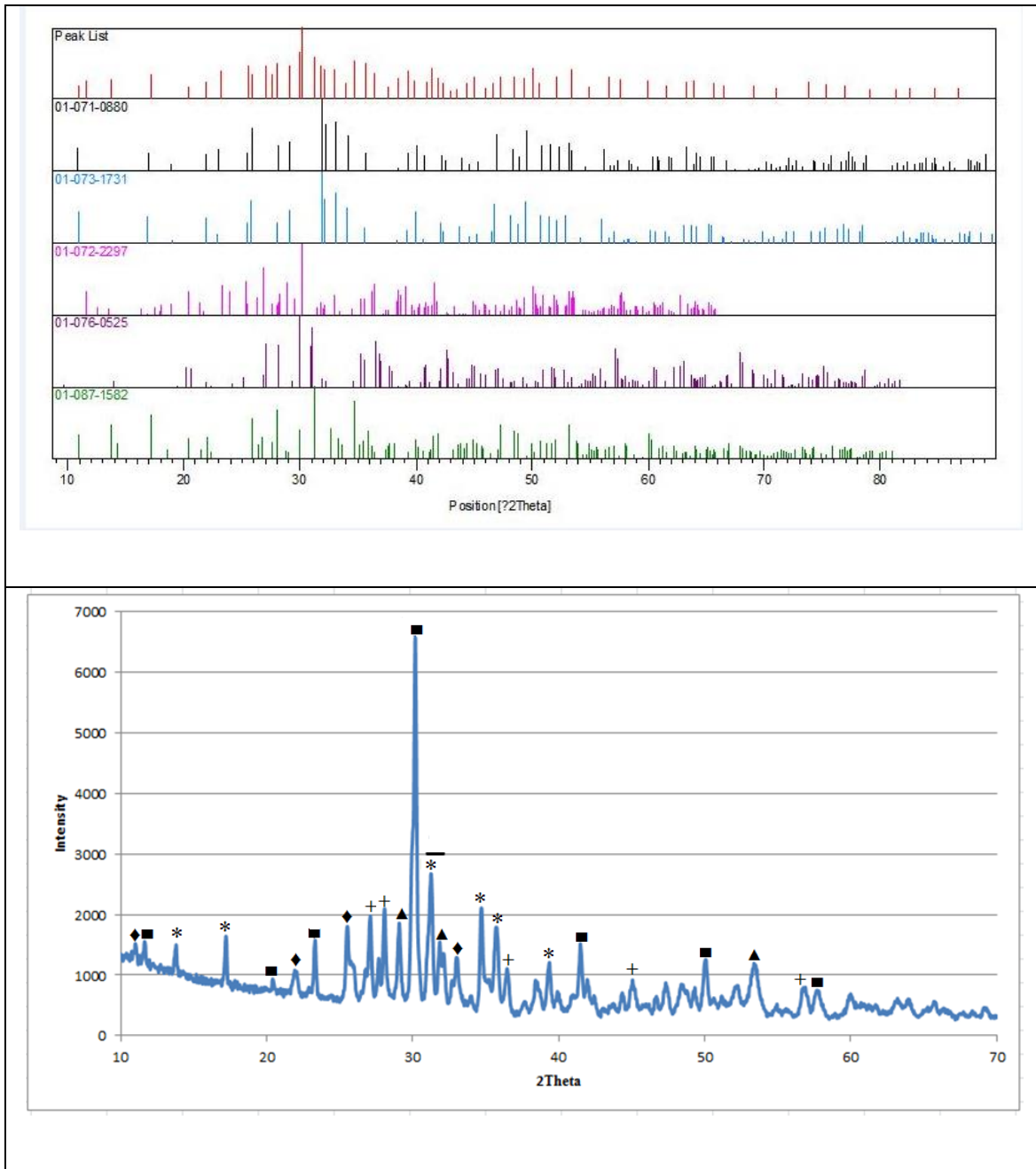


Figure 3.3 XRD pattern of the sintered AW

Table 3.3 Chemical compounds based on XRD database.

Ref. Code	Symbol	Compound Name
01-071-0880	▲	Fluorapatite
01-073-1731	◆	Hydroxylapatite
01-072-2297	■	wollastonite
01-076-0525	+	Calcium Magnesium Silicate non- stoichiometric
01-087-1582	*	Calcium Magnesium Phosphate non- stoichiometric

3.1.2 Maltodextrin Powders

Maltodextrin (MD) powders with a particle size range of 5-200 μm were purchased from Oneon (Bristol, UK) (purity = 99.5%). MD powders were used to react with liquid binder (DW, zb[®]60) to improve the bonding of A-W particles.

3.1.3 Polymers

Poly(lactic acid) (PLA) is one of the most common synthetic polymers used in medical applications. PLA discs have been fused together with A-W discs to form scaffolds. PLA 2.85-3.00mm filament was purchased from Technology Supplies Ltd. (Shrewsbury, UK), with density of 1.24 g/cm^3 , molecular weight (Mw) of 190802 Da and polydispersity index (PDI) of 1.22.

3.1.4 Phosphate glass powder

The phosphate glass was supplied by GTS (Sheffield, UK). The density of the phosphate glass was 2.60 g/cm^3 as measured using the digital scale and density kit (Archimedes' method). The composition and weight ratio for phosphate glass components are shown in Table 3.4.

Table 3.4 Chemical composition (wt %) of phosphate glass

Composition	Weight Ratio (%)
P ₂ O ₅	71.29
CaO	22.49
Na ₂ O	6.22

3.1.5 Zb[®]60 binder

The zb[®]60 clear binder solution was purchased from Technology Supplies LTD. The zb[®]60 solution was used to bind A-W particles during printing process. Table 3.5 illustrates the approximate composition of zb[®]60 as percent by weight.

Table 3.5 The approximate composition as percent by weight (%) of binder zb@60*

Component	Approximate weight %
Humectant 1	<10%
Humectant 2	<8.0%
Polymer	<4.0%
Water	85–95%

*(Technology Supplies LTD, 2007)

3.1.6 Distilled Water and Glycerol binder (DW)

The glycerol was purchased from Bilston Homebrew (Bilston, UK) (purity $\geq 99.5\%$). 98% distilled water and 2% glycerol were mixed together and used as a binder solution to bind A-W particles during printing process. The glycerol was used to increase the viscosity of the distilled water and to improve the printing process.

3.2 Powder Preparation

Powder blends of A-W and maltodextrin were prepared to fabricate scaffolds by indirect 3DP. Materials were ground and sieved separately and then mixed together in different weight ratios. First, a one-bowl ball mill machine (Planetary Mono Mill Pulverisette 6, Fritsch GmbH, Germany) (Figure 3.4) was used to grind A-W (frit, powder) and maltodextrin powder to the necessary fineness by friction and impact with tumbling balls. Approximately 200 g of A-W powders were put in the bowl of the milling machine, which was programmed for two repetitions of: rotational speed 400 rpm; milling time 5 min; pause time 5 min; reverse time 5 min.



Figure 3.4 The ball mill used to grind the A-W and maltodextrin into powders

Next, powders were sieved using a mechanical sieve shaker with sieves of sizes 53 and 90 micron (Impact Test Equipment Ltd) to give a range of particle sizes, as shown in Figure 3.5. For the present study, two different particle size ranges of A-W and maltodextrin powders were used: 0-53 μm and 54-90 μm .



Figure 3.5 The sieve shaker used to give a range of particle sizes of AW and maltodextrin

Finally, powders of A-W and maltodextrin were mixed using analogue tube rollers (Stuart, SRT6). The roller mixer has 6 rollers, analogue control, and fixed speed and provides “rocking and rolling” action for high-efficiency mixing. As large (>1 l) plastic containers are not appropriate for the roller mixer, small containers (500 ml) were used to mix the A-W and maltodextrin powders together. The various weight ratio mixtures of A-W and maltodextrin were divided into 3 equal portions (measured using a Lakeland digital scale balance to an accuracy of 1g). Each portion was placed in a small plastic container and mixed for 2 h on the roller mixer (Stuart, SRT6). After that, the contents of each of the 3 small containers were transferred to a wider container and mixed manually. Table 3.6 shows the seven powder blends each containing different weight ratios of A-W and maltodextrin and particles sizes that were prepared to investigate the processing parameters and suitability of 3DP for fabrication of porous scaffolds. PB1 contains A-W particle sizes in the range of 53–90 μm and 70% by wt. of A-W mixed with 30% by wt. of MD. PB2 contains A-W particle sizes in the range of 0–53 μm and 85% by wt. A-W mixed with 15% by wt. MD. PB3 contains A-W particle sizes in the range of 0–53 μm and 80% by wt. of A-W mixed with 20% by wt. of MD. PB4 contains A-W particle sizes in the range of 0–53 μm and comprised of 70% by wt. A-W mixed with 30% by wt. MD. PB5 contains A-W particle sizes in the range of 53–90 μm at 55% by wt. and A-W particle sizes in the range of 0–53 μm at 15% wt., mixed with 30% by wt. MD. PB6 contains 60% by wt. A-W particle sizes in the range of 53–90 μm and 10% by wt. A-W particle sizes in the range of 0–53 μm , mixed with 30% by wt. MD. PB7 contains 65% by wt. A-W particle sizes in the range of 53–90 μm and 5% by wt. A-W particle sizes in the range 0–53 μm , mixed with 30% by wt. MD. The selection of these powder blends based on (Xiao, 2007). Initially PB1, PB2 and PB3 were processed using DW binder. DW binder causes clogging of the print head of the 3D printer. As a result, DW binder was replaced by zb[®]60 binder for all printing processes.

The Z Corp. 3DP ZPrinter requires a minimum quantity of about 500 g of material to process into green parts. It is worth noting that the weighing of A-W and maltodextrin powders was taking three times using a Lakeland digital scale.

Table 3.6 Powder blends (PB) used for fabrication of green parts

	Material	A-W	Maltodextrin
PB1	Particle size (μm)	54-90	0-53
	Weight ratio (%)	70	30
	Average Quantity (g)	665	285
	standard error (SE)	0.17	0.15
PB2	Particle size (μm)	0-53	0-53
	Weight ratio (%)	85	15
	Average Quantity (g)	765	135
	standard error (SE)	0.13	0.09
PB3	Particle size (μm)	0-53	0-53
	Weight ratio (%)	80	20
	Average Quantity (g)	720	180
	standard error (SE)	0.12	0.15
PB4	Particle size (μm)	0-53	0-53
	Weight ratio (%)	70	30
	Average Quantity (g)	700	300
	standard error (SE)	0.06	0.03
PB5		54-90 (55%)	
	Particle size (μm)	&	0-53
		0-53 (15%)	
	Weight ratio (%)	70	30
	Average Quantity (g)	700	300
	standard error (SE)	0.06	0.03

Material	A-W	Maltodextrin	
PB6	54-90 (60%)		
	Particle size (μm)	&	0-53
		0-53 (10%)	
	Weight ratio (%)	70	30
	Average Quantity (g)	350	150
	standard error (SE)	0.06	0.07
PB7	54-90 (65%)		
	Particle size (μm)	&	0-53
		0-53 (5%)	
	Weight ratio (%)	70	30
	Average Quantity (g)	350	150
	standard error (SE)	0.06	0.04

3.3 Manufacture of Scaffolds

3.3.1 Preparing the 3D printer

A commercial ZPrinter 310 Plus 3D printer (Z Corp., USA) was used for all printing experiments in the present study. Samples of different shapes and sizes were designed using Autodesk Inventor Professional (CAD) software (Autodesk, USA). The CAD files were saved in *.STL file format, then transferred to the 3DP software that sliced the model into two-dimensional layers. The structures were then built layer by layer from the bottom of the part to the top. Figure 3.6 illustrates the main components of the Z 310 Plus printer that are most important for printing parts. There are some critical steps for preparing the ZPrinter to print accurate samples. The most important step is to remove any bubbles from the binder tube after filling the binder bottle. Then the black ink is purged out from the HP 10 print head. The next step is to prepare the build area. First, the feed container is filled with powder and the air removed from the powder by compacting the bed several times until it feels firm, by pressing the powder slowly with a tamp until a smooth, flat, and compact surface is obtained. Then, using the control

panel, the build piston is moved up until it stops and the feed piston is moved up until the surface of the powder reaches the top deck. Finally, the spread button is pressed to spread the powder onto the build area.

The ZPrinter 310 Plus uses a powder and binder system to build green parts. Two binder solutions were used for the 3D printing process in the present study: (i) 98% distilled water and 2% glycerol (DW) or (ii) the zb®60 clear binder solution from Z Corp.

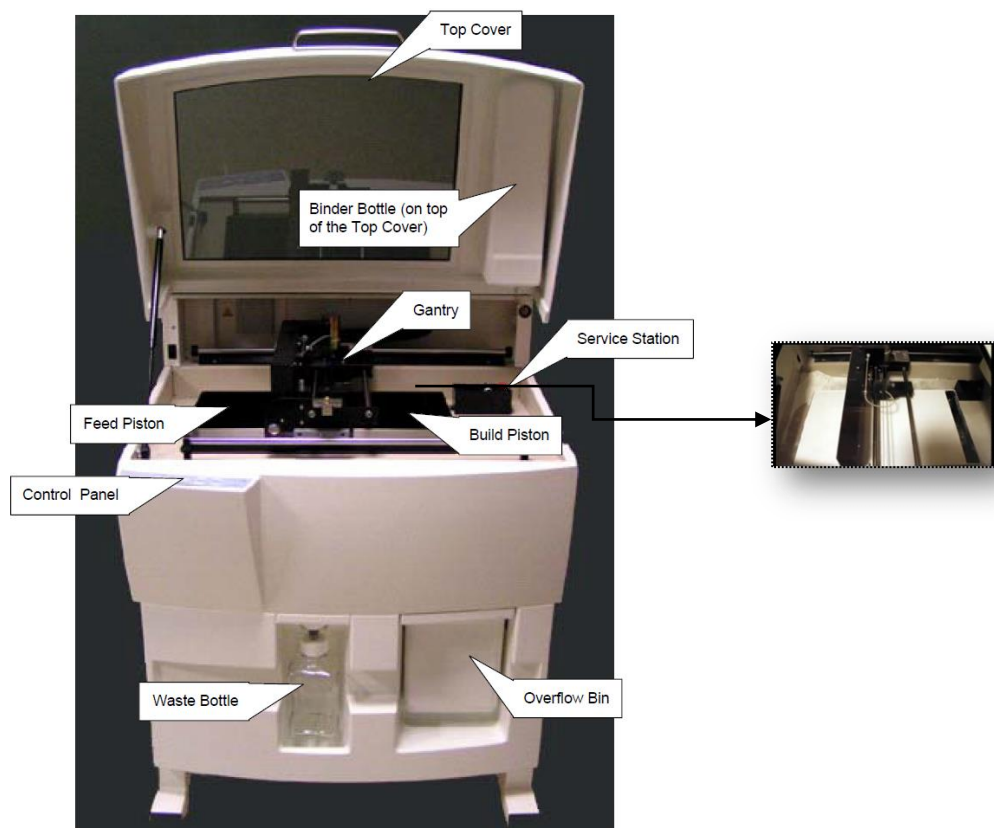


Figure 3.6 The main working components of a commercial Z 310 Plus 3D printer (Z Corp, 2009)

The Z 310 Plus software has some adjustable parameters that will affect the accuracy and strength of the part, such as the layer thickness, shell/core saturation levels, and bleed compensation. The layer thickness in the Z310 Plus printer can be adjusted between 0.0875 mm and 0.1 mm. In all printing processes for the present research, the layer thickness was adjusted to 0.1 mm. The shell and core saturation level refers to the ratio of binder dropped on the edges and surfaces of the part relative to its interior areas, as shown in Figure 3.7. The shell saturation level of the Z 310 Plus printer can be adjusted from 24% to 194% and the core saturation level can be adjusted from 0% to 200%. The bleed compensation is used if necessary to cut off a small amount of area from other areas of the part to limit binder spread into areas that should not become solidified. Table 3.7 shows the shell/core saturation, layer thickness, and bleed compensation levels that were used in the present study. This setting was based on (Khan, 2015).

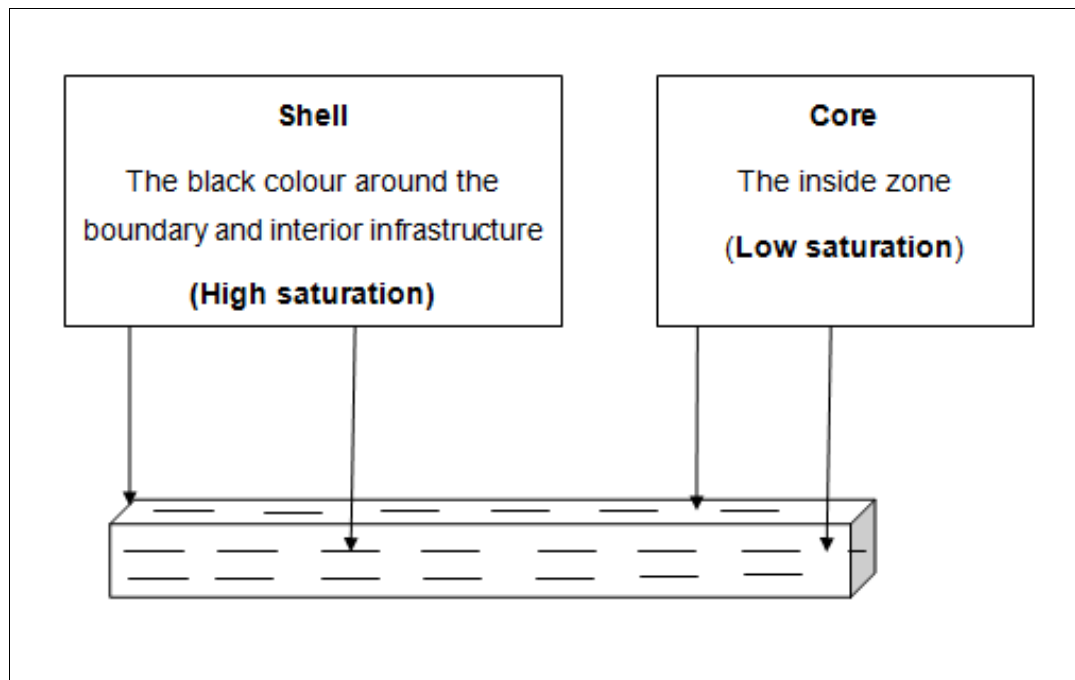


Figure 3.7 Definition of shell and core (The black line of the diagram denotes the high saturation)

Table 3.7 Powder and binder settings for the z 310 Plus printer

Setting	Layer Thickness (mm)	Shell		Core		Bleed Compensation		
		Saturation Level (%)	Binder/Volume Ratio	Saturation Level (%)	Binder/Volume Ratio	ON/OFF		
						X (mm)	Y (mm)	Z (mm)
A	0.1	100	0.214962	100	0.107481	Off	Off	Off

3.3.2 Post-processing

The indirect stage of the process begins after creating the green part by 3DP. The green parts have relatively delicate, weak structure at this stage. Prior to sintering, a soft brush, an air blower, and a needle were used to clean and remove any unbound powder from the printed structure, as shown in Figure 3.8.



Figure 3.8 The kit for cleaning printed structures

3.3.2.1 Sintering

The green parts were thermally post-processed to burn off the binder, to sinter the powder particles to obtain the desired mechanical properties, and to create a solid porous structure. The start point of the sintering process of A-W material was selected based on the protocol developed by (Xiao *et al.*, 2008), as shown in Figure 3.9. Heat treatment was carried out in two stages: increase temperature to 779 °C with a hold time of 1 h and a heating rate of 10 °C/min, and increase temperature to 1150 °C with a hold time of 1 h and heat rate of 10 °C/min. Then cool down to room temperature with natural rate of furnace. The green parts were sintered in a chamber furnace (Carbolite, 1200 °C, Company, City, Germany) in ambient air as illustrate in Figure 3.10.

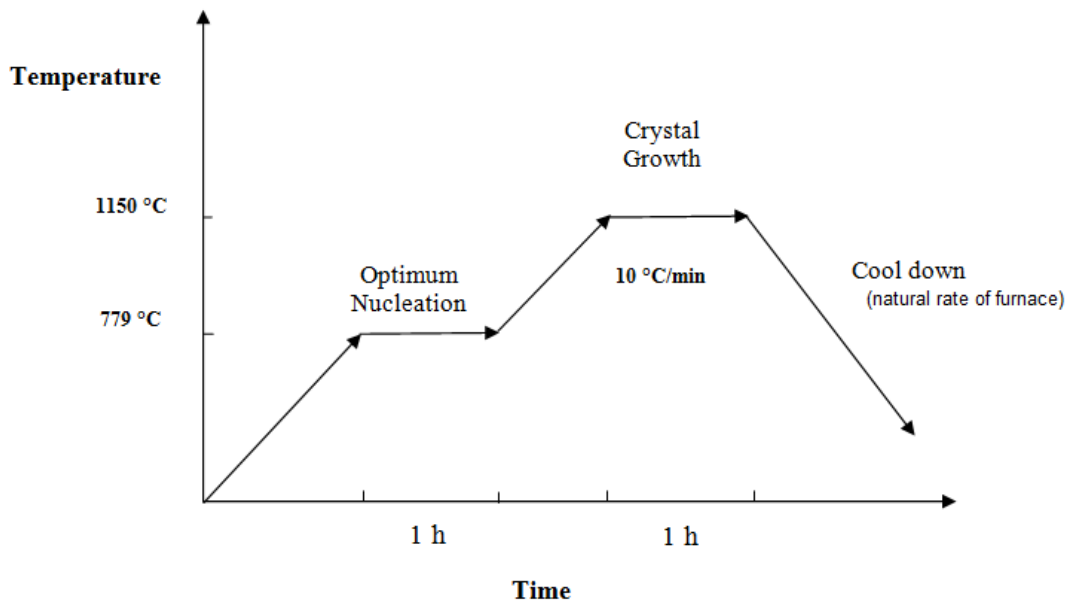


Figure 3.9 A-W Sintering cycle (Xiao *et al.*, 2008)



Figure 3.10 chamber furnace used for sintering AW green Parts

3.3.2.2 Infiltration

More than forty A-W sintered beams of PB5, PB6 and PB7 were infiltrated with a lower melting-point material. Phosphate glass was used to infiltrate the porous A-W structure. The phosphate glass was ground and sieved to particle sizes of less than 90 microns. Two possible methods of phosphate glass infiltration were then applied. In method A, the loose phosphate glass powder was directly placed onto the porous A-W part, and then the construct was placed into the furnace and heated from RT to 900 °C for 30 min at a heating rate of 5 °C/min. In method B, the phosphate glass powder was heated from RT to 600 °C for 30 min at a heating rate of 10 °C/min to form a phosphate beam shape, which was then placed onto the porous A-W part. The phosphate glass beam and the part were then placed into the furnace and heated to 900 °C for 30 min at a heating rate of 5 °C/min. All heat treatments for phosphate infiltration were based on (Xiao, 2007).

3.3.3 PLA Discs Printing Processes

PLA porous discs with 10.25mm diameter by 2.25mm height were designed using Autodesk Inventor Professional software (Autodesk, USA). The CAD files were saved in *.STL file format, then transferred to Cura (Ultimaker) software that sliced the model into two-dimensional layers with a defined thickness of 0.2 mm. After this process a gcode file is created. The gcode file sent to the Ultimaker printer (FDM). The Ultimaker printer uses a temperature controlled nozzle with 0.4mm diameter to extrude the PLA and deposit the semi-molten material onto a platform. The filament is moved by two rollers and acts as a piston to drive the material. After each printed layer, the platform is lowered and the next layer is deposited. The temperature and speed of PLA printing process were 210°C and 30mm/s, respectively.

The bonding of the PLA to A-W discs was performed in three steps. First, the A-W discs were put on a hot plate and pre-heated to 280⁰ C. Then the PLA structure was placed onto the top of the preheated A-W discs for five seconds. This allowed the bottom layer of PLA to partially melt into the surface of the A-W discs. Finally, the bonded A-W/PLA discs were quenched in alcohol before being left on a paper towel to dry.

3.4 Testing

3.4.1 Physical properties of DW and zb@60 binder solution

The binder materials used were assessed in terms of viscosity, surface tension and contact angle in order to assess their printability.

3.4.1.1 Viscosity

A rheometer (Kinexus rheometer, Malvern Instruments, Ltd., UK) was used to measure the viscosity of DW and Zb60 binder. Viscosity was determined as a function of frequency from 0.1Hz to 100Hz, at constant strain amplitude of 0.1%, at 25 °C.

3.4.1.2 Surface Tension and Contact Angle

A silicon wafer substrate was used in this test as the drop generator chamber and the orifice (nozzle) plate within the printhead are made from silicon (HP Technology, 2012). The contact angle and the surface tension were measured at room temperature. First, a silicon wafer substrate was cleaned by acetone and methanol. Following this, the

silicon was treated in oxygen plasma for 2 min at 80 W using a plasma system (Diener Electronic, Germany). The silicon was immediately transferred to the CAM 101 optical contact angle and surface tension meter (KSV instruments Ltd, USA) to measure the contact angle and the surface tension.

3.4.2 Accuracy and Shrinkage

The accuracy and consistency of samples of 3D-printed parts were measured using digital caliper and microscope as shown in Figure 3.11. Each dimension was measured three times and the mean value was recorded for calculating accuracy.

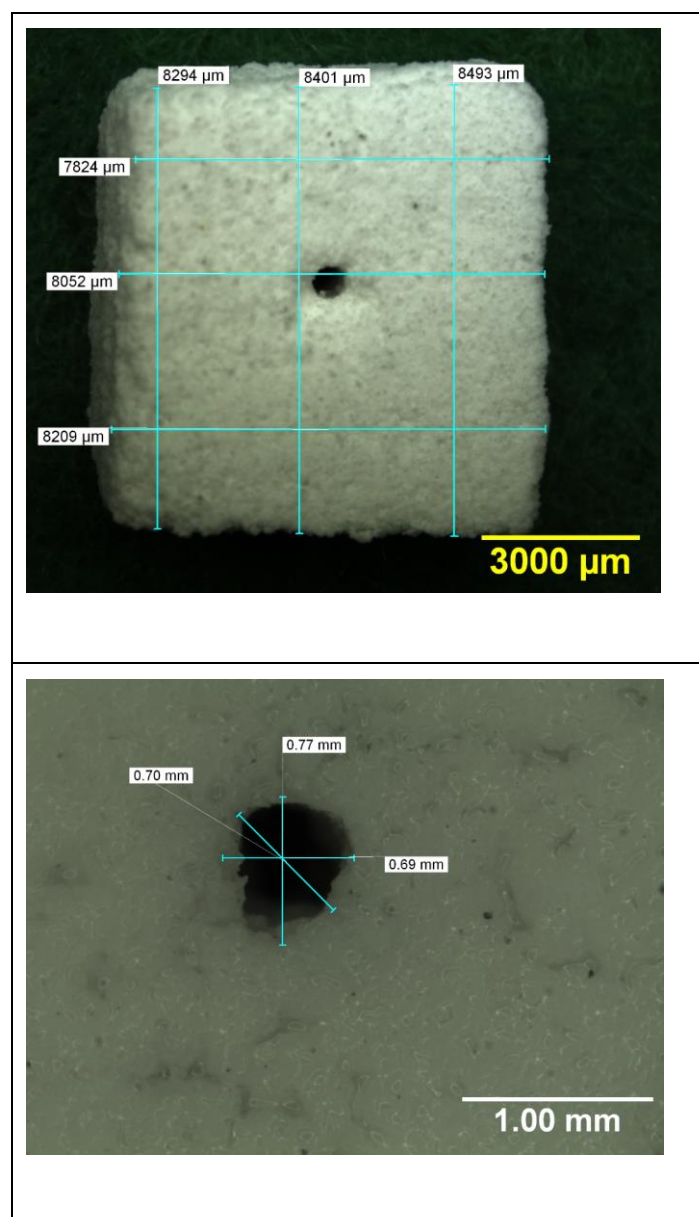


Figure 3.11 Measuring the samples using microscope

Sintering typically causes shrinkage of the specimens, so linear and volumetric shrinkage percentages were calculated according to the following equations:

$$\text{Linear Shrinkage}(\%) = \left(\frac{l_1 - l_2}{l_1} \right) \times 100, \quad (3.1)$$

where l_1 is the length of the sample before sintering (mm), and l_2 is the length of the sample after sintering (mm).

$$\text{Volumetric Shrinkage}(\%) = \left(\frac{V_1 - V_2}{V_1} \right) \times 100, \quad (3.2)$$

where V_1 is the volume of the sample before sintering (mm^3), and V_2 is the volume of the sample after sintering (mm^3). The volume of the samples before and after sintering was calculated by measuring the sample's dimensions with a Mitutoyo digital caliper (accuracy of ± 0.02 mm) (Mitutoyo Ltd, UK). Each dimension was measured three times, and the mean value of the measurement was used for the calculation of linear and volumetric shrinkage.

3.4.3 Specimen density and porosity

A digital scale (KERN ABT 220-5DM, 0.1mg, a maximum weight capacity of 220 g, Germany) was used for the present study. Each weight or dimension was measured three times, and the mean value of the measurement was used for the calculation of density and porosity.

3.4.3.1 Density of A-W Powder

The density of A-W powder was determined using the pycnometer method (Figure 3.12). The density of an object represents the mass per unit volume as the following equation:

$$\rho = \frac{M}{V}, \quad (3.3)$$



Figure 3.12 Pycnometer bottle

Four steps are needed to determine the density of A-W powder. First, the weight of an empty, dry pycnometer is determined (m_0). Second, the pycnometer is filled completely with distilled water and the mass is determined ($m_0 + m_d$). Third, the dry and clean pycnometer is filled to about 2/3 with A-W powder and the mass is determined ($m_0 + m_p$). Finally, the pycnometer with A-W powder is filled completely with distilled water and the mass is determined ($m_0 + m_p + m_d$). After that the following equation is used to determine the density of A-W powder:

$$\rho_{A-W} = \rho_d \times \frac{m_2}{m_1 + m_2 - m_3} \quad (3.4)$$

in which ρ_{A-W} is the density of A-W powder (g/cm^3), ρ_d is the density of distilled water at room temperature ($20\text{ }^\circ\text{C}$, $0.9982\text{ g}/\text{cm}^3$), m_1 is the mass of the liquid ($m_d - m_0$) (g), m_2 is the mass of the sample ($m_p - m_0$) (g), and m_3 is the mass of the sample and liquid together in the pycnometer ($m_p + m_d - m_0$) (g).

3.4.3.2 Apparent density

The apparent, or bulk, density of porous solids can be defined as the mass of material per unit external volume that includes the open and closed porosity of the object (Keulen, 1973). The geometric apparent density of all specimens was calculated by measuring the weight of a uniform-sized specimen with the following equation:

$$r_g = \frac{M}{V_g}, \quad (3.5)$$

where M is the mass of the sample (g), V_g is the external geometric (apparent) volume of the sample (cm^3), and ρ_g is the apparent density of the sample (g/cm^3).

3.4.3.3 Open Porosity

The open porosity of samples were determined by applying Archimedes' principle. The dry, wet, and submerged weights of specimen (M) were measured with a digital scale (KERN, ABT 220-5DM). The open porosity of each sample was then calculated using the following equation (BS EN 993-1, 1995):

$$\text{open porosity} = \frac{m_{\text{wet}} - m_{\text{dry}}}{m_{\text{wet}} - m_{\text{submerged}}}, \quad (3.6)$$

where M_{wet} is the wet mass of the sample (g), M_{dry} is the dry mass of the sample (g), and $M_{\text{submerged}}$ is the mass of the sample submerged in water (g).

3.4.3.4 Total Porosity

The porosity of sintered samples was determined by calculating the volumes of A-W and the geometrical volume of the specimen. The dry weight of specimen (M) was measured with a digital scale (Kern Analytical Balances, ABT 220-5DM). Then the volume of A-W and the porosity percentage of the specimen were calculated using the following equations (Maspero *et al.*, 2002):

$$V_g = L \cdot W \cdot h, \quad (3.7)$$

$$V_{AW} = \frac{M}{d_{AW}}, \quad (3.8)$$

$$\text{porosity}(\%) = \left(1 - \frac{V_{AW}}{V_g}\right) \cdot 100, \quad (3.9)$$

where V_g is the geometric volume of the sample (cm^3), L is the length, W is the width, and h is the height. M is the mass of the porous sample (g), and d_{AW} is the density of A-W (as reported in (Nicolodi, 2004)), which is equal to $3.078 \text{ g}/\text{cm}^3$.

3.4.4 Mechanical Properties Analysis

Bending test is very useful approach for the evaluation of porous glass-ceramic material. The flexural strength and Young's modulus of the A-W beams was evaluated using 3-point bending test. The dimension of the samples was measured using a Mitutoyo digital caliper (accuracy of ± 0.02 mm) (Mitutoyo Ltd, UK). Each dimension of the beams was measured three times, and the mean value of the measurement was used for the calculation of bending strength and Young's modulus.

3.4.4.1 Flexural strength

A 3-point bending test was carried out using an Instron 5567 testing machine (Figure 3.11). The setup was based on BS EN ISO 6872:2008 (BS EN ISO 6872, 2008), with a 1kN load cell, span length L of 30mm and a crosshead speed of 1 mm/min. The load was applied at the mid-point length of the sample (Figure 3.13). The test was carried out at room temperature. The sample's bending strength was calculated according to the following equation (BS EN ISO 6872, 2008):

$$\text{Bending strength stress: } f = \frac{3PL}{2bh^2}, \quad (3.10)$$

where P is the applied load (N), L is the test length (30mm), b is the sample breadth (mm), h is the sample height (mm), and f is the flexural strength (MPa), as depicted in Figure 3.14.

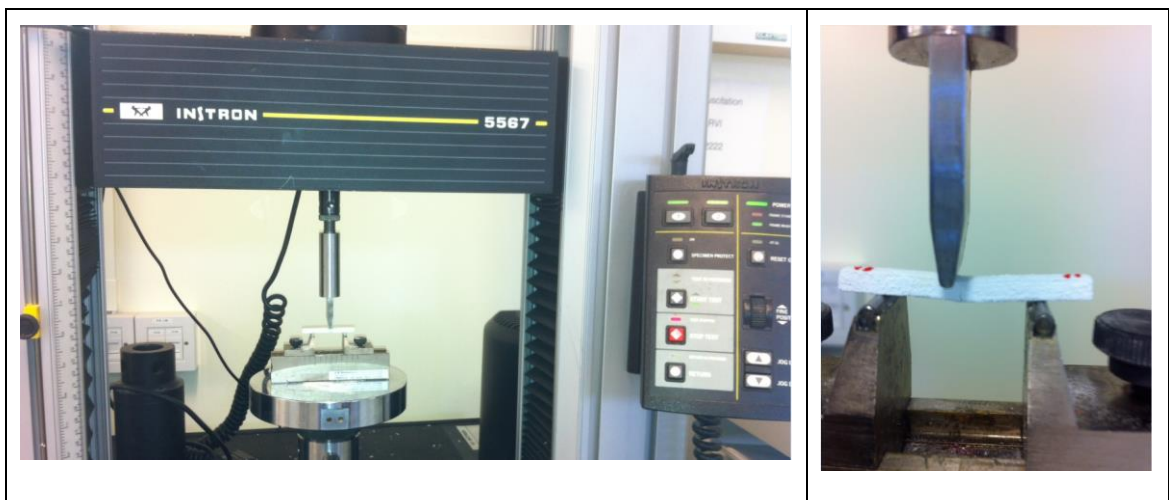


Figure 3.13 Three-point bending testing machine used to calculate A-W flexural strength

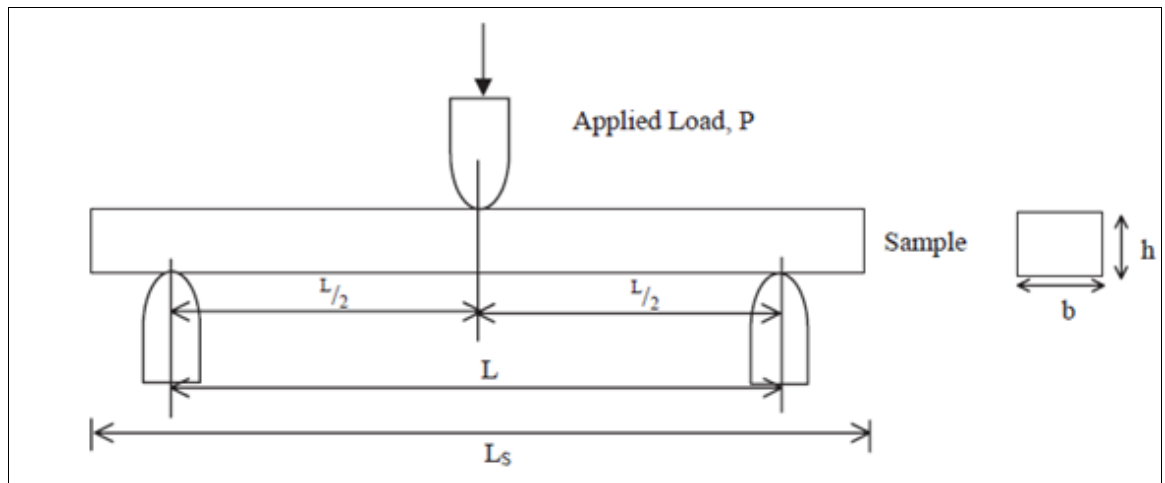


Figure 3.14 Three-point bending testing (Juhasz *et al.*, 2004)

3.4.4.2 Sample stiffness determined using Young's modulus

The stiffness of the samples was calculated from the slope of the graph of load versus displacement using the following equation.

$$E = \frac{M \times L^3}{4 \times b \times h^3}, \quad (3.11)$$

where M is the slope of a straight line of the load-deflection curve (N/mm), L is the test length (30 mm), b is the sample breadth (mm), h is the sample height (mm), and E is Young's modulus (GPa).

3.4.5 Scanning Electronic Microscopy (SEM)

An SEM analyser was used to examine A-W particles, and to observe the surface microstructure of materials and obtain images of their fine-scale surface topography to show how particles were being connected together. A SEM Philips XL30 ESEM-FEG was used for this research. The samples were mounted on the aluminium holder by means of a double sided sticky carbon tape and then coated with gold (Au). The SEM experimental conditions were 20 kV (HV), 7-8.5mm (WD) and 100x-500x magnification.

3.4.6 Microscopy

An Olympus micropublisher 5.0 RTV digital microscope camera was used to record images of the samples and to measure the small holes. The features of Olympus micropublisher were 2560 x 1920 pixels, 3.4 μ m x 3.4 μ m pixel size and 2/3" optical format.

3.4.7 Micro-Computed Tomography (micro-CT)

X-ray computed tomography is a reconstructive method in which x-ray absorption data governed by the density of a material are used to generate 3D images of the internal structure of an object. An Xradia VersaXRM-410 apparatus at Durham University was used to take 3D micro-CT images of samples to investigate their porosity. The micro-CT experimental conditions appear in each image.

3.4.8 Data Analysis and Statistical Test

All data analyses were performed using the Statistical Package for the Social Sciences (SPSS) for Windows, version 21 (SPSS Inc., Chicago, IL, USA). Data was described using descriptive statistics, the mean, median, minimum, maximum, standard deviation (SD) and standard Error of the mean (SE) were calculated to describe the numerical quantitative data.

Shapiro-Wilk and Kolmogorov-Smirnov tests were used to examine the normality. For the normally distributed data, T-test for independent samples was used for comparing two independent groups. In addition, Analysis of variance (ANOVA) was used to analyse the differences between the means of quantitative data, finally Tukey and Scheffe tests of a post hoc multiple comparison were used to get more comparison between each two samples to show which exact means of the samples have significantly different from each other. Kruskal-Wallis test was used for the non-normally distributed data. All the analysis tests were performed significant level $\alpha = 0.05$, and statistical significance ($p < 0.05$).

3.4.9 Bioactivity

A-W is a bioactive glass ceramic that can bond to living bone (Kokubo, 2008). An initial objective of the present project was to supply batches of scaffolds for further biological characterisation.

3.4.9.1 *In vitro* cell-compatibility assessment

Rat bone marrow-derived stromal cells (BMSCs) were seeded onto 8mm diameter x 2 mm high A-W discs (as shown in Figure 5.11) (10,000 cells/well). The cells were cultured for one, two, seven and 14 days in a humidified atmosphere of 5% CO₂ at 37 °C. The viability of BMSCs seeded on A-W compared with culture-plastic was assessed by MTT assay.

3.4.9.2 *In vitro* osteogenic differentiation

The osteogenic properties of AW discs were assessed by measuring alkaline phosphatase (ALP) activity of rat BMSCs seeded onto the discs.

3.4.9.3 *In vivo* evaluation of A-W and AW/PLA discs for non-load-bearing applications.

Calvarial critical size defect surgery was performed on 3 rats. This involves cutting an 8 mm diameter hole in the top of the calvaria to create the defect, then filling the defect with an 8 mm diameter scaffold. Two types of scaffold were used: A-W alone (discs as shown in Figure 3.15a) and AW/PLA composite (as shown in Figure 3.15b).

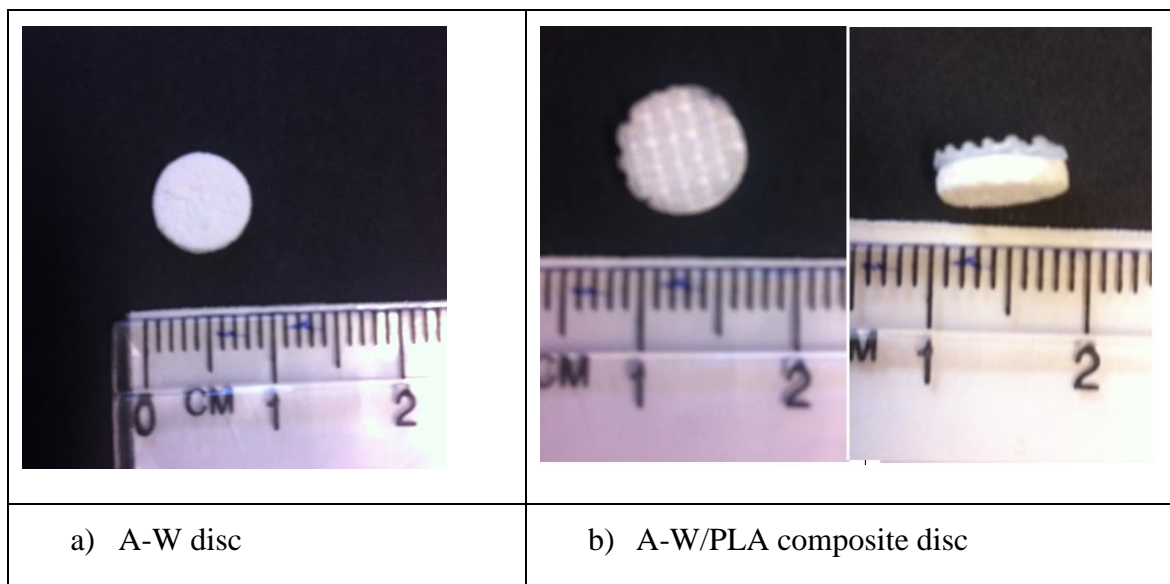


Figure 3.15 A-W and A-W/PLA composite discs (8mm diameter x 2 mm high)

3.4.10 Summary of the samples manufactured and post processes

Table 3.8 show the summary of the samples manufactured, post treatments and testing in this study.

Table 3.8 Summary of the samples manufactured and post processes

Printed Samples		Post process			Shrinkage	Test							
		Heat Treatment (779°C,1150°C,1h, 10°C / min)	Phosphate glass infiltration			Bending Strength	Young's modulus	Total porosity	Open porosity	Apparent density	Micro- CT	SEM	
			Method A	Method B									Green
Beams	PB1/DW	√			√	√	√	√	√	√	√		
	PB1/zb®60	√			√	√	√	√	√	√	√	√	
	PB2/DW	√			√	√	√		√	√	√		
	PB2/zb®60	√			√		√	√				√	
	PB3/DW	√			√	√	√		√	√	√		
	PB3/zb®60	√			√		√	√				√	
	PB4/zb®60	√			√	√	√	√	√	√	√	√	√
	PB5/zb®60	√	√	√	√	√	√	√	√	√	√	√	√
	PB6/zb®60	√		√	√	√	√	√	√	√	√		
	PB7/zb®60	√		√	√	√	√	√	√	√	√		

Printed Samples		Post process			Test								
		Heat Treatment (779°C,1150°C,1h, 10°C / min)	Phosphate glass infiltration		Shrinkage	Bending Strength		Young's modulus	Total porosity	Open porosity	Apparent density	Micro- CT	SEM
			Method A	Method B		Green	Sintered						
Beams	PB5/zb®60/InfilA	√	√			√		√	√			√	
	PB5/zb®60/InfilB	√		√		√		√	√		√		
	PB6/zb®60/InfilB	√		√		√		√					
	PB7/zb®60/InfilB	√		√		√		√					
Disc/PB1									√				
Disc/PB5											√		
Disc with four pockets/PB1									√		√		
Plug/PB5									√		√		
Plug with two through holes/PB5									√		√		
Plug with two through holes and one pocket hole/PB5									√		√		
Hollow cylinder/PB5									√		√		

Chapter 4

Process Characterisation and Mechanical Properties Development

A key aim of this study was to investigate the optimal strength of porous A-W scaffolds when fabricated by indirect 3DP. This investigation was undertaken in several steps. The first step was to examine the effect of the binder solution, A-W particle sizes, and the weight concentration of the MD binder on processing and mechanical properties. The second step was to examine the effect of build orientation on bending strength. Then in the third step, the effect of heat treatment and powder setting on bending strength and shrinkage was examined. Optimisation of powder particle sizes and relative concentrations and binder solution was then performed and their effects on mechanical properties were examined. Finally, the effect of infiltration of parts with phosphate glass on bending strength was evaluated.

4.1 Process Characterisation

4.1.1 Powder characterisation

Seven powder blends with different sized particles and weight concentrations were prepared, and the samples were printed by 3DP using the same powder setting and two different binder solutions. Figure 4.1 shows the morphology of A-W powders with particle sizes ranging from 0–53 μm and 53–90 μm , MD powders, and the blend of A-W and MD. A-W powders (Figures 4.1a and 4.1b) had sharp-edged particles with irregular shapes caused by the milling process, whilst MD powders (Figure 4.1c) had round-edged particles. Figure 4.1d shows a blend of these materials.

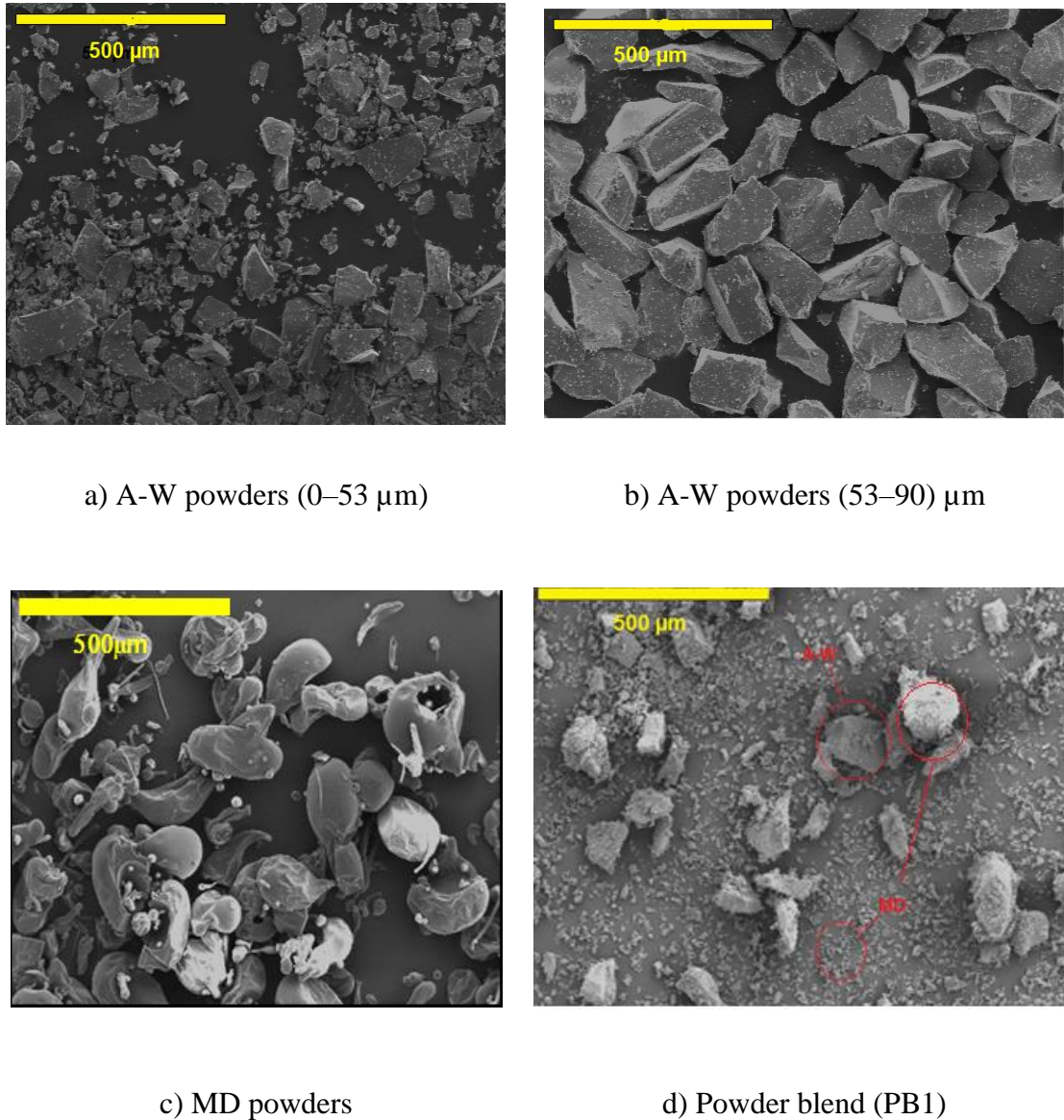


Figure 4.1 SEM micrographs of A-W, MD and Powder blend

4.1.2 Printing and handling characteristics

Table 4.1 shows the printing characteristics of A-W and A-W with MD blends in different weight concentrations and particle sizes. Seven powder blends were printed using the same powder setting on the 3DP, as illustrated in Chapter 3. One binder composed of 98% distilled water and 2% glycerol (DW) was used with powder blends 1, 2, and 3, while the zb[®]60 binder was used with powder blends 1, 2, 3, 4, 5, 6 and 7. Table 4.2 shows the measured contact angle and surface tension of DW and zb[®]60 binder solution. Figure 4.2 shows the viscosity of the two binders.

Twenty rectangular specimens with dimensions of 50 x 6 x 4 mm were designed and printed for all the powder blends. The first attempt was to print A-W without MD; however, this proved impossible. After A-W was mixed with the MD binder, the samples were printed successfully. When using these blends to fabricate specimens with a 3DP machine, it was possible to print several specimens successfully without any problems. The specimens with a high MD content (30% by wt.) were sufficiently strong for handling and passed through all the cleaning process without any damage, whereas the specimens made with a lower MD content (15% by wt.) and the 98% DW/2% glycerol binder were more fragile. In addition, 40% of the PB2 green specimens were destroyed in post-processing.

Table 4.1 Printing and handling characteristics

Powder/Blend	Binder	Printing of 20 specimens		Handling of 20 specimens	
		Yes	No	Yes	No
A-W	zb [®] 60	0	0	0	0
PB1	98% distilled water & 2% Glycerol	20	0	20	0
	zb [®] 60	20	0	20	0
PB2	98% distilled water & 2% Glycerol	20	0	12	8
	zb [®] 60	20	0	20	0
PB3	98% distilled water & 2% Glycerol	20	0	20	0
	zb [®] 60	20	0	20	0
PB4	zb [®] 60	20	0	20	0
PB5	zb [®] 60	20	0	20	0
PB6	zb [®] 60	20	0	20	0
PB7	zb [®] 60	20	0	20	0

Table 4.2 Measured contact angle and surface tension of DW and zb[®]60 binder solution

Binder solution	Contact angle±SE (deg)	Surface tension±SE (mN/m)
DW	93.23±1.53	20.89±2.66
zb [®] 60	41.47±2.78	29.05±3.09

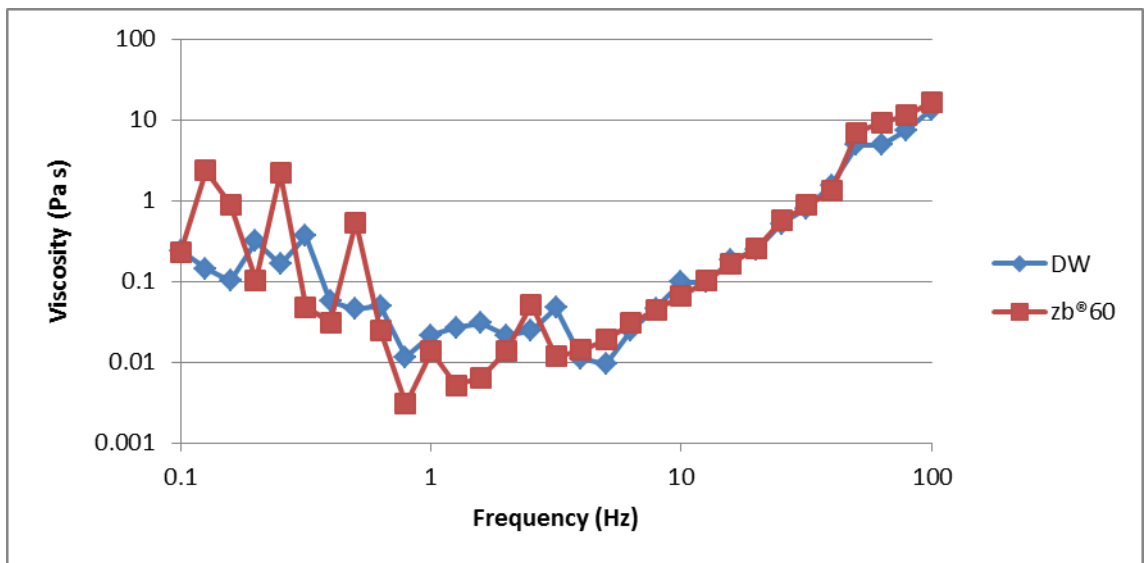


Figure 4.2 Shear viscosity of DW and zb[®]60 binder solution

It was possible to successfully produce scaffolds with a porous structure, which had excellent integrity, defined edges, and rough surfaces, as shown in Figure 4.3. Some of these beams had small distortions after sintering. A possible explanation for this might be that the top surface shrank more than the bottom surface because the bottom surface lay on brick surface in the furnace. The top surfaces of the parts are rougher as assessed by eye compared to the bottom surfaces. The reason for this roughness may be due to binder jetting on the powder bed and sintering process, which has been observed in earlier studies (Farzadi *et al.*, 2014; Seitz *et al.*, 2005). A SEM result for a top surface of PB4 and PB5 green parts are shown in Figure 4.4. It can be seen that the binder binds A-W Particles together.

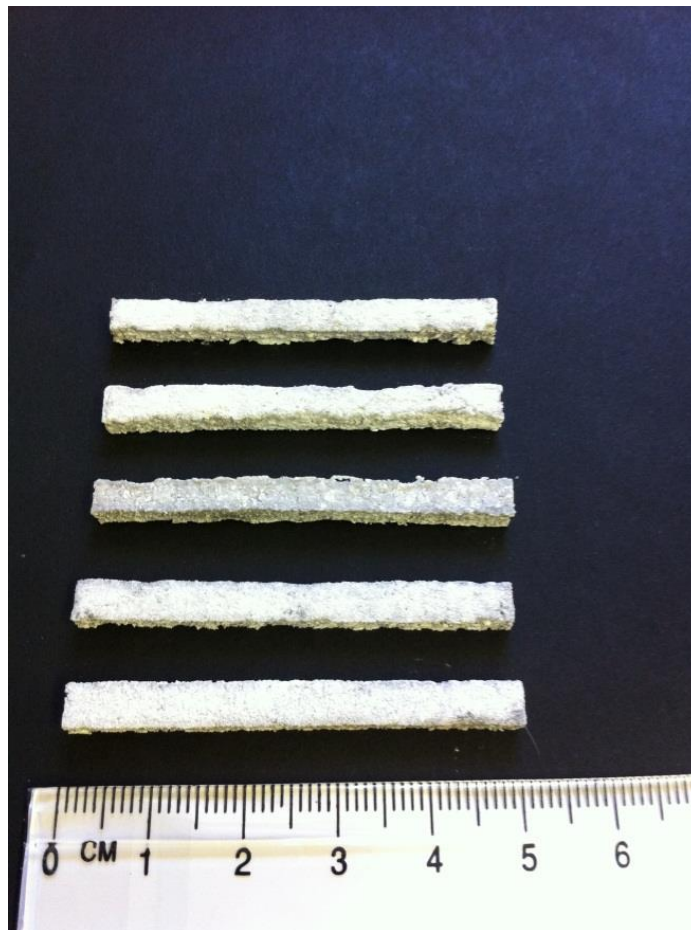


Figure 4.3 The green part (50 X 6 X 4 mm) of PB5

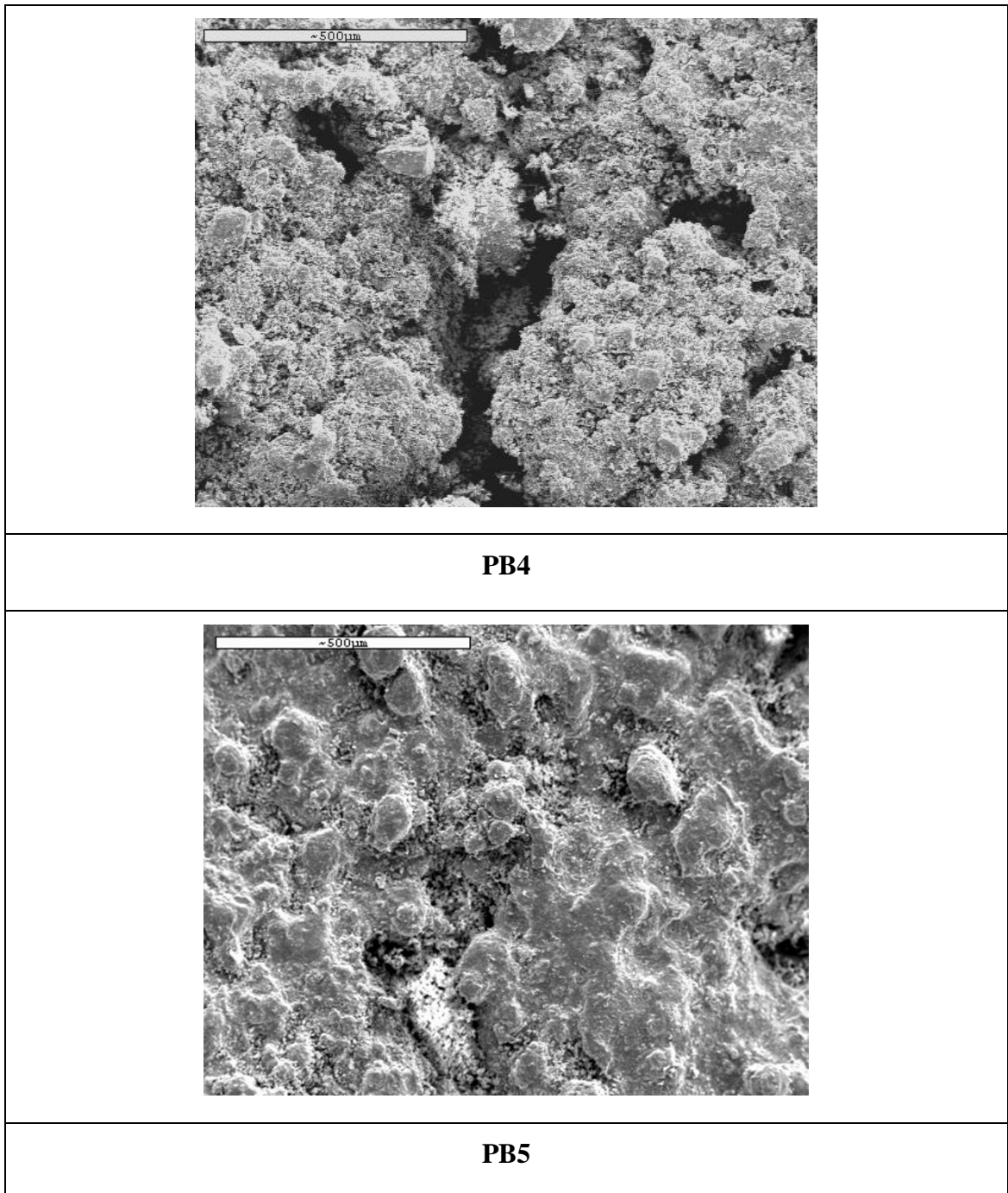


Figure 4.4 SEM result of the green part of PB4 and PB5, at 100x magnification

4.1.3 Effect of build orientation on bending strength

The aim of this experiment was to test the effect of build orientation on the bending strength of the parts. Figure 4.5 demonstrates that the part is stronger in both the x-axis (gantry direction of travel) and y-axis (binder cartridge direction of travel) than in the z-axis. Printing is carried out in three forms: along the x-axis - in bands; along the y-axis - continuous strips; along the z-axis - laminated layers (Z Corp, 2009). Ten samples were built in two different orientations (Figure 4.6) using the same powder blend (PB5) and post-processing methods. Five specimens were built in a 0–0 orientation and five specimens were built in a 0–90 orientation. Tables 4.3 and Table 4.4 show the results of the bending strength tests of the two build orientations. As can be seen from the data in these tables, It is clear that the data has normal distribution and the difference in bending strengths between build orientations is not statistically significant, $P = 0.303$ (t-test). Hence, the build orientation of the parts appears to have no obvious effect on their respective bending strengths.

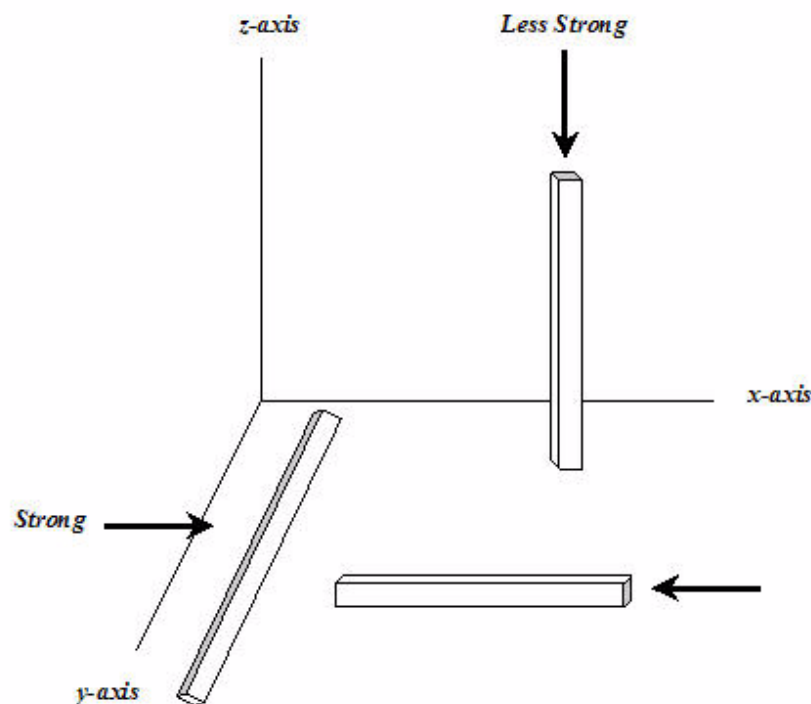


Figure 4.5 Diagram displaying the strength characteristics in X, Y and Z direction (Z Corp, 2009)

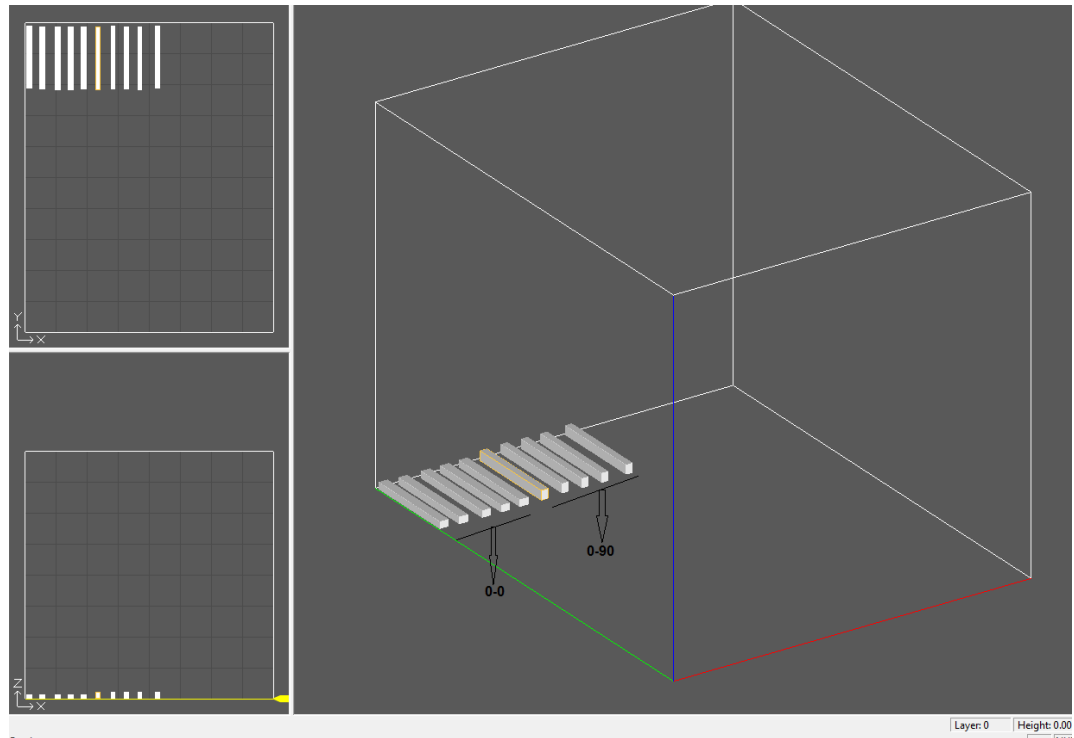


Figure 4.6 Diagram displaying 0–0 and 0–90 build orientation

Table 4.3 Three-point bending results of sintered parts produced using PB5 in a 0–0 build orientation

Beam	Span (L) (mm)	Fracture Force (p) (N)	Width (b) (mm)	Height (h) (mm)	Bending Strength (f) (MPa)
1	30	11.93	4.63	3.53	9.31
2	30	13.4	4.5	3.59	10.40
3	30	16.04	4.56	3.65	11.88
4	30	15.54	4.56	3.43	13.03
5	30	16.95	4.76	3.54	12.79
Average [MPa]					11.48
SD [MPa]					1.60
SE					0.71
<i>P</i> -Value					0.503
95% CI					(9.50, 13.46)

Table 4.4 Three-Point bending results of green parts produced using PB5 in a 0–90 build orientation

Beam	Span (L) (mm)	Fracture Force (p) (N)	Width (b) (mm)	Height (h) (mm)	Bending Strength (f) (MPa)
6	30	14.66	4.45	3.65	11.13
7	30	14	4.43	3.61	10.91
8	30	11.87	4.4	3.58	9.47
9	30	14.18	4.42	3.59	11.20
10	30	13.21	4.41	3.6	10.40
Average [MPa]					10.62
SD [MPa]					0.72
SE					0.32
<i>P</i> -Value					0.218
95% CI					(9.73, 11.51)

4.1.4 Effect of heat treatment and powder setting on bending strength and shrinkage

The main purpose of this trial was to test the effect of heat treatment and 3DP setting parameters on the bending strength and shrinkage of the specimens. Three heat treatments and three powder settings were used, as shown in Table 4.5 and Table 4.6. Ten rectangular specimens with CAD dimensions of 52 mm x 5.2 mm x 3.9 mm were printed for each powder setting, and then three specimens from each setting were collected and subjected to a common heat treatment.

The average bending strength results and the average volume shrinkage percentage for this experiment are given in Table 4.7 (Appendix A). From the table it can be seen that the data has normal distribution and the difference in average bending strength is not statistically significant for the three heat treatment and powder settings, $P > 0.05$ (one-way ANOVA tests). The linear percentage shrinkage in the X, Y, and Z directions were very close in all the specimens and were approximately 19%, whilst the volumetric percentage shrinkage was about 46%. Therefore, the optimal approach to compensate

for product shrinkage is to change the CAD input according to predictions for the shrinkage.

Table 4.5 Post-process heat treatments used on green parts

Heat treatment	Rate [T° C/min]	T° C	Dwell [h]	Rate [T° C/min]	T° C	Dwell [h]
HT1	10	779	1	10	1150	1
HT2	10	779	1	10	1140	1
HT3	10	779	1	10	1160	1

Table 4.6 3DP Powder settings

Setting	Layer Thickness (mm)	Shell		Core		Bleed compensation		
		Saturation Level	Binder/Volume Ratio	Saturation Level	Binder/Volume Ratio	ON/OFF		
						X (mm)	Y (mm)	Z (mm)
A	0.1	100%	0.214962	100%	0.107481	Off	Off	Off
B	0.1	100%	0.214962	100%	0.107481	0.127	0.127	0.1016
C	0.1	150%	0.322443	150%	0.161222	0.00508	0.00508	0.00508

Table 4.7 Summary of average bending strength and average volume shrinkage of printed parts

Setting	Heat treatment	Average Volume Shrinkage upon Sintering (%)	Average Bending Strength±SE (MPa)	ANOVA (P value)	See Appendix A
A	HT1	46.41	13.17±1.18	0.29	Table A-3, A-12
A	HT2	46.68	14.56±1.16		Table A-4, A-13
A	HT3	46.62	13.02±0.71		Table A-5, A-14
B	HT1	46.38	14.44±0.58		Table A-6, A-15
B	HT2	46.56	14.68±0.27		Table A-7, A-16
B	HT3	45.53	16.58±0.28		Table A-8, A-17
C	HT1	46.95	15.44±0.64		Table A-9, A-18
C	HT2	46.63	15.62±1.81		Table A-10, A-19
C	HT3	44.74	15.73±1.31		Table A-11, A-20

4.1.5 Effects of different particle sizes of A-W on density of powder

Three ranges of A-W particle sizes were tested to determine the density of A-W powder using the pycnometer method. Table 4.8 illustrates the density of A-W powder. These results indicate that the large particle sizes (53-90) μm have internal porosity as a result of the grinding process and surface characterization. Very small particle sizes (0-20) μm give density values consistent with those for A-W density in literature. Table 4.8 shows normal distribution ($P > 0.05$) of the density data, and a significant difference ($P = 0.008$) between the smallest particle sizes (0-20) μm and the largest particle sizes (53-90) μm .

Table 4.8 Density of A-W powder of three ranges of particle sizes using pycnometer method

Particle size		A-W powder		
		(0-20) μm	(20-53) μm	(53-90) μm
Mass of Pycnometer (g)		16.79		
Mass of Pycnometer & distilled water (g)		27.36		
Mass of Pycnometer & A-W powder (g)	Sample1	20.41	22.01	22.87
	Sample2	20.18	22.02	21.2
	Sample3	20.11	22.01	22.31
Mass of Pycnometer & A-W powder & distilled water (g)	Sample1	29.78	30.77	31.21
	Sample2	29.61	30.72	30.2
	Sample3	29.54	30.75	30.9
Mass of distilled water (g)	Sample1	10.57		
	Sample2			
	Sample3			
Mass of A-W powder (g)	Sample1	3.617	5.22	6.08
	Sample2	3.387	5.227	4.407
	Sample3	3.317	5.217	5.517
Mass of A-W powder & distilled water (g)	Sample1	12.99	13.98	14.41
	Sample2	12.82	13.93	13.41
	Sample3	12.75	13.96	14.11
Density [g/cm^3]	Sample1	3.01	2.88	2.71
	Sample2	2.96	2.79	2.80
	Sample3	2.90	2.84	2.78
Mean of Density [g/cm^3]		2.96	2.84	2.76
SD		0.05	0.04	0.04
SE		0.03	0.03	0.03
<i>P</i> -Value		0.90	0.88	0.41

4.2 Mechanical Properties Development

The 3DP setting parameters and the post-process, such as the heat treatment to burn off the binder and to sinter the parts, were the same in all the printing processes, as illustrated in Chapter 3. PB1, PB2 and PB3 were processed using DW binder, which consistently caused the print head to become blocked, unlike the zb®60 binder which did not cause such blocking. As test results had shown no clear advantage to using the DW binder, its use was discontinued.

Table 4.9 shows the following properties in relation to each powder blend: average green and sintered flexural strength, Young's modulus, volumetric shrinkage percentage, total porosity, and open porosity.

Table 4.9 Mechanical properties of all powder blends

Powder Blend	Average Bending Strength of green parts±SE (Mpa)	Average Bending Strength of sintered parts±SE (MPa)	Average Young's Modulus of sintered parts ±SE (GPa)	Average Total Porosity (%)±SE	Average Open Porosity (%)±SE	Average Volume Shinkage in Sintering (%)±SE
PB1/DW	3.93±1.25	8.95±1.42	4.55±1.35	51.76±1.94	33.08±3.25	34.38±0.37
PB1/zb®60	6.14±0.30	23.65±0.73	7.27±0.52	47.95±0.49	15.43±0.01	34.55±1.16
PB2/DW	0.38±0.16	11.56±0.74	5.40±0.93	53.67±0.76	39.48±0.03	47.6±1.24
PB2/zb®60	*	8.23±0.23	2.82±0.12	*	*	34.96±2.32
PB3/DW	0.37±0.11	8.09±0.63	4.20±0.20	52.24±0.50	39.08±0.27	50.32±0.40
PB3/zb®60	*	6.13±0.32	1.87±0.09	*	*	15.77±1.10
PB4/zb®60	8.63±0.35	35.64±1.48	15.04±0.89	35.27±0.76	11.62±0.10	48.56±0.67
PB5/zb®60	8.53±0.73	25.68±1.59	11.18±0.94	41.85±0.94	12.4±0.29	41.30±1.69
PB6/zb®60	2.33±0.10	17.20±0.6	5.40±0.19	54.03±0.97	17.07±0.97	21.53±0.09
PB7/zb®60	2.08±0.27	18.36±0.34	7.77±0.31	59.38±0.98	19.20±0.87	34.06±2.01

*Due to low bending strength, this material was not evaluated further; hence green part strength and porosity measurements are not shown.

4.2.1 Green Parts

Green structure is brittle and has low strength. This strength varied with each powder blends. Typical SEM microstructures of green parts printed using PB4 and PB5 are illustrated in Figure 4.7 and Figure 4.8.

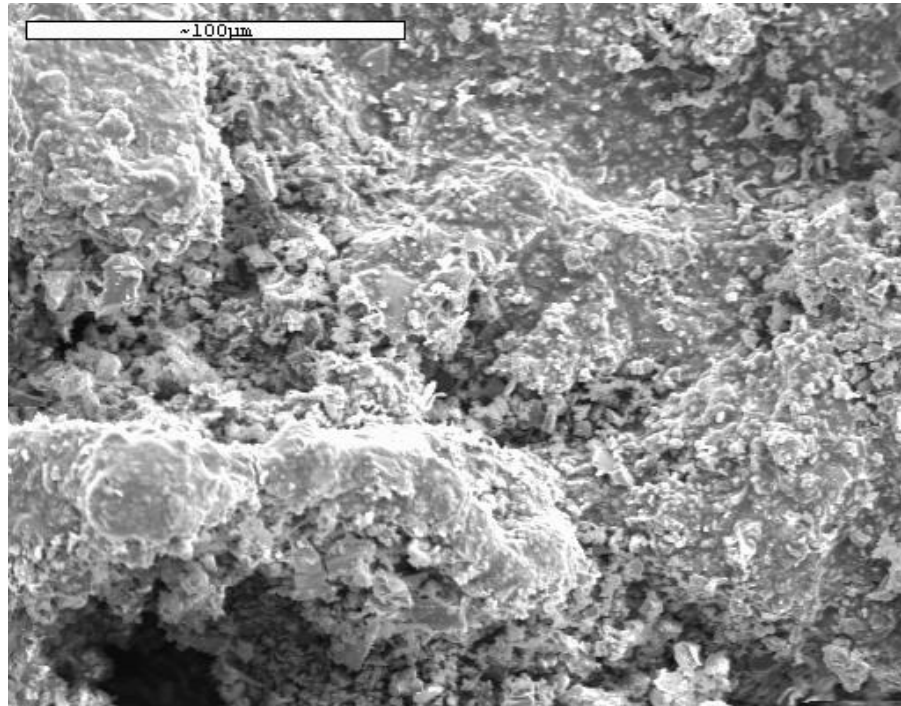


Figure 4.7 SEM of a green part made using PB4 at 500x magnification

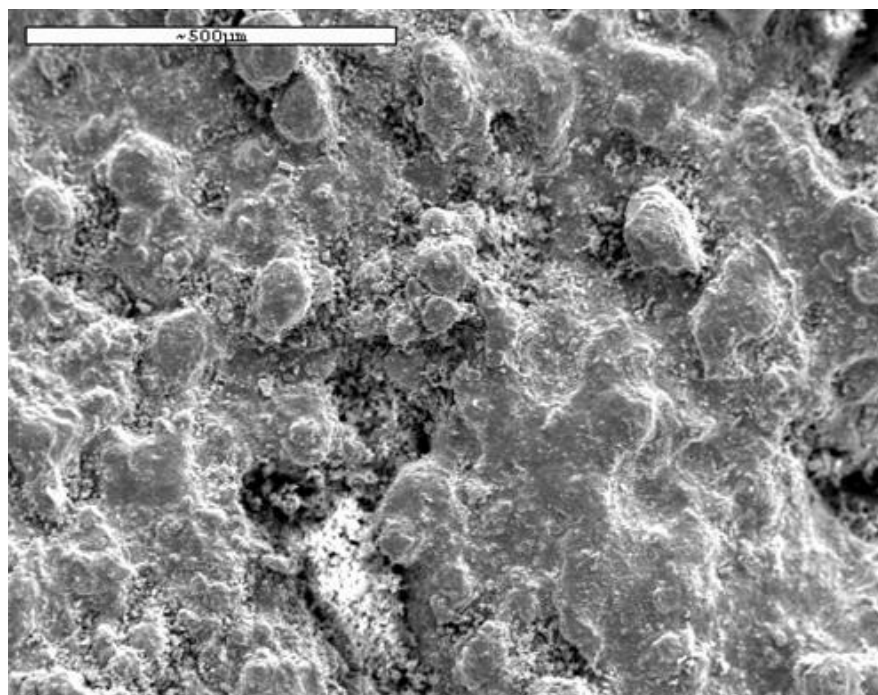


Figure 4.8 SEM of a green part made using PB5 at 100x magnification

The green specimens produced with PB1, PB4, PB5, PB6 and PB7 were sufficiently robust to undergo handling and cleaning processes without breakage. However, in contrast, the green specimens produced with PB2 and PB3 were very fragile.

Figure 4.9 shows the green flexural strength of all printed parts. The data has normal distribution and no significant difference ($P = 0.117$; ANOVA tests) between parts produced with DW binder solution. In contrast, parts produced with zb®60 binder solution resulted in a significant difference ($P < 0.001$; Kruskal-Wallis test). The average green strength results show that the parts produced with zb®60 binder solution have the highest flexural strength compared to the parts produced with DW binder solution. Furthermore, there was no significant difference between PB4 and PB5.

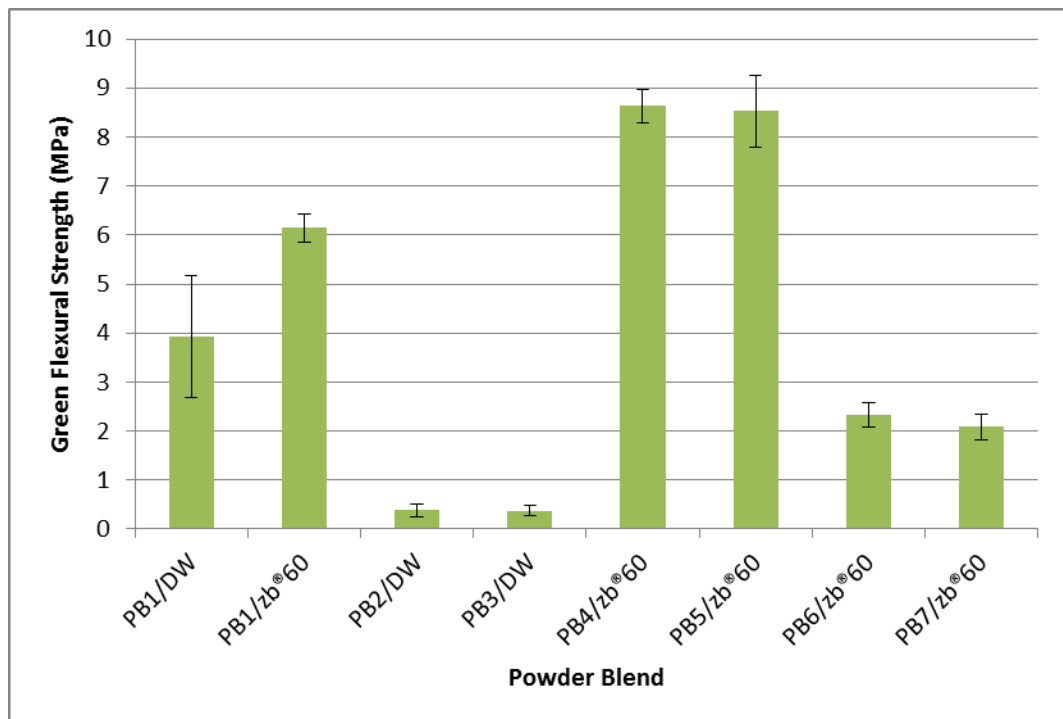


Figure 4.9 Average flexural strength of green parts \pm SE

4.2.2 Sintered Parts

Figure 4.10 and Figure 4.11 show the mechanical properties of the seven A-W powder blends. The data for sintered flexural strength of the parts made with DW binder solution is not normally distributed and there is significant difference between the sintered flexural strength of parts made with DW binder solution ($P = 0.025$; Kruskal-Wallis test).

The data for the average sintered flexural strength and Young's modulus of the parts made with zb@60 binder solution is normally distributed and there is significant difference between the average sintered flexural strength and Young's modulus of parts made with zb@60 binder solution ($P < 0.001$; ANOVA tests).

The results of PB1 show that there is an increase in sintered flexural strength for the parts made with zb@60 binder solution compared to PB2 and PB3. PB4, with small particles, produced high sintered flexural strength and Young's modulus. The mixed-sized A-W powder particles, such as PB5, PB6 and PB7, were tested and PB5 produced high sintered flexural strength and Young's modulus.

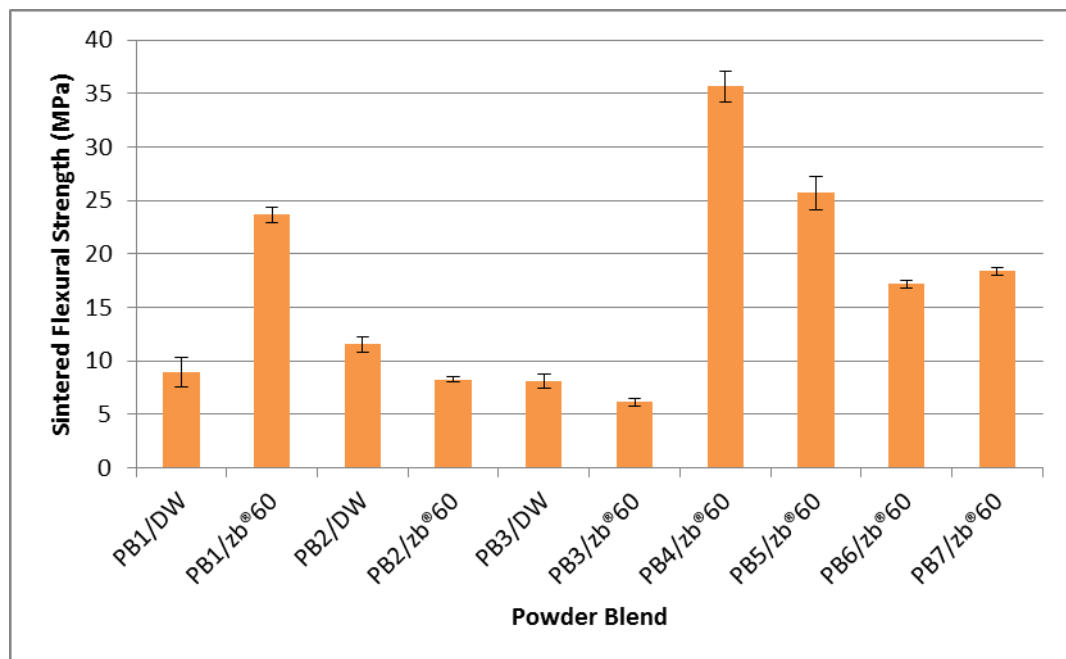


Figure 4.10 Average flexural strength of sintered parts \pm SE

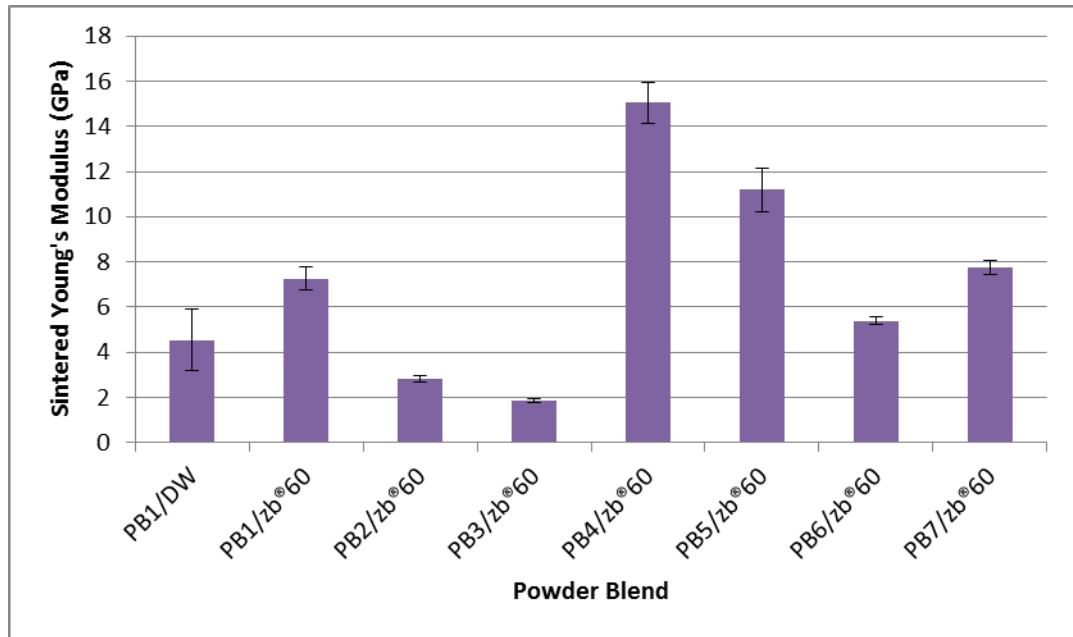


Figure 4.11 Average young's modulus of sintered parts \pm SE

4.2.3 Shrinkage and Accuracy

Figure 4.12 shows the average volume shrinkage of the sintered parts. In general, the volume shrinkage achieved is mostly within the range of 34~50% except for PB3/DW and PB6/zb@60 which is within the range of 15~22%.

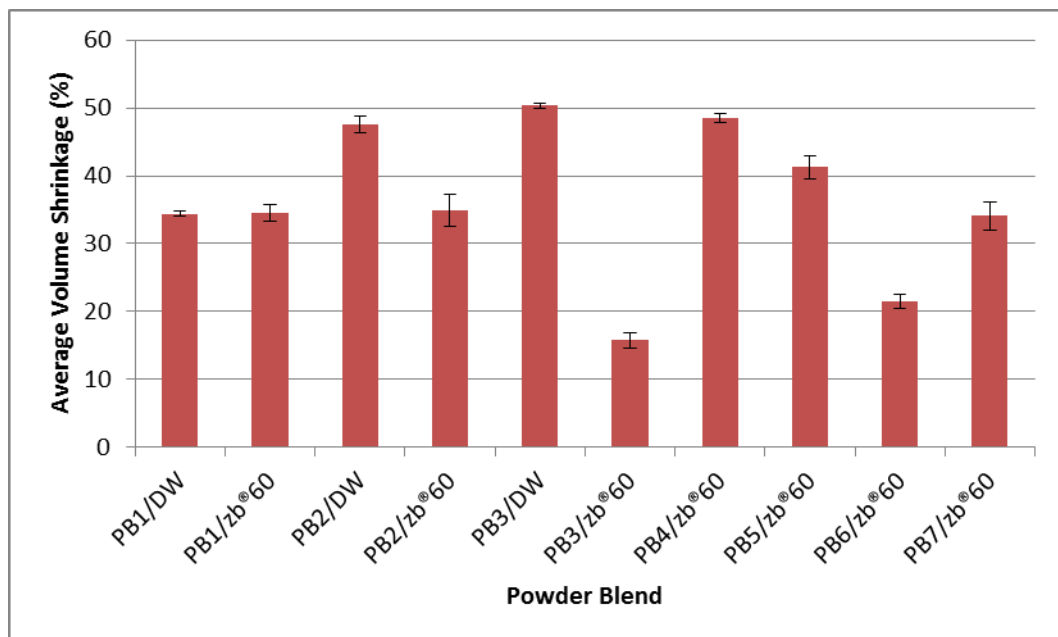


Figure 4.12 Average volume shrinkage of sintered parts \pm SE

Table 4.10 shows the volumetric shrinkage data for PB1/DW, PB2/DW and PB3/DW. The data has normal distribution ($P > 0.05$) and there is a highly significant difference between PB1/DW and the other blends. PB1/DW has significantly less volumetric shrinkage than PB2/DW and PB3/DW, whereas there is no significant difference between PB2/DW and PB3/DW.

Table 4.10 Average volume shrinkage and the statistical analysis of all blends printed with DW

Powder Blend	Average Volume Shrinkage in Sintering (%)±SE	Shapiro-Wilk P value	ANOVA Test P value
PB1/DW	34.38±0.37	0.97	
PB2/DW	47.6±1.24	0.92	< 0.001
PB3/DW	50.32±0.40	0.39	

Table 4.11 shows the volumetric shrinkage data for all powder blends printed with zb®60. The data does not have normal distribution and there is a significant difference.

Table 4.11 Average volume shrinkage and the statistical analysis of all blends printed with zb®60

Powder Blend	Average Volume Shrinkage in Sintering (%)±SE	Shapiro-Wilk P value	Kruskal Wallis P value
PB1/zb®60	34.55±1.16	0.62	
PB2/zb®60	34.96±2.32	<0.001	
PB3/zb®60	15.77±1.10	0.80	
PB4/zb®60	48.56±0.67	0.02	< 0.001
PB5/zb®60	41.30±1.69	0.91	
PB6/zb®60	21.53±0.09	0.97	
PB7/zb®60	34.06±2.01	0.01	

Test samples were measured for consistency and accuracy of printing. Each dimension was measured three times and the average value was recorded. A CAD model of dimensions 50mm by 6mm by 4mm was created for all powder blends. Figure 4.12~ Figures 4.13 to 4.21 show the average linear shrinkage of green and sintered parts. Consequently, the linear shrinkage percentage must be taken into account and compensated for in the input for the CAD design in order to produce the desired parts.

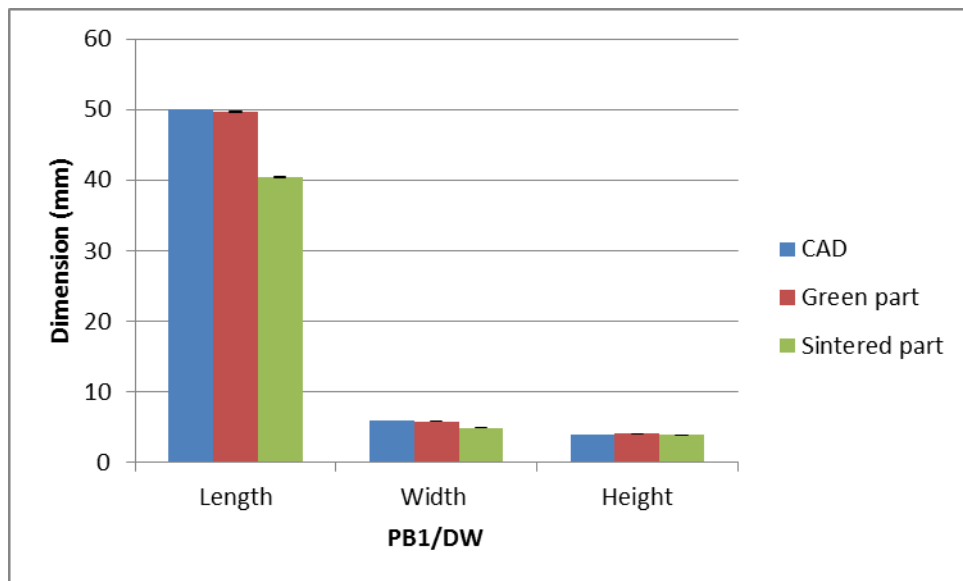


Figure 4.13 Average linear shrinkage of green and sintered parts \pm SE for PB1/DW

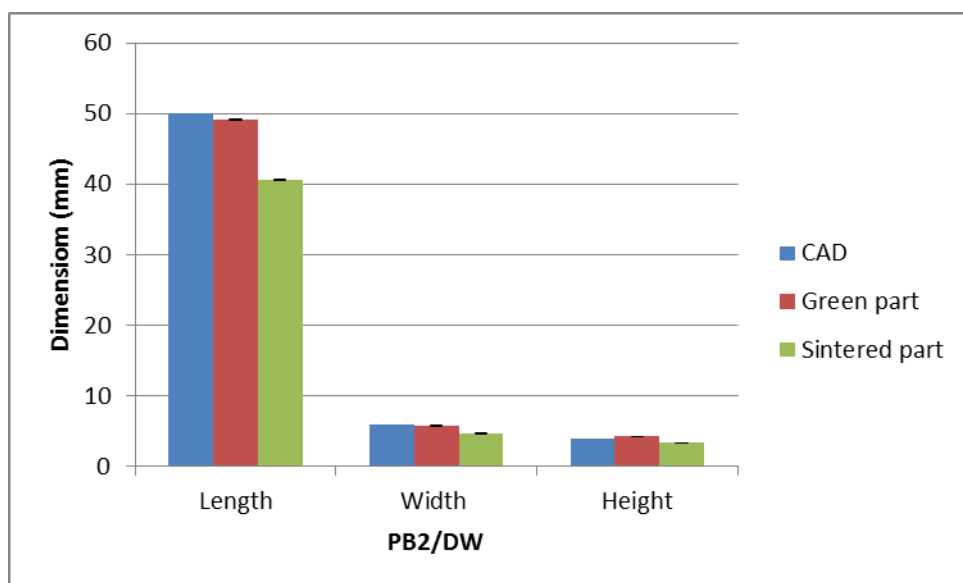


Figure 4.14 Average linear shrinkage of green and sintered parts \pm SE for PB2/DW

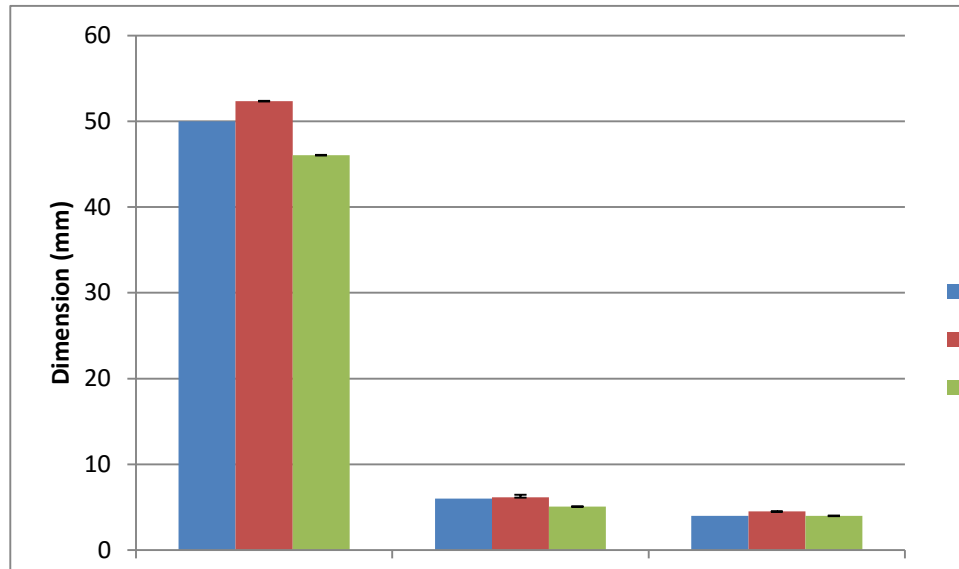


Figure 4.15 Average linear shrinkage of green and sintered parts \pm SE for PB2/ zb@60

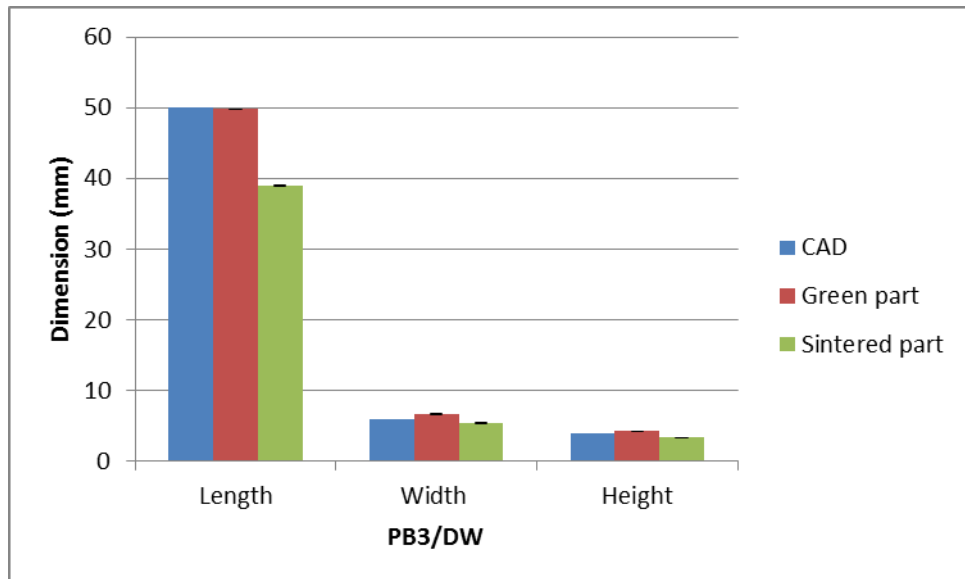


Figure 4.16 Average linear shrinkage of green and sintered parts \pm SE for PB3/DW

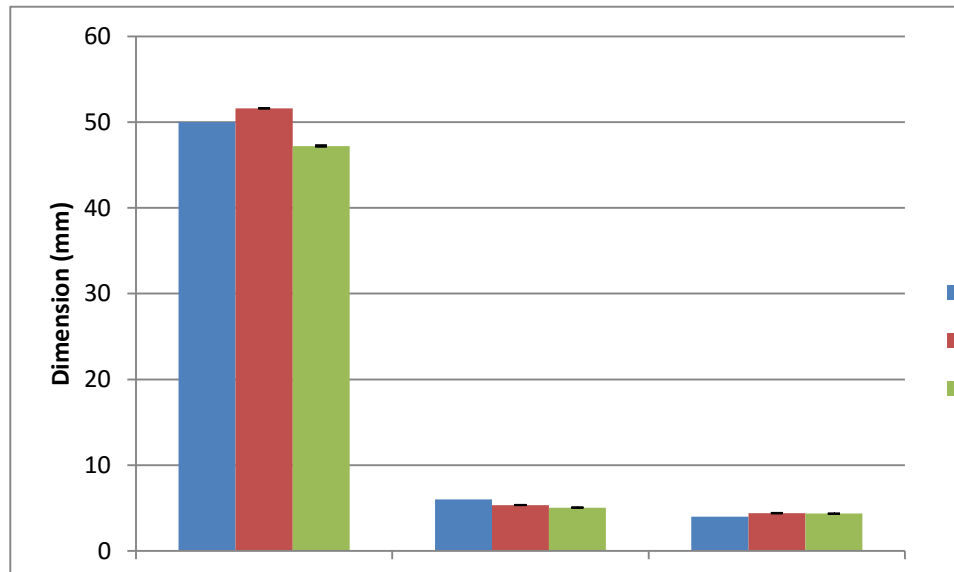


Figure 4.17 Average linear shrinkage of green and sintered parts \pm SE for PB3/ zb@60

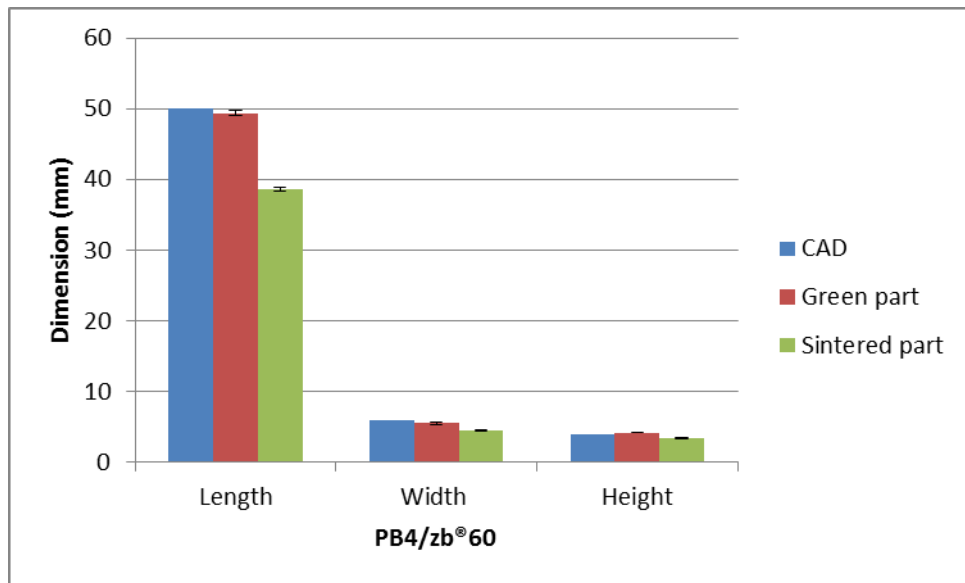


Figure 4.18 Average linear shrinkage of green and sintered parts \pm SE for PB4/ zb@60

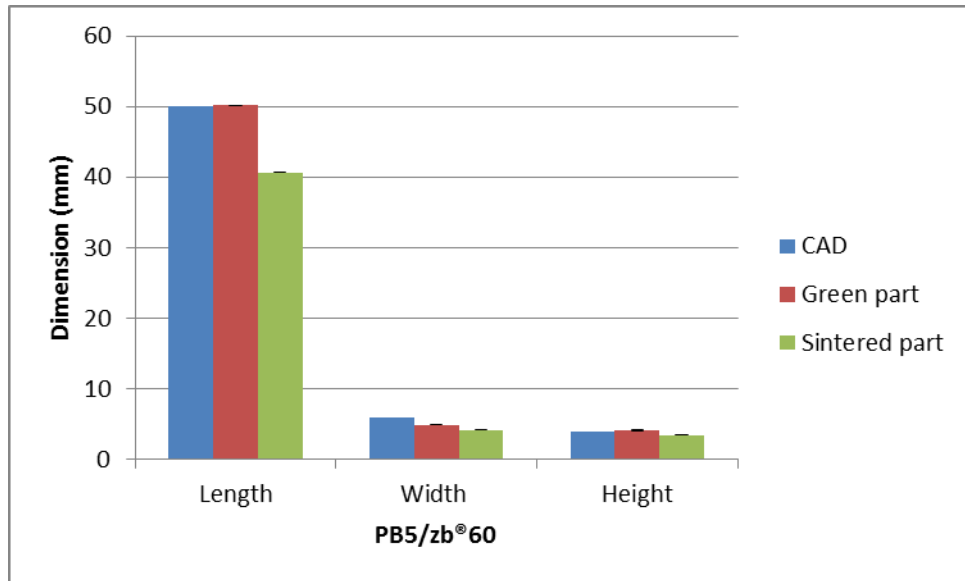


Figure 4.19 Average linear shrinkage of green and sintered parts \pm SE for PB5/ zb@60

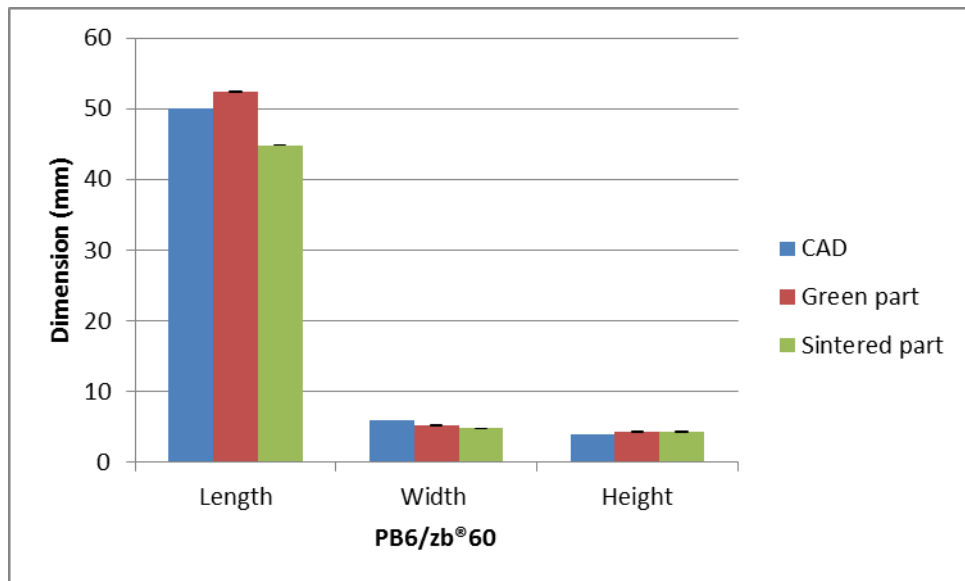


Figure 4.20 Average linear shrinkage of green and sintered parts \pm SE for PB6/ zb@60

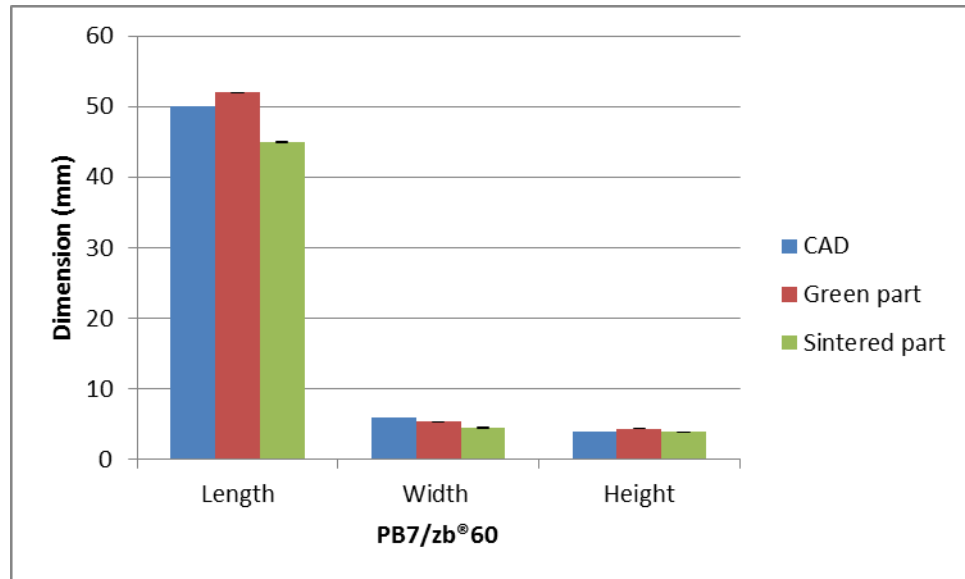


Figure 4.21 Average linear shrinkage of green and sintered parts \pm SE for PB7/ zb@60

4.2.4 Interconnectivity and Porosity

Figure 4.22 shows the average total porosity and open porosity of the sintered parts. In general, the total porosity of all powder blends was acceptable. PB7 produced the highest total porosity and PB4 produced the lowest total and open porosity.

The data for average total porosity has normal distribution and there is no significant difference between the average total porosity for the parts produced with DW binder solution ($P = 0.539$; ANOVA test). In contrast, there is a significant difference between the average total porosity for the parts produced with zb@60 binder solution ($P < 0.001$; ANOVA test).

The data for average open porosity does not have normal distribution and there is no significant difference between the average open porosity for the parts produced with DW binder solution ($P = 0.093$; ANOVA test). In contrast, there is a significant difference between the average open porosity for the parts produced with zb@60 binder solution ($P = 0.002$; Kruskal-Wallis test).

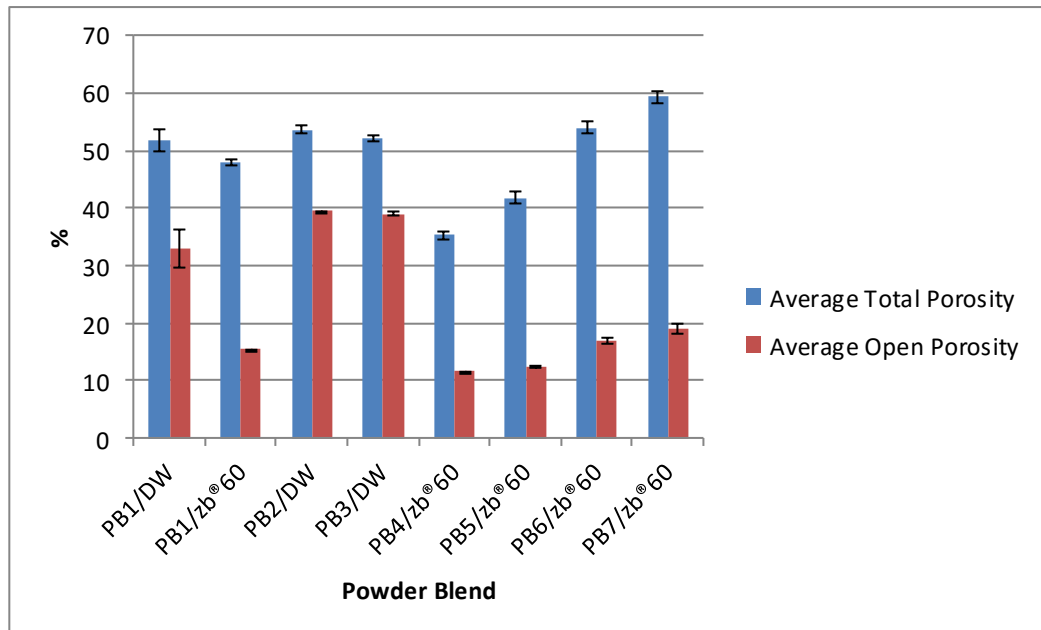


Figure 4.22 Average total and open porosity of sintered parts \pm SE

Figures 4.23 to 4.27 show the 3D micro-CT (computed tomography) investigation of powder blends made with zb®60 binder solution. The 3D images indicate that the structure of the blends have interconnected micro and macro pore networks. Notably, the structure of PB2 has more interconnected micro pore networks than macro pore networks. The structure of PB3 has interconnected macro pore networks along the core of the structure and micro pores in the outermost layers of the structure, and the structure of PB4 has more interconnected micro pore networks than macro pores.

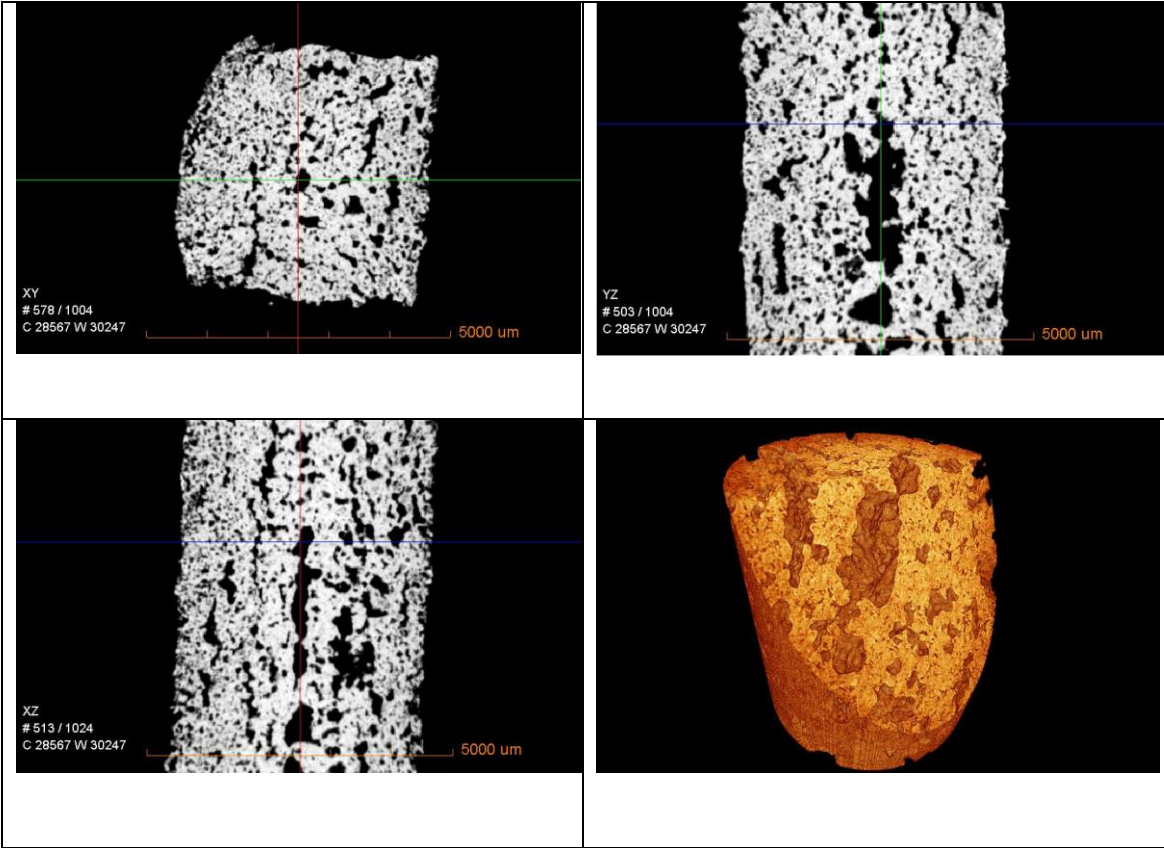


Figure 4.23 3D micro-CT images of parts made using PB1 and zb@60; Voxel size: 11.90 μm , Diameter of scanned volume is 5 mm

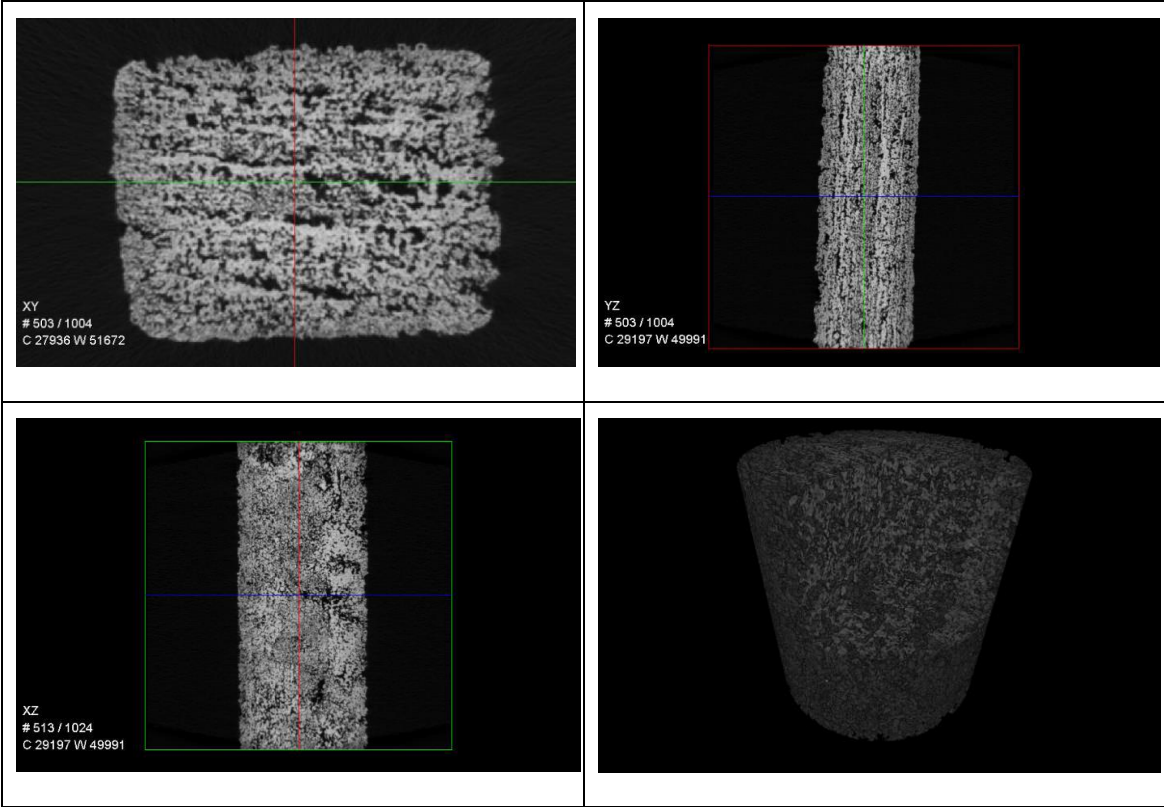


Figure 4.24 3D micro-CT images of parts made using PB2 and zb@60; Voxel size: 11.90 μm , Diameter of scanned volume is 5 mm

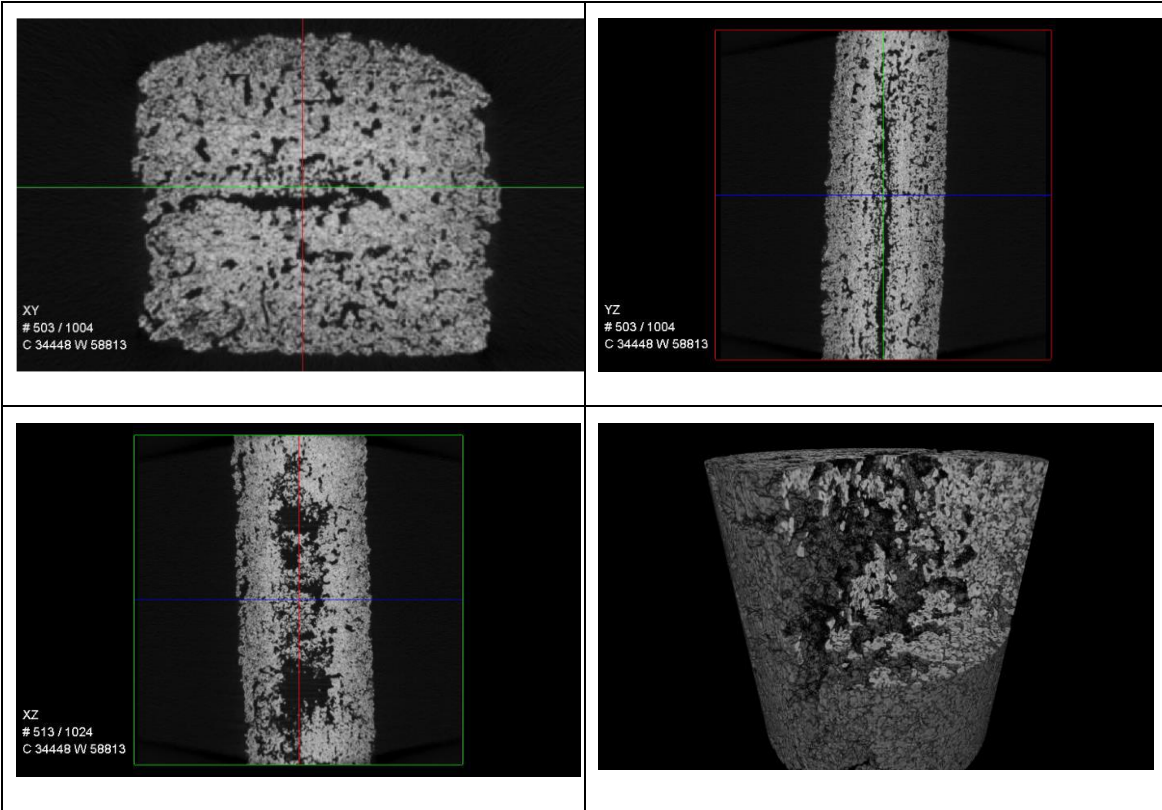


Figure 4.25 3D micro-CT images of parts made using PB3 and zb@60; Voxel size: 11.90 μm , Diameter of scanned volume is 5 mm

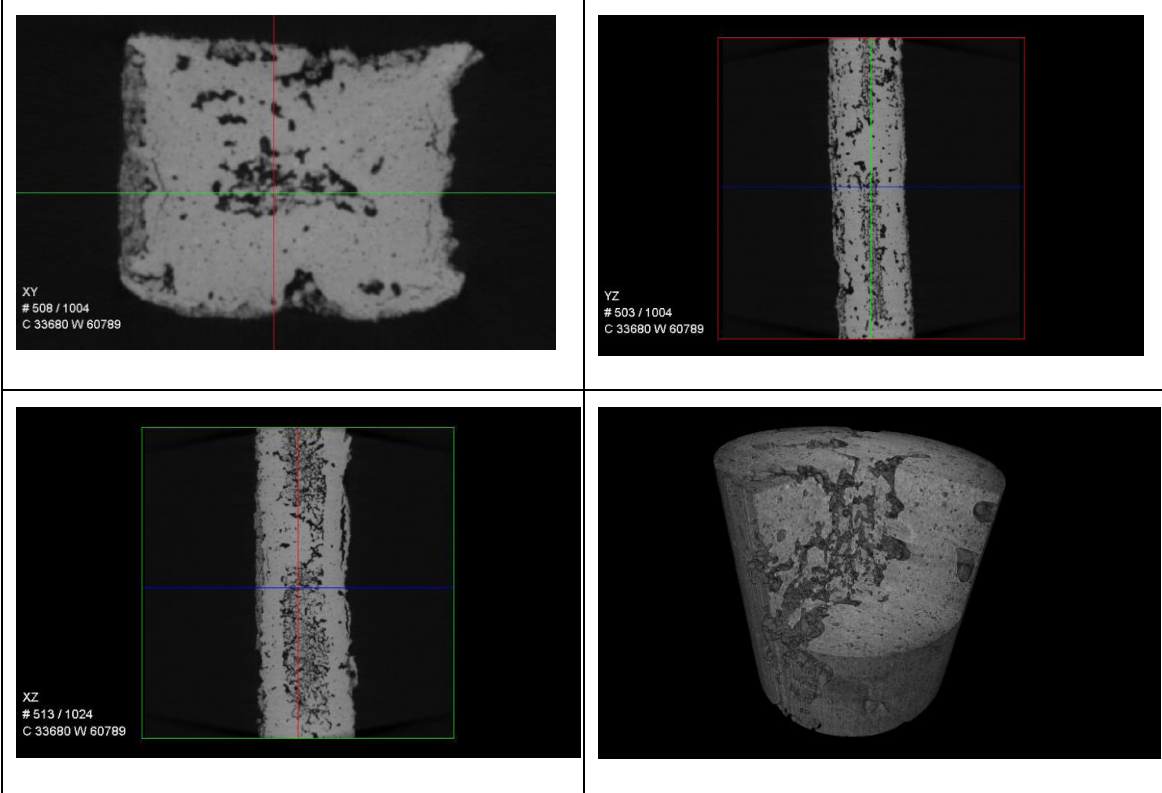


Figure 4.26 3D micro-CT images of parts made using PB4 and zb@60; Voxel size: 11.90 μm , Diameter of scanned volume is 5 mm

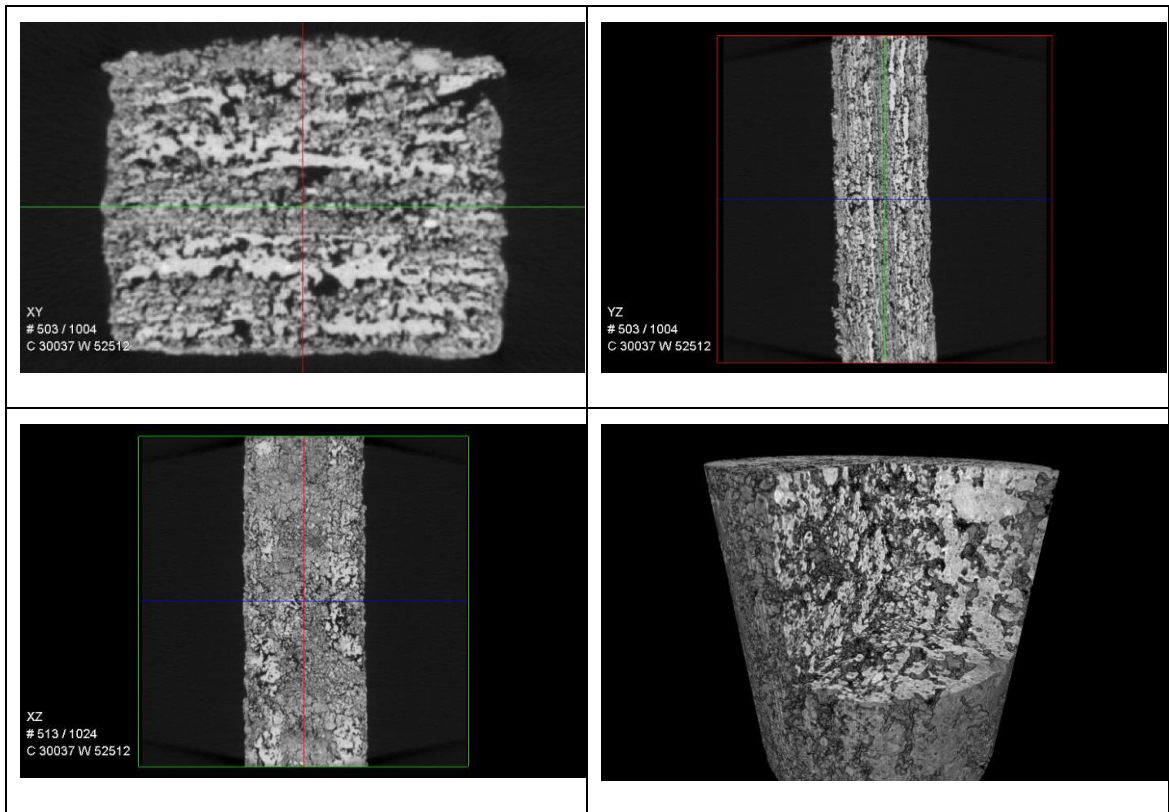


Figure 4.27 3D micro-CT images of parts made using PB5 and zb®60; Voxel size: 11.90 μm , Diameter of scanned volume is 5 mm

Figure 4.28 and Figure 4.29 show SEM images of the external surface for the sintered parts made of PB4 and PB5. The SEM morphology indicates that the structures have sintered particles (circled region) and pores (squared region).

Figure 4.30 and Figure 4.31 show SEM images of the fractured surface for the sintered parts made of PB4 and PB5. From examination of these micrographs, the porous structure of these printed samples derived from the constituents in question is clearly evident, and the interconnected micro and macro pores can be seen. SEM images of the external surface and cross sectional surface indicate that the structure is porous, containing both open and closed pores in the range 5-600 μm .

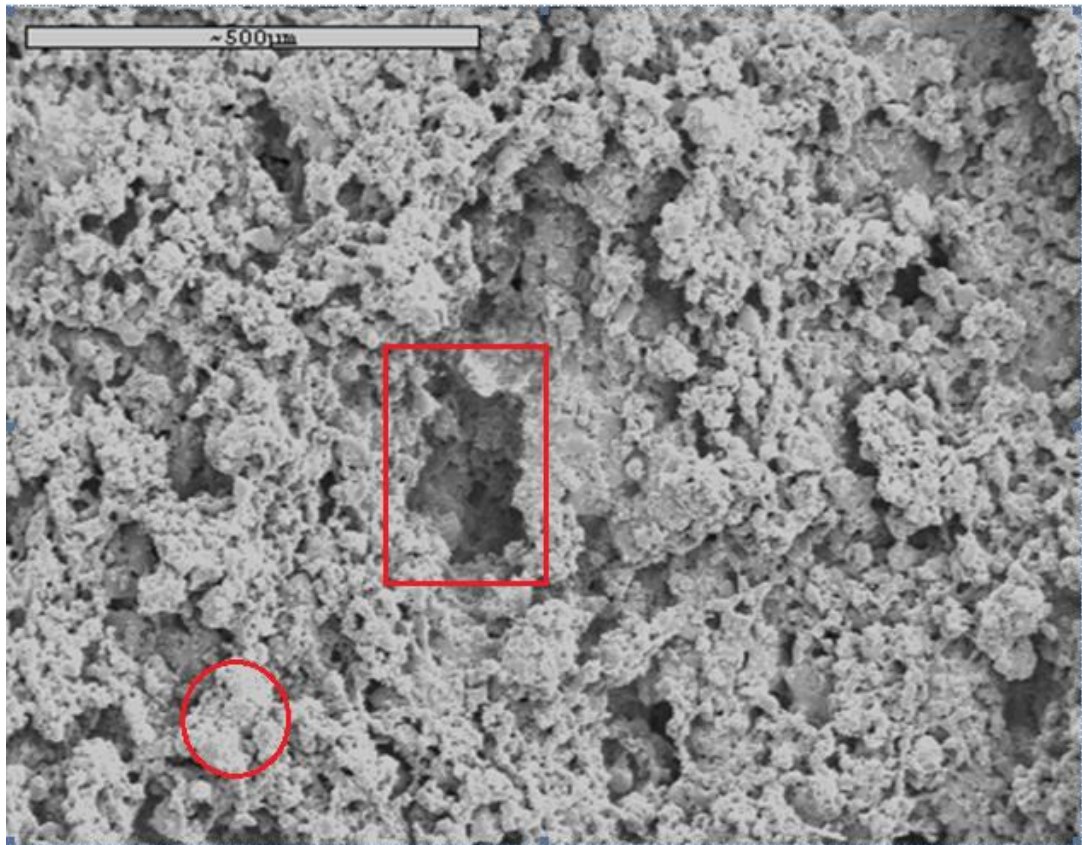


Figure 4.28 SEM of external surface of a sintered part made using PB4 at 100x magnification

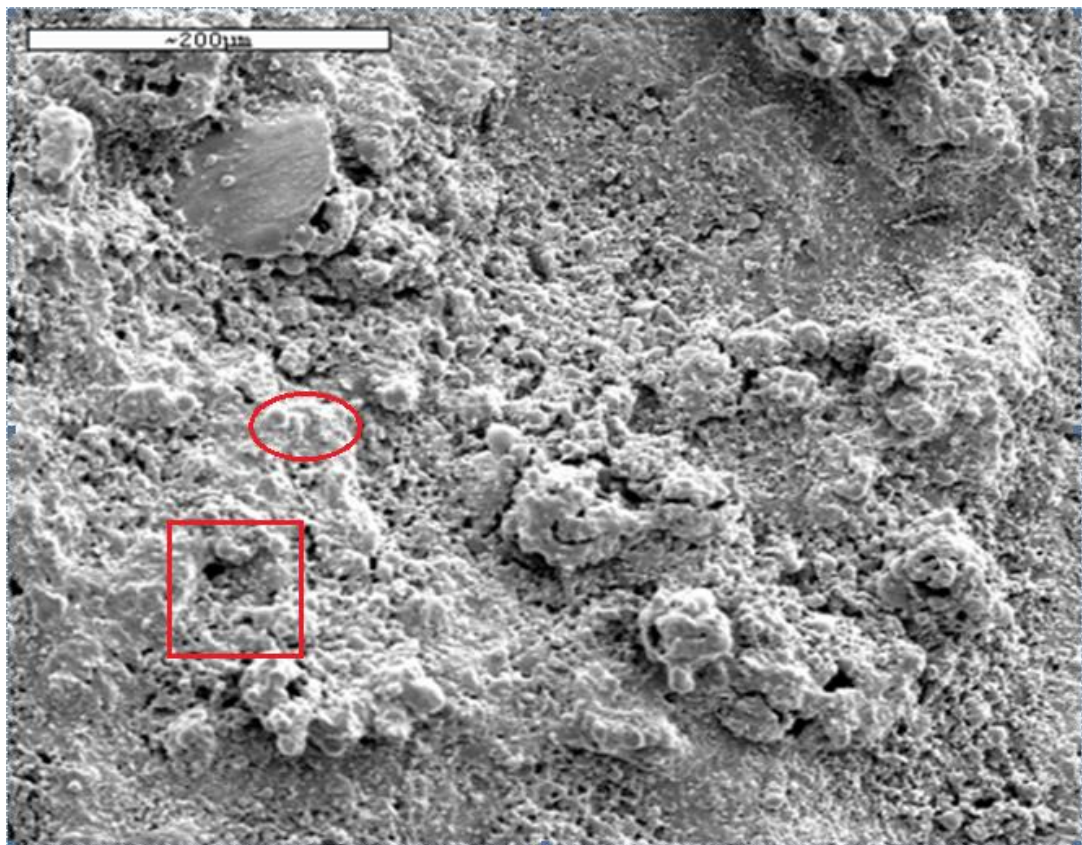


Figure 4.29 SEM of external surface of a sintered part made using PB5 at 200x magnification

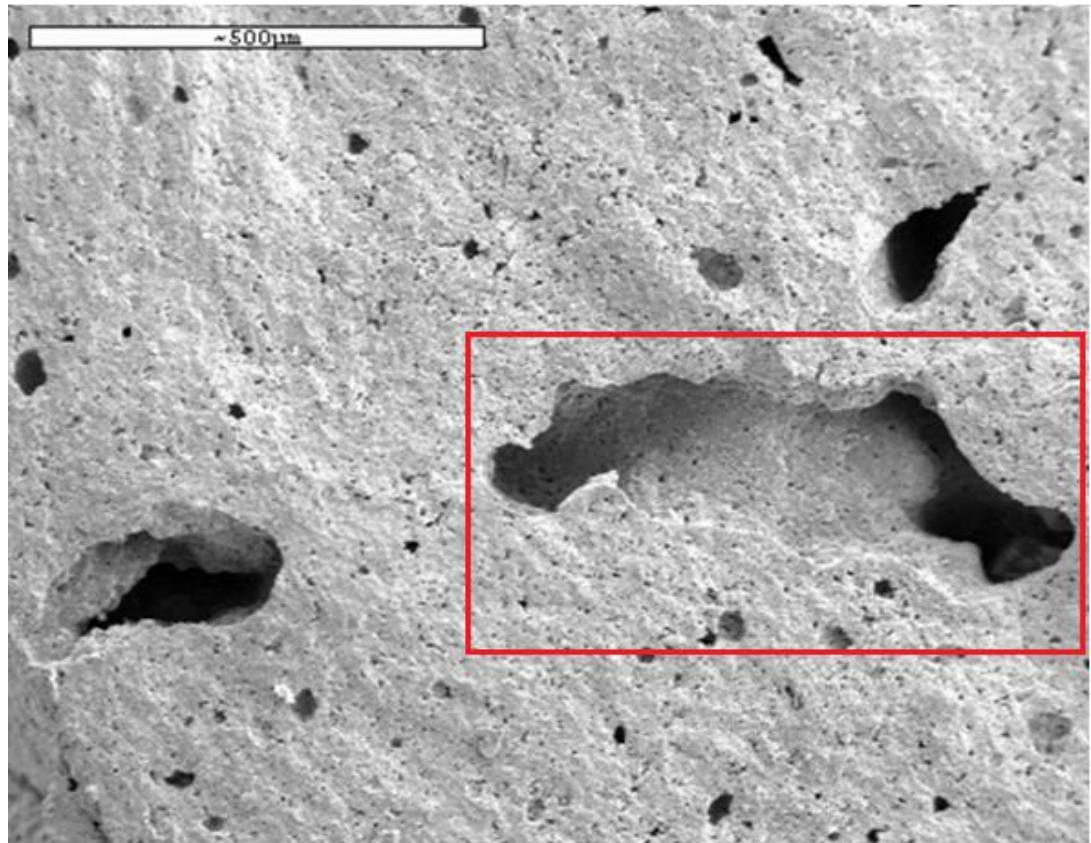


Figure 4.30 SEM of the fractured surface of a sintered part made using PB4 at 100x magnification

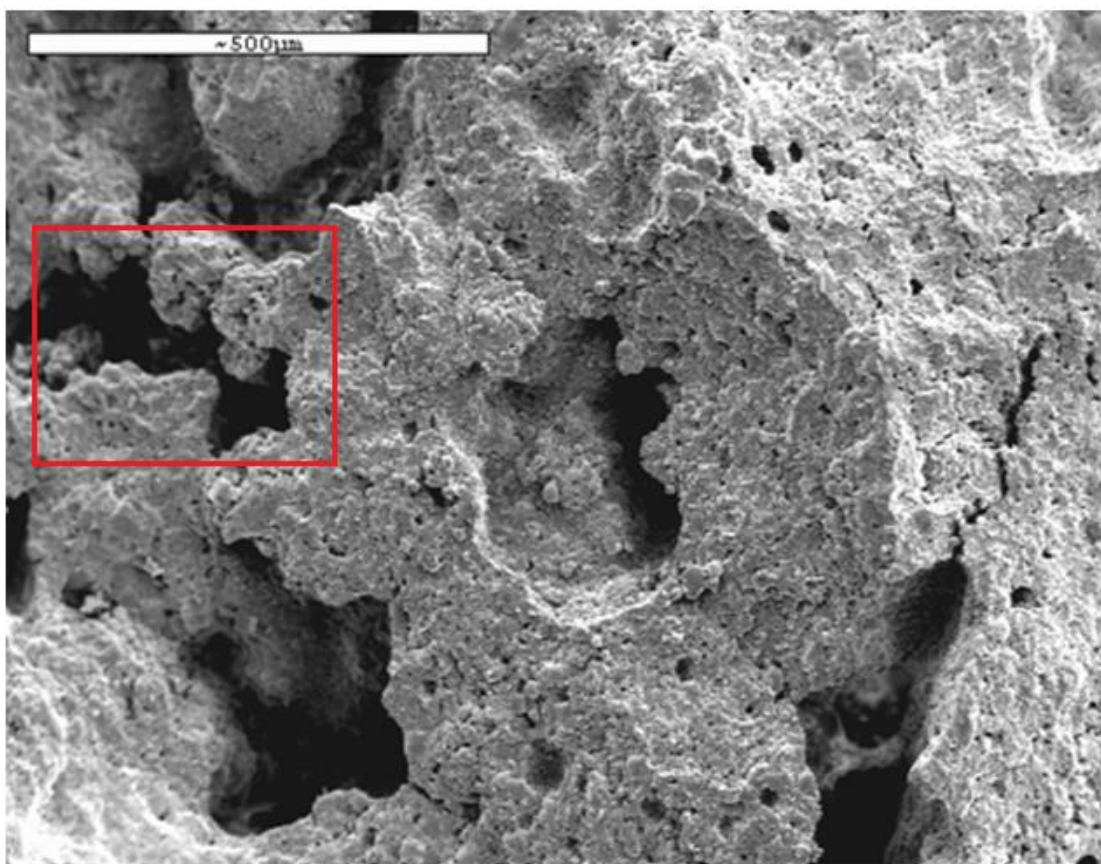


Figure 4.31 SEM of the fractured surface of a sintered part made using PB5 at 100x magnification

4.2.5 Effect of Phosphate glass Infiltration on the bending strength

The main purpose of using the phosphate glass powder was to increase the mechanical strength of the sintered parts. Two methods of infiltration were used, as described in Chapter 3. Method A presented a challenge in terms of being able to apply a sufficient quantity of phosphate glass powder on top of the A-W beams. Figures 4.32 and 4.33 depict the characteristics of a partially infiltrated beam (made from PB5) using method A for phosphate glass infiltration. SEM images show that the infiltration has only a limited effect on the sintered part. Using method B, the quantity of phosphate glass applied was acceptable. Figure 4.34 illustrates, by 3D micro-CT, the structure of a part made using PB5 after infiltration using phosphate glass infiltration method B.

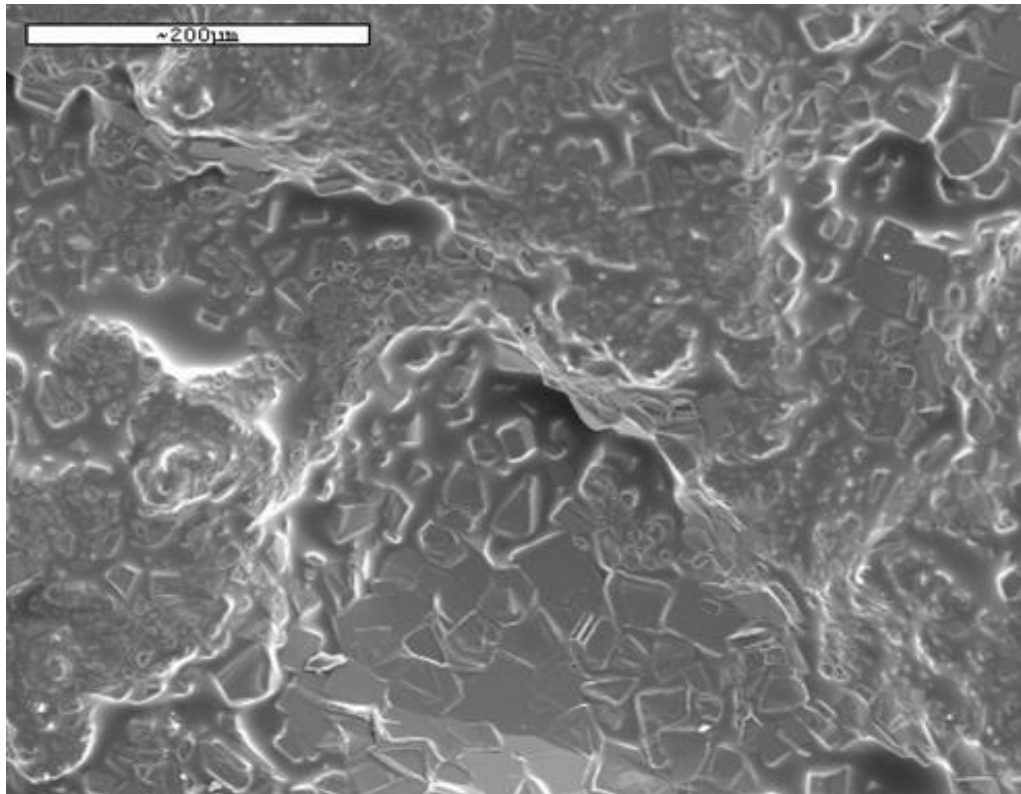


Figure 4.32 SEM of a sintered part made using PB5 after phosphate glass infiltration using Method A at 200x magnification

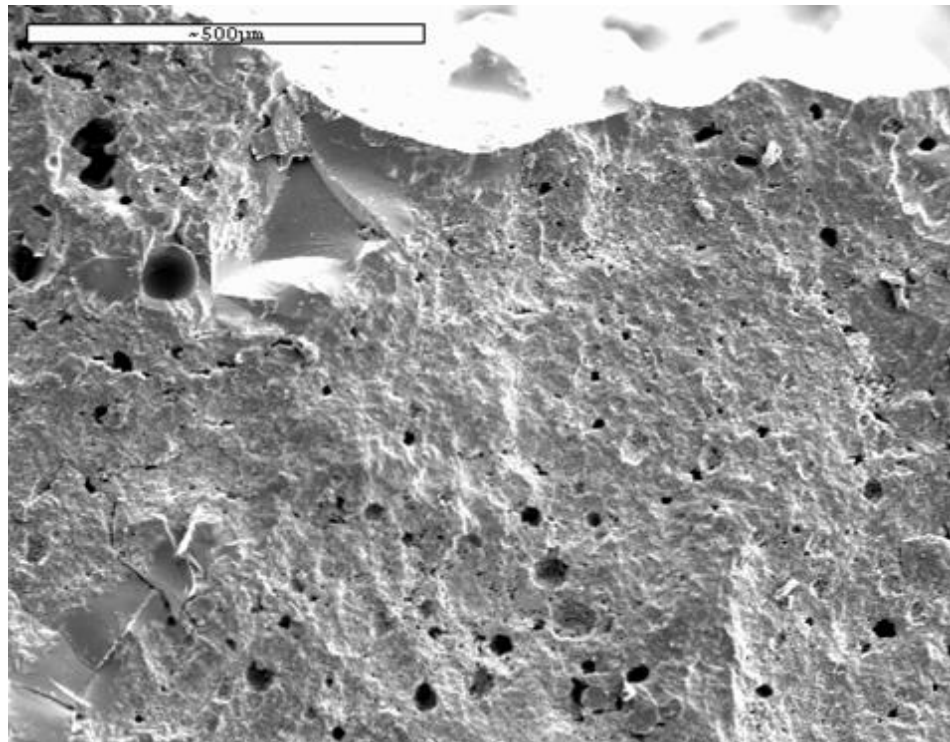


Figure 4.33 SEM of the fractured surface of a sintered part made using PB5 after phosphate glass infiltration using Method A at 100x magnification

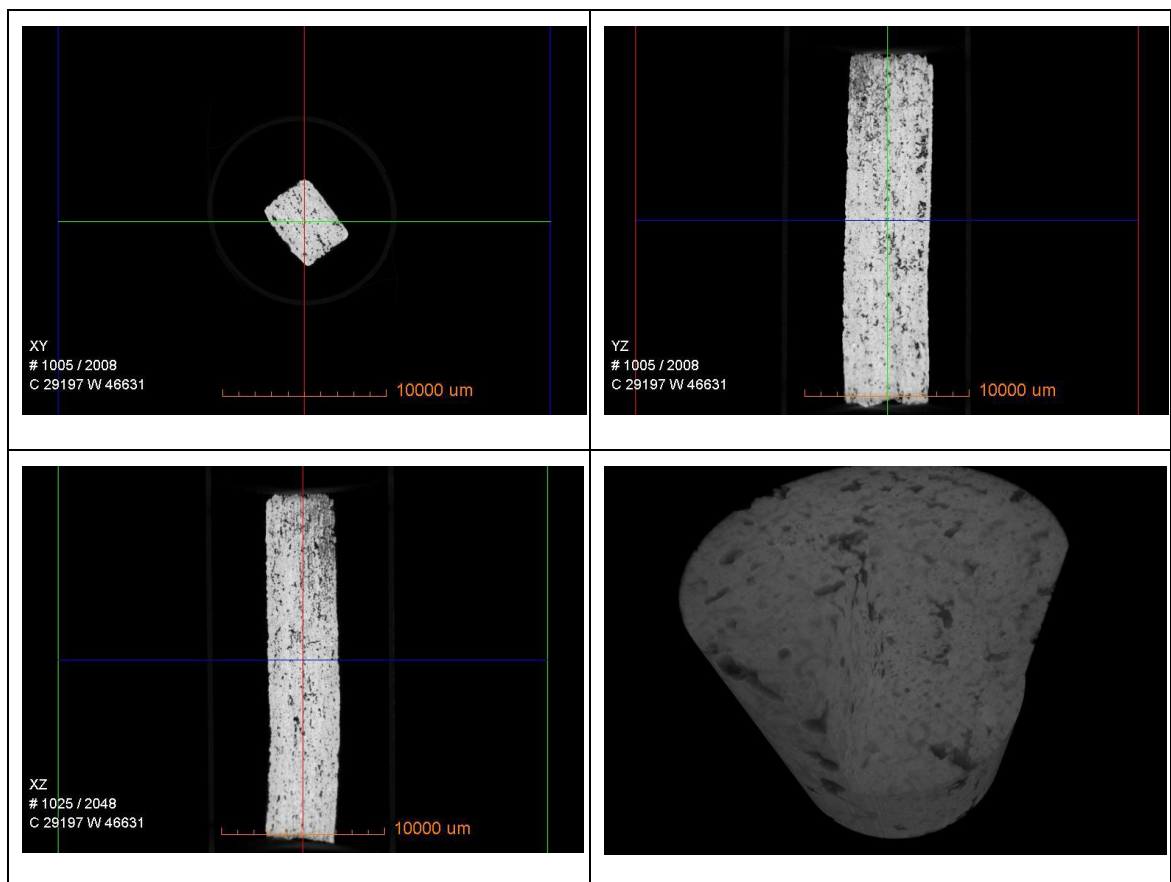


Figure 4.34 3D micro-CT images of parts made using PB5 and phosphate glass Infiltration Method B; Voxel size: 14.9 μm , Diameter of scanned volume is 10 mm

Table 4.12 shows the average bending strength and porosity (after infiltration by method A and B) for the part made using PB5. Test results showed no advantage to using method A, and therefore its use was discontinued.

Table 4.12 Summary of properties of parts made using PB5 after phosphate glass infiltration

Powder Blend	Average Bending Strength\pmSE (MPa)	Average Total Porosity (%)\pmSE	Average open Porosity (%)\pmSE	Quantity of phosphate glass (g)
PB5/zb [®] 60/InfilA	27.68 \pm 1.26	38.51 \pm 0.91	5.08 \pm 0.58	0.01-0.24
PB5/zb [®] 60/InfilB	31.34 \pm 3.12	21.75 \pm 1.46	2.46 \pm 1.56	0.15-0.58

Table 4.13 shows the average bending strength, Young's modulus and the total porosity (after infiltration by Method B) of the parts made using PB5, PB6 and PB7. The results show that PB5 has the highest average flexural strength after phosphate glass infiltration. Notably, the results of PB6 and PB7 indicate that the infiltration had only a limited effect.

Table 4.13 Summary of average bending strength, young's modulus and total porosity after phosphate glass infiltration of parts made using PB5, PB6 and PB7 by Method B

Powder Blend	Average Bending Strength\pmSE (MPa)	Average Young's Modulus \pmSE (GPa)	Average Total Porosity (%)\pmSE
PB5/zb [®] 60/InfilB	31.34 \pm 3.12	19.46 \pm 2.51	21.75 \pm 1.46
PB6/zb [®] 60/InfilB	17.89 \pm 1.66	8.94 \pm 0.94	42.22 \pm 1.21
PB7/zb [®] 60/InfilB	21.56 \pm 3.17	13.08 \pm 2.06	44.53 \pm 2.50

Chapter 5

Design and Manufacture of A-W Scaffolds

This chapter introduces the design and manufacture of several A-W scaffolds printed using the indirect 3DP. Moreover, some results of study of the interconnectivity, porosity, and accuracy of the manufactured parts will be presented. Finally, an *ex vivo* trial will be introduced.

5.1 Manufacturing of Parts with Internal Channels

Several A-W specimens with different shapes and sizes were successfully designed using Autodesk Inventor Professional (2012) CAD and were manufactured by indirect 3DP. The parts made with PB1 and zb@60 binder solution. The 3DP setting parameters and the post-process were the same in all the printing process as illustrated in chapter 3.

Slight linear shrinkage of the sintered parts was observed. As a result, the CAD dimensions were compensated to produce dimensionally accurate parts by adding the exact values of the linear variation for each dimension. The linear variation was calculated by the following equation:

$$\text{Linear Variation} = \text{CAD dimension} - \text{Sintered part dimension.}$$

It was possible to print samples successfully with internal channels and with different thicknesses, as illustrated in Figure 5.1. Powder that did not bind was brushed away from the channels using an air blower and needle. After sintering, the channel decreased more than 50% in diameter. Figure 5.2 shows the process capability in terms of defining channel and specimen dimensions. Channels with a diameter of less than 1 mm could not be printed for any thickness of sample as the powder was too difficult to remove, and the minimum printable diameter increased with thickness as powder removal become more difficult. Figure 5.3 shows images of 3D-printed samples with internal channels that were made from PB1.

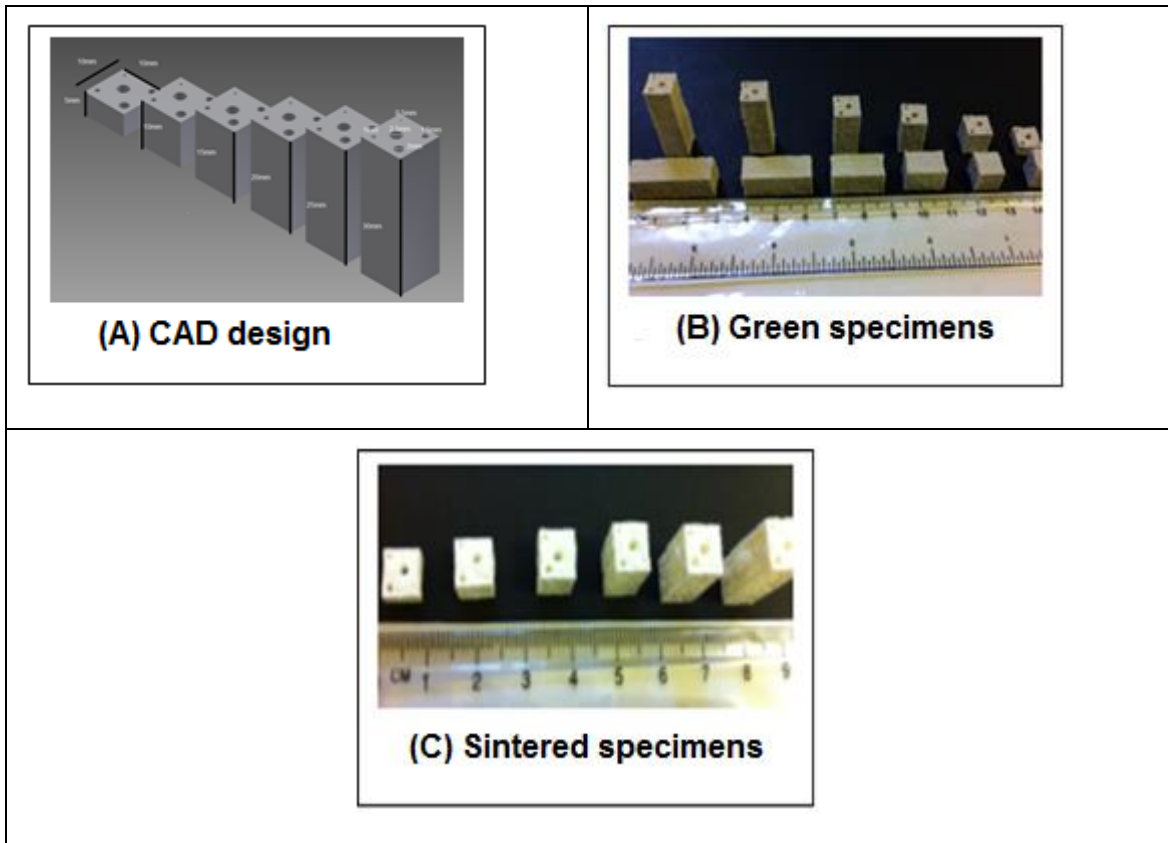


Figure 5.1 CAD design (A), green (B) and sintered (C) A-W specimens with internal channels

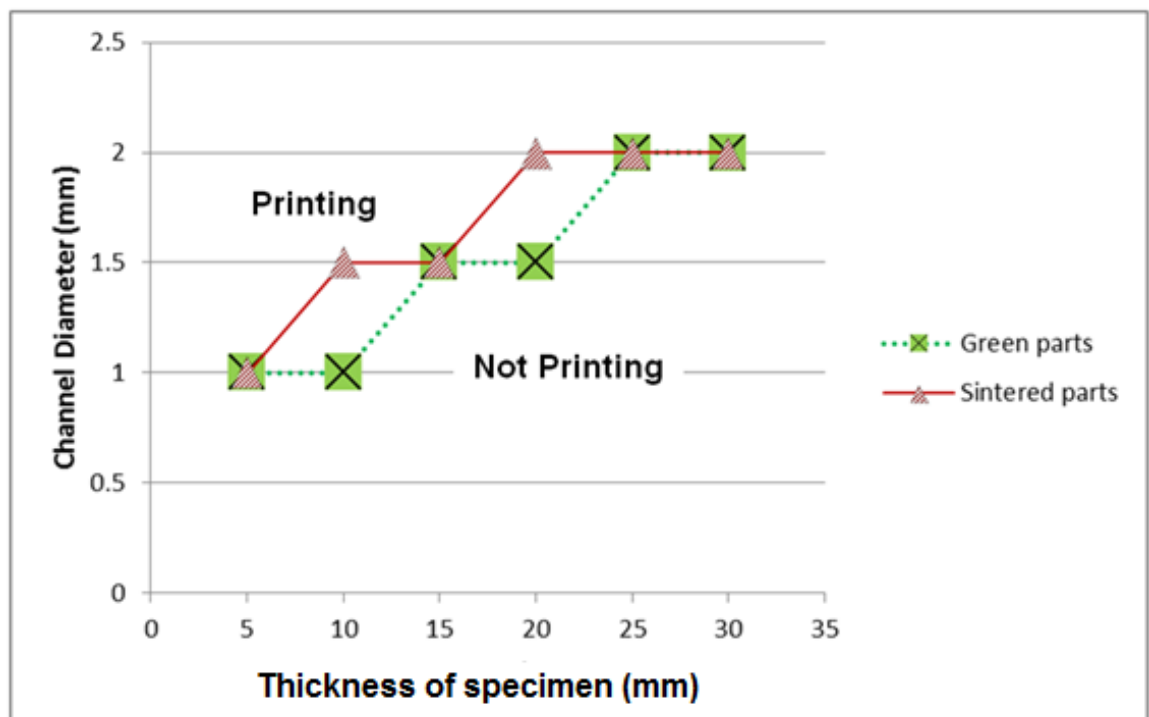


Figure 5.2 Relationship between the possible channel diameter and the thickness of the green and sintered part

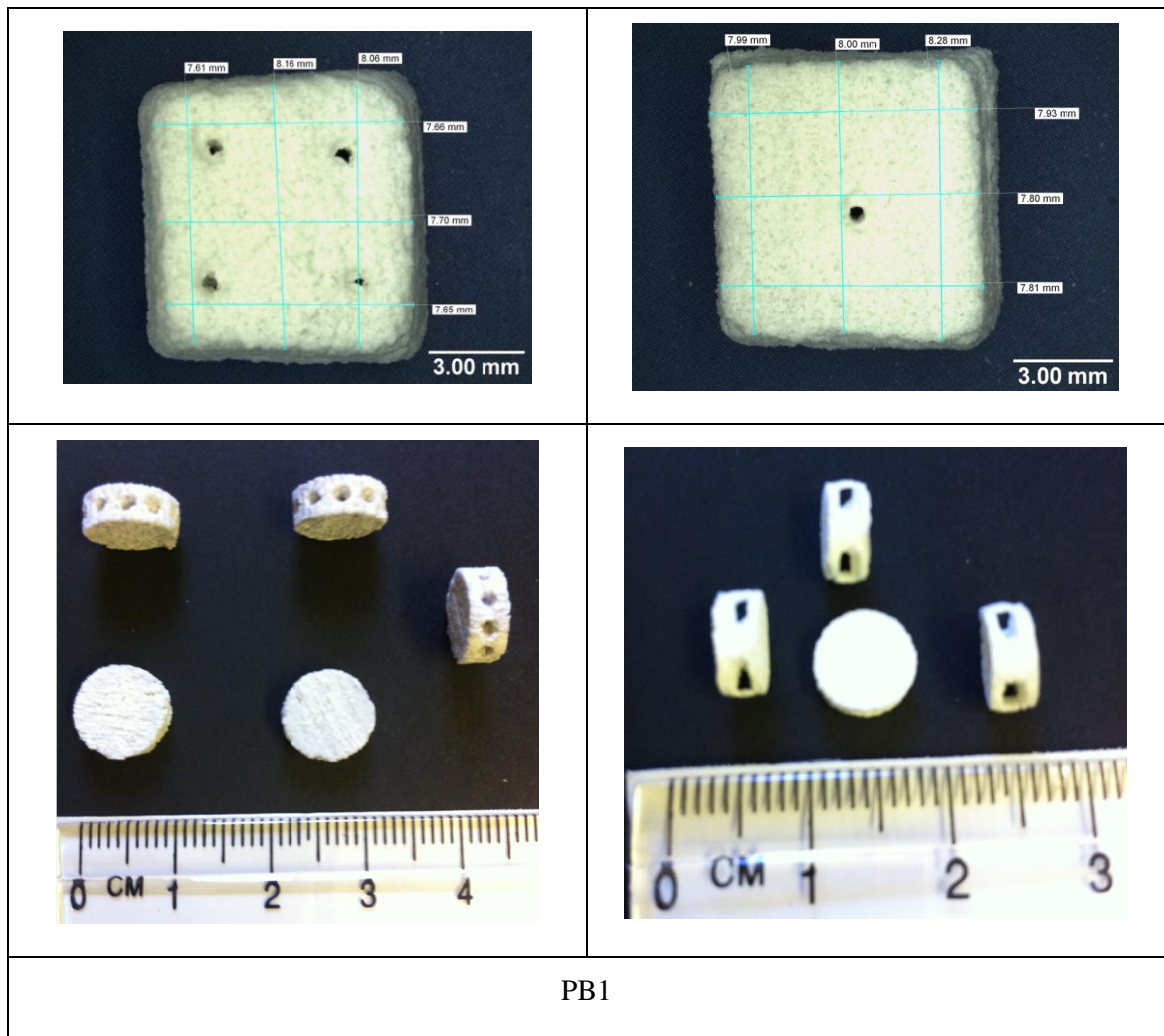
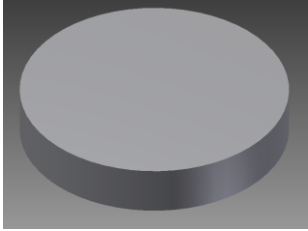
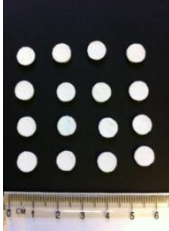
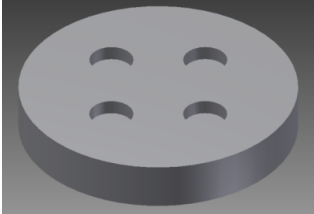
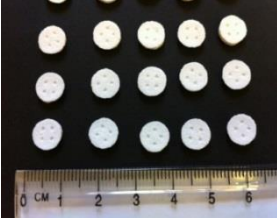
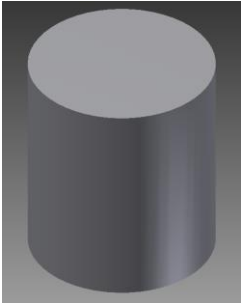
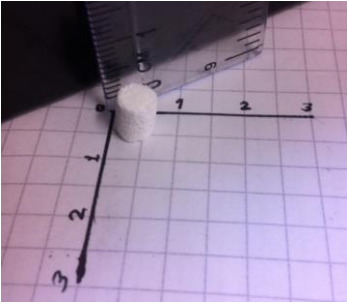




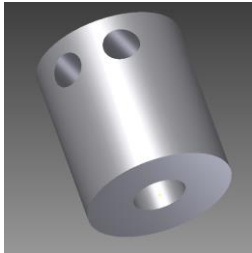

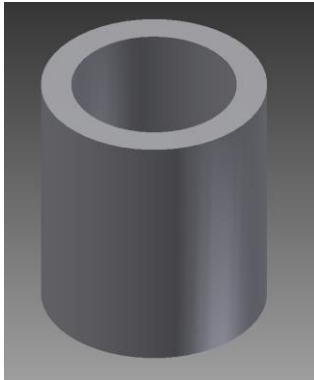
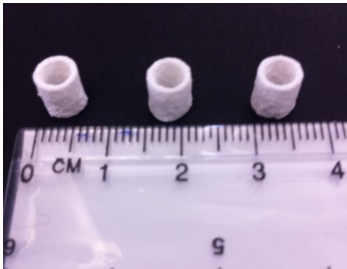
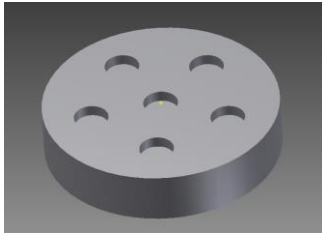
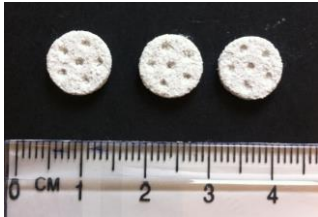
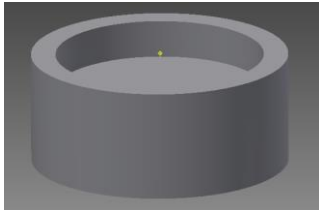
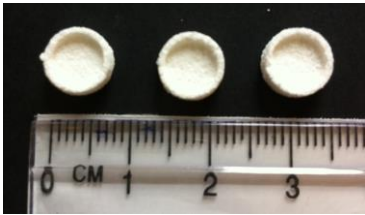
Figure 5.3 A-W Sintered specimens with internal channels made from PB1

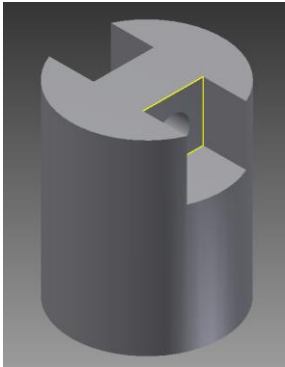

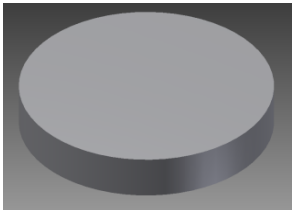
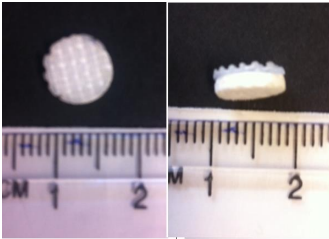
5.2 Implantable Devices

A number of implantable devices with different geometries were successfully printed using indirect 3DP. The estimated lead time for fabrication of 50 scaffolds was 37 h. Some of these devices were examined *in vitro* and *in vivo* and have shown the ability of 3D printed A-W scaffolds to support osteogenic differentiation of bone marrow stromal cells (BMSCs) *in vitro* and osteointegration and new bone growth *in vivo*. *In vitro* and *in vivo* trials were performed by other groups at different universities in the UK and Europe. Table 5.1 shows the CAD model, 3DP parts, quantity, target, and date of production of these devices.

Table 5.1 CAD model and indirect 3DP sintered specimens

Type	CAD Model	Indirect 3DP Parts (PB5)	Quantity	Purpose	Date
Disc		 $\phi = 8\text{mm}, h = 2\text{mm}$	700	In vitro and in vivo tests	9/2012
Disc with four pockets		 $\phi = 8\text{mm}, h = 2\text{mm} \ \&$ $\phi = 1\text{mm}, d = 0.5\text{mm}$	200	In vitro tests co-culture devices, pocket dimension as requested for cell volume	4/2013
Plug		 $\phi = 6\text{mm}, h = 7\text{mm}$	50	Prototype	6/2013
Plug with two through holes		 $\phi = 6\text{mm}, h = 7\text{mm}$	50	Osteochondral plug design for Ex vivo assesment and in vivo tests	3/2014

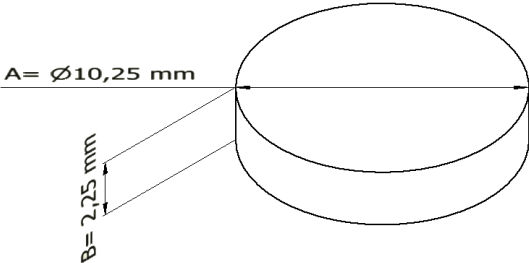
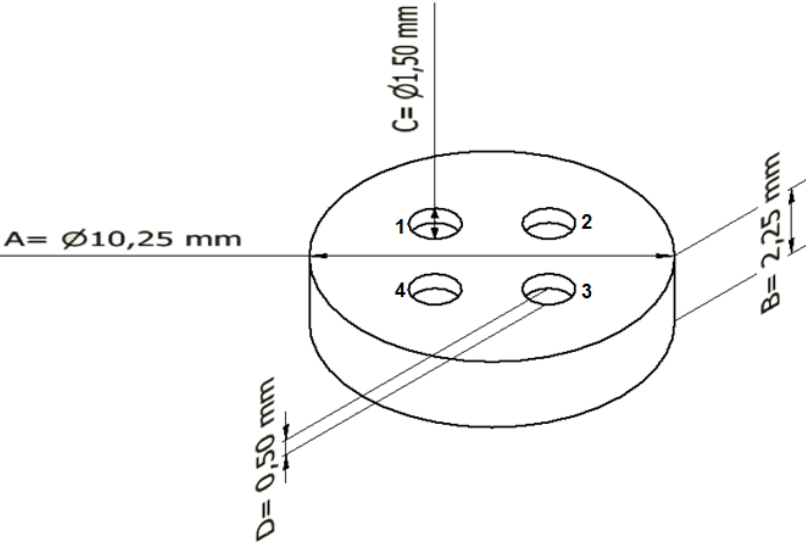
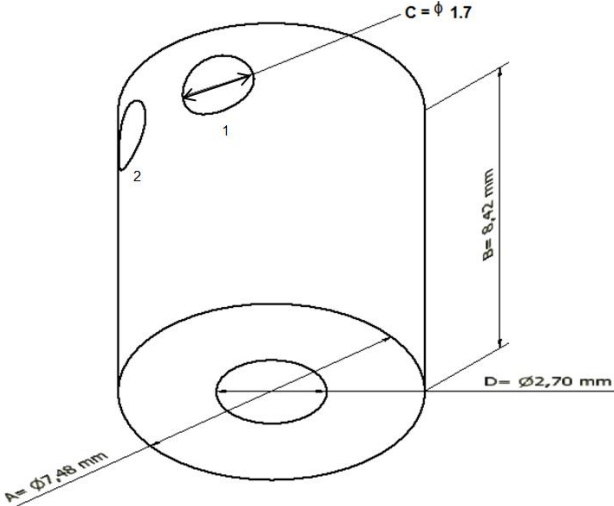
Type	CAD Model	Indirect 3DP Parts (PB5)	Quantity	Purpose	Date
Plug with two through holes and one pocket hole		 $\phi = 6\text{mm}, h = 7\text{mm}$	12	Prototype osteochondral plug design	3/2014
Hollow Cylinder		 $\phi = 6\text{mm}, h = 7\text{mm}$	12	Prototype	3/2014
Disc with six pockets		 $\phi = 8\text{mm}, h = 2\text{mm} \&$ $\phi = 1\text{mm}, d = 0.5\text{mm}$	100	In vitro tests revised design of co-cultural device	5/2014
Disc with lip		 $\phi = 8\text{mm}, h = 2\text{mm}$	250	Long term cell culture tests	10/2014

Type	CAD Model	Indirect 3DP Parts (PB5)	Quantity	Purpose	Date
Anchor plug		 ϕ= 6mm, h=8mm	10	Prototype bone anchor device	6/2014
Two phase A-W & PLA Disc		 A-W (3DP) + PLA (FDM)	200	Prototype osteochondral device for In vitro and in vivo tests	2/2014

5.2.1 Accuracy of Printed Parts

The CAD model and dimensions are presented in Table 5.2. The accuracy of parts made using PB5 are introduced in detail below in Table 5.3.

Table 5.2 CAD model and dimension of devices

Type	CAD dimension (mm)
Disc	 <p>A = Ø10,25 mm B = 2,25 mm</p>
Disc with four pockets	 <p>A = Ø10,25 mm B = 2,25 mm C = Ø1,50 mm D = 0,50 mm</p>
Plug with two through holes and one pocket hole	 <p>A = Ø7,68 mm B = 8,82 mm C = Ø 1.7 mm D = Ø2,70 mm</p>

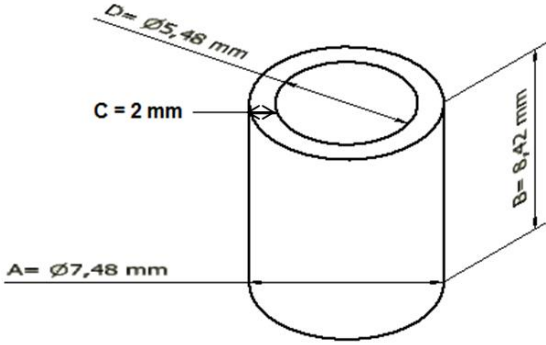
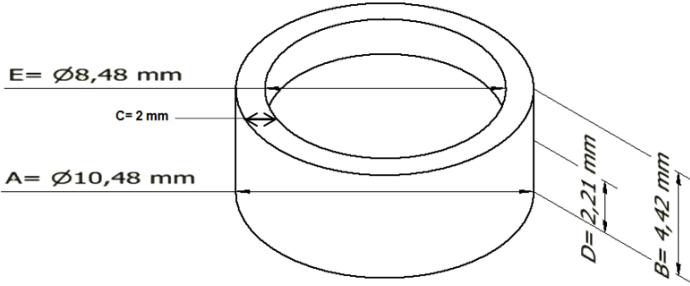
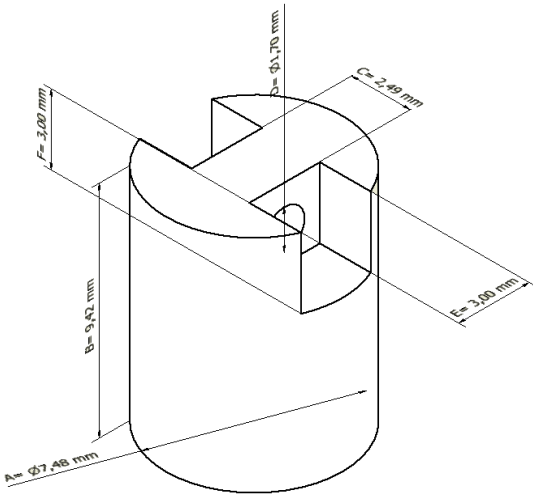
Type	CAD dimension (mm)
<p>Hollow cylinder</p>	 <p> $D = \text{Ø}5,48 \text{ mm}$ $C = 2 \text{ mm}$ $B = 8,42 \text{ mm}$ $A = \text{Ø}7,48 \text{ mm}$ </p>
<p>Disc with lip</p>	 <p> $E = \text{Ø}8,48 \text{ mm}$ $C = 2 \text{ mm}$ $A = \text{Ø}10,48 \text{ mm}$ $D = 2,21 \text{ mm}$ $B = 4,42 \text{ mm}$ </p>
<p>Anchor plug</p>	 <p> $F = 3,00 \text{ mm}$ $B = 9,42 \text{ mm}$ $A = \text{Ø}7,48 \text{ mm}$ $D = \text{Ø}1,70 \text{ mm}$ $C = 2,49 \text{ mm}$ </p>

Table 5.3 Accuracy of devices

Type of device	Required dimensions (mm)		n	Mean±SE	Max	Min	95% CI
Disc	A	8	10	7.94±0.03	8.11	7.85	(7.87,8.00)
	B	2	10	1.87±0.01	1.91	1.82	(1.85,1.88)
Disc with four pockets	A	8	10	8.09±0.14	8.09	7.96	(7.9, 8.1)
	B	2	10	1.97±0.01	2.02	1.93	(1.95, 1.99)
	C1	1	10	0.98±0.01	1.01	0.95	(0.96, 0.99)
	D1	0.5	10	0.48±0.02	0.60	0.40	(0.44, 0.52)
	C2	1	10	0.98±0.04	1.01	0.97	(0.97, 0.99)
	D2	0.5	10	0.48±0.01	0.55	0.45	(0.44, 0.51)
	C3	1	10	0.98±0.01	1.02	0.97	(0.97, 0.99)
	D3	0.5	10	0.49±0.02	0.60	0.40	(0.45, 0.53)
	C4	1	10	0.99±0.01	1.01	0.97	(0.98, 1.00)
	D4	0.5	10	0.47±0.02	0.60	0.45	(0.44, 0.50)
Plug with two through holes and one pocket hole	A	6	10	6.02±0.02	6.10	5.96	(5.98, 6.05)
	B	7	10	7.01±0.01	7.07	6.98	(6.99, 7.04)
	C1	1	10	0.98±0.01	1.01	0.96	(0.97, 0.99)
	C2	1	10	0.99±0.01	1.01	0.96	(0.97, 1.00)
	D	2	10	2.13±0.03	2.24	1.98	(2.07, 2.19)

Type of device	Required dimensions		n	Mean±SE	Max	Min	95% CI
	(mm)						
Hollow cylinder	A	6	10	5.97±0.01	6.05	5.95	(5.95, 5.99)
	B	7	10	6.86±0.01	6.91	6.81	(6.83, 6.88)
	C	1	10	1.03±0.03	1.16	0.95	(5.95, 5.99)
Disc with lip	A	8	10	8.27±0.04	8.42	8.08	(8.19, 8.35)
	B	4	10	4.04±0.03	4.16	3.90	(3.97, 4.10)
	C	1	10	1.11±0.02	1.20	1.00	(1.07, 1.15)
	D	2	10	2.40±0.01	2.43	2.39	(2.40, 2.41)
Anchor plug	A	6	10	6.07±0.02	6.20	6.00	(6.03, 6.12)
	B	8	10	7.95±0.02	8.01	7.89	(7.91, 7.98)
	C	2	10	2.11±0.01	2.19	2.06	(2.08, 2.14)
	D	1	10	0.95±0.01	0.97	0.92	(0.94, 0.96)
	E	2	10	1.99±0.02	2.10	1.90	(1.95, 2.03)
	F	2	10	2.28±0.02	2.40	2.20	(2.23, 2.34)

5.2.2 Interconnectivity and porosity

The interconnectivity was determined by observation of 3D micro-CT images. Porosity and density measurements of sintered specimens were performed using the Archimedes principle as described in Chapter 3. Table 5.4 summarises the results. There are significant differences which it was thought might be related to differences in the surface area to volume ratio, as a greater external surface area means a greater area for powder cleaning and more potential for erosion in the powder cleaning process. Figure 5.4 plots the open porosity against the surface area to volume ratio (calculated from the CAD models) and shows a general trend forwards increasing open porosity with increasing surface area to volume ratio, but this would require further testing to confirm.

Table 5.4 Summary of average open porosity and apparent surface area and volume of devices

Device	Average Open Porosity \pm SE (%)	Apparent Surface Area (from CAD) (mm ²)	Volume (from CAD) (mm ³)	Surface Area to Volume Ratio (from CAD) (mm ⁻¹)
Disc	14.20 \pm 0.19	237.58	185.74	1.28
Disc with four pockets	28.78 \pm 1.08	247.02	184.64	1.46
Plug	20.51 \pm 0.53	285.86	370.15	0.77
Plug with two through holes	28.97 \pm 1.01	356.7	336.28	1.06
Plug with two through holes and one pocket hole	28.89 \pm 0.43	399.13	307.64	1.30
Hollow cylinder	33.29 \pm 1.17	383.54	171.41	2.24

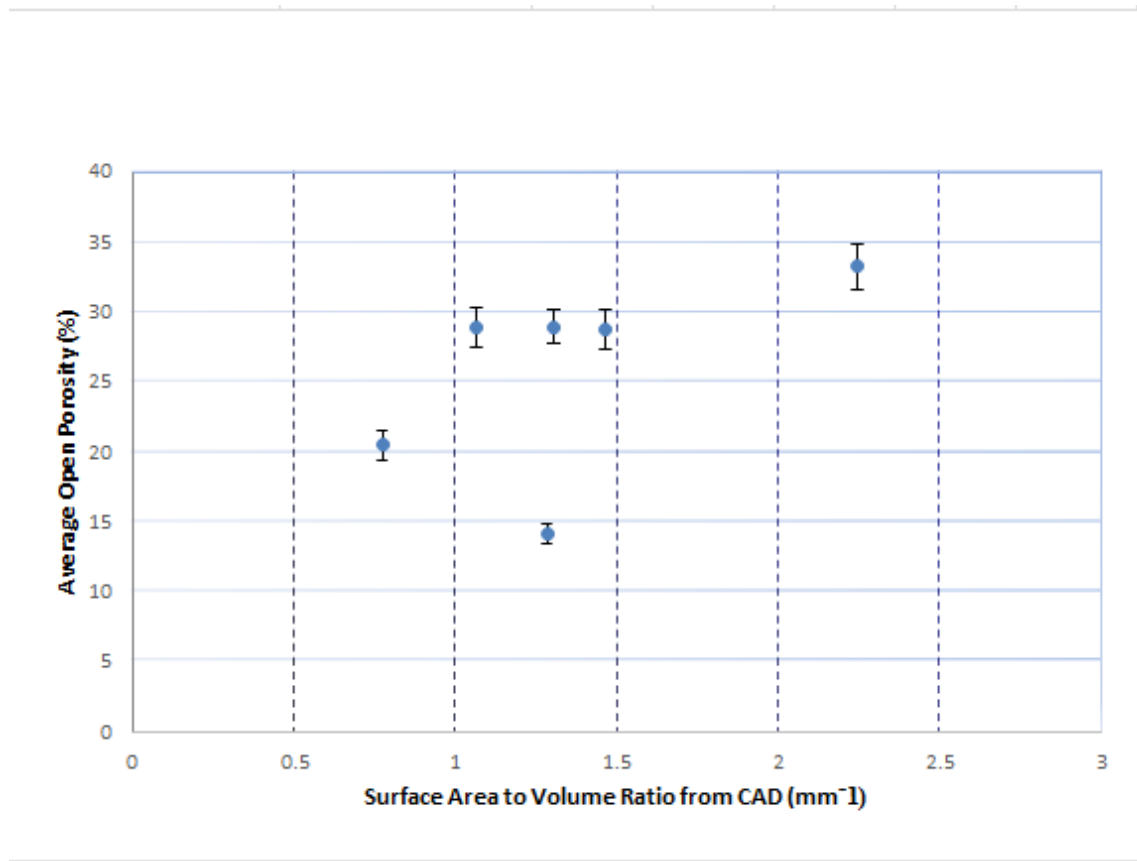


Figure 5.4 Relationship between the average open porosity and surface area/ volume ratio
*Error bars indicate standard error of open porosity

5.2.2.1 Printed and sintered 8 mm (diameter) by 2 mm (height) discs of PB1

Several discs of PB1 were successfully printed (Figure 5.5) and the average open porosity of A-W disks was 14.20 %, as shown in Table 5.5.



Figure 5.5 Printed and sintered discs of PB1

Table 5.5 Open porosity of PB1 disks

Specimens	Mass (dry) (g)	Mass (submerged) (g)	Mass (wet) (g)	Open Porosity %
1	0.16832	0.1045	0.17918	14.54
2	0.1635	0.10081	0.17362	13.90
3	0.16552	0.10288	0.17586	14.17
Mean				14.20
SD				0.32
SE				0.19

5.2.2.2 Printed and sintered 8 mm (diameter) by 2 mm (height) discs of PB5

An investigation of A-W disks printed from PB5 3D by micro-CT indicates that the specimens have micro (pore size < 10) and macro (pore size > 50) pores and some of these pores are connected together and to the surfaces of the specimens, as shown in Figure 5.6.

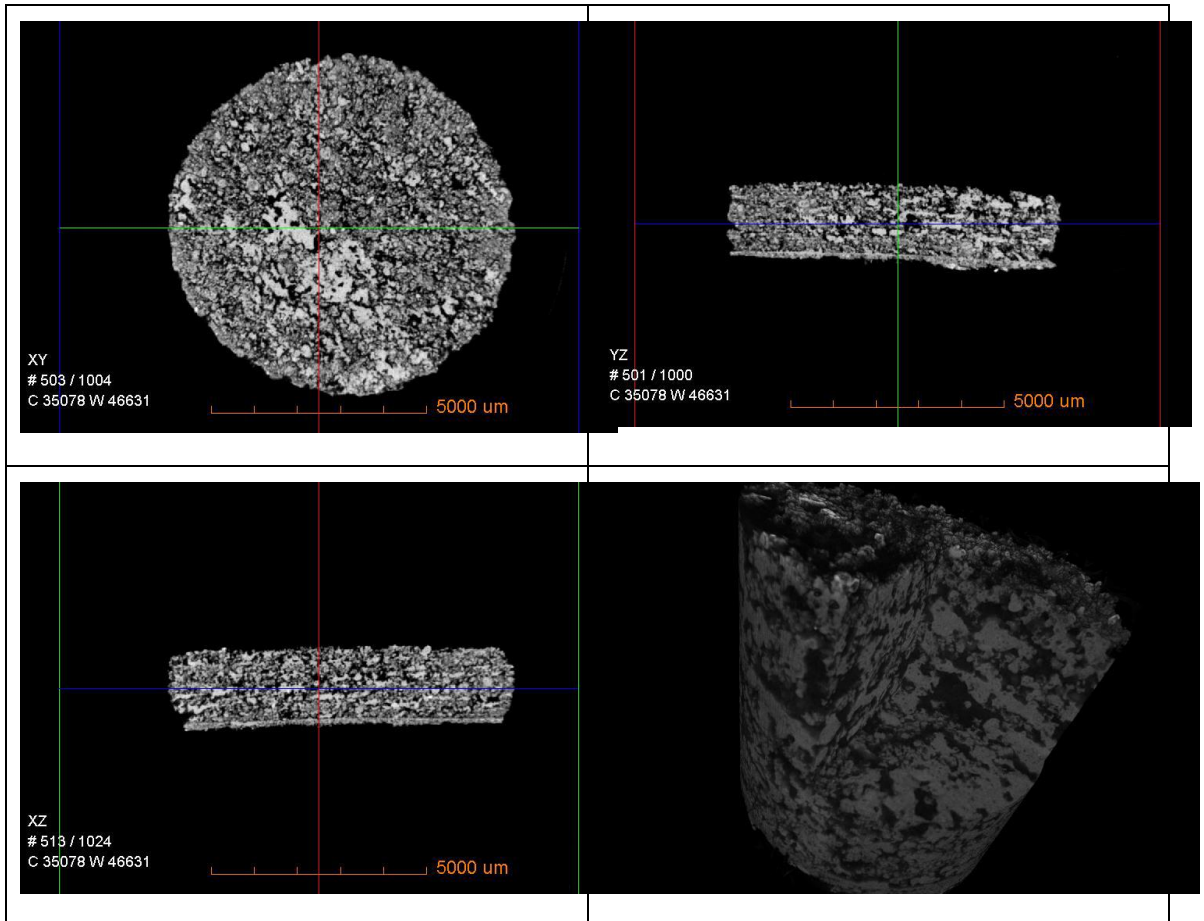


Figure 5.6 3D micro-CT images of PB5 discs, Voxel size; 12.01 μm , Diameter of scanned volume is 5 mm

5.2.2.3 Printed and sintered 8 mm (diameter) by 2 mm (height) disc with four pockets of PB1

In this design (Figure 5.7), the open porosity increased up to 28.78%, as shown in Table 5.6. Investigation by 3D micro-CT showed that there are interconnected micro and macro pores in these disks, as illustrated in Figure 5.8.



Figure 5.7 Printed and sintered discs with four pockets of PB1

Table 5.6 Open porosity of PB1 discs with four pockets

Specimens	Mass (dry) (g)	Mass (submerged) (g)	Mass (wet) (g)	Open Porosity %
1	0.14073	0.09203	0.16225	30.65
2	0.13145	0.08623	0.14811	26.92
3	0.13245	0.08875	0.15010	28.77
Mean				28.78
SD				1.86
SE				1.08

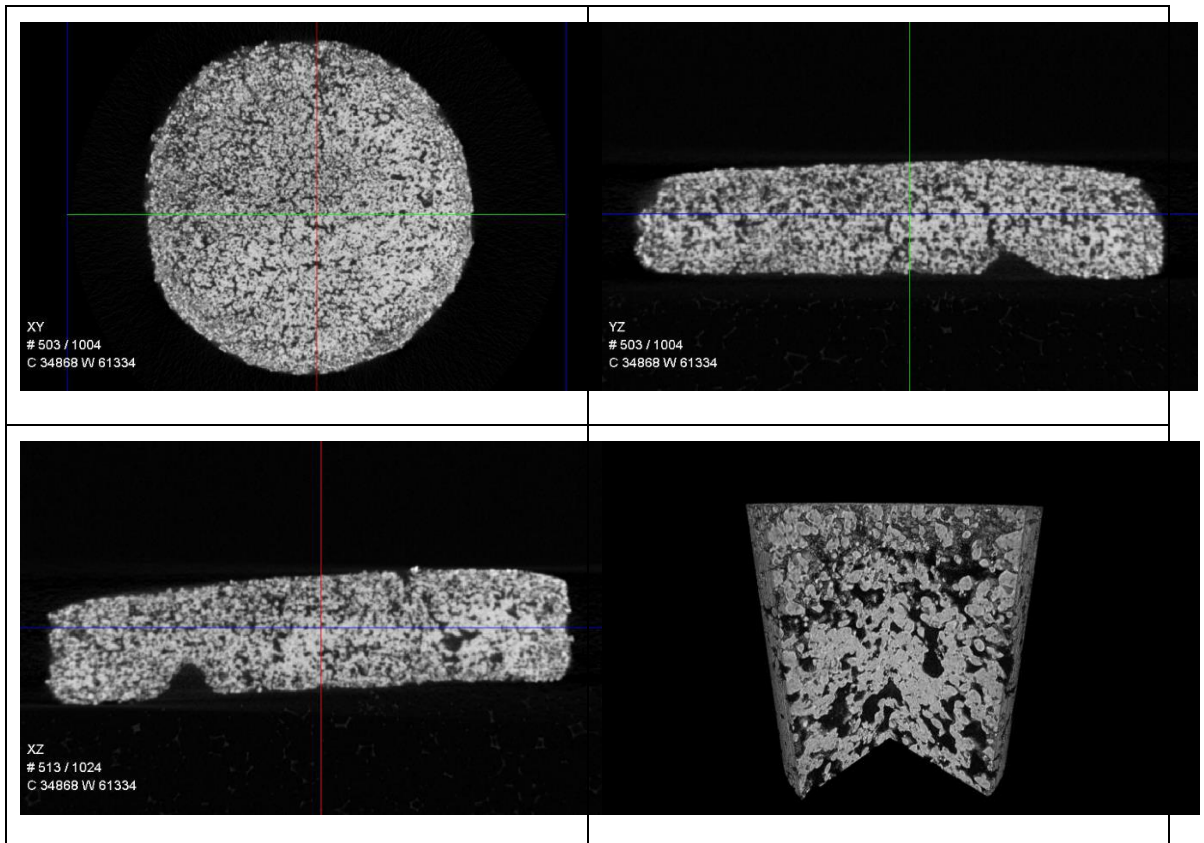


Figure 5.8 3D micro-CT images of PB1 discs with four pockets, Voxel size; 11.90 μm , Diameter of scanned volume is 5 mm

5.2.2.4 Printed and sintered 6 mm (diameter) by 7 mm (height) plugs of PB5

The average open porosity for this design (Figure 5.9) is 20.51%, as shown in Table 5.7. Investigation of A-W plugs printed from PB5 by 3D micro-CT shows that there are interconnected micro and macro pores, and this design is denser in the center and more porous near the surfaces as shown in Figure 5.10.



Figure 5.9 Printed and sintered plugs of PB5

Table 5.7 Open porosity of PB5 plugs

Specimens	Mass (dry) (g)	Mass (submerged) (g)	Mass (wet) (g)	Open Porosity %
1	0.31732	0.19512	0.35135	21.78
2	0.31965	0.19805	0.34984	19.89
3	0.31902	1.19735	0.34837	19.43
4	0.32338	0.20047	0.35591	20.93
Mean				20.51
SD				1.05
SE				0.53

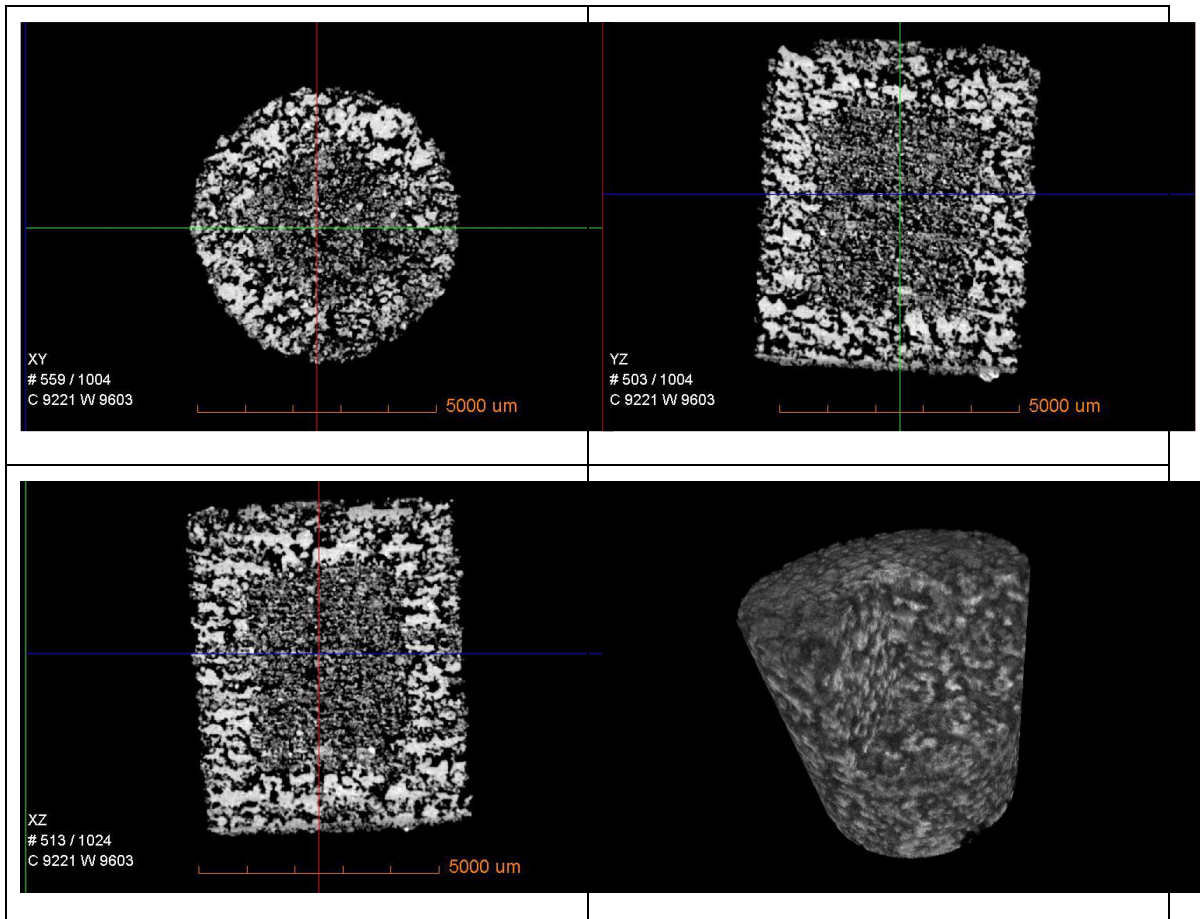


Figure 5.10 3D micro-CT images of PB5 plug, Voxel size; 12.12 μm , Diameter of scanned volume is 5 mm

5.2.2.5 Printed and sintered 6 mm (diameter) by 7 mm (height) plugs with two through holes of PB5

The open porosity for this design (Figure 5.11) increased up to 28.97 %, as shown in Table 5.8. Figure 5.12 shows the micro-CT images, which indicate that there are interconnected micro and macro pores, and it has more porosity near the surfaces.



Figure 5.11 Printed and sintered plugs with two through holes of PB5

Table 5.8 Open porosity of PB5 plugs with two through holes

Specimens	Mass (dry) (g)	Mass (submerged) (g)	Mass (wet) (g)	Open Porosity %
1	0.27825	0.1742	0.3182	27.74
2	0.27475	0.1732	0.32032	30.97
3	0.27566	0.17226	0.31625	28.19
Mean				28.97
SD				1.75
SE				1.01

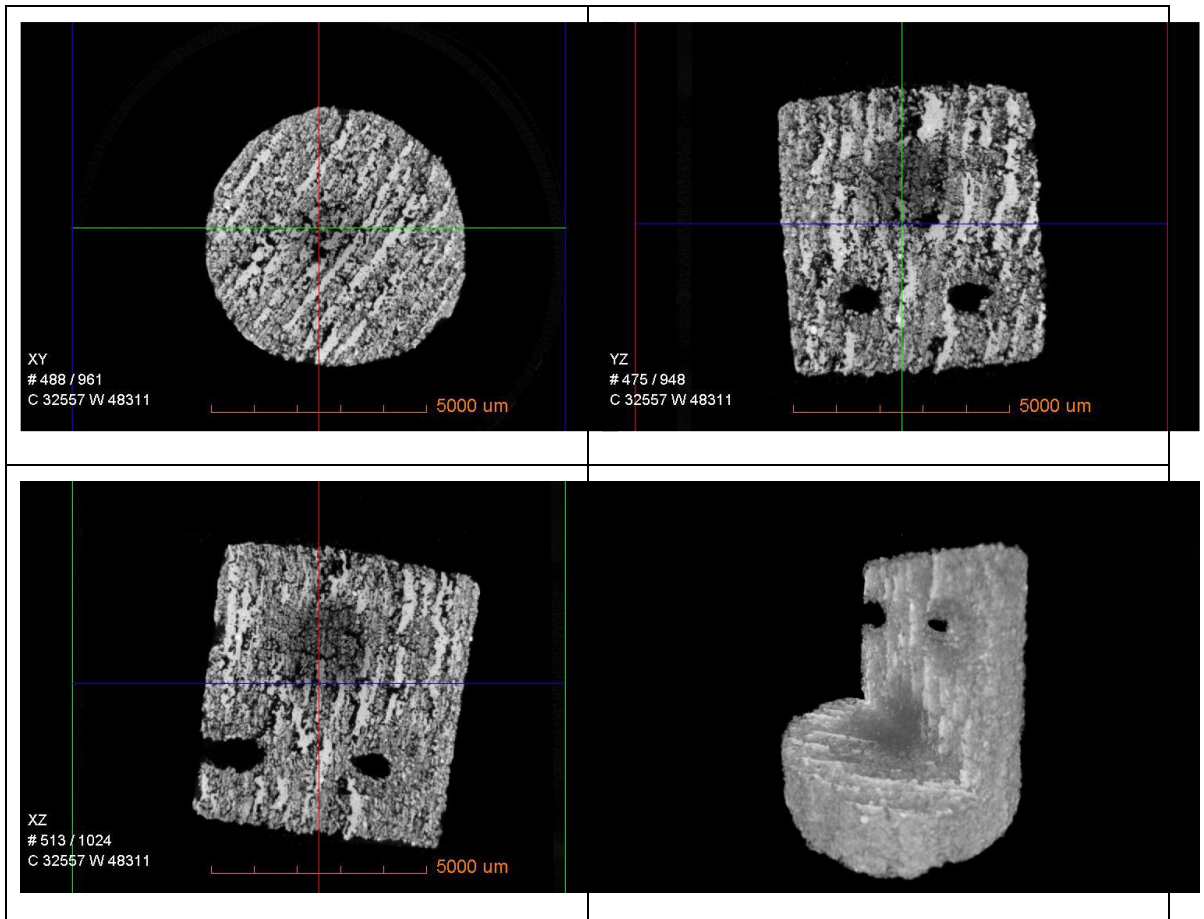


Figure 5.12 3D micro-CT images of PB5 plugs with two through holes, Voxel size; 12.01 μm , Diameter of scanned volume is 5 mm

5.2.2.6 Plugs with two through holes and one pocket hole of PB5

Figure 5.13 shows the printed and sintered parts of this design. Table 5.9 shows the open porosity of this part. An analysis by 3D micro-CT indicates that this part has interconnected micro and macro pores, as shown in Figure 5.14.



Figure 5.13 Printed and sintered plugs with two through holes and one pocket hole of PB5

Table 5.9 Open porosity of PB5 plugs with two through holes and one pocket hole

Specimens	Mass (dry) (g)	Mass (submerged) (g)	Mass (wet) (g)	Open Porosity %
1	0.2472	0.15564	0.28316	28.20
2	0.25592	0.1614	0.29412	28.78
3	0.25208	0.15845	0.29162	29.69
Average				28.89
SD				0.75
SE				0.43

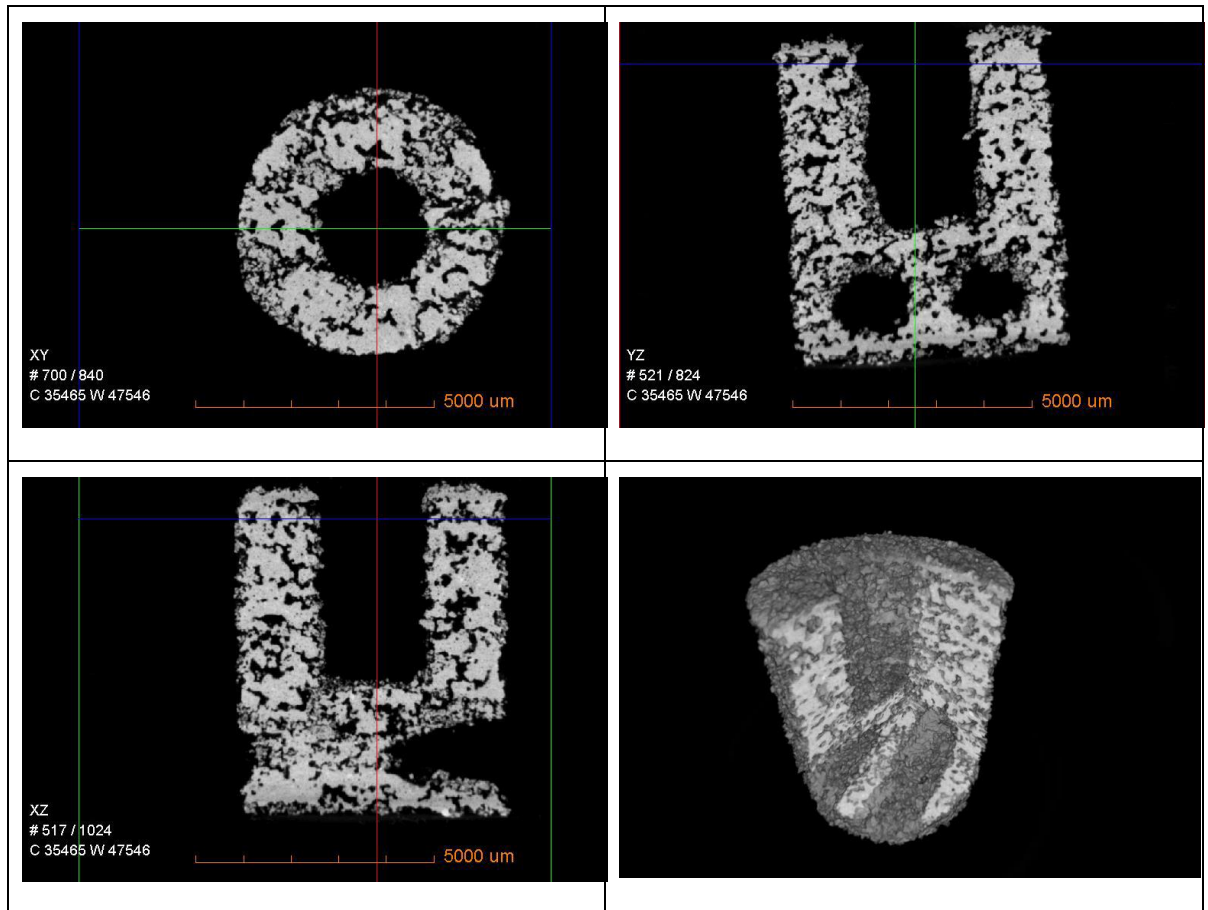


Figure 5.14 3D micro-CT images of PB5 plug two through holes and one pocket hole, Voxel size; 12.01 μm , Diameter of scanned volume is 5 mm

5.2.2.7 Hollow Cylinders

Figure 5.15 shows the printed and sintered parts of the hollow cylinders of PB5. Table 5.10 shows the open porosity of the hollow cylinder. The 3D micro-CT analysis shows that there are interconnected micro and macro pores, as shown in Figure 5.16.

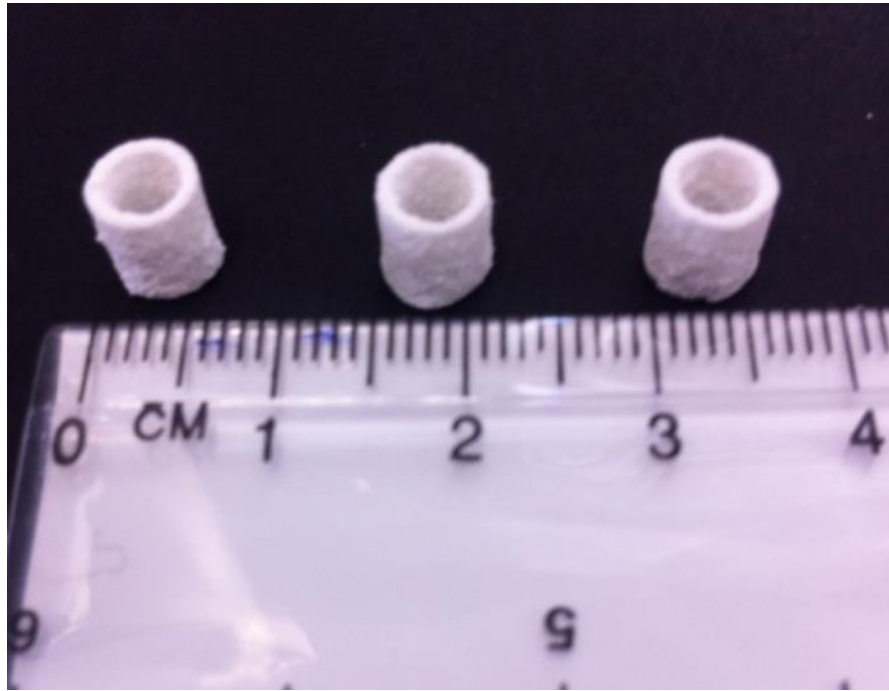


Figure 5.15 Printed and sintered hollow cylinders of PB5

Table 5.10 Open porosity of PB5 cylinder device

Specimens	Mass(dry) (g)	Mass(submerged) (g)	Mass(wet) (g)	Open Porosity %
1	0.14583	0.09242	0.17009	31.23
2	0.15245	0.09711	0.1826	35.27
3	0.14436	0.09262	0.17028	33.38
Mean				33.29
SD				2.02
SE				1.17

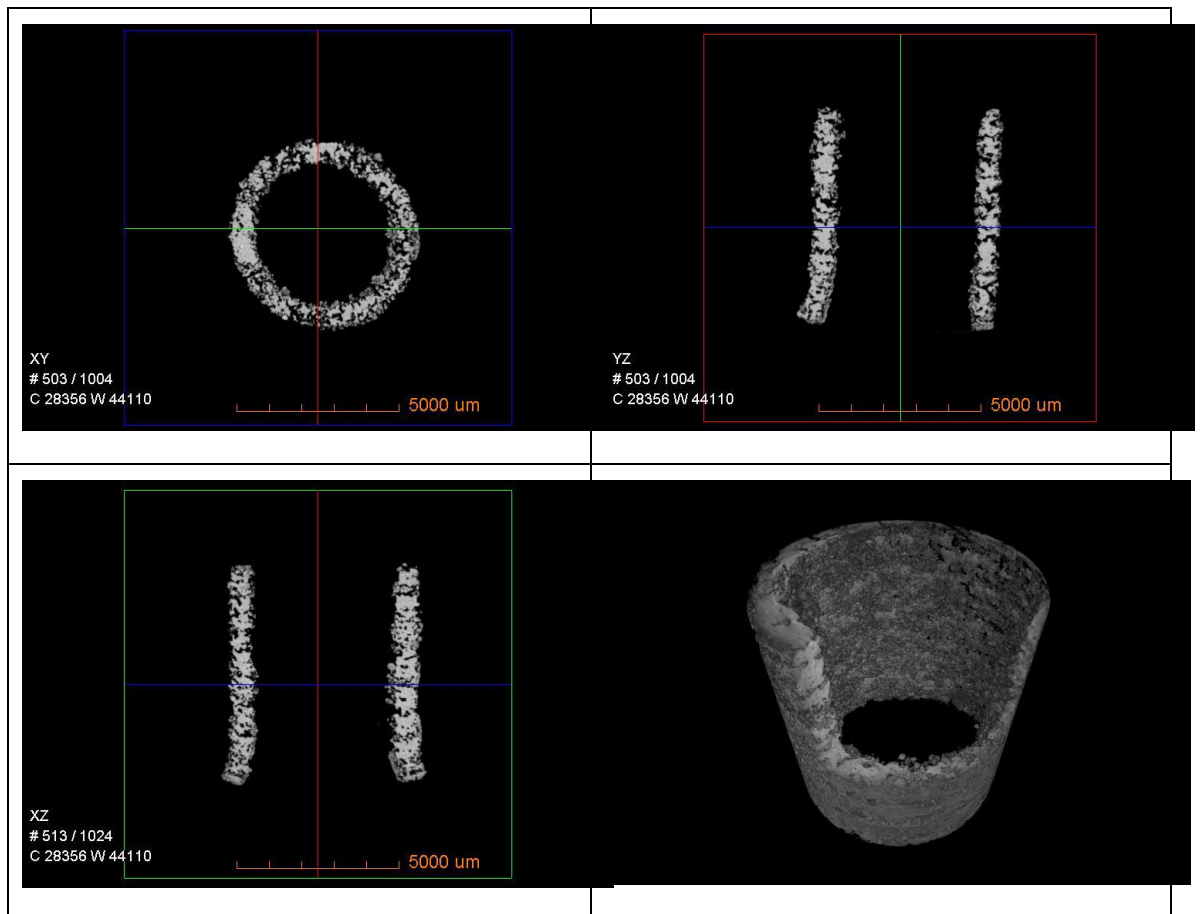


Figure 5.16 3D micro-CT images of PB5 cylinder device, Voxel size; 11.86 μm , Diameter of scanned volume is 5 mm

5.2.3 Bioactivity

As mentioned in this Chapter, several batches of A-W scaffolds were supplied to European project groups (Resorbable Ceramic Biocomposites for Orthopaedic and Maxillofacial Applications) for the *in vitro* and *in vivo* assessments. Their results will be presented to confirm the bioactivity and applications of A-W scaffolds. This work was performed by Dr. Ion Tcacencu at the Karolinska Institute in Sweden.

5.2.3.1 *In vitro* cell-compatibility assessment

The results showed that rat BMSCs could grow and expand on the surface of A-W discs, as illustrated in Figure 5.17. Figure 5.18 shows the compatibility of rat BMSCs with A-W after 7 d in culture on A-W discs compared with plastic. Figure 5.19 shows the compatibility of rat primary calvaria osteoblasts (COB) with A-W after 7 d in culture on A-W discs compared with plastic. Figure 5.20 shows the compatibility of rat COB with A-W after 14 d in culture on A-W discs compared with plastic. These results

indicated that A-W has a short term negative effect on rat BMSCs viability, which the cells rapidly recover from, and that A-W supports the proliferation of the rat COBs.

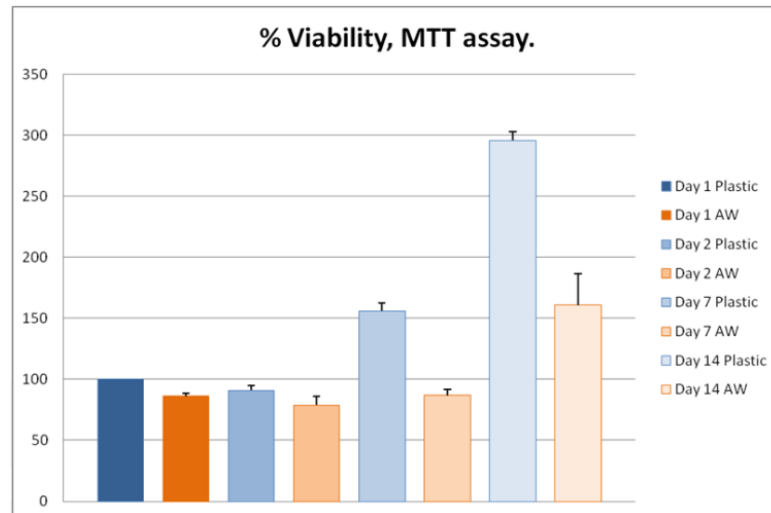


Figure 5.17 Viability of rat BMSCs on A-W discs compared with plastic on Day 1 through Day 14

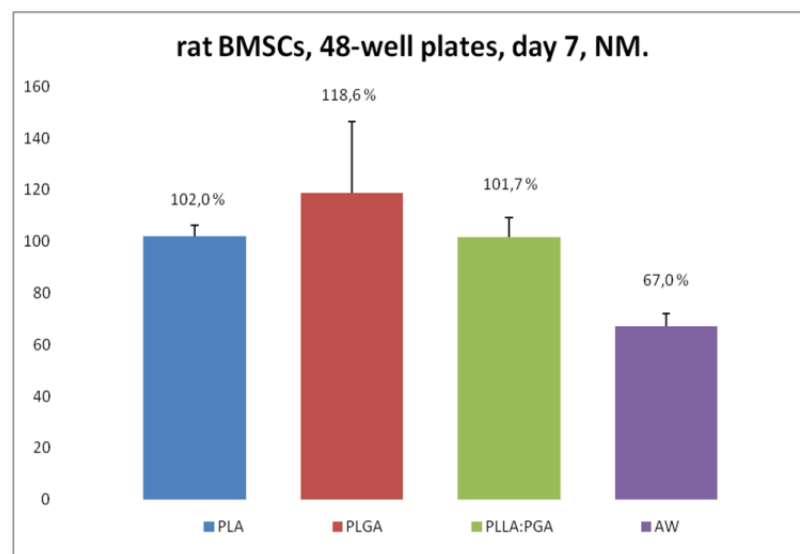


Figure 5.18 Growth of rat BMSCs on A-W compared with common biopolymers after 7 d in culture

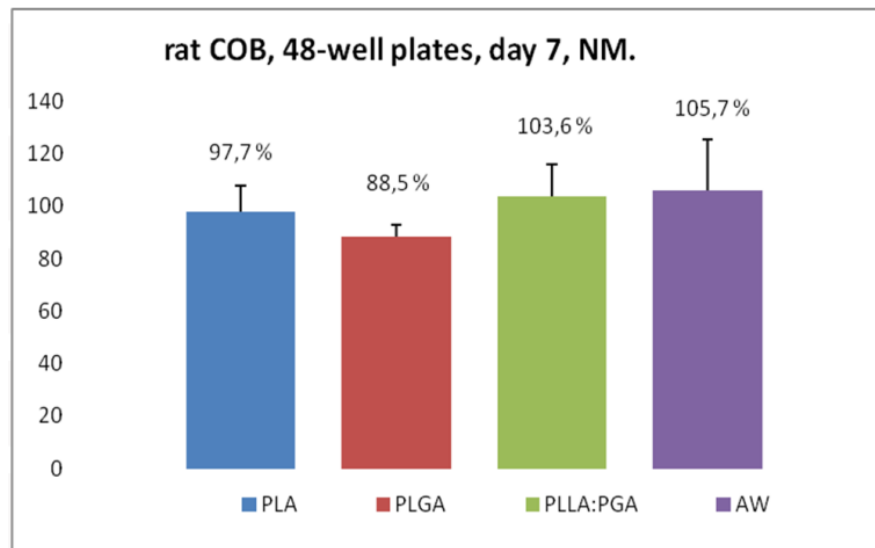


Figure 5.19 Growth of rat COB on A-W compared with common biopolymers after 7 d in culture

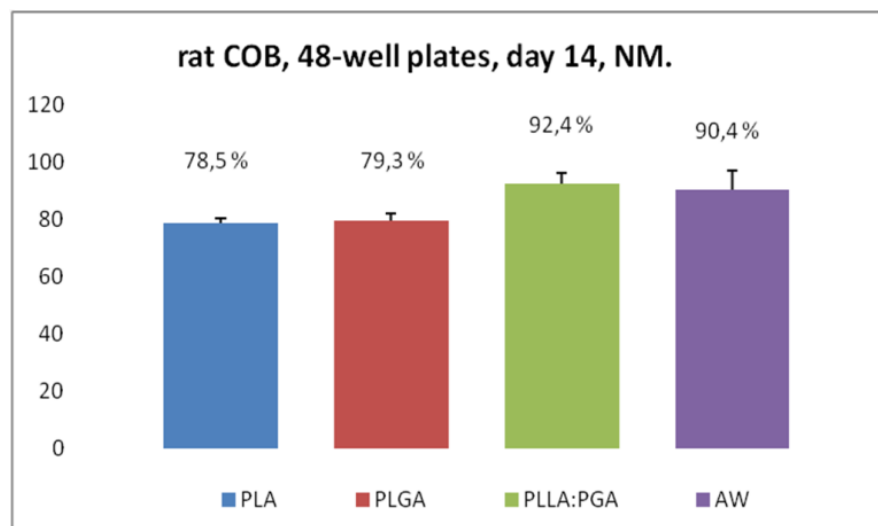


Figure 5.20 Growth of rat COB on A-W compared with common biopolymers after 14 d in culture

5.2.3.2 *In vitro* osteogenic differentiation

The osteogenic experiment indicated that cells grown on A-W discs have the highest levels of ALP and better osteogenic properties than those grown on culture plastic, as shown in Figure 5.21 Figure 5.22 shows a comparison with common biopolymers.

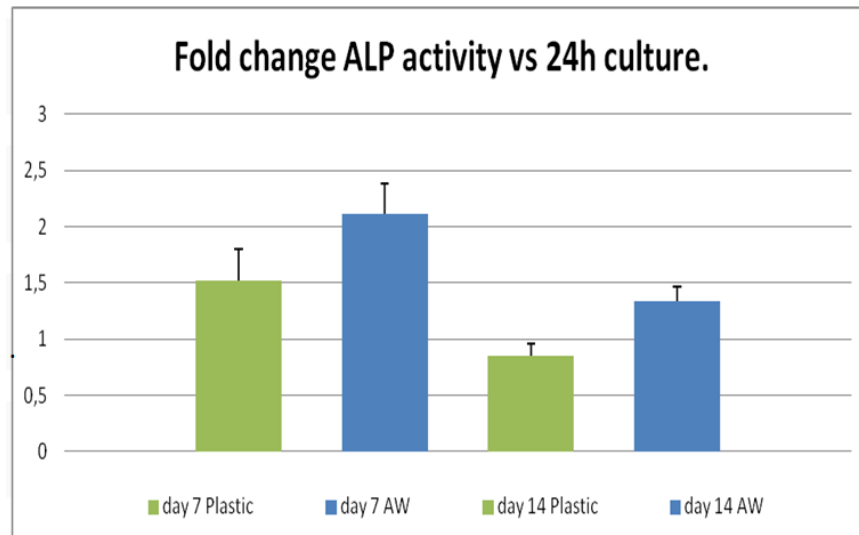


Figure 5.21 Fold change in ALP activity compared with 24-h culture at 7 and 14 d

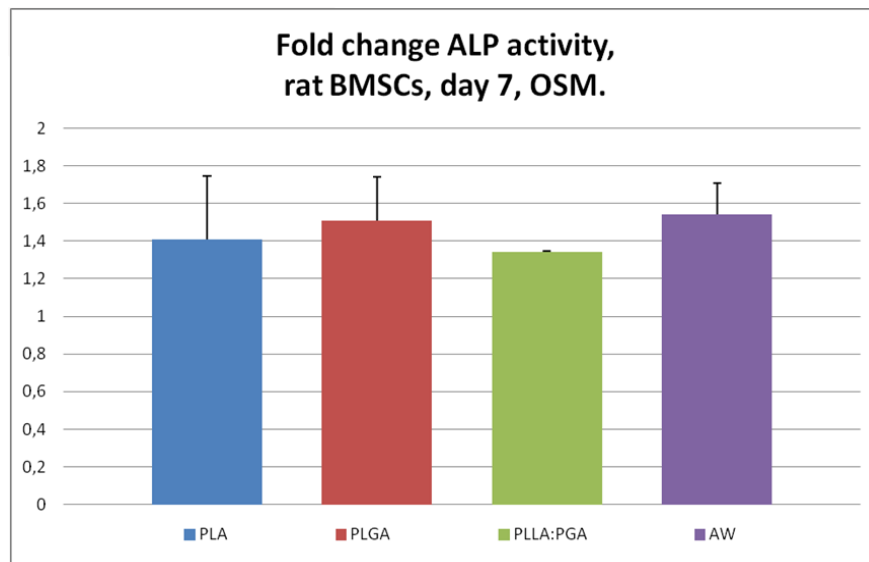


Figure 5.22 Fold change in ALP activity on synthetic scaffold materials compared with common biopolymers at Day 7 of culture

5.2.3.3 *In vivo* evaluation of A-W and AW/PLA discs for non-load-bearing applications.

Histological assessment of the calvaria defects treated with A-W alone and or with AW/PLA discs, followed up at 2 weeks and 12 weeks, was made. Figures 5.23 – 5.26 show that the scaffolds supported bone ongrowth and ingrowth indicating that the scaffolds are biocompatible and osteoconductive.

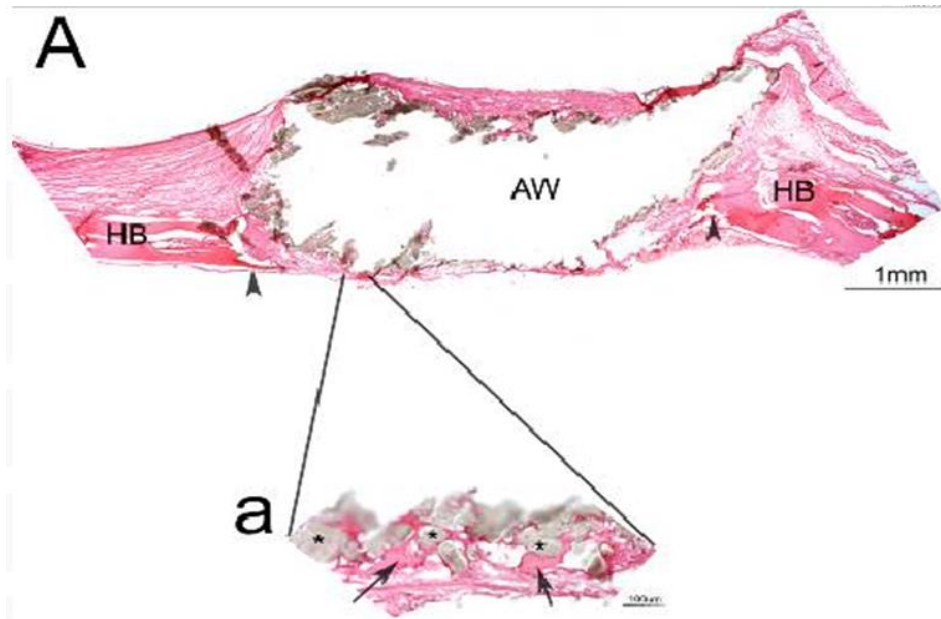


Figure 5.23 Representative morphology of the calvarial defects treated with AW bioceramic discs, 2 weeks after surgery; overview image. (A) HB – host bone; defect margins indicated by arrowheads; Bar = 1 mm. (a) new bone formation indicated by arrows, * residual biomaterial; Bar = 100 µm. Haematoxylin and eosin staining.

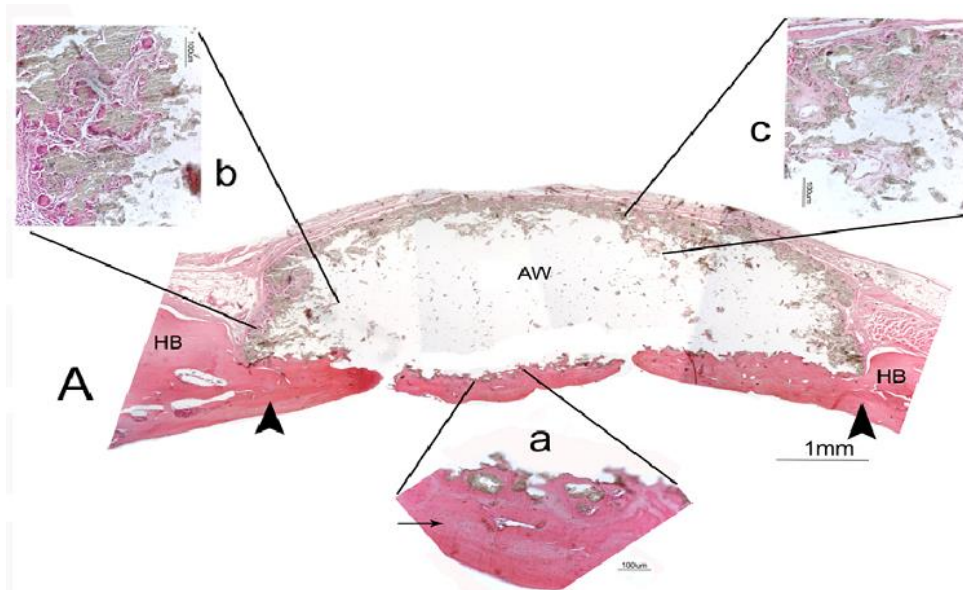


Figure 5.24 Representative morphology of the calvarial defects treated with AW discs, 12 weeks after surgery; overview image. (A) HB – host bone; defect margins indicated by arrowheads; Bar = 1 mm; (a), (b), and (c) new bone formation indicated by arrow; Bar = 100 µm. Haematoxylin and eosin staining.

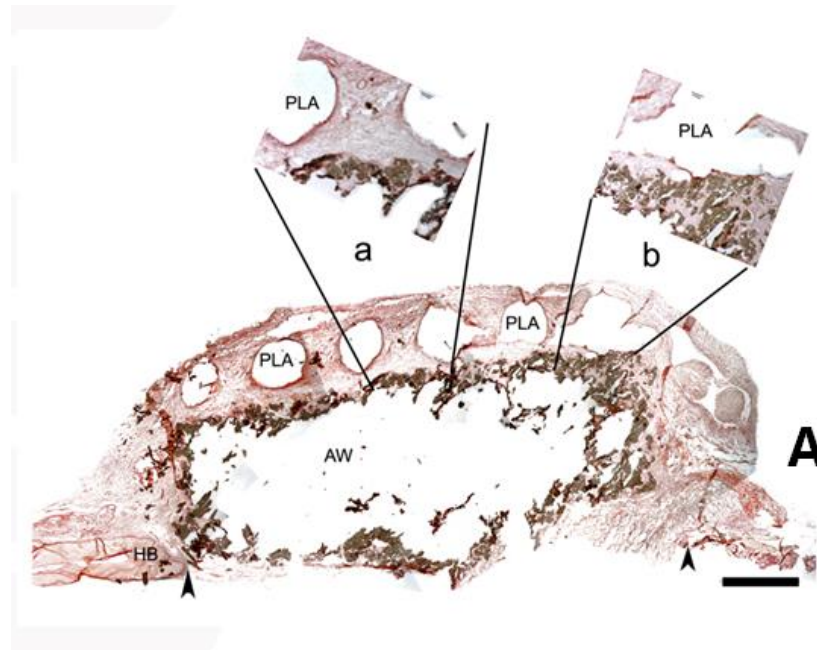


Figure 5.25 Representative morphology of the calvarial defects treated with the AW/PLA discs, 2 weeks after surgery; overview image. Haematoxylin and eosin staining. (A) HB – host bone; defect margins indicated by arrowheads; Bar = 1 mm.

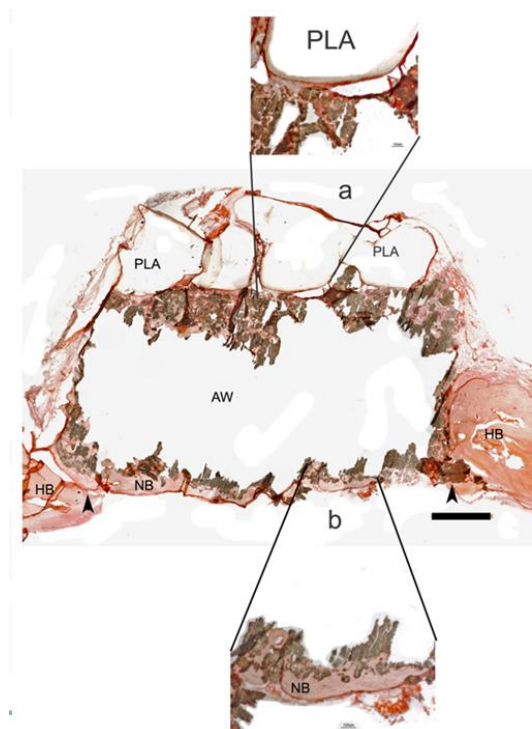


Figure 5.26 Representative morphology of the calvarial defects treated with the AW/PLA discs, 12 weeks after surgery; overview image. Haematoxylin and eosin staining. (A) HB – host bone; NB – new bone; defect margins indicated by arrowheads; Bar = 1 mm.

5.2.4 Ex Vivo Case Study

This case study was developed to produce A-W scaffold via 3DP to fill bone voids in pig mandible jaw drilled using a manual drill with a drill bit diameter of 6.0 mm. The shapes and sizes of the 3D-printed scaffolds were designed with the specification that the parts should fit into and remain in the voids. PB5 selected as it gave best combination of porosity and strength. Porous A-W implantable plugs were printed using the same setting parameters and the post-process as illustrated in chapter 3. Shrinkage assessed on initial builds and changed CAD to give parts with correct dimensions.

5.2.4.1 Introduction

Surgery, tumours, and trauma are the most common factors that cause bone defects. The healing of bone fractures is a complex physiological process that leads to joining bone together (Tsiridis *et al.*, 2007). Annually, 2.2 million bone graft procedures such as autografts and allografts are used worldwide, and only 10% of these use synthetic materials (Cook *et al.*, 1995). A number of synthetic bioresorbable materials have been investigated for use as implantable devices instead of autografts and allografts (Lewandrowski *et al.*, 2000). A-W glass-ceramic is an attractive candidate bioresorbable material to substitute for bone grafts because it has both biocompatibility and strong mechanical properties. Moreover, dense and porous A-W structures have been used as bone spacers and fillers (Kokubo *et al.*, 2003).

5.2.4.2 Experimental procedures

In this study, several steps were developed before printing the porous scaffolds. The first step was to use a manual drill with a 6 mm drill bit to make a hole in hardwood to create holes of precise diameter, as shown in Figure 5.27. Next, porous A-W implantable plugs were printed and placed into the holes drilled in the hardwood to make sure that shapes and sizes of the printed parts will fit and remain in the voids, as illustrated in Figure 5.28.

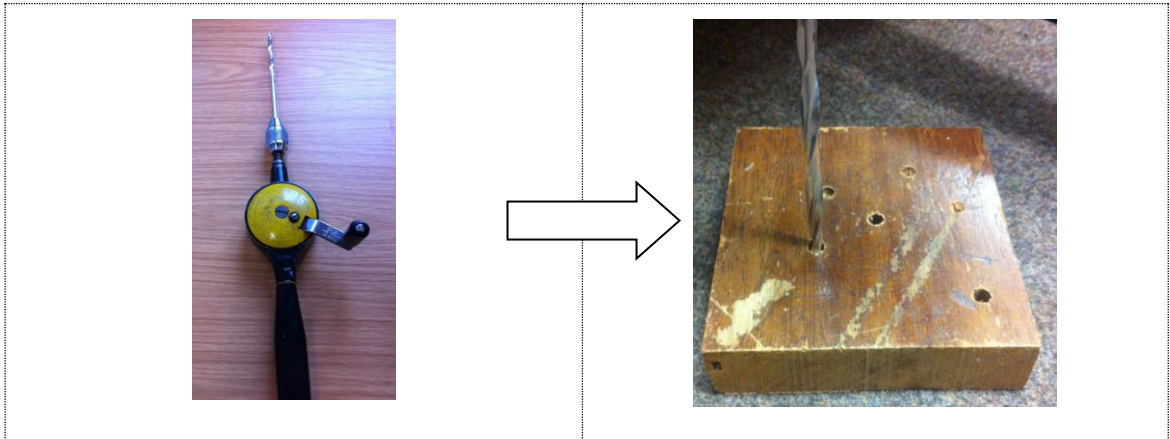


Figure 5.27 A manual drill with 6 mm drill bit; drilling holes in hardwood

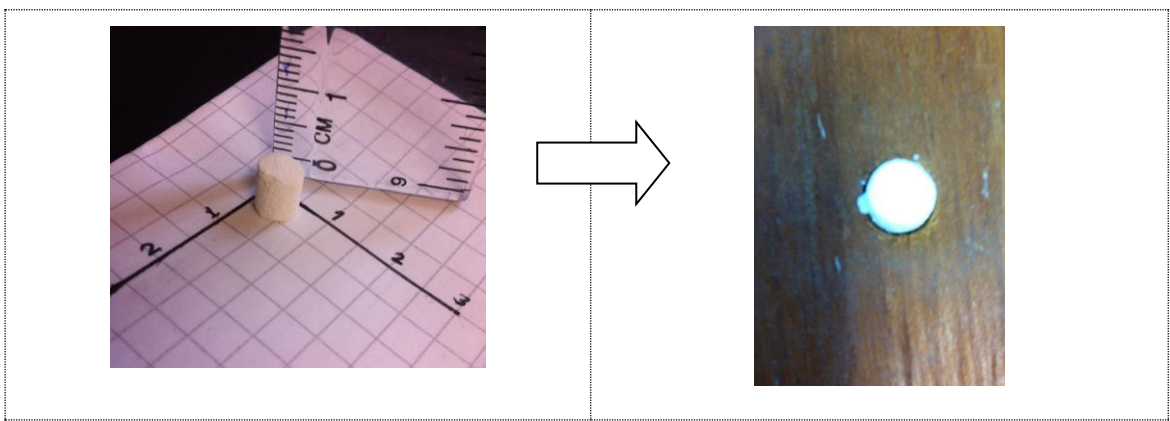


Figure 5.28 A-W scaffold fit into the 6 mm drilled hole

The third step was to repeat the previous steps with the pig mandible in the lap. The mandible was drilled and A-W plugs made from PB5 were fit into the mandible voids and remained in place, as shown in Figure 5.29.

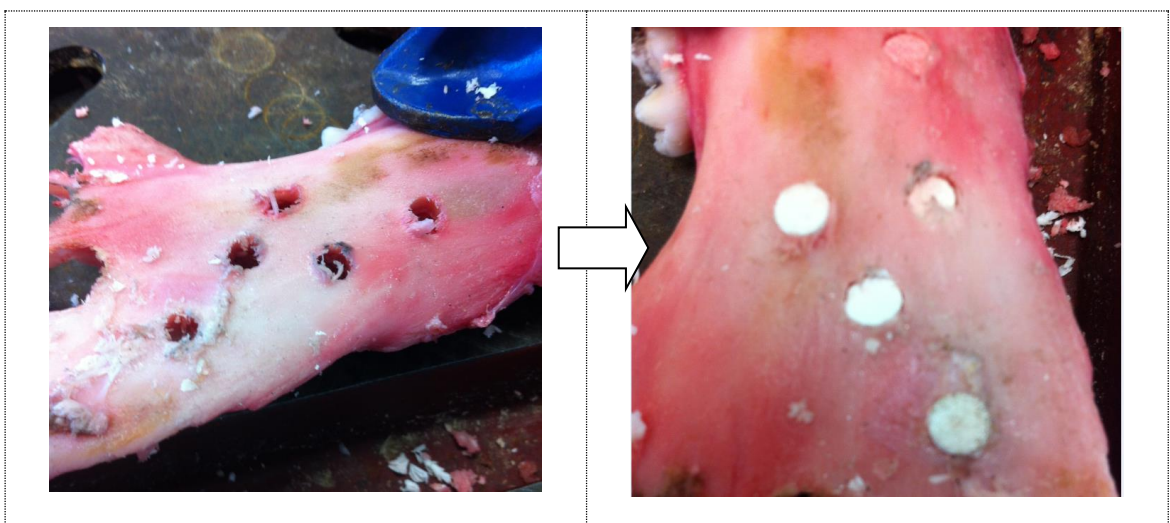


Figure 5.29 A-W scaffold fit in the 6mm drilled hole in pig mandible

Finally, four through holes and four holes of 6 mm diameter and 7 mm depth were drilled in a pig mandible using a manual cylindrical drill with a drill bit diameter of 6.0 mm to investigate the force required to fix the scaffolds into the mandible voids and to remove them from the mandible voids. An Instron 5567 testing machine was used to measure the force, as shown in Figure 5.30.

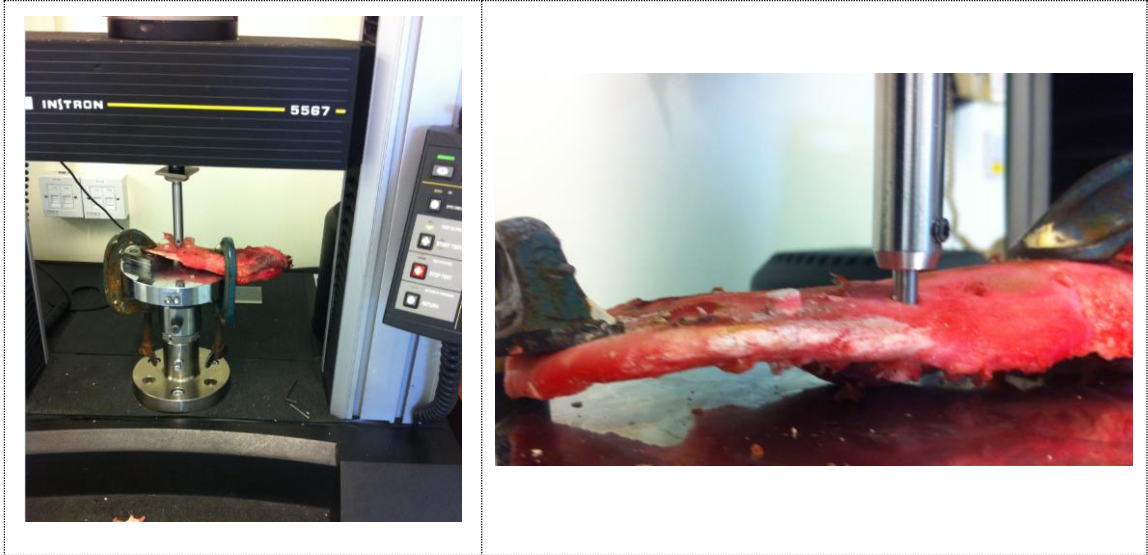


Figure 5.30 A-W measuring the force necessary to install or remove the 3D-printed parts using an Instron 5567 testing machine

5.2.4.3 Results

Cylindrical plugs of PB5 with dimensions of 6 mm in diameter by 7 mm in height were successfully printed using the 3DP and the dimensional accuracy of the parts is summarized in Table 5.11. In the present study, the ideal diameter for a printed plug to fit into and remain in the mandible void was found to be between 5.95 mm and 6.04 mm. The plugs could successfully fit into the bone void with minor manual pressure and could remain in the void. The average force to remove the plugs from the through holes was about 44 N (Figure 5.31).

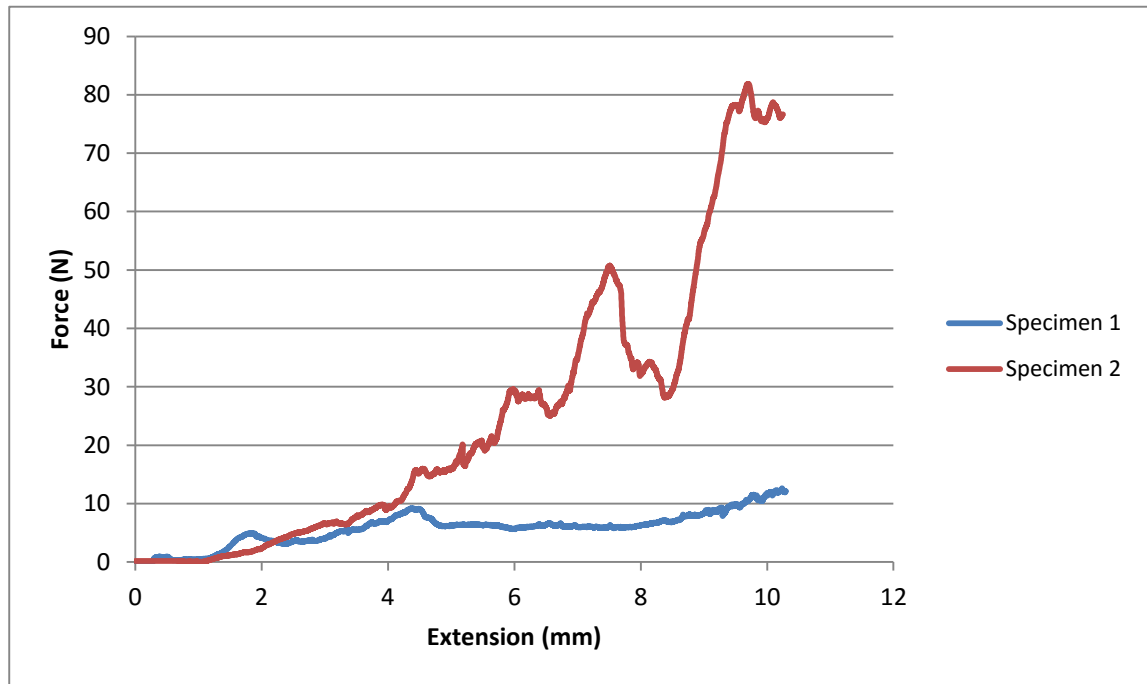


Figure 5.31 Force-distance curves of specimens

Table 5.11 Accuracy of 6 mm (diameter) by 7 mm (height) plugs

Disk	Diameter (Φ) (mm)	Height(h) (mm)
1	6.03	6.99
2	6.00	6.93
3	6.04	6.96
4	6.01	7.00
5	6.00	6.90
6	5.98	7.02
7	6.03	6.78
8	6.02	6.86
9	6.04	6.89
10	5.99	7.05
Mean	6.01	6.93
SD	0.021	0.082
SE	0.01	0.03
95% CI	(5.99, 6.02)	(6.87, 6.99)

Chapter 6

Discussion

6.1 Introduction

Several bone substitute materials have been developed for clinical applications, but bone grafts still remain the preferred treatment for critical defects (Schieker *et al.*, 2006). Therefore, this challenge has led to the investigation of more approaches to bone scaffold design. Scaffolds must be 3D hierarchical porous structures with suitable mechanical properties to mimic natural bone (Hollister, 2005). Various synthetic biomaterials that are usually manufactured into simple shapes such as blocks or pins (Seitz *et al.*, 2005) are available today for bone replacement. On the other hand, additive manufacturing approaches are suitable for the process of creating scaffolds with complex shapes. In particular, 3DP is a good candidate method for manufacturing the required scaffolds regarding its capabilities for creating complex geometries, controlling external and internal structure, and using a variety of materials (Lam *et al.*, 2002). An initial objective of the project was to investigate the capabilities of the indirect three-dimensional printing process when used with apatite-wollastonite glass-ceramic powders, in terms of lead time, reproducibility, productivity, and quality. Through this work it is clear that a range of geometries, and strong, complex, and highly porous structures can be created indirectly by the 3DP process, using A-W powder, MD solid binder, and zb[®]60 liquid binder. Furthermore, the results of bioactivity investigations of the fabricated A-W scaffolds have been positive. A detailed discussion of these results will be presented in this chapter.

6.2 Process Development

6.2.1 Powder Particle Size Range

Particle size is a critical factor in the 3D printing process. Utela *et al.* (2008) claimed that the ideal particle sizes for 3DP are between 20 and 40 μm . Another study has shown good results using larger particles between 75 and 150 μm (Yoo *et al.*, 1993). The current study found that milling processes gave A-W powder with irregular shapes

and sharp-edges. Moreover, the most interesting finding was that the packing into a feed bed of small particles (0-53 μm) and large particles (53-90 μm) has a direct impact on accuracy, surface morphology, strength and porosity of the 3D printed samples. These results match those observed in earlier studies (Bourell *et al.*, 2011; Karageorgiou and Kaplan, 2005; Juhasz *et al.*, 2004; and Suwanprateeb *et al.*, 2009). PB4/ with small particles gave high flexural strength with low porosity, while the blends with large particles only gave low flexural strength with high porosity. A possible explanation for this is that the gaps between large particles are bigger than the gaps between small particles, as shown in Figure 6.1 (a, b). This phenomenon supports the formation of micro and macro porous structures, and in order to fulfil the requirement of ideal scaffolds to have micro and macro porous structure, mixed-size A-W powder particles (78.5% 53-90 μm particles with 21.5% 0-53 μm particles) have been tested and gave the required results in terms of micro and macro porous structure, but with decreased flexural strength of the parts. In mixed A-W powder, some of the small particles fill the gaps between the large particles and form the micro porosity of the structure as shown in Figure 6.1 (c).

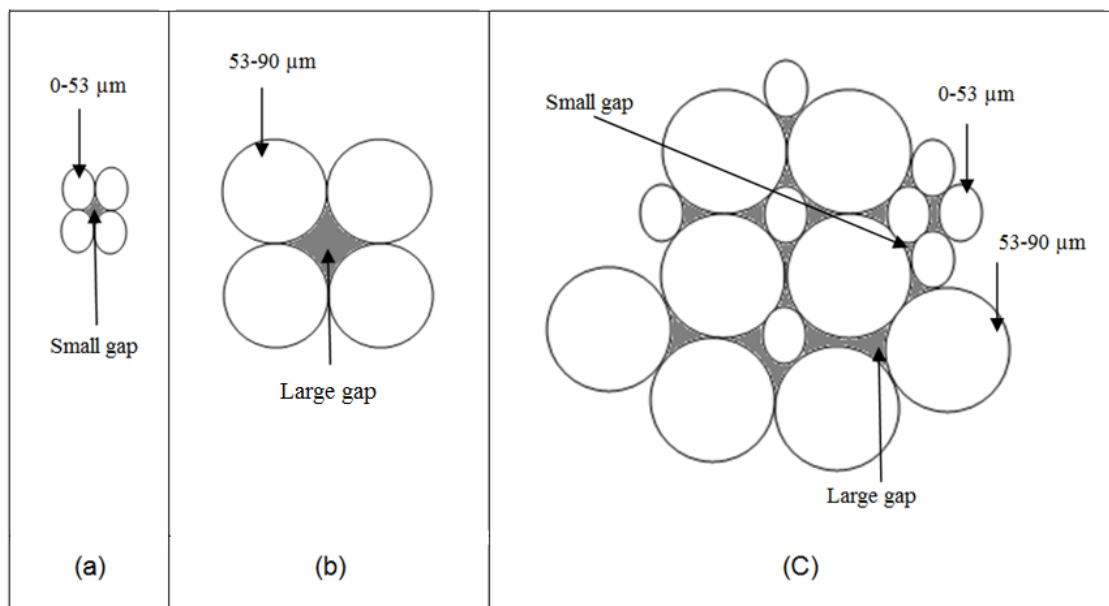


Figure 6.1 Effect of particle sizes on porosity: (a) powder blend with small particles (0-53 μm), (b) powder blend with large particles (53-90 μm), (c) mixed powder with small particles (0-53 μm) and large particles (53-90 μm)

6.2.2 Binder Optimisation

It is interesting to note that a powder blend with a high maltodextrin solid binder content (30% by wt.) could be used to successfully produce sufficiently strong green parts, whereas with a low MD content the green parts were not strong enough for handling and cleaning processes. This result matched those observed in an earlier study by Chumnanklang *et al.* (2007). A number of recent studies have used this binder additive for the 3DP of ceramic powder (Bourell *et al.*, 2011; Utela *et al.*, 2010; and Suwanprateeb *et al.*, 2010). This may be explained by the fact that MD reacts with the liquid binder during the printing process to consolidate the blend and improve the bonding of A-W particles during the printing process (Visavarungroj and Remon, 1992; Nonaka, 1997). Contrary to expectations, this study found a significant difference in flexural strength between the parts made with zb®60 and DW fluid binder. The parts made with zb®60 are stronger than the parts made with DW. Surprisingly, clogging of the print head occurred after limited printing with DW binder. The measurements of contact angle, surface tension and viscosity presented in Chapter 4 showed that the two binders had similar surface tension and viscosity properties, but quite different contact angles measured on a silicon substrate, with the contact angle much higher for DW binder. This could mean that the DW binder did not wet the droplet chamber or nozzle to some extent as the zb®60, making flow more difficult and clogging easier.

6.3 Device Design Rules

6.3.1 Possible Geometries

The 3DP technique is suitable for producing 3D parts using CAD data (Dimitrov *et al.*, 2006; Zhou *et al.*, 2014; and Liu *et al.*, 2013). The current study found that it is possible to create several parts with different geometries using indirect 3DP. Furthermore, it is possible to print samples with internal channels and of different thicknesses. However, channels with a diameter of less than 1 mm could not be printed for any thickness of samples. There are two likely causes for this result: depowdering and shrinkage. Normally, removing the loose powder from 3D green parts is a critical process, especially for parts with internal channels. During the depowdering process some of the loose powder remains in place and is difficult to remove.

6.3.2 Accuracy and Repeatability

It is interesting to note that in all printed beams using 3DP with each of the seven powder blends, the difference between the mean linear and volumetric shrinkage was statistically highly significant ($P < 0.001$). These differences can be explained by the impact of several factors such as powder particle sizes, layer thickness, binder saturation, and powder flowability. The findings of the present study mirror those of previous studies that have examined the effects of such factors (Vaezi and Chua, 2011; Lozo *et al.*, 2008; and Farzadi *et al.*, 2014). Therefore, to produce the desired parts, the linear shrinkage percentage must be taken into account and the CAD design input must be compensated for this shrinkage to obtain parts with high accuracy and repeatability. In this project, batches of scaffolds with different design and geometries were successfully printed using indirect 3DP. As mentioned earlier, the printed scaffolds have rough surfaces, a property that made measurement verification difficult. To eliminate such variability, the measurements were taken three times per side and the average of the three readings was recorded. The small features in the scaffolds such as holes were measured by optical microscopy and the rest were measured by digital caliper. The measurements of these scaffolds have revealed good geometries with acceptable size tolerances that matched the desired design, as illustrated in detail in Chapter 5. These batches of scaffolds were printed several times to examine the accuracy and repeatability and the dimensions were very repeatable. Six different designs of devices were measured and the mean, standard deviation, maximum, minimum and 95% confidence interval was conducted as shown in Chapter 5. In general, the outer dimensions were more accurate than the inner and small dimensions. In small holes it is difficult to clean and remove the loose powder. This loose powder will consolidate in the furnace with the other particles and then the dimensions will change.

6.4 Potential for Scale Up and Application

6.4.1 Lead Time

As mentioned in the literature review traditional manufacturing technology has some limitations for producing complex structures. In contrast, 3DP can create complex structures with low cost and leadtime (Jumani, 2013). The current study found that the estimated lead time for producing 50 devices is approximately 37 h (Table 6.1). The build time/run was changeable depending on the shape and size of the part. Drying and cleaning processes took 24 h. It may be possible to reduce the drying time in order to reduce the lead time further. Sintering and cooling process took 12 h.

Table 6.1 Lead time for producing 50 parts using 3DP

Process	Lead Time	
	Disc	Plug
	(Diameter = 8 mm, high = 2 mm)	(Diameter = 6 mm, high = 7 mm)
Build time/run	12 min	42 min
Drying and cleaning	24 h	24 h
Sintering and cooling	12 h	12 h

6.4.2 Material Utilization and Productivity

In this experiment, several devices were successfully produced using indirect 3DP with high mass-productivity and low material consumption. One of the advantages of 3DP process is that unused powder can be recycled to reduce the waste of materials. More than 1500 devices were produced with approximately 1000 g of PB5, as mentioned in Chapter 5. Approximately 60% of material in a build was converted to devices, 30% was recycled and 10% was waste during cleaning process. At full capacity the printer and furnace can produce 200 devices per machine per hour and 400 devices per furnace per hour. This finding further supports the idea of Carmen *et al.* (2012) that 3D printing can be used to create parts with high productivity and low cost.

6.4.3 Quality

Ten beams of each powder blend were printed and examined to investigate the mechanical properties of the sintered parts. As mentioned earlier, bone scaffolds have several requirements to mimic the structures and properties of human bone, such as mechanical properties and porosity.

6.4.3.1 Mechanical properties

This study set out with the aim of assessing the mechanical characteristics of three-dimensional printed A-W parts. What is surprising in the results is that the percentage by weight concentration of MD has a significant impact on the strength of the sintered samples. The blends with a sufficient quantity of MD gave a good green flexural strength as shown in Table 6.2. During printing process MD reacts with the liquid binder to fuse and bind A-W particles together. As mentioned earlier, 30% by wt. of MD is the useable quantity to produce strong and porous structures. Optimisation of powder blends has been undertaken here to obtain the ideal mechanical properties to mimic natural bone. Flexural strength and Young's modulus results for powder blends that contain 70% by wt. of A-W mixed with 30% by wt. of MD are presented in Table 6.3 compared with natural cortical, cancellous, and subchondral bone. The achieved flexural strength is higher than the result of Suwanprateeb *et al.* (2009), which is 21.01 ± 0.09 MPa, when porous hydroxyapatite/Apatite-wollastonite (HAAW) parts were printed using 3DP. On the other hand, the achieved flexural strength is lower than the result of Xiao *et al.* (2008), which is 65.97 ± 5.4 MPa, when porous AW parts were printed using SLS. The mechanical properties of the printed A-W parts using 3DP are in the range of cancellous and subchondral bone and very close to the range of cortical bone. It is clear that the printed A-W structures can be used for load-bearing and non-load-bearing applications. PB1 and PB5 have acceptable flexural strength and porosity. PB 4 has the highest flexural strength, but with low porosity due to the impact of small particles (0-53 μm) of A-W. As discussed in Chapter 4, phosphate glass infiltration was applied to the sintered parts made from PB5, PB6, and PB7 to try to fill the porosity of the parts with a bioactive glass that can dissolve very quickly in body fluid and to increase the mechanical properties. The infiltration had only a limited effect on all three types of scaffold (Table 6.4). Powder particle sizes, wettability and processing temperature are play an important role in the infiltration capability. The capillary force becomes more effective with smaller particle diameter (Kobayashi *et al.*, 2008).

Table 6.2 Average bending strength of green parts (powder blends contain 70% by wt. of A-W mixed with 30% by wt. of MD)

Powder Blend	Average Bending Strength±SE (MPa)
PB1/DW	3.93 ± 1.25
PB4/zb [®] 60	8.63 ± 0.35
PB5/zb [®] 60	8.53 ± 0.73
PB6/zb [®] 60	2.33 ± 0.10
PB7/zb [®] 60	2.08 ± 0.27

Table 6.3 Average bending strength, Young's modulus and porosity of porous parts printed from A-W (powder blends contain 70% by wt. of A-W mixed with 30% by wt. of MD) and natural bone

		Average Bending Strength±SE (MPa)	Average Young's Modulus±SE (GPa)	Average Total Porosity±SE (%)	Average Open Porosity±SE (%)
Natural Bone	Cortical bone	50-160	13-17	10	-
	Cancellous	10-20	1-13	50-90	-
	Subchondral	-	1-3	-	-
	PB1/zb [®] 60	23.65 ± 0.73	7.27 ± 0.52	47.95 ± 0.49	15.43 ± 0.01
	PB4/zb [®] 60	35.64 ± 1.48	15.04 ± 0.89	35.27 ± 0.76	11.62 ± 0.10
	PB5/zb [®] 60	25.95 ± 1.59	11.18 ± 0.94	41.85 ± 0.94	12.4 ± 0.29
	PB6/zb [®] 60	17.20 ± 0.6	5.40 ± 0.19	54.03 ± 0.97	17.07 ± 0.97
	PB7/zb [®] 60	18.36 ± 0.34	7.77 ± 0.31	59.38 ± 0.98	19.20 ± 0.87

Table 6.4 Average total porosity and bending strength of infiltrated parts

Samples	Average Total Porosity \pmSE (%)	Average Bending Strength \pmSE (MPa)	Average Young's Modulus \pmSE (GPa)
PB5/zb [®] 60/InfilB	21.75 \pm 1.46	31.34 \pm 3.12	19.46 \pm 2.51
PB6/zb [®] 60/InfilB	42.22 \pm 1.21	17.89 \pm 1.66	8.94 \pm 0.94
PB7/zb [®] 60/InfilB	44.53 \pm 2.50	21.56 \pm 3.17	13.08 \pm 2.06

6.4.3.2 Porosity

In reviewing the literature, the porosity of cortical or cancellous bone is 10% and 50-90%, respectively. Table 6.3 summarizes the total porosity and open porosity of powder blends that contain 70% by wt. of A-W mixed with 30% by wt. of MD. Parts printed from the blend with small particles (0-53 μ m) have the lowest porosity. These differences in porosity can be explained by the impact of particle sizes during the heat treatment process.

6.5 Achievement of Objectives

The present study was designed to determine the capabilities of the indirect 3DP process when used to process A-W glass-ceramic powders. The following objectives were tested in this study.

- To comprehend the capabilities of the indirect three-dimensional printing process when used in combination with bioceramic powders, in terms of lead time, reproducibility, productivity, and quality.

It is clear that indirect 3DP can create strong, complex, and porous A-W structures with acceptable levels of accuracy and repeatability. Approximately 37 h lead time is required to produce 50 batches of scaffolds (disc, Diameter = 8 mm, Thickness = 2 mm) using 3DP with a potential steady state productions of 200 scaffolds per printer per hour, and an overall material utilisation of 60-90%. Several powder blends with different mechanical properties and porosities were prepared for load-bearing and nonload-bearing applications with different qualities.

- To produce an optimized binder that results in high-quality interaction with the bioceramic particles for the three-dimensional printing process.

The use of the commercial zb®60 binder solution with the ZPrinter® 310 Plus 3D printer gave A-W parts a higher flexural strength compared with DW fluid binder. Moreover, the powder blends that contain 30% by wt. of MD solid binder showed good green strength, suggesting that for this approach to processing, 30% by wt. MD is the useable quantity to produce strong green parts.

- To realize the post-processing conditions needed for three-dimensional printed bioceramic scaffolds (sintering conditions).

Removing the loose powder from 3D green parts is a key factor in the accuracy of final products. The protocol developed by (Xiao *et al.*, 2008) for the sintering process was successful for this project, so there was no need to modify it.

- To evaluate the mechanical characteristics of three-dimensional printed bioceramic scaffolds.

Three-point bending test results for sintered A-W parts are shown below in Table 6.5.

Table 6.5 Average bending strength and Young's modulus of porous A-W printed parts using zb®60 binder solution

Powder Blend	Average Bending Strength \pmSD (MPa)	Average Young's Modulus \pmSD (GPa)
PB1/zb®60	23.65 \pm 2.31	7.27 \pm 1.64
PB2/zb®60	8.23 \pm 0.73	2.82 \pm 0.39
PB3/zb®60	6.13 \pm 1.01	1.87 \pm 0.30
PB4/zb®60	35.64 \pm 4.69	15.04 \pm 2.81
PB5/zb®60	25.68 \pm 5.02	11.18 \pm 2.98
PB5/zb®60/InfilB	31.34 \pm 5.40	19.46 \pm 4.35
PB6/zb®60	17.20 \pm 1.14	5.40 \pm 0.59
PB6/zb®60/InfilB	17.89 \pm 3.72	8.94 \pm 1.63
PB7/zb®60	18.36 \pm 1.06	7.77 \pm 0.98
PB7/zb®60/InfilB	21.56 \pm 7.08	13.08 \pm 3.57

- To supply batches of scaffolds for biological characterisation.

More than a thousand A-W scaffolds were supplied to the Restoration project group for *in vitro* and *in vivo* assessments.

6.6 Novelty and Originality

Prior studies have noted the importance of A-W glass ceramic biomaterial in bone tissue applications. A-W is one of the best candidate biomaterials in the field of bone tissue engineering with regard to its high mechanical strength and excellent bioactivity. The best fabrication technique for A-W scaffolds is another important factor. This study showed the excellent capabilities of indirect 3DP to create complex, strong, and highly porous A-W glass ceramic scaffolds. In addition, this study for the first time examined the effect of A-W particle sizes and binder concentration on the flexural strength and porosity of printed parts.

Chapter 7

Conclusion and Future Work

7.1 Conclusion

The present study set out to explore the required processing for indirect 3DP using A-W powders and to evaluate the mechanical properties of 3D printed bioceramic scaffolds. A-W glass ceramic is a bioactive material that is used clinically for bone substitutes due to its suitable mechanical properties (Kokubo *et al.*, 2003). This study has also sought to supply batches of scaffold for biological characterisation.

The most obvious finding to emerge from this study is that the production of complex, strong, and porous A-W structures is possible with indirect 3DP. The investigation of the 3DP process has shown that the powder particle sizes, binder fluid, and MD binder concentration all have important impacts on the flexural strength of the printed parts. It was also shown that post processing such as depowdering and heat treatment are significant factors that can affect the quality of the printed parts. Removing the loose powder from the green parts is a critical process, and care must be taken especially when removing loose powder from channels of small diameter. The ideal heat treatment conditions for A-W printed parts include two stages: increase temperature to 779 °C with a hold time of 1 h and a heating rate of 10 °C/min, and increase temperature to 1150 °C with a hold time of 1 h and heat rate of 10 °C/min (Xiao *et al.*, 2008). This heat treatment resulted in sintered parts with volumetric shrinkage ranges between 15% and 50%, depending on the powder blend. For each powder blend, the CAD dimensions were compensated for this shrinkage to obtain the ideal accuracy. This study found that the flexural strength and Young's modulus of printed parts are generally different for each powder blend. These differences can be explained by the effect of particle sizes and maltodextrin concentration. The mechanical properties achieved with PB1 or PB5 are equivalent to that of cancellous and subchondral bone and approach those of cortical bone. Depending on the requirements for ideal scaffolds, PB5 that contains mixed particle sizes can be used to print parts that are relatively comparable to ideal scaffolds,

even after phosphate infiltration. The implication of the successful biological assessment is that indirect 3DP does not deleteriously affect the bioactivity of A-W.

The results of this research support the idea that A-W glass ceramic is an excellent biomaterial for bone tissue engineering scaffolds. Moreover, additive manufacturing techniques are the good approaches for creating complex, strong, and porous 3D structures. As mentioned in Chapter 6, the flexural strength results for A-W sintered parts using indirect SLS are higher than the achieved flexural strength of A-W sintered parts using indirect 3DP. A possible reason for such variation may be due to the differences between these processes for fusing the binding powder. SLS uses a laser to sinter the powder particles together, whereas 3DP uses a liquid binder inkjet. In general, the choice of the best AM technique depends on several factors, such as material properties, surface finishes, accuracy, quality, and production cost. Taking into account these factors, and particularly cost indirect 3DP is a promising manufacturing technique for bone tissue engineering applications.

7.2 Limitations of the current study

This study has offered an evaluation of and perspective on the mechanical properties of A-W parts printed using indirect 3DP. Several limitations to this study need to be acknowledged. Powder blending has so far highlighted some weaknesses in the quantity of particle sizes when sieves were used in this experiment. Because two different particle size ranges were used (0 to 53 μm and 53 to 90 μm), it was not possible fully to explore the exact ranges of particle sizes. For example, if the powder blend contains A-W particle sizes in the range of 53 to 90 μm perhaps the quantity of powders in the range of 53 to 60 μm might represent 90% of the blend. In the current study, the purpose for choosing these sieves was only to explore the effect of particle sizes of the two ranges (0 to 53 μm and 53 to 90 μm) on the flexural strength of the parts. Exploring new particle size blends would require further research. The infiltration experiments did not produce useful results, and it may be that further work with alternative materials would produce better results.

7.3 Suggestion for future work

The main aim and objectives of this research have been achieved. Indirect 3DP can create strong A-W scaffolds for bone tissue engineering applications. It is recommended that further research be undertaken in the following areas:

- Additional testing of mechanical properties such as compression, fracture toughness, and fatigue tests;
- Explore a wider range of powder size blends to further optimise mechanical properties and porosity.
- Explore new methods of infiltration and new infiltration materials of the sintered parts to achieve optimum results to fill all the porosities of the structure; and
- Further investigation of the settings, such as saturation level, on the 3D printer that might improve the quality of the printed parts.

References

- Agrawal, C.M. and Ray, R.B. (2001) 'Biodegradable polymeric scaffolds for musculoskeletal tissue engineering', *Journal of Biomedical Materials Research*, 55(2), pp. 141-150.
- Albrektsson, T. and Johansson, C. (2001) 'Osteoinduction, osteoconduction and osseointegration', *European Spine Journal*, 10(2), pp. S96-S101.
- Aparicio, C., Gil, F.J. and Planell, J.A. (2002) 'Human-osteoblast proliferation and differentiation on grit-blasted and bioactive titanium for dental applications', *Journal of Materials Science: Materials in Medicine*, 13(12), pp. 1105-1111.
- Arthur, T.L. (1996) *Factors limiting the surface finish of three dimensional printed parts*. Massachusetts Institute of Technology.
- Ascenzi, A. and Bonucci, E. (1968) 'The compressive properties of single osteons', *Anatomical Record*, 161(3), pp. 377-391.
- Athanasίου, K.A., Zhu, C.F., Lanctot, D.R., Agrawal, C.M. and Wang, X. (2000) 'Fundamentals of biomechanics in tissue engineering of bone', *Tissue Engineering*, 6(4), pp. 361-381.
- Bacon, A. (2002) 'Polymers - A synthetic or natural choice?', *Drug Discovery Today*, 7(24), pp. 1202-1203.
- Bergeron, E., Marquis, M.E., Chretien, I. and Fauchoux, N. (2007) 'Differentiation of preosteoblasts using a delivery system with BMPs and bioactive glass microspheres', *Journal of Materials Science: Materials in Medicine*, 18(2), pp. 255-263.
- Bergmann, C., Lindner, M., Zhang, W., Koczur, K., Kirsten, A., Telle, R. and Fischer, H. (2010) '3D printing of bone substitute implants using calcium phosphate and bioactive glasses', *Journal of the European Ceramic Society*, 30(12), pp. 2563-2567.
- Bohner, M., Brunner, T.J. and Stark, W.J. (2008) 'Controlling the reactivity of calcium phosphate cements', *Journal of Materials Chemistry*, 18(46), pp. 5669-5675.

- Bohner, M., van Lenthe, G., Grunenfelder, S., Hirsiger, W., Evison, R. and Muller, R. (2005) 'Synthesis and characterization of porous beta-tricalcium phosphate blocks', *Biomaterials*, 26(31), pp. 6099-6105.
- Bose, S., Roy, M. and Bandyopadhyay, A. (2012) 'Recent advances in bone tissue engineering scaffolds', *Trends in biotechnology*, 30(10), pp. 546-554.
- Bose, S., Vahabzadeh, S. and Bandyopadhyay, A. (2013) 'Bone tissue engineering using 3D printing', *Materials Today*, 16(12), pp. 496-504.
- Bourell, D., Stucker, B., Marchelli, G., Prabhakar, R., Storti, D. and Ganter, M. (2011) 'The guide to glass 3D printing: developments, methods, diagnostics and results', *Rapid Prototyping Journal*, 17(3), pp. 187-194.
- Bremen, S., Meiners, W. and Diatlov, A. (2012) 'Selective Laser Melting', *Laser Technik Journal*, 9(2), pp. 33-38.
- BSI (1995) BS EN 993-1:1995 BS 1902-3.8:1995-Methods of test for dense shaped refractory products. Determination of bulk density, apparent porosity and true porosity. IN INSTITUTE, B. S. (Ed.), British Standards Institute, London.
- BSI (2008) BS EN ISO 6872:2008-Dentistry. Ceramic materials. IN INSTITUTE, B. S. (Ed.), British Standards Institute, London.
- Buckwalter, J.A., Glimcher, M.J., Cooper, R.R. and Recker, R. (1996) 'Bone biology. I: Structure, blood supply, cells, matrix, and mineralization', *Instructional course lectures*, 45, pp. 371-386.
- Burg, K.J.L., Holder Jr, W.D., Culberson, C.R., Beiler, R.J., Greene, K.G., Loeb sack, A.B., Roland, W.D., Mooney, D.J. and Halberstadt, C.R. (1999) 'Parameters affecting cellular adhesion to polylactide films', *Journal of Biomaterials Science, Polymer Edition*, 10(2), pp. 147-161.
- Butscher, A., Bohner, M., Hofmann, S., Gauckler, L. and Müller, R. (2011) 'Structural and material approaches to bone tissue engineering in powder-based three-dimensional printing', *Acta Biomaterialia*, 7(3), pp. 907-920.
- Butscher, A., Bohner, M., Roth, C., Ernstberger, A., Heuberger, R., Doebelin, N., Von Rohr, P.R. and Müller, R. (2012) 'Printability of calcium phosphate powders for three-dimensional printing of tissue engineering scaffolds', *Acta biomaterialia*, 8(1), pp. 373-385.

- Calori, G.M., Mazza, E., Colombo, M. and Ripamonti, C. (2011) 'The use of bone-graft substitutes in large bone defects: any specific needs?', *Injury*, 42, pp. S56-S63.
- Cao, B., Zhou, D., Xue, M., Li, G., Yang, W., Long, Q. and Ji, L. (2008) 'Study on surface modification of porous apatite-wollastonite bioactive glass ceramic scaffold', *Applied Surface Science*, 255(2), pp. 505-508.
- Carmen, K., Niklas, C.S., Ming-Tsang, L., Seung Hwan, K., Nico, H., Costas, P.G. and Dimos, P. (2012) '3D micro-structures by piezoelectric inkjet printing of gold nanofluids', *Journal of Micromechanics and Microengineering*, 22(5), p. 055022.
- Castilho, M., Pires, I., Gouveia, B. and Rodrigues, J. (2011) 'Structural evaluation of scaffolds prototypes produced by three-dimensional printing', *International Journal of Advanced Manufacturing Technology*, 56(5-8), pp. 561-569.
- Chau, T.T. (2009) 'A review of techniques for measurement of contact angles and their applicability on mineral surfaces', *Minerals Engineering*, 22(3), pp. 213-219.
- Choi, K., Kuhn, J.L., Ciarelli, M.J. and Goldstein, S.A. (1990) 'The elastic moduli of human subchondral, trabecular, and cortical bone tissue and the size-dependency of cortical bone modulus', *Journal of Biomechanics*, 23(11), pp. 1103-1113.
- Chumnanklang, R., Panyathanmaporn, T., Sitthiseripratip, K. and Suwanprateeb, J. (2007) '3D printing of hydroxyapatite: Effect of binder concentration in pre-coated particle on part strength', *Materials Science and Engineering: C*, 27(4), pp. 914-921.
- Cima, L.G., Vacanti, J.P., Vacanti, C., Ingber, D., Mooney, D. and Langer, R. (1991) 'Tissue engineering by cell transplantation using degradable polymer substrates', *Journal of biomechanical engineering*, 113(2), pp. 143-151.
- Clokie, C.M.L. and Urist, M.R. (2000) 'Bone morphogenetic protein excipients: comparative observations on poloxamer', *Plastic and reconstructive surgery*, 105(2), pp. 628-637.
- Cook D.S., Salkeld S.L., and Rueger D.C. (1995) 'Comparison of osteoinductive and osteoconductive biomaterials in healing large segmental bone defects', *American Academy of Orthopaedic Surgeon*, Paper NO. 005.
- Corporation, Z. (2009) 'Zprinter 310 Plus Hardware Manual'.
- Creagh, L.T. and McDonald, M. (2003) 'Design and performance of inkjet print heads for non-graphic-arts applications', *MRS bulletin*, 28(11), pp. 807-811.

- Damien, C.J. and Parsons, J.R. (1991) 'Bone graft and bone graft substitutes: a review of current technology and applications', *Journal of Applied Biomaterials*, 2(3), pp. 187-208.
- Daniels, A.U., Andriano, K.P., Smutz, W.P., Chang, M.K.O. and Heller, J. (1994) 'Evaluation of absorbable poly (ortho esters) for use in surgical implants', *Journal of Applied Biomaterials*, 5(1), pp. 51-64.
- de Oliveira, P.T. and Nanci, A. (2004) 'Nanotexturing of titanium-based surfaces upregulates expression of bone sialoprotein and osteopontin by cultured osteogenic cells', *Biomaterials*, 25(3), pp. 403-413.
- Dean, D., Min, K.J. and Bond, A. (2003) 'Computer aided design of large-format prefabricated cranial plates', *The Journal of Craniofacial Surgery*, 14(6), pp. 819-832.
- Derby, B. (2012) 'Printing and prototyping of tissues and scaffolds', *Science*, 338(6109), pp. 921-926.
- Dimitriou, R., Tsiridis, E. and Giannoudis, P.V. (2005) 'Current concepts of molecular aspects of bone healing', *Injury*, 36(12), pp. 1392-1404.
- Dimitrov, D., Schreve, K. and De Beer, N. (2006) 'Advances in three dimensional printing-state of the art and future perspectives', *Journal for New Generation Sciences*, 4(1), pp. p. 21-49.
- Dimitrov, D., van Wijck, W., Schreve, K. and de Beer, N. (2006) 'Investigating the achievable accuracy of three dimensional printing', *Rapid Prototyping Journal*, 12(1), pp. 42-52.
- Duncan, H., Jundt, J., Riddle, J.M., Pitchford, W. and Christopherson, T. (1987) 'The tibial subchondral plate. A scanning electron microscopic study', *Journal of Bone & Joint Surgery*, 69(8), pp. 1212-1220.
- Edalat, F., Bae, H., Manoucheri, S., Cha, J.M. and Khademhosseini, A. (2012) 'Engineering approaches toward deconstructing and controlling the stem cell environment', *Annals of biomedical engineering*, 40(6), pp. 1301-1315.
- Edwards, R.B., Seeherman, H.J., Bogdanske, J.J., Devitt, J., Vanderby, R. and Markel, M.D. (2004) 'Percutaneous injection of recombinant human bone morphogenetic protein-2 in a calcium phosphate paste accelerates healing of a canine tibial osteotomy', *The Journal of Bone & Joint Surgery*, 86(7), pp. 1425-1438.

- Eglin, D., Maalheem, S., Livage, J. and Coradin, T. (2006) 'In vitro apatite forming ability of type I collagen hydrogels containing bioactive glass and silica sol-gel particles', *Journal of Materials Science: Materials in Medicine*, 17(2), pp. 161-167.
- Farzadi, A., Solati-Hashjin, M., Asadi-Eydivand, M. and Abu Osman, N. A. (2014) 'Effect of layer thickness and printing orientation on mechanical properties and dimensional accuracy of 3D printed porous samples for bone tissue engineering', *PLoS ONE*, 9, p. 18.
- Gao, T., Lindholm, T.S., Marttinen, A. and Urist, M.R. (1996) 'Composites of bone morphogenetic protein (BMP) and type IV collagen, coral-derived coral hydroxyapatite, and tricalcium phosphate ceramics', *International orthopaedics*, 20(5), pp. 321-325.
- Ge, Z., Jin, Z. and Cao, T. (2008) 'Manufacture of degradable polymeric scaffolds for bone regeneration', *Biomedical Materials*, 3(2), p. 22001.
- Geiger, M., Li, R.H. and Friess, W. (2003) 'Collagen sponges for bone regeneration with rhBMP-2', *Advanced drug delivery reviews*, 55(12), pp. 1613-1629.
- Giannitelli, S.M., Accoto, D., Trombetta, M. and Rainer, A. (2014) 'Current trends in the design of scaffolds for computer-aided tissue engineering', *Acta biomaterialia*, 10(2), pp. 580-594.
- Giannoudis, P.V., Dinopoulos, H. and Tsiridis, E. (2005) 'Bone substitutes: an update', *Injury*, 36(3), pp. S20-S27.
- Giannoudis, P.V., Einhorn, T.A. and Marsh, D. (2007) 'Fracture healing: the diamond concept', *Injury*, 38, pp. S3-S6.
- Gullberg, B., Johnell, O. and Kanis, J. (1997) 'World-wide projections for hip fracture', *Osteoporosis International*, 7(5), pp. 407-413.
- Haghighi, P. (1989) 'Structure, function and adaptation of compact bone', *Skeletal Radiology*, 18(7), pp. 506-506.
- Higuchi, T., Kinoshita, A., Takahashi, K., Oda, S. and Ishikawa, I. (1999) 'Bone regeneration by recombinant human bone morphogenetic protein-2 in rat mandibular defects. An experimental model of defect filling', *Journal of periodontology*, 70(9), pp. 1026-1031.
- Holland, T.A., Tessmar, J.K.V., Tabata, Y. and Mikos, A.G. (2004) 'Transforming growth factor- β 1 release from oligo (poly (ethylene glycol) fumarate) hydrogels in

conditions that model the cartilage wound healing environment', *Journal of controlled release*, 94(1), pp. 101-114.

Hollinger, J.O. and Kleinschmidt, J.C. (1990) 'The critical size defect as an experimental model to test bone repair materials', *Journal of Craniofacial Surgery*, 1(1), pp. 60-68.

Hollinger, J.O. and Leong, K. (1996) 'Poly (α -hydroxy acids): carriers for bone morphogenetic proteins', *Biomaterials*, 17(2), pp. 187-194.

Hollister, S.J. (2005) 'Porous scaffold design for tissue engineering', *Nat Mater*, 4(7), pp. 518-524.

Holmgren, S.K., Taylor, K.M., Bretscher, L.E. and Raines, R.T. (1998) 'Code for collagen's stability deciphered', *Nature*, 392(6677), pp. 666-667.

Holy, C.E., Dang, S.M., Davies, J.E. and Shoichet, M.S. (1999) 'In vitro degradation of a novel poly(lactide-co-glycolide) 75/25 foam', *Biomaterials*, 20(13), pp. 1177-1185.

HP Technology, (2012) HP scalable printing technology [online] Available at: http://isites.hp.com/hpinfo/newsroom/press_kits/2012/FallBizPrinting/HPPageWideTechnologyWhitePaper.pdf (Accessed: 13/11/2015)

Hsu, Y.Y., Gresser, J.D., Trantolo, D.J., Lyons, C.M., Gangadharam, P.R.J. and Wise, D.L. (1997) 'Effect of polymer foam morphology and density on kinetics of in vitro controlled release of isoniazid from compressed foam matrices', *Journal of biomedical materials research*, 35(1), pp. 107-116.

Hutmacher, D.W. (2000) 'Scaffolds in tissue engineering bone and cartilage', *Biomaterials*, 21(24), pp. 2529-2543.

Hutmacher, D.W., Sittinger, M. and Risbud, M.V. (2004) 'Scaffold-based tissue engineering: rationale for computer-aided design and solid free-form fabrication systems', *Trends in Biotechnology*, 22(7), pp. 354-362.

Irsen, S.H., Leukers, B., Höckling, C., Tille, C. and Seitz, H. (2006) 'Bioceramic granulates for use in 3D printing: process engineering aspects', *Materialwissenschaft und Werkstofftechnik*, 37(6), pp. 533-537.

Ishizaki, K.Z. (1998) 'Porous materials : process technology and applications' Komarneni, S. and Nanko, M. Dordrecht ;London: Kluwer Academic Publishers.

- Jin, Q.M., Takita, H., Kohgo, T., Atsumi, K., Itoh, H. and Kuboki, Y. (2000) 'Effects of geometry of hydroxyapatite as a cell substratum in BMP-induced ectopic bone formation', *Journal of biomedical materials research*, 51(3), pp. 491-499.
- Juhasz, J.A., Best, S.M., Brooks, R., Kawashita, M., Miyata, N., Kokubo, T., Nakamura, T. and Bonfield, W. (2004) 'Mechanical properties of glass-ceramic A-W-polyethylene composites: Effect of filler content and particle size', *Biomaterials*, 25(6), pp. 949-955.
- Jumani, M. S. (2013) Cost modelling of rapid manufacturing based mass customisation system for fabrication of custom foot orthoses PhD, University of Newcastle, School of Mechanical and Systems Engineering
- Karageorgiou, V. and Kaplan, D. (2005) 'Porosity of 3D biomaterial scaffolds and osteogenesis', *Biomaterials*, 26(27), pp. 5474-5491.
- Karunakaran, K.P., Shanmuganathan, P.V., Jadhav, S.J., Bhadauria, P. and Pandey, A. (2000) 'Rapid prototyping of metallic parts and moulds', *Journal of Materials Processing Technology*, 105(3), pp. 371-381.
- Kato, M., Toyoda, H., Namikawa, T., Hoshino, M., Terai, H., Miyamoto, S. and Takaoka, K. (2006) 'Optimized use of a biodegradable polymer as a carrier material for the local delivery of recombinant human bone morphogenetic protein-2 (rhBMP-2)', *Biomaterials*, 27(9), pp. 2035-2041.
- Keulen, J. (1973) 'Density of porous solids', *Matériaux et Construction*, 6(3), pp. 181-183.
- Khalyfa, A., Vogt, S., Weisser, J., Grimm, G., Rechtenbach, A., Meyer, W. and Schnabelrauch, M. (2007) 'Development of a new calcium phosphate powder-binder system for the 3D printing of patient specific implants', *Journal of Materials Science: Materials in Medicine*, 18(5), pp. 909-916.
- Khan, S.F. (2015) Novel indirect additive manufacturing for processing biomaterials PhD, Newcastle University, School of Mechanical and System Engineering.
- Kim, S.-H., Shin, J.-W., Park, S.-A., Kim, Y.K., Park, M.S., Mok, J.M., Yang, W.I. and Lee, J.W. (2004) 'Chemical, structural properties, and osteoconductive effectiveness of bone block derived from porcine cancellous bone', *Journal of Biomedical Materials Research Part B: Applied Biomaterials*, 68B(1), pp. 69-74.

- Klammert, U., Gbureck, U., Vorndran, E., Rödiger, J., Meyer-Marcotty, P. and Kübler, A.C. (2010) '3D powder printed calcium phosphate implants for reconstruction of cranial and maxillofacial defects', *Journal of Cranio-Maxillofacial Surgery*, 38(8), pp. 565-570.
- Kobayashi, Y., Kobashi, M. and Kanetake, N. (2008) 'Reactive infiltration of TiN powder preform with molten aluminum for the fabrication of nitride ceramics composite', *Materials Transactions*, 49(7), pp. 1616-1620.
- Koempel, J.A., Patt, B.S., O'Grady, K., Wozney, J. and Toriumi, D.M. (1998) 'The effect of recombinant human bone morphogenetic protein-2 on the integration of porous hydroxyapatite implants with bone', *Journal of biomedical materials research*, 41(3), pp. 359-363.
- Kokubo, T. (1991) 'Bioactive glass ceramics: properties and applications', *Biomaterials*, 12(2), pp. 155-163.
- Kokubo, T. (2008) *Bioceramics and their clinical applications*. North America: CRC Press LLC.
- Kokubo, T., Kim, H.M. and Kawashita, M. (2003) 'Novel bioactive materials with different mechanical properties', *Biomaterials*, 24(13), pp. 2161-2175.
- Kokubo, T., Shigematsu, M., Nagashima, Y., Tashiro, M., Nakamura, T., Yamamuro, T. and Higashi, S. (1982) 'Apatite- and wollastonite-containing glass-ceramics for prosthetic application', *Bulletin of the Institute of Chemical Research, Kyoto University*, 60, pp. 260-268.
- Kolk, A., Handschel, J., Drescher, W., Rothamel, D., Kloss, F., Blessmann, M., Heiland, M., Wolff, K.-D. and Smeets, R. (2012) 'Current trends and future perspectives of bone substitute materials—from space holders to innovative biomaterials', *Journal of Cranio-Maxillofacial Surgery*, 40(8), pp. 706-718.
- Kurz, L.T., Garfin, S.R. and Booth Jr, R.E. (1989) 'Harvesting autogenous iliac bone grafts: a review of complications and techniques', *Spine*, 14(12), pp. 1324-1331.
- Lam, C.X.F., Mo, X.M., Teoh, S.H. and Hutmacher, D.W. (2002) 'Scaffold development using 3D printing with a starch-based polymer', *Materials Science and Engineering: C*, 20(1–2), pp. 49-56.

- Langer, R. and Vacanti, J.P. (1993) 'Tissue engineering', *Science*, 260(5110), pp. 920-926.
- Laurencin, C.T., Norman, M.E., Elgendy, H.M., El-Amin, S.F., Allcock, H.R., Pucher, S.R. and Ambrosio, A.A. (1993) 'Use of polyphosphazenes for skeletal tissue regeneration', *Journal of biomedical materials research*, 27(7), pp. 963-973.
- Lee, J.-Y., Nam, S.-H., Im, S.-Y., Park, Y.-J., Lee, Y.-M., Seol, Y.-J., Chung, C.-P. and Lee, S.-J. (2002) 'Enhanced bone formation by controlled growth factor delivery from chitosan-based biomaterials', *Journal of Controlled Release*, 78(1), pp. 187-197.
- Lee, M. and Wu, B.M. (2012) 'Recent advances in 3D printing of tissue engineering scaffolds', in *Computer-Aided Tissue Engineering*. Springer, pp. 257-267.
- Lee, S.J., Sachs, E. and Cima, M. (1995) 'Layer position accuracy in powder-based rapid prototyping', *Rapid Prototyping Journal*, 1(4), pp. 24-37.
- Lewandrowski, K.-U., D. Gresser, J., Wise, D.L. and Trantolo, D.J. (2000) 'Bioresorbable bone graft substitutes of different osteoconductivities: a histologic evaluation of osteointegration of poly(propylene glycol-co-fumaric acid)-based cement implants in rats', *Biomaterials*, 21(8), pp. 757-764.
- Lichte, P., Pape, H.C., Pufe, T., Kobbe, P. and Fischer, H. (2011) 'Scaffolds for bone healing: concepts, materials and evidence', *Injury*, 42(6), pp. 569-573.
- Liu, C., Xia, Z. and Czernuszka, J.T. (2007) 'Design and development of three-dimensional scaffolds for tissue engineering', *Chemical Engineering Research and Design*, 85(7), pp. 1051-1064.
- Liu, C.Z. and Czernuszka, J.T. (2007) 'Development of biodegradable scaffolds for tissue engineering: a perspective on emerging technology', *Materials Science and Technology*, (23)4, pp. 379-391.
- Liu, W., Li, Y., Liu, J., Niu, X., Wang, Y. and Li, D. (2013) 'Application and performance of 3D printing in nanobiomaterials', *Journal of Nanomaterials*, 2013, p. 7.
- Lo, H., Ponticello, M.S. and Leong, K.W. (1995) 'Fabrication of controlled release biodegradable foams by phase separation', *Tissue engineering*, 1(1), pp. 15-28.
- Lozo, B., Stanic, M., Jamnicki, S., Mahovic Poljacek, M. and Muck, T. (2008) 'Three-dimensional ink jet prints - impact of infiltrants', *Journal of Imaging Science and Technology*, 52(5), p. /Oct.

- Lu, H.H., El-Amin, S.F., Scott, K.D. and Laurencin, C.T. (2003) 'Three-dimensional, bioactive, biodegradable, polymer–bioactive glass composite scaffolds with improved mechanical properties support collagen synthesis and mineralization of human osteoblast-like cells in vitro', *Journal of Biomedical Materials Research Part A*, 64(3), pp. 465-474.
- Lu, J.X., Flautre, B., Anselme, K., Hardouin, P., Gallur, A., Descamps, M. and Thierry, B. (1999) 'Role of interconnections in porous bioceramics on bone recolonization in vitro and in vivo', *Journal of Materials Science: Materials in Medicine*, 10(2), pp. 111-120.
- Lucas, P.A., Laurencin, C., Syftestad, G.T., Domb, A., Goldberg, V.M., Caplan, A.I. and Langer, R. (1990) 'Ectopic induction of cartilage and bone by water-soluble proteins from bovine bone using a polyanhydride delivery vehicle', *Journal of biomedical materials research*, 24(7), pp. 901-911.
- Madihally, S.V. and Matthew, H.W.T. (1999) 'Porous chitosan scaffolds for tissue engineering', *Biomaterials*, 20(12), pp. 1133-1142.
- Madry, H., van Dijk, C.N. and Mueller-Gerbl, M. (2010) 'The basic science of the subchondral bone', *Knee Surgery, Sports Traumatology, Arthroscopy*, 18(4), pp. 419-433.
- Marques, A.P., Reis, R.L. and Hunt, J.A. (2002) 'The biocompatibility of novel starch-based polymers and composites: in vitro studies', *Biomaterials*, 23(6), pp. 1471-1478.
- Marquis, M.E., Lord, E., Bergeron, E., Drevelle, O., Park, H., Cabana, F., Senta, H. and Faucheux, N. (2009) 'Bone cells-biomaterials interactions', *Frontiers in Bioscience*, 14(3), pp. 1023-1067.
- Marsell, R. and Einhorn, T.A. (2011) 'The biology of fracture healing', *Injury*, 42(6), pp. 551-555.
- Maspero, F.A., Ruffieux, K., Müller, B. and Wintermantel, E. (2002) 'Resorbable defect analog PLGA scaffolds using CO₂ as solvent: Structural characterization', *Journal of Biomedical Materials Research*, 62(1), pp. 89-98.
- Mastrogiacomo, M., Scaglione, S., Martinetti, R., Dolcini, L., Beltrame, F., Cancedda, R. and Quarto, R. (2006) 'Role of scaffold internal structure on in vivo bone formation in macroporous calcium phosphate bioceramics', *Biomaterials*, 27(17), pp. 3230-3237.

- Melchels, F.P.W., Feijen, J. and Grijpma, D.W. (2010) 'A review on stereolithography and its applications in biomedical engineering', *Biomaterials*, 31(24), pp. 6121-6130.
- Melton, L.J.I., Atkinson, E.J., O'Fallon, W.M. and Heath III, H. (1992) 'Risk of age-related fracture in patients with primary hyperparathyroidism', *Archives of Internal Medicine*, 152(11), pp. 2269-2273.
- Mendes, S.C., Sleijster, M., van den Muysenberg, A., de Bruijn, J.D. and van Blitterswijk, C.A. (2002) 'A cultured living bone equivalent enhances bone formation when compared to a cell seeding approach', *Journal of Materials Science: Materials in Medicine*, 13(6), pp. 575-581.
- Mikos, A.G., Sarakinos, G., Vacanti, J.P., Langer, R.S. and Cima, L.G. (1996) 'Biocompatible polymer membranes and methods of preparation of three dimensional membrane structures'. Google Patents.
- Milovanovic, P., Zimmermann, E.A., Hahn, M., Djonic, D., Püschel, K., Djuric, M., Amling, M. and Busse, B.r. (2013) 'Osteocytic canalicular networks: morphological implications for altered mechanosensitivity', *ACS nano*, 7(9), pp. 7542-7551.
- Ming, L.W. and Gibson, I. (2006) 'Experimental investigation of ink on powder used for selective laser sintering', *Journal of materials processing technology*, 174(1), pp. 91-101.
- Mistry, A.S. and Mikos, A.G. (2005) 'Tissue Engineering Strategies for Bone Regeneration' *Regenerative Medicine II, Advances in Biochemical Engineering*, 94, pp 1-22.
- Mooney, D.J., Baldwin, D.F., Suh, N.P., Vacanti, J.P. and Langer, R. (1996) 'Novel approach to fabricate porous sponges of poly (D, L-lactic-co-glycolic acid) without the use of organic solvents', *Biomaterials*, 17(14), pp. 1417-1422.
- Morgan, E.F., Barnes, G.L., Einhorn, T.A., Marcus, R., Feldman, D., Nelson, D. and Rosen, C.J. (2013) *The bone organ system: form and function*. Academic Press.
- Mow, V.C., Bachrach, N.M., Setton, L.A. and Guilak, F. (1994) 'Stress, strain, pressure and flow fields in articular cartilage and chondrocytes', in *Cell mechanics and cellular engineering*. Springer, pp. 345-379.
- Nagarjan, T., Shivalinge, G., Syed, M. and Badami, S. (2008) 'Rapid Prototype Technique in Medical Field', *Research J. Pharm and Tech.*, 1(4), pp. 341-344.

- Nakashima, K. and de Crombrughe, B. (2003) 'Transcriptional mechanisms in osteoblast differentiation and bone formation', *TRENDS in Genetics*, 19(8), pp. 458-466.
- Navarro, M., Michiardi, A., Castaño, O. and Planell, J.A. (2008) 'Biomaterials in orthopaedics', *Journal of the Royal Society, Interface*, 5(27), pp. 1137-58.
- Nicolodi, L., Sjolander, E., Olsson, K. (2004) 'Biocompatible Ceramics- An Overview of Applications and Novel Materials', *KTH*, p. 4.
- Nonaka, H.H. (1997) 'Plant carbohydrate-derived products as fat replacers and calorie reducers', *Cereal Foods World.*, 42(5), pp. 377-378.
- Oklund, S.A., Prolo, D.J., Gutierrez, R.V. and King, S.E. (1986) 'Quantitative comparisons of healing in cranial fresh autografts, frozen autografts and processed autografts, and allografts in canine skull defects', *Clinical orthopaedics and related research*, 205, pp. 269-291.
- Olszta, M.J., Cheng, X., Jee, S.S., Kumar, R., Kim, Y.-Y., Kaufman, M.J., Douglas, E.P. and Gower, L.B. (2007) 'Bone structure and formation: a new perspective', *Materials Science and Engineering: R: Reports*, 58(3), pp. 77-116.
- Oonishi, H., Hench, L.L., Wilson, J., Sugihara, F., Tsuji, E., Kushitani, S. and Iwaki, H. (1999) 'Comparative bone growth behavior in granules of bioceramic materials of various sizes', *Journal of Biomedical Materials Research*, 44(1), pp. 31-43.
- Oonishi, H., Hench, L.L., Wilson, J., Sugihara, F., Tsuji, E., Matsuura, M., Kin, S., Yamamoto, T. and Mizokawa, S. (2000) 'Quantitative comparison of bone growth behavior in granules of Bioglass®, A-W glass-ceramic, and hydroxyapatite', *Journal of Biomedical Materials Research*, 51(1), pp. 37-46.
- Peltola, S.M., Melchels, F.P.W., Grijpma, D.W. and Kellomäki, M. (2008) 'A review of rapid prototyping techniques for tissue engineering purposes', *Annals of Medicine*, 40(4), pp. 268-280.
- Phillips, A.M. (2005) 'Overview of the fracture healing cascade', *Injury*, 36(3), pp. S5-S7.
- Pigott, J.H., Ishihara, A., Wellman, M.L., Russell, D.S. and Bertone, A.L. (2013) 'Investigation of the immune response to autologous, allogeneic, and xenogeneic mesenchymal stem cells after intra-articular injection in horses', *Veterinary immunology and immunopathology*, 156(1), pp. 99-106.

- Polak, J.M., Hench, L.L. and Kemp, P. (2002) *Future strategies for tissue and organ replacement*. World Scientific.
- Poole, C.A. (1997) 'Review. Articular cartilage chondrons: form, function and failure', *Journal of anatomy*, 191(01), pp. 1-13.
- Porter, J.R., Ruckh, T.T. and Popat, K.C. (2009) 'Bone Tissue Engineering: A review in bone biomimetics and drug delivery strategies', *Biotechnology Progress*, 25(6), pp. 1539-1560.
- Rabkin, E. and Schoen, F.J. (2002) 'Cardiovascular tissue engineering', *Cardiovascular Pathology*, 11(6), pp. 305-317.
- Rho, J.-Y., Kuhn-Spearing, L. and Zioupos, P. (1998) 'Mechanical properties and the hierarchical structure of bone', *Medical Engineering & Physics*, 20(2), pp. 92-102.
- Richards, M., Dahiyat, B.I., Arm, D.M., Brown, P.R. and Leong, K.W. (1991) 'Evaluation of polyphosphates and polyphosphonates as degradable biomaterials', *Journal of biomedical materials research*, 25(9), pp. 1151-1167.
- Sachlos, E. and Czernuszka, J.T. (2003) 'Making tissue engineering scaffolds work. Review: the application of solid freeform fabrication technology to the production of tissue engineering scaffolds', *Eur Cell Mater*, 5(29), pp. 39-40.
- Sachs, E., Cima, M., Williams, P., Brancazio, D. and Cornie, J. (1992) 'Three dimensional printing: rapid tooling and prototypes directly from a CAD model', *Journal of Manufacturing Science and Engineering*, 114(4), pp. 481-488.
- Saito, N., Murakami, N., Takahashi, J., Horiuchi, H., Ota, H., Kato, H., Okada, T., Nozaki, K. and Takaoka, K. (2005) 'Synthetic biodegradable polymers as drug delivery systems for bone morphogenetic proteins', *Advanced drug delivery reviews*, 57(7), pp. 1037-1048.
- Saito, N., Okada, T., Horiuchi, H., Ota, H., Takahashi, J., Murakami, N., Nawata, M., Kojima, S., Nozaki, K. and Takaoka, K. (2003) 'Local bone formation by injection of recombinant human bone morphogenetic protein-2 contained in polymer carriers', *Bone*, 32(4), pp. 381-386.
- Schaffler, M.B. and Kennedy, O.D. (2012) 'Osteocyte signaling in bone', *Current osteoporosis reports*, 10(2), pp. 118-125.

- Schieker, M., Seitz, H., Drosse, I., Seitz, S. and Mutschler, W. (2006) 'Biomaterials as scaffold for bone tissue engineering', *European Journal of Trauma*, 32(2), pp. 114-124.
- Schindeler, A., McDonald, M.M., Bokko, P. and Little, D.G. (2008) *Seminars in cell & developmental biology*. Elsevier.
- Schmitz, J.P. and Hollinger, J.O. (1986) 'The critical size defect as an experimental model for raniomandibulofacial nonunions', *Clinical Orthopaedics and Related Research*, 205, pp. 299-308.
- Schmitz, J.P. and Hollinger, J.O. (1988) 'A preliminary study of the osteogenic potential of a biodegradable alloplastic-osteoinductive alloimplant', *Clinical orthopaedics and related research*, 237, pp. 245-255.
- Seeherman, H.J., Boussein, M., Kim, H., Li, R., Li, X.J., Aiolova, M. and Wozney, J.M. (2004) 'Recombinant human bone morphogenetic protein-2 delivered in an injectable calcium phosphate paste accelerates osteotomy-site healing in a nonhuman primate model', *The Journal of Bone & Joint Surgery*, 86(9), pp. 1961-1972.
- Seitz, H., Rieder, W., Irsen, S., Leukers, B. and Tille, C. (2005) 'Three-dimensional printing of porous ceramic scaffolds for bone tissue engineering', *Journal of Biomedical Materials Research Part B: Applied Biomaterials*, 74B(2), pp. 782-788.
- Shanjani, Y. (2011) *Solid Freeform Fabrication of Porous Calcium Polyphosphate Structures for Use in Orthopaedics*. University of Waterloo.
- Shapiro, F. (2008) 'Bone development and its relation to fracture repair. The role of mesenchymal osteoblasts and surface osteoblasts', *Eur Cell Mater*, 15(53), p. e76.
- Sikavitsas, V.I., Temenoff, J.S. and Mikos, A.G. (2001) 'Biomaterials and bone mechanotransduction', *Biomaterials*, 22(19), pp. 2581-2593.
- Silva, G.A., Pedro, A., Costa, F.J., Neves, N.M., Coutinho, O.P. and Reis, R.L. (2005) 'Soluble starch and composite starch Bioactive Glass 45S5 particles: Synthesis, bioactivity, and interaction with rat bone marrow cells', *Materials Science and Engineering: C*, 25(2), pp. 237-246.
- Simmons, C.A., Alsberg, E., Hsiong, S., Kim, W.J. and Mooney, D.J. (2004) 'Dual growth factor delivery and controlled scaffold degradation enhance in vivo bone formation by transplanted bone marrow stromal cells', *Bone*, 35(2), pp. 562-569.

- Sotome, S., Uemura, T., Kikuchi, M., Chen, J., Itoh, S., Tanaka, J., Tateishi, T. and Shinomiya, K. (2004) 'Synthesis and in vivo evaluation of a novel hydroxyapatite/collagen–alginate as a bone filler and a drug delivery carrier of bone morphogenetic protein', *Materials Science and Engineering: C*, 24(3), pp. 341-347.
- Spiro, R.C., Thompson, A.Y. and Poser, J.W. (2001) 'Spinal fusion with recombinant human growth and differentiation factor-5 combined with a mineralized collagen matrix', *The Anatomical Record*, 263(4), pp. 388-395.
- Spoerke, E.D. and Stupp, S.I. (2003) 'Colonization of organoapatite–titanium mesh by preosteoblastic cells', *Journal of Biomedical Materials Research Part A*, 67(3), pp. 960-969.
- Stevens, B., Yang, Y., Mohandas, A., Stucker, B. and Nguyen, K.T. (2008) 'A review of materials, fabrication methods, and strategies used to enhance bone regeneration in engineered bone tissues', *Journal of Biomedical Materials Research Part B: Applied Biomaterials*, 85(2), pp. 573-582.
- Suwanprateeb, J., Sanngam, R. and Panyathanmaporn, T. (2010) 'Influence of raw powder preparation routes on properties of hydroxyapatite fabricated by 3D printing technique', *Materials Science and Engineering: C*, 30(4), pp. 610-617.
- Suwanprateeb, J., Sanngam, R., Suvannapruk, W. and Panyathanmaporn, T. (2009) 'Mechanical and *in vitro* performance of apatite-wollastonite glass ceramic reinforced hydroxyapatite composite fabricated by 3D-printing', *Journal of Materials Science: Materials in Medicine*, 20(6), pp. 1281-1289.
- Tamai, N., Myoui, A., Hirao, M., Kaito, T., Ochi, T., Tanaka, J., Takaoka, K. and Yoshikawa, H. (2005) 'A new biotechnology for articular cartilage repair: subchondral implantation of a composite of interconnected porous hydroxyapatite, synthetic polymer (PLA-PEG), and bone morphogenetic protein-2 (rhBMP-2)', *Osteoarthritis and cartilage*, 13(5), pp. 405-417.
- Tan, K.H., Chua, C.K., Leong, K.F., Cheah, C.M., Cheang, P., Abu Bakar, M.S. and Cha, S.W. (2003) 'Scaffold development using selective laser sintering of polyetheretherketone–hydroxyapatite biocomposite blends', *Biomaterials*, 24(18), pp. 3115-3123.
- Taton, T.A. (2001) 'Boning up on biology', *Nature*, 412(6846), pp. 491-492.

- Technology Supplies LTD, (2007) *Material safety data sheet* [online] Available at: <http://sites.harvard.edu/fs/docs/icb.topic993207.files/zb60.pdf> (Accessed: 28/01/2015).
- Teti, A. (2011) 'Bone development: overview of bone cells and signaling', *Current osteoporosis reports*, 9(4), pp. 264-273.
- Thompson, J.B., Kindt, J.H., Drake, B., Hansma, H.G., Morse, D.E. and Hansma, P.K. (2001) 'Bone indentation recovery time correlates with bond reforming time', *Nature*, 414(6865), pp. 773-776.
- Thomson, R.C., Yaszemski, M.J., Powers, J.M. and Mikos, A.G. (1996) 'Fabrication of biodegradable polymer scaffolds to engineer trabecular bone', *Journal of Biomaterials Science, Polymer Edition*, 7(1), pp. 23-38.
- Triplett, R.G. and Schow, S.R. (1996) 'Autologous bone grafts and endosseous implants: complementary techniques', *Journal of Oral and Maxillofacial Surgery*, 54(4), pp. 486-494.
- Tsang, V.L. and Bhatia, S.N. (2004) 'Three-dimensional tissue fabrication', *Advanced drug delivery reviews*, 56(11), pp. 1635-1647.
- Tsiridis, E., Upadhyay, N. and Giannoudis, P. (2007) 'Molecular aspects of fracture healing: Which are the important molecules?', *Injury*, 38(1, Supplement), pp. S11-S25.
- Uhland, S.A., Holman, R.K., Morissette, S., Cima, M.J. and Sachs, E.M. (2001) 'Strength of green ceramics with low binder content', *Journal of the American Ceramic Society*, 84(12), pp. 2809-2818.
- Urist, M.R., DeLange, R.J. and Finerman, G.A. (1983) 'Bone cell differentiation and growth factors', *Science*, 220(4598), pp. 680-686.
- Utela, B. (2008) *Development and Application of New Material Systems for Three Dimensional Printing (3DP)*. ProQuest.
- Utela, B., Storti, D., Anderson, R. and Ganter, M. (2008) 'A review of process development steps for new material systems in three dimensional printing (3DP)', *Journal of Manufacturing Processes*, 10(2), pp. 96-104.
- Utela, B., Storti, D., Anderson, R. and Ganter, M. (2010) 'Development process for custom three-dimensional printing (3DP) material system', *Journal of Manufacturing Science and Engineering*, 132.

- Vaezi, M. and Chua, C. (2011) 'Effects of layer thickness and binder saturation level parameters on 3D printing process', *The International Journal of Advanced Manufacturing Technology*, 53(1-4), pp. 275-284.
- Vainionpää, S., Kilpikari, J., Laiho, J., Helevirta, P., Rokkanen, P. and Törmälä, P. (1987) 'Strength and strength retention *in vitro*, of absorbable, self-reinforced polyglycolide (PGA) rods for fracture fixation', *Biomaterials*, 8(1), pp. 46-48.
- Velasco, M.A., Narváez-Tovar, C.A. and Garzón-Alvarado, D.A. (2015) 'Design, Materials, and Mechanobiology of Biodegradable Scaffolds for Bone Tissue Engineering', *BioMed research international*, 2015.
- Venuvinod, P.K. and Ma, W. (2013) *Rapid prototyping: laser-based and other technologies*. Springer Science & Business Media.
- Visavarungroj, N. and Remon, J.P. (1992) 'Evaluation of maltodextrin as binding agent', *Drug Development and Industrial Pharmacy*, 18(15), pp. 1691-1700.
- Wang, X., Nyman, J.S., Dong, X., Leng, H. and Reyes, M. (2010) *Fundamental biomechanics in bone tissue engineering*. Place of Publication: Morgan & Claypool.
- Webb, P. (2000) 'A review of rapid prototyping (RP) techniques in the medical and biomedical sector', *Journal of Medical Engineering Technology*, 24(4), pp. 149-53.
- Weiner, S. and Traub, W. (1992) 'Bone structure: From angstroms to microns', *FASEB Journal*, 6(3), pp. 879-885.
- Whang, K., Thomas, C.H., Healy, K.E. and Nuber, G. (1995) 'A novel method to fabricate bioabsorbable scaffolds', *Polymer*, 36(4), pp. 837-842.
- Whang, K., Tsai, D.C., Nam, E.K., Aitken, M., Sprague, S.M., Patel, P.K. and Healy, K.E. (1998) 'Ectopic bone formation via rhBMP-2 delivery from porous bioabsorbable polymer scaffolds', *Journal of biomedical materials research*, 42(4), pp. 491-499.
- Williams, D.F. (2008) 'On the mechanisms of biocompatibility', *Biomaterials*, 29(20), pp. 2941-2953.
- Woodard, J.R., Hilldore, A.J., Lan, S.K., Park, C.J., Morgan, A.W., Eurell, J.A.C., Clark, S.G., Wheeler, M.B., Jamison, R.D. and Johnson, A.J.W. (2007) 'The mechanical properties and osteoconductivity of hydroxyapatite bone scaffolds with multi-scale porosity', *Biomaterials*, 28(1), pp. 45-54.

- Xiao, K. (2007) Indirect selective laser sintering of apatite-wollastonite glass-ceramic PhD, University of Leeds, School of Mechanical Engineering.
- Xiao, K., Dalgarno, K.W., Wood, D.J., Goodridge, R.D. and Ohtsuki, C. (2008) 'Indirect selective laser sintering of apatite—wollastonite glass—ceramic', *Proceedings of the Institution of Mechanical Engineers, Part H: Journal of Engineering in Medicine*, 222(7), pp. 1107-1114.
- Yang, S., Leong, K.F., Du, Z. and Chua, C.K. (2001) 'The design of scaffolds for use in tissue engineering. Part I. Traditional factors', *Tissue Engineering*, 7(6), pp. 679-689.
- Yang, S., Leong, K.F., Du, Z. and Chua, C.K. (2002) 'The design of scaffolds for use in tissue engineering. Part II. Rapid prototyping techniques', *Tissue Engineering*, 8(1), pp. 1-11.
- Yaszemski, M.J., Payne, R.G., Hayes, W.C., Langer, R. and Mikos, A.G. (1996a) 'Evolution of bone transplantation: Molecular, cellular and tissue strategies to engineer human bone', *Biomaterials*, 17(2), pp. 175-185.
- Yaszemski, M.J., Payne, R.G., Hayes, W.C., Langer, R. and Mikos, A.G. (1996b) 'In vitro degradation of a poly(propylene fumarate)-based composite material', *Biomaterials*, 17(22), pp. 2127-2130.
- Yeong, W.Y., Chua, C.K., Leong, K.F. and Chandrasekaran, M. (2004) 'Rapid prototyping in tissue engineering: Challenges and potential', *Trends in Biotechnology*, 22(12), pp. 643-652.
- Yin, L., Peng, H.X., Yang, L. and Su, B. (2008) 'Fabrication of three-dimensional inter-connective porous ceramics via ceramic green machining and bonding', *Journal of the European Ceramic Society*, 28(3), pp. 531-537.
- Yoo, J., Cima, M.J., Khanuja, S. and Sachs, E.M. (1993), 'Structural ceramic components by 3D printing', Proceedings of the Fourth International Solid Freeform Fabrication Symposium, University of Texas, Austin, TX, USA.
- Younger, E.M. and Chapman, M.W. (1989) 'Morbidity at bone graft donor sites', *Journal of orthopaedic trauma*, 3(3), pp. 192-195.
- Zegzula, H.D., Buck, D.C., Brekke, J., Wozney, J.M. and Hollinger, J.O. (1997) 'Bone formation with use of rhBMP-2 (recombinant human bone morphogenetic protein-2)*', *The Journal of Bone & Joint Surgery*, 79(12), pp. 1778-90.

Zein, I., Hutmacher, D.W., Tan, K.C. and Teoh, S.H. (2002) 'Fused deposition modeling of novel scaffold architectures for tissue engineering applications', *Biomaterials*, 23(4), pp. 1169-1185.

Zhou, Z., Buchanan, F., Mitchell, C. and Dunne, N. (2014) 'Printability of calcium phosphate: Calcium sulfate powders for the application of tissue engineered bone scaffolds using the 3D printing technique', *Materials Science and Engineering: C*, 38(0), pp. 1-10.

Zimmermann, I., Eber, M. and Meyer, K. (2004) 'Nanomaterials as flow regulators in dry powders', *Zeitschrift für Physikalische Chemie/International journal of research in physical chemistry and chemical physics*, 218(1/2004), pp. 51-102.

Appendix

Appendix A. Effect of powder setting and heat treatment and on bending strength and shrinkage

Table A-1 Three-point bending results for beams printed from PB5 with (Binder = zb[®]60) using Setting A and HT1

Beam	Span (L) (mm)	Fracture Force (P) (N)	Width (b) (mm)	Height (h) (mm)	Bending Strength (f) (MPa)
1	30	16.07	4.5	3.45	13.50
2	30	16.73	4.36	3.39	15.03
3	30	14.58	4.43	3.67	10.99
Mean (MPa)					13.17
Standard Deviation (MPa)					2.03
95% Confidence Interval					8.10, 18.24

Table A-2 Three-point bending results for beams printed from PB5 with (Binder = zb[®]60) using Setting A and HT2

Beam	Span (L) (mm)	Fracture Force (P) (N)	Width (b) (mm)	Height (h) (mm)	Bending Strength (f) (MPa)
4	30	16.7	4.47	3.54	13.42
5	30	13.65	4.46	3.54	15.66
6	30	12.11	4.53	3.54	15.45
7	30	16.04	4.37	3.47	13.71
Mean (MPa)					14.56
Standard Deviation (MPa)					1.16
95% Confidence Interval					12.71, 16.40

Appendix

Table A-3 Three-point bending results for beams printed from PB5 with (Binder = zb[®]60) using Setting A and HT3

Beam	Span (L) (mm)	Fracture Force (P) (N)	Width (b) (mm)	Height (h) (mm)	Bending Strength (f) (MPa)
8	30	16.02	4.38	3.43	13.99
9	30	15.27	4.46	3.61	11.82
10	30	16.75	4.51	3.55	13.26
Mean ((MPa)					13.02
Standard Deviation (MPa)					1.10
95% Confidence Interval					10.28, 15.76

Table A-4 Three-point bending results for beams printed from PB5 with (Binder = zb[®]60) using Setting B and HT1

Beam	Span (L) (mm)	Fracture Force (P) (N)	Width (b) (mm)	Height (h) (mm)	Bending Strength (f) (MPa)
11	30	21.16	4.45	3.53	17.17
12	30	16.89	4.51	3.53	13.52
13	30	18.68	4.51	3.49	15.30
14	30	14.93	4.46	3.58	11.75
Mean (MPa)					14.44
Standard Deviation (MPa)					2.33
95% Confidence Interval					10.72, 18.14

Appendix

Table A-5 Three-point bending results for beams printed from PB5 with (Binder = zb[®]60) using Setting B and HT2

Beam	Span (L) (mm)	Fracture Force (P) (N)	Width (b) (mm)	Height (h) (mm)	Bending Strength (f) (MPa)
15	30	17.3	4.45	3.46	14.61
16	30	17.81	4.46	3.55	14.26
17	30	18.18	4.4	3.5	15.18
Mean (MPa)					14.68
Standard Deviation (MPa)					0.46
95% Confidence Interval					13.52, 15.83

Table A-6 Three-point bending results for beams printed from PB5 with (Binder = zb[®]60) using Setting B and HT3

Beam	Span (L) (mm)	Fracture Force (P) (N)	Width (b) (mm)	Height (h) (mm)	Bending Strength (f) (MPa)
18	30	23.2	4.47	3.6	18.02
19	30	21.61	4.41	3.43	18.74
20	30	16.67	4.61	3.54	12.98
Mean (MPa)					16.58
Standard Deviation (MPa)					3.14
95% Confidence Interval					8.78, 24.37

Appendix

Table A-7 Three-point bending results for beams printed from PB5 with (Binder = zb[®]60) using Setting C and HT1

Beam	Span (L) (mm)	Fracture Force (P) (N)	Width (b) (mm)	Height (h) (mm)	Bending Strength (f) (MPa)
21	30	15.29	4.37	3.42	13.46
22	30	18.16	4.4	3.46	15.51
23	30	19.52	4.43	3.44	16.76
24	30	18.37	4.41	3.42	16.03
Mean (MPa)					15.44
Standard Deviation (MPa)					1.414
95% Confidence Interval					13.18, 17.69

Table A-8 Three-point bending results for beams printed with PB5 with (Binder = zb[®]60) using Setting C and HT2

Beam	Span (L) (mm)	Fracture Force (P) (N)	Width (b) (mm)	Height (h) (mm)	Bending Strength (f) (MPa)
25	30	18.4	4.47	3.44	15.65
26	30	17.55	4.47	3.42	15.11
27	30	17.71	4.36	3.37	16.09
Mean (MPa)					15.62
Standard Deviation (MPa)					0.50
95% Confidence Interval					14.39, 16.83

Appendix

Table A-9 Three-point bending results for beams printed from PB5 with (Binder = zb[®]60) using Setting C and HT3

Beam	Span (L) (mm)	Fracture Force (P) (N)	Width (b) (mm)	Height (h) (mm)	Bending Strength (f) (MPa)
28	30	20.87	4.51	3.47	17.29
29	30	15.54	4.4	3.48	13.12
30	30	20.98	4.52	3.53	16.76
Mean (MPa)					15.73
Standard Deviation (MPa)					2.27
95% Confidence Interval					10.08, 21.36

Appendix B. Properties of parts made from PB1

Table B-1 Three-point bending results for green beams printed from PB1 (Binder = 98% distilled water/2% glycerol)

Beam	Span (L) (mm)	Fracture Force (P) (N)	Width (b) (mm)	Height (h) (mm)	Bending Strength (f) (MPa)
1	30	13.79	5.9	4.05	6.41
2	30	1.97	5.8	4.1	0.91
3	30	6.08	5.8	4	2.95
4	30	11.7	5.8	4.08	5.45
Mean Bending Strength (MPa)					3.93
Standard Deviation (MPa)					2.49
Standard Error					1.25
95% Confidence Interval					-0.03, 7.88
Maximum (MPa)					6.41
Minimum(MPa)					0.91

Appendix

Table B-2 Three-point bending results for sintered beams printed from PB1 (Binder = 98% distilled water/2% glycerol)

Beam	Span (L) (mm)	Fracture Force (P) (N)	Width (b) (mm)	Height (h) (mm)	Bending Strength (f) (MPa)
1	30	25.62	4.88	3.9	15.53
2	30	6.34	4.85	3.85	3.97
3	30	9.18	4.79	3.86	5.79
4	30	11.35	4.94	3.95	6.63
5	30	9.77	4.96	3.75	6.30
6	30	6.85	4.98	3.78	4.33
7	30	22.22	4.98	3.85	13.55
8	30	22.35	4.83	3.96	13.28
9	30	9.84	4.94	3.77	6.31
10	30	23.8	4.98	3.95	13.78
Mean Bending Strength (MPa)					8.95
Standard Deviation (MPa)					4.5
Standard Error					1.42
95% Confidence Interval					5.73, 12.16
Maximum (MPa)					15.53
Minimum(MPa)					3.97

Appendix

Table B-3 Young's modulus of sintered beams printed from PB1 (Binder = 98% distilled water/2% glycerol))

Beam	Span (L) (mm)	(F/δ)Slope (N/mm)	Width (b) (mm)	Height (h) (mm)	Young's modulus (GPa)
1	30	299.27	4.88	3.9	6.98
2	30	95.41	4.85	3.95	2.33
3	30	176.69	4.79	3.86	4.33
Mean Young's modulus (GPa)					4.55
Standard Deviation (GPa)					2.33
Standard Error					1.35
95% Confidence Interval					1.91, 7.19
Maximum (GPa)					6.98
Minimum(GPa)					2.33

Appendix

Table B-4 Measured lengths (X), widths (Y), and heights (Z) for green parts and sintered parts made from PB1 (Binder = 98% distilled water/2% glycerol)

PB1 Beam	Green Part			Sintered Part		
	Length (mm)	Width (mm)	Height (mm)	Length (mm)	Width (mm)	Height (mm)
	X	Y	Z	X	Y	Z
1	49.8	5.9	4.09	40.27	4.88	3.9
2	49.6	5.8	4.01	40.74	4.85	3.85
3	49.6	5.6	4.11	40.55	4.79	3.86
4	49.6	5.8	4.12	40.16	4.94	3.95
5	49.6	5.8	4.04	40.2	4.96	3.75
6	49.8	5.8	4.05	40.24	4.98	3.78
7	49.5	5.9	4.01	40.29	4.98	3.85
8	49.6	5.8	4	40.71	4.83	3.96
9	49.7	5.8	4	40.26	4.94	3.77
10	49.8	5.9	4.05	40.48	4.98	3.95
Mean Linear Shrinkage (%)				18.67	15.44	4.59
Mean Volumetric Shrinkage (%)					34.38	
Standard Deviation					1.18	
Standard Error					0.37	

Appendix

Table B-5 Measured lengths (X), widths (Y), and heights (Z) and total porosity of sintered parts made from PB1 (Binder = 98% distilled water/2% glycerol)

PB1		Sintered Part			
Beam	Length (mm)	Width (mm)	Height (mm)	Weight (g)	Porosity (%)
1	16.92	4.94	3.95	0.44	57.08
2	18.06	4.96	3.75	0.49	52.39
3	20.41	4.98	3.78	0.55	53.71
4	20.47	4.98	3.83	0.66	44.94
5	18.85	4.94	3.77	0.48	55.28
6	20.37	4.98	3.95	0.65	47.16
Mean					51.76
Standard Deviation					4.75
Standard Error					1.94

Table B-6 Apparent density (g/cm^3) of sintered parts made from PB1 (Binder = 98% distilled water/2% glycerol)

Specimen	Mass (g)	V (cm^3)	D (g/cm^3)
1	1.35	0.77	1.76
2	1.11	0.76	1.46
3	1.03	0.75	1.37
4	1.07	0.78	1.37
5	1.12	0.75	1.50
6	1.07	0.76	1.41
7	1.22	0.77	1.58
8	1.25	0.78	1.61
9	1.1	0.75	1.47
10	1.2	0.80	1.51
Mean			1.50
Standard Deviation			0.12
Standard Error			0.04

Appendix

Table B-7 Open porosity of sintered specimens made from PB1 (Binder = 98% distilled water/2% glycerol)

Specimens	Mass (dry) (g)	Mass (submerged) (g)	Mass (wet) (g)	Open Porosity (%)
1	0.60848	0.36768	0.6993	27.39
2	0.62429	0.38324	0.7761	38.64
3	0.61232	0.36154	0.7371	33.23
Mean				33.08
Standard Deviation				5.63
Standard Error				3.25

Table B-8 Three-point bending results for green beams printed from PB1 (Binder = zb[®]60)

Beam	Span (L) (mm)	Fracture Force (P) (N)	Width (b) (mm)	Height (h) (mm)	Bending Strength (f) (MPa)
1	30	20.90	5.5	5.2	6.32
2	30	17.87	5.7	5.1	5.42
3	30	18.57	5.6	5	5.97
4	30	21.2	5.8	4.9	6.85
Mean Bending Strength (MPa)					6.14
Standard Deviation (MPa)					0.60
Standard Error					0.30
95% Confidence Interval					5.55,6.73
Maximum (MPa)					6.85
Minimum(MPa)					5.42

Appendix

Table B-9 Three-point bending results of sintered beams produced from PB1 (Binder = zb®60)

Beam	Span (L) (mm)	Fracture Force (P) (N)	Width (b) (mm)	Height (h) (mm)	Bending Strength (f) (MPa)
1	30	47.88	4.6	4.47	23.44
2	30	49.38	4.67	4.45	24.03
3	30	49.96	4.59	4.59	23.25
4	30	51.86	4.51	4.43	26.37
5	30	45.49	4.59	4.48	22.22
6	30	55.28	4.48	4.41	28.55
7	30	54.99	4.72	4.66	24.14
8	30	47.5	4.75	4.58	21.45
9	30	45.09	4.59	4.57	21.17
10	30	47.81	4.59	4.63	21.87
Mean Bending Strength (MPa)					23.65
Standard Deviation (MPa)					2.31
Standard Error					0.73
95% Confidence Interval					21.99, 25.30
Maximum (MPa)					28.55
Minimum(MPa)					21.17

Appendix

Table B-10 Young's modulus of sintered beams printed from PB1 (Binder = zb[®]60)

Beam	Span (L) (mm)	(F/δ)Slope (N/mm)	Width (b) (mm)	Height (h) (mm)	Young's modulus (GPa)
1	30	549.01	4.6	4.47	9.02
2	30	442.08	4.67	4.45	7.25
3	30	544.78	4.59	4.59	8.28
4	30	439.03	4.51	4.43	7.56
5	30	316.86	4.59	4.48	5.18
6	30	495.93	4.48	4.41	8.71
7	30	480.04	4.72	4.66	6.78
8	30	377.66	4.75	4.58	5.59
9	30	314.90	4.59	4.57	4.85
10	30	636.45	4.59	4.63	9.43
Mean Young's modulus (GPa)					7.27
Standard Deviation (GPa)					1.64
Standard Error					0.52
95% Confidence Interval					6.09, 8.43
Maximum (GPa)					9.43
Minimum(GPa)					4.85

Appendix

Table B-11 Measured lengths (X), widths (Y), and heights (Z) for green parts and sintered parts made from PB1 (Binder = zb@60)

PB1	Green Part			Sintered Part		
	Length (mm)	Width (mm)	Height (mm)	Length (mm)	Width (mm)	Height (mm)
	X	Y	Z	X	Y	Z
1	50.56	5.5	5.2	44.42	4.6	4.47
2	51.14	5.7	5.1	44.44	4.67	4.45
3	51.09	5.6	5	44.61	4.59	4.59
4	50.82	5.8	4.9	44.69	4.51	4.43
5	50.25	5.7	4.85	44.58	4.59	4.48
6	50.60	5.7	5.1	44.28	4.48	4.41
7	50.45	5.75	4.9	44.49	4.72	4.66
8	51	5.8	4.75	44.65	4.75	4.58
9	50.70	5.5	4.75	44.43	4.59	4.57
10	50.45	5.75	4.8	44.48	4.59	4.63
Mean Linear Shrinkage (%)				12.23	18.86	8.27
Mean Volumetric Shrinkage (%)					34.55	
Standard Deviation					3.66	
Standard Error					1.16	

Appendix

Table B-12 Measured lengths (X), widths (Y), and heights (Z) and total porosity of sintered parts of beams made from PB1 (Binder = zb®60)

PB1		Sintered Part			
Beam	Length (mm)	Width (mm)	Height (mm)	Weight (g)	Porosity (%)
1	21.74	4.58	4.38	0.69	48.46
2	22.94	4.52	4.44	0.72	49.06
3	22.15	4.51	4.27	0.7	46.55
4	21.01	4.54	4.39	0.67	47.88
5	23.36	4.56	4.29	0.75	46.54
6	20.83	4.68	4.41	0.67	49.24
Mean					47.95
Standard Deviation					1.19
Standard Error					0.49

Table B-13 Apparent density of sintered specimens made from PB1 (Binder = zb®60)

Specimens	Mass (g)	V (cm ³)	D (g/cm ³)
1	1.41	0.91	1.54
2	1.41	0.92	1.53
3	1.42	0.94	1.51
4	1.43	0.89	1.60
5	1.43	0.92	1.56
6	1.4	0.87	1.60
7	1.47	0.98	1.50
8	1.42	0.97	1.46
9	1.42	0.93	1.52
10	1.43	0.95	1.51
Mean			1.53
Standard Deviation			0.04
Standard Error			0.48

Appendix

Table B-14 Open porosity of sintered specimens made from PB1 (Binder = zb®60)

Specimens	Mass (dry) (g)	Mass (submerged) (g)	Mass (wet) (g)	Open Porosity (%)
1	0.67125	0.39732	0.72115	15.41
2	0.72497	0.42349	0.78007	15.45
3	0.70524	0.40725	0.75954	15.41
Mean				15.43
Standard Deviation				0.02
Standard Error				0.01

Appendix C. Properties of parts made from PB2

Table C-1 Three-point bending results of green beams printed from PB2 (Binder = 98% distilled water/2% glycerol)

Beam	Span (L) (mm)	Fracture Force (P) (N)	Width (b) (mm)	Height (h) (mm)	Bending Strength (f) (MPa)
1	30	1.2	5.9	4.1	0.54
2	30	0.49	5.8	4.2	0.22
Mean Bending Strength (MPa)					0.38
Standard Error					0.16

Table C-2 Three-point bending results of sintered beams printed from PB2 (Binder = 98% distilled water/2% glycerol)

Beam	Span (L) (mm)	Fracture Force (P) (N)	Width (b) (mm)	Height (h) (mm)	Bending Strength (f) (MPa)
1	30	12.92	4.95	3.44	9.93
2	30	11.8	4.6	3.35	10.29
3	30	17.88	4.57	3.26	16.57
4	30	12.41	4.55	3.42	10.49
5	30	17.01	4.98	3.35	13.70
6	30	15.59	4.61	3.2	14.86
7	30	12.47	4.74	3.24	11.28
8	30	10.97	4.52	3.15	11.01
9	30	12.61	4.62	3.5	10.03
10	30	11.06	4.38	3.3	10.43
Mean Bending Strength (MPa)					11.56
Standard Deviation (MPa)					2.33
Standard Error					0.74
95% Confidence Interval					10.18, 13.52
Maximum (MPa)					16.57
Minimum(MPa)					9.93

Appendix

Table C-3 Three-point bending results of sintered beams printed from PB2 (Binder = zb[®]60)

Beam	Span (L) (mm)	Fracture Force (P) (N)	Width (b) (mm)	Height (h) (mm)	Bending Strength (f) (MPa)
1	30	17.19	5	4.05	9.43
2	30	14.8	5.08	3.95	8.40
3	30	14.62	5.03	4.01	8.13
4	30	16.52	5.18	4.05	8.75
5	30	14.41	5.06	3.95	8.21
6	30	13.83	5	3.92	8.10
7	30	12.34	5.07	4.02	6.78
8	30	15.29	5.03	3.98	8.64
9	30	16.12	5.11	4.09	8.49
10	30	13.27	5.14	3.97	7.37
Mean Bending Strength (MPa)					8.23
Standard Deviation (MPa)					0.73
Standard Error					0.23
95% Confidence Interval					7.70, 8.75
Maximum (MPa)					9.43
Minimum(MPa)					6.78

Appendix

Table C-4 Young's modulus of sintered beams printed from PB2 (Binder = zb®60)

Beam	Span (L) (mm)	(F/δ)Slope (N/mm)	Width (b) (mm)	Height (h) (mm)	Young's modulus (GPa)
1	30	113.69	5	4.05	2.31
2	30	168.39	5.08	3.95	3.63
3	30	137.70	5.03	4.01	2.87
4	30	136.31	5.18	4.05	2.67
5	30	145.77	5.06	3.95	3.16
6	30	127.93	5	3.92	2.87
7	30	131.71	5.07	4.02	2.7
8	30	108.34	5.03	3.98	2.31
9	30	150.59	5.11	4.09	2.91
10	30	130.64	5.14	3.97	2.74
Mean Young's modulus (GPa)					2.82
Standard Deviation (GPa)					0.39
Standard Error					0.12
95% Confidence Interval					2.54, 3.09
Maximum (GPa)					3.63
Minimum(GPa)					2.31

Appendix

Table C-5 Measured lengths (X), widths (Y), and heights (Z) for beams made from PB2 (Binder = 98% distilled water/2% glycerol)

PB2 Beam	Green Part			Sintered Part		
	Length (mm)	Width (mm)	Height (mm)	Length (mm)	Width (mm)	Height (mm)
	X	Y	Z	X	Y	Z
1	49.38	5.6	4.2	40.6	4.95	3.44
2	49.23	5.9	4.15	39.8	4.6	3.35
3	49.22	5.53	4.25	40.8	4.57	3.26
4	49.12	5.95	4.3	40.5	4.55	3.42
5	49.21	5.88	4.3	40.48	4.98	3.35
6	49.19	5.45	4.35	40.8	4.61	3.2
7	49.01	5.48	4.3	40.78	4.74	3.24
8	49.1	5.83	4.25	40.52	4.52	3.15
9	49.12	5.52	4.32	40.9	4.62	3.5
10	49.06	5.92	4.28	40.3	4.38	3.3
Mean Linear Shrinkage (%)				17.53	18.47	22.22
Mean Volumetric Shrinkage (%)					47.60	
Standard Deviation					3.91	
Standard Error					1.24	

Appendix

Table C-6 Measured lengths (X), widths (Y), and heights (Z) for beams made from PB2 (Binder = zb®60)

PB2 Beam	Green Part			Sintered Part		
	Length (mm)	Width (mm)	Height (mm)	Length (mm)	Width (mm)	Height (mm)
	X	Y	Z	X	Y	Z
1	52.34	5.81	4.55	45.99	5	4.05
2	52.42	5.82	4.56	46.04	5.08	3.95
3	52.34	8.85	4.47	45.78	5.03	4.01
4	52.3	5.92	4.59	46.11	5.18	4.05
5	52.27	5.8	4.46	46.18	5.06	3.95
6	52.32	5.89	4.47	46.01	5	3.92
7	52.36	5.91	4.51	45.98	5.07	4.02
8	52.34	5.98	4.54	46	5.03	3.98
9	52.46	5.88	4.57	45.96	5.11	4.09
10	52.4	5.73	4.48	46.27	5.14	3.97
Mean Linear Shrinkage (%)				12.08	17.68	11.53
Mean Volumetric Shrinkage (%)				34.96		
Standard Deviation				7.34		
Standard Error				2.32		

Appendix

Table C-7 Measured lengths (X), widths (Y), and heights (Z) and total porosity of sintered beams made from PB2 (Binder= 98% distilled water/2% glycerol)

PB2		Sintered Part			
Beam	Length (mm)	Width (mm)	Height (mm)	Weight (g)	Porosity (%)
1	17.25	4.95	3.33	0.384	56.01
2	17.13	4.94	3.33	0.403	53.42
3	18.89	4.57	3.26	0.404	53.24
4	14.7	4.98	3.3	0.335	54.83
5	17.45	4.6	3.31	0.404	50.47
6	16.98	4.74	3.24	0.368	54.03
Mean					53.67
Standard Deviation					1.87
Standard Error					0.76

Table C-8 Open porosity of sintered parts for specimens made from PB2 (Binder= 98% distilled water/2% glycerol)

Specimens	Mass (dry) (g)	Mass (submerged) (g)	Mass (wet) (g)	Open Porosity (%)
1	0.93377	0.58593	1.1601	39.42
2	0.52483	0.32855	0.65314	39.53
3	0.67261	0.43762	0.82589	39.48
Mean				39.48
Standard Deviation				0.06
Standard Error				0.03

Appendix

Table C-9 Apparent density of sintered made from PB2 (Binder = 98% distilled water/2% glycerol)

Specimens	Mass (g)	V (cm ³)	D (g/cm ³)
1	0.92	0.69	1.33
2	0.88	0.61	1.43
3	0.89	0.61	1.46
4	0.93	0.63	1.48
5	0.94	0.68	1.39
6	0.88	0.60	1.46
7	0.89	0.63	1.42
8	0.9	0.58	1.56
9	0.89	0.66	1.35
10	0.9	0.58	1.55
Mean			1.44
Standard Deviation			0.08
Standard Error			0.03

Appendix D. Properties of parts made from PB3

Table D-1 Three-point bending results for green beams printed from PB3 (Binder = 98% distilled water/2% glycerol)

Beam	Span (L) (mm)	Fracture Force (P) (N)	Width (b) (mm)	Height (h) (mm)	Bending Strength (f) (MPa)
1	30	1.01	5.85	3.98	0.49
2	30	0.5	5.8	3.9	0.26
Mean Bending Strength (MPa)					0.37
Standard Error					0.11

Table D-2 Three-point bending results for sintered beams printed from PB3 (Binder = 98% distilled water/2% glycerol)

Beam	Span (L) (mm)	Fracture Force (P) (N)	Width (b) (mm)	Height (h) (mm)	Bending Strength (f) (MPa)
1	30	12.993	5.47	3.36	9.47
2	30	10.671	5.57	3.39	7.50
3	30	10.199	5.36	3.32	7.77
4	30	13.312	4.92	3.32	11.05
5	30	13.294	5.4	3.3	10.17
6	30	9.473	5.46	3.27	7.30
7	30	14.135	5.52	3.41	9.91
8	30	6.5145	5.51	3.26	5.01
9	30	9.412	5.56	3.31	6.95
10	30	7.682	5.36	3.33	5.82
Mean Bending Strength (MPa)					8.09
Standard Deviation (MPa)					1.98
Standard Error					0.63
95% Confidence Interval					6.67, 9.51
Maximum (MPa)					11.05
Minimum(MPa)					5.01

Appendix

Table D-3 Three-point bending results for sintered beams printed from PB3 (Binder solution = zb®60)

Beam	Span (L) (mm)	Fracture Force (P) (N)	Width (b) (mm)	Height (h) (mm)	Bending Strength (f) (MPa)
1	30	12.83	5.02	4.29	6.25
2	30	13.72	5.1	4.26	6.675
3	30	15.35	5.12	4.25	7.47
4	30	14.1	5.12	4.3	6.70
5	30	14.1	5.08	4.24	6.95
6	30	13.69	5	4.2	6.98
7	30	11.83	4.91	4.31	5.84
8	30	11.01	5.14	4.34	5.12
9	30	9.76	4.95	4.43	4.52
10	30	10.43	5.03	4.4	4.82
Mean Bending Strength (MPa)					6.13
Standard Deviation (MPa)					1.01
Standard Error					0.32
95% Confidence Interval					5.40, 6.85
Maximum (MPa)					7.47
Minimum(MPa)					4.52

Appendix

Table D-4 Young's modulus of sintered beams printed from PB3 (Binder solution = zb[®]60)

Beam	Span (L)(mm)	(F/δ)Slope (N/mm)	Width (b)(mm)	Height (h)(mm)	Young's modulus (GPa)
1	30	120.71	5.02	4.29	2.06
2	30	127.19	5.1	4.26	2.18
3	30	123.35	5.12	4.25	2.12
4	30	123.06	5.12	4.3	2.04
5	30	105.02	5.08	4.24	1.83
6	30	112.15	5	4.2	2.04
7	30	113.48	4.91	4.31	1.95
8	30	109.61	5.14	4.34	1.76
9	30	88.83	4.95	4.43	1.39
10	30	84.30	5.03	4.4	1.33
Mean Young's modulus (GPa)					1.87
Standard Deviation (GPa)					0.30
Standard Error					0.09
95% Confidence Interval					1.65, 2.08
Maximum (GPa)					2.18
Minimum(GPa)					1.33

Appendix

Table D-5 Measured lengths (X), widths (Y), and heights (Z) of beams made from PB3 (Binder solution = 98% distilled water/2% glycerol)

Beam	Green Part			Sintered Part		
	Length (mm)	Width (mm)	Height (mm)	Length (mm)	Width (mm)	Height (mm)
	X	Y	Z	X	Y	Z
1	50.06	6.7	4.2	39.2	5.47	3.36
2	49.9	6.74	4.22	39.02	5.57	3.39
3	49.55	6.67	4.3	38.9	5.36	3.32
4	49.68	6.14	4.3	38.7	4.92	3.32
5	49.82	6.68	4.26	38.95	5.4	3.3
6	49.67	6.72	4.25	38.75	5.46	3.27
7	50.08	6.78	4.3	39.18	5.52	3.41
8	49.36	6.75	4.32	38.86	5.51	3.26
9	50.04	6.76	4.28	39.34	5.56	3.31
10	49.58	6.6	4.23	38.83	5.36	3.33
Mean Linear Shrinkage (%)				21.70	18.65	22.01
Mean Volumetric Shrinkage (%)					50.32	
Standard Deviation					1.25	
Standard Error					0.40	

Appendix

Table D-6 Measured lengths (X), widths (Y), and heights (Z) of beams made from PB3 (Binder = zb®60)

PB3 Beam	Green Part			Sintered Part		
	Length (mm)	Width (mm)	Height (mm)	Length (mm)	Width (mm)	Height (mm)
	X	Y	Z	X	Y	Z
1	51.56	5.33	4.34	46.87	5.02	4.29
2	51.61	5.36	4.4	46.74	5.1	4.26
3	51.57	5.34	4.45	47.1	5.12	4.25
4	51.56	5.56	4.45	47.33	5.12	4.3
5	51.55	5.37	4.5	47.16	5.08	4.24
6	51.81	5.5	4.46	47.46	5	4.2
7	51.71	5.3	4.35	47.18	4.91	4.31
8	51.58	5.21	4.34	47.15	5.14	4.34
9	51.62	5.27	4.33	47.76	4.95	4.43
10	51.58	5.31	4.45	47.41	5.03	4.4
Mean Linear Shrinkage (%)				8.52	5.75	2.38
Mean Volumetric Shrinkage (%)					15.77	
Standard Deviation					3.49	
Standard Error					1.10	

Appendix

Table D-7 Measured lengths (X), widths (Y), and heights (Z) and total porosity of sintered beams made from PB3 (Binder = 98% distilled water/2% glycerol)

PB3		Sintered Part			
Beam	Length (mm)	Width (mm)	Height (mm)	Weight (g)	Porosity (%)
1	16.5	4.38	3.3	0.354	51.65
2	21.25	4.9	3.73	0.561	52.95
3	17.18	4.95	3.29	0.401	53.31
4	18.66	4.57	3.26	0.4	53.13
5	14.65	4.88	3.25	0.34	52.33
6	17.41	4.6	3.29	0.404	50.06
Mean					52.24
Standard Deviation					1.23
Standard Error					0.50

Table D-8 Open porosity of sintered parts for specimens made from PB3 (Binder = 98% distilled water/2% glycerol)

Specimens	Mass (dry) (g)	Mass (submerged) (g)	Mass (wet) (g)	Open Porosity (%)
1	0.42071	0.26557	0.51826	38.60
2	0.42111	0.26128	0.5257	39.55
3	0.42088	0.26654	0.51988	39.08
Mean				39.08
Standard Deviation				0.47
Standard Error				0.27

Appendix

Table D-9 Apparent density of sintered parts for specimens made from PB3 (Binder = 98% distilled water/2% glycerol)

Specimens	Mass (g)	V (cm³)	D (g/cm³)
1	0.89	0.72	1.24
2	0.89	0.74	1.21
3	0.87	0.69	1.26
4	0.82	0.63	1.30
5	0.9	0.69	1.30
6	0.86	0.69	1.24
7	0.88	0.74	1.19
8	0.87	0.70	1.25
9	0.86	0.72	1.19
10	0.86	0.69	1.24
Mean			1.24
Standard Deviation			0.04
Standard Error			0.01

Appendix E. Properties of parts made from PB4

Table E-1 Three-point bending results for green beams printed from PB4 (Binder solution = zb®60)

Beam	Span (L) (mm)	Fracture Force (P) (N)	Width (b) (mm)	Height (h) (mm)	Bending Strength (f) (MPa)
1	30	15.543	4.95	3.97	8.97
2	30	14.289	4.93	3.93	8.44
3	30	17.036	4.93	3.99	9.77
4	30	14.483	4.95	3.98	8.31
5	30	13.639	5.02	3.99	7.68
Mean Bending Strength (MPa)					8.63
Standard Deviation (MPa)					0.78
Standard Error					0.35
95% Confidence Interval					7.66, 9.60
Maximum (MPa)					9.77
Minimum(MPa)					7.68

Appendix

Table E-2 Three-point bending results for sintered beams printed from PB4 (Binder solution = zb®60)

Beam	Span (L) (mm)	Fracture Force (P) (N)	Width (b) (mm)	Height (h) (mm)	Bending Strength (f) (MPa)
1	30	37.05	4.55	3.68	27.06
2	30	48.37	4.75	3.31	41.82
3	30	40.15	4.62	3.55	31.03
4	30	39.68	4.5	3.3	36.44
5	30	45.89	4.58	3.38	39.47
6	30	49.70	4.89	3.4	39.57
7	30	38.55	4.51	3.42	32.89
8	30	35.69	3.94	3.21	39.56
9	30	35.03	4.04	3.28	36.27
10	30	29.98	3.93	3.26	32.30
Mean Bending Strength (MPa)					35.64
Standard Deviation (MPa)					4.69
Standard Error					1.48
95% Confidence Interval					32.28, 38.99
Maximum (MPa)					41.82
Minimum(MPa)					27.06

Appendix

Table E-3 Young's modulus of sintered beams printed from PB4 (Binder solution = zb[®]60)

Beam	Span (L) (mm)	(F/δ)Slope (N/mm)	Width (b) (mm)	Height (h) (mm)	Young's modulus (GPa)
1	30	426.52	4.55	3.68	12.7
2	30	487.12	4.75	3.31	19.09
3	30	382.03	4.62	3.55	12.48
4	30	373.49	4.5	3.3	15.59
5	30	330.41	4.58	3.38	12.61
6	30	478.35	4.89	3.4	16.8
7	30	339.01	4.51	3.42	12.68
8	30	351.63	3.94	3.21	18.21
9	30	382.58	4.04	3.28	18.11
10	30	245.54	3.93	3.26	12.17
Mean Young's modulus (GPa)					15.04
Standard Deviation (GPa)					2.81
Standard Error					0.89
95% Confidence Interval					13.03, 17.05
Maximum (GPa)					19.09
Minimum(GPa)					12.17

Appendix

Table E-4 Measured lengths (X), widths (Y), and heights (Z) green and sintered beams printed from PB4 (Binder = zb®60)

PB4	Green Part			Sintered Part		
Beam	Length (mm)	Width (mm)	Height (mm)	Length (mm)	Width (mm)	Height (mm)
	X	Y	Z	X	Y	Z
1	49.29	5.72	4.15	38.6	4.55	3.68
2	48.78	5.74	4.14	38.12	4.75	3.31
3	48.91	5.8	4.28	38.22	4.62	3.55
4	48.67	5.62	4.17	38.12	4.5	3.3
5	48.77	5.8	4.11	38.13	4.58	3.38
6	48.61	5.68	4.17	38.14	4.89	3.4
7	48.79	5.73	4.24	38.16	4.51	3.42
8	50.74	4.8	4.01	39.62	3.94	3.21
9	50.69	5.07	4.1	39.65	4.04	3.28
10	50.69	4.95	4.1	39.76	3.93	3.26
Mean Linear Shrinkage (%)				21.75	19.30	18.52
Mean Volumetric Shrinkage (%)					48.56	
Standard Deviation					2.13	
Standard Error					0.67	

Appendix

Table E-5 Total porosity of sintered beams made from PB4 (Binder = zb®60)

PB4		Sintered Part			
Beam	Length (mm)	Width (mm)	Height (mm)	Weight (g)	Porosity (%)
1	17.52	3.76	3.16	0.4	37.41
2	18.52	4.31	3.32	0.52	36.08
3	18.16	4.3	3.18	0.51	33.10
4	18.89	4.49	3.29	0.54	36.97
5	15.52	4.34	3.11	0.43	33.14
6	17.34	4.3	3.29	0.49	34.94
Mean					35.27
Standard Deviation					1.87
Standard Error					0.76

Table E-6 Open porosity of sintered specimens made from PB4 (Binder = zb®60)

Specimens	Mass (dry) (g)	Mass (submerged) (g)	Mass (wet) (g)	Open Porosity (%)
1	0.91293	0.56611	0.95771	11.44
2	0.90048	0.55953	0.9461	11.80
3	0.90186	0.56894	0.94559	11.61
Mean				11.62
Standard Deviation				0.18
Standard Error				0.10

Appendix

Table E-7 Apparent density of sintered specimens made from PB4 (Binder = zb[®]60)

Specimens	Mass (g)	V (cm ³)	D (g/cm ³)
1	1.09	0.65	1.69
2	1.08	0.60	1.80
3	1.08	0.63	1.72
4	1.07	0.57	1.89
5	1.1	0.60	1.86
6	1.05	0.63	1.66
7	1.05	0.59	1.78
8	0.92	0.50	1.83
9	0.92	0.53	1.75
10	0.92	0.51	1.81
Mean			1.78
Standard Deviation			0.08
Standard Error			0.03

Appendix F. Properties of parts made from PB5

Table F-1 Three-point bending results of green beams printed from PB5 (Binder = zb[®]60)

Beam	Span (L) (mm)	Fracture Force (P) (N)	Width (b) (mm)	Height (h) (mm)	Bending Strength (f) (MPa)
1	30	16.658	4.79	3.9	10.29
2	30	15.348	4.72	3.94	9.43
3	30	15.387	4.72	4.12	8.64
4	30	10.538	4.76	4.1	5.93
5	30	14.719	4.74	4.09	8.35
Mean Bending Strength (MPa)					8.53
Standard Deviation (MPa)					1.64
Standard Error					0.73
95% Confidence Interval					6.49, 10.55
Maximum (MPa)					10.29
Minimum(MPa)					5.93

Appendix

Table F-2 Three-point bending results for sintered beams printed from PB5 (Binder = zb[®]60)

Beam	Span (L) (mm)	Fracture Force (P) (N)	Width (b) (mm)	Height (h) (mm)	Bending Strength (f) (MPa)
1	30	19.58	4.24	3.54	16.58
2	30	33.40	4.17	3.61	27.654
3	30	32.31	4.22	3.34	30.884
4	30	31.98	3.96	3.54	29.00
5	30	23.91	4.31	3.38	21.84
6	30	20.78	4.08	3.36	20.30
7	30	34.83	4.01	3.58	30.50
8	30	32.42	4.21	3.31	31.63
9	30	31.24	4.59	3.45	25.73
10	30	25.89	4.17	3.32	25.34
Mean Bending Strength (MPa)					25.95
Standard Deviation (MPa)					5.02
Standard Error					1.59
95% Confidence Interval					22.35, 29.53
Maximum (MPa)					31.63
Minimum(MPa)					16.58

Appendix

Table F-3 Young's modulus results for sintered beams printed from PB5 (Binder = zb®60)

Beam	Span (L) (mm)	(F/δ)Slope (N/mm)	Width (b) (mm)	Height (h) (mm)	Young's modulus (GPa)
1	30	219.42	4.24	3.54	7.87
2	30	283.29	4.17	3.61	9.75
3	30	337.83	4.22	3.34	14.5
4	30	230.28	3.96	3.54	8.85
5	30	168.01	4.31	3.38	6.81
6	30	329.86	4.08	3.36	14.39
7	30	295.81	4.01	3.58	10.85
8	30	329.44	4.21	3.31	14.57
9	30	281.56	4.59	3.45	10.08
10	30	318.35	4.17	3.32	14.08
Mean Young's modulus (GPa)					11.18
Standard Deviation (GPa)					2.98
Standard Error					0.94
95% Confidence Interval					9.04, 13.30
Maximum (GPa)					14.57
Minimum(GPa)					6.81

Appendix

Table F-4 Measured lengths, widths, and heights for beams made from PB5 (Binder = zb[®]60)

PB5 Beam	Green Part			Sintered Part		
	Length (mm)	Width (mm)	Height (mm)	Length (mm)	Width (mm)	Height (mm)
	X	Y	Z	X	Y	Z
1	50.24	5.12	4.05	40.83	4.24	3.54
2	50.02	4.79	4.06	40.67	4.17	3.61
3	50.06	5.13	4.07	40.63	4.22	3.34
4	50.09	5.04	4.56	40.65	3.96	3.54
5	50.2	5.01	4.02	40.96	4.31	3.38
6	50.26	5.04	4	40.72	4.08	3.36
7	50.22	4.56	4.02	40.62	4.01	3.58
8	50.15	4.94	3.96	40.5	4.21	3.31
9	50.23	4.68	4	40.81	4.59	3.45
10	50.06	4.9	3.97	40.29	4.17	3.32
Mean Linear Shrinkage (%)				18.91	14.73	15.43
Mean Volumetric Shrinkage (%)					41.30	
Standard Deviation					5.34	
Standard Error					1.69	

Appendix

Table F-5 Total porosity of sintered beams made from PB5 (Binder = zb®60)

PB5		Sintered Part			
Beam	Length (mm)	Width (mm)	Height (mm)	Weight (g)	Porosity (%)
1	18.12	3.89	3.24	0.42	40.10
2	21.27	4	3.4	0.5	43.70
3	23.92	3.74	3.25	0.55	38.38
4	19.71	3.88	3.37	0.44	44.39
5	23.86	3.89	3.33	0.54	43.09
6	19.25	3.95	3.22	0.44	41.46
Mean					41.85
Standard Deviation					2.31
Standard Error					0.94

Table F-6 Open porosity of sintered specimens made from PB5 (Binder = zb®60)

Specimens	Mass (dry) (g)	Mass (submerged) (g)	Mass (wet) (g)	Open Porosity (%)
1	0.55267	0.33215	0.58244	11.89
2	0.96095	0.59263	1.01557	12.91
3	0.56285	0.34325	0.59394	12.40
Mean				12.40
Standard Deviation				0.51
Standard Error				0.29

Appendix

Table F-7 Apparent density of sintered specimens made from PB5 (Binder = zb[®]60)

Specimens	Mass (g)	V (cm ³)	D (g/cm ³)
1	0.94	0.61	1.53
2	0.93	0.61	1.52
3	0.95	0.57	1.66
4	0.9	0.57	1.58
5	0.94	0.6	1.58
6	0.95	0.56	1.70
7	0.91	0.58	1.56
8	0.95	0.56	1.68
9	0.93	0.65	1.44
10	0.94	0.56	1.69
Mean			1.59
Standard Deviation			0.09
Standard Error			0.03

Appendix G. Properties of parts made from PB6

Table G-1 Three-point bending results for green beams printed from PB6 (Binder = zb®60)

Beam	Span (L) (mm)	Fracture Force (P) (N)	Width (b) (mm)	Height (h) (mm)	Bending Strength (f) (MPa)
1	30	2.46	4.11	3.54	2.15
2	30	2.60	4.01	3.45	2.46
3	30	2.61	4.05	3.39	2.52
4	30	2.55	4.1	3.42	2.39
5	30	2.77	4.04	3.46	2.58
6	30	2.19	3.85	3.65	1.92
Mean Bending Strength (MPa)					2.33
Standard Deviation (MPa)					0.25
Standard Error					0.10
95% Confidence Interval					2.07, 2.60
Maximum (MPa)					2.58
Minimum(MPa)					1.92

Appendix

Table G-2 Three-point bending results for sintered beams printed from PB6 (Binder = zb[®]60)

Beam	Span (L) (mm)	Fracture Force (P) (N)	Width (b) (mm)	Height (h) (mm)	Bending Strength (f) (MPa)
1	30	35.06	4.76	4.28	18.10
2	30	33.43	4.93	4.35	16.13
3	30	30.72	4.83	4.18	16.38
4	30	34.20	4.69	4.47	16.42
5	30	31.86	4.62	4.24	17.26
6	30	35.66	4.79	4.27	18.37
7	30	33.83	4.96	4.34	16.29
8	30	33.11	4.95	4.35	15.91
9	30	34.13	4.65	4.3	17.86
10	30	34.73	4.41	4.29	19.26
Mean Bending Strength (MPa)					17.20
Standard Deviation (MPa)					1.14
Standard Error					0.36
95% Confidence Interval					16.37, 18.01
Maximum (MPa)					19.26
Minimum(MPa)					15.91

Appendix

Table G-3 Young's modulus of sintered beams printed from PB6 (Binder = zb®60)

Beam	Span (L)(mm)	(F/δ)Slope (N/mm)	Width (b)(mm)	Height (h)(mm)	Young's modulus (GPa)
1	30	340.48	4.76	4.28	6.16
2	30	283.30	4.93	4.35	4.71
3	30	301.17	4.83	4.18	5.76
4	30	268.29	4.69	4.47	4.32
5	30	273.49	4.62	4.24	5.24
6	30	281.86	4.79	4.27	5.1
7	30	358.41	4.96	4.34	5.97
8	30	358.95	4.95	4.35	5.95
9	30	290.67	4.65	4.3	5.31
10	30	280.74	4.41	4.29	5.44
Mean Young's modulus (GPa)					5.40
Standard Deviation (GPa)					0.59
Standard Error					0.19
95% Confidence Interval					4.97, 5.81
Maximum (GPa)					6.16
Minimum(GPa)					4.32

Appendix

Table G-4 Measured lengths (X), widths (Y), and heights (Z) for beams made from PB6 (Binder = zb[®]60)

PB6 Beam	Green Part			Sintered Part		
	Length (mm)	Width (mm)	Height (mm)	Length (mm)	Width (mm)	Height (mm)
	X	Y	Z	X	Y	Z
1	52.41	5.14	4.38	44.51	4.76	4.28
2	52.47	5.3	4.25	44.89	4.93	4.35
3	52.38	5.12	4.23	44.74	4.83	4.18
4	52.37	5.22	4.45	44.88	4.69	4.47
5	52.44	5.14	4.31	45.06	4.62	4.24
6	52.34	5.42	4.28	44.67	4.79	4.27
7	52.47	5.35	4.29	45.09	4.96	4.34
8	52.41	5.13	4.25	45.11	4.95	4.35
9	52.32	5.09	4.23	44.8	4.65	4.3
10	52.47	5.18	4.28	44.94	4.41	4.29
Mean Linear Shrinkage (%)				14.39	8.64	0.28
Mean Volumetric Shrinkage (%)					21.53	
Standard Deviation					3.46	
Standard Error					1.09	

Appendix

Table G-5 Total porosity of sintered beams made from PB6 (Binder = zb®60)

PB6		Sintered Part			
Beam	Length (mm)	Width (mm)	Height (mm)	Weight (g)	Porosity (%)
1	20.49	4.87	4.44	0.5912	56.53
2	23.97	4.73	4.26	0.66102	55.42
3	22.79	4.61	4.34	0.64701	53.78
4	20.91	4.77	4.26	0.57956	55.57
5	22.32	4.33	4.19	0.62183	49.98
6	21.51	4.81	4.11	0.61475	52.91
Mean					54.03
Standard Deviation					2.38
Standard Error					0.97

Table G-6 Open porosity of sintered specimens made from PB6 (Binder = zb®60)

Specimens	Mass (dry) (g)	Mass (submerged) (g)	Mass (wet) (g)	Open Porosity (%)
1	0.5912	0.32895	0.64222	16.29
2	0.66102	0.37382	0.72355	17.88
3	0.64701	0.36201	0.70123	15.98
4	0.57956	0.32114	0.6359	17.90
5	0.62183	0.3483	0.67238	15.60
6	0.61475	0.3214	0.68244	18.75
Mean				17.07
Standard Deviation				1.27
Standard Error				0.52

Appendix

Table G-7 Apparent density of sintered specimens made from PB6 (Binder = zb[®]60)

Specimens	Mass (g)	V (cm ³)	D (g/cm ³)
1	1.28	0.91	1.41
2	1.32	0.96	1.37
3	1.27	0.90	1.41
4	1.29	0.94	1.37
5	1.23	0.88	1.39
6	1.27	0.91	1.39
7	1.32	0.97	1.36
8	1.22	0.97	1.26
9	1.3	0.90	1.45
10	1.25	0.85	1.47
Mean			1.39
Standard Deviation			0.06
Standard Error			0.02

Appendix H. Properties of parts made from PB7

Table H-1 Three-point bending results for green beams printed from PB7 (Binder = zb®60)

Beam	Span (L) (mm)	Fracture Force (P) (N)	Width (b) (mm)	Height (h) (mm)	Bending Strength (f) (MPa)
1	30	2.23	3.89	3.57	2.03
2	30	1.74	4.19	3.47	1.55
3	30	2.36	3.61	4.05	1.79
4	30	1.78	3.85	3.44	1.76
5	30	2.42	3.12	3.21	3.38
6	30	2.12	3.91	3.5	1.99
Mean Bending Strength (MPa)					2.08
Standard Deviation (MPa)					0.66
Standard Error					0.27
95% Confidence Interval					1.39, 2.77
Maximum (MPa)					3.38
Minimum(MPa)					1.55

Appendix

Table H-2 Three-point bending results for sintered beams printed from PB7 (Binder = zb[®]60)

Beam	Span (L) (mm)	Fracture Force (P) (N)	Width (b) (mm)	Height (h) (mm)	Bending Strength (f) (MPa)
1	30	26.18	4.78	3.74	17.62
2	30	28.60	4.49	3.97	18.19
3	30	25.48	4.35	3.8	18.25
4	30	27.03	4.37	3.76	19.69
5	30	26.71	4.75	3.99	15.90
6	30	28.43	4.46	3.97	18.20
7	30	27.65	4.35	3.87	19.10
8	30	30.76	4.75	3.9	19.16
9	30	28.12	4.55	3.88	18.47
10	30	28.15	4.44	3.87	19.05
Mean Bending Strength (MPa)					18.36
Standard Deviation (MPa)					1.06
Standard Error					0.34
95% Confidence Interval					17.60, 19.12
Maximum (MPa)					19.69
Minimum(MPa)					15.90

Appendix

Table H-3 Young's modulus results of sintered beams printed from PB7 (Binder = zb[®]60)

Beam	Span (L) (mm)	(F/δ)Slope (N/mm)	Width (b) (mm)	Height (h) (mm)	Young's modulus (GPa)
1	30	260.17	4.78	3.74	7.02
2	30	332.34	4.49	3.97	7.98
3	30	324.39	4.35	3.8	9.17
4	30	259.99	4.37	3.76	7.55
5	30	287.74	4.75	3.99	6.44
6	30	347.84	4.46	3.97	8.41
7	30	349.24	4.35	3.87	9.35
8	30	299.77	4.75	3.9	7.18
9	30	267.03	4.55	3.88	6.78
10	30	299.75	4.44	3.87	7.86
Mean Young's modulus (GPa)					7.77
Standard Deviation (GPa)					0.98
Standard Error					0.31
95% Confidence Interval					7.07, 8.47
Maximum (GPa)					9.35
Minimum(GPa)					6.44

Appendix

Table H-4 Measured lengths (X), widths (Y), and heights (Z) of green and sintered beams made from PB7(Binder = zb®60)

PB7 Beam	Green Part			Sintered Part		
	Length (mm)	Width (mm)	Height (mm)	Length (mm)	Width (mm)	Height (mm)
	X	Y	Z	X	Y	Z
1	52.21	5.41	4.46	44.7	4.78	3.74
2	52.08	5.26	4.25	44.67	4.49	3.97
3	51.71	5.1	4.23	44.85	4.35	3.8
4	51.97	5.1	4.1	45.02	4.37	3.76
5	51.78	4.98	4.03	45.02	4.75	3.99
6	52.05	5.29	4.61	45.6	4.46	3.97
7	51.92	5.16	4.8	45.19	4.35	3.87
8	52.15	5.88	4.31	45.46	4.75	3.9
9	52.02	5.54	4.4	45.23	4.55	3.88
10	51.98	5.49	4.34	44.31	4.44	3.87
Mean Linear Shrinkage (%)				13.43	14.88	10.98
Mean Volumetric Shrinkage (%)					34.06	
Standard Deviation					6.36	
Standard Error					2.01	

Appendix

Table H-5 Total porosity of sintered beams made from PB7 (Binder = zb®60)

PB7		Sintered Part			
Beam	Length (mm)	Width (mm)	Height (mm)	Weight (g)	Porosity (%)
1	21.34	4.67	4.28	0.59259	54.75
2	21.52	5.15	4.46	0.61621	59.39
3	22.75	5.27	4.21	0.61539	60.29
4	22.31	5.22	4.37	0.59853	61.69
5	22.19	5.41	4.22	0.6263	59.73
6	22.65	5.44	4.42	0.66155	60.43
Mean					59.38
Standard Deviation					2.40
Standard Error					0.98

Table H-6 Open porosity of sintered specimens made from PB7 (Binder = zb®60)

Specimens	Mass (dry) (g)	Mass (submerged) (g)	Mass (wet) (g)	Open Porosity (%)
1	0.59259	0.31594	0.6668	21.15
2	0.61621	0.31317	0.69147	19.89
3	0.61539	0.31684	0.6923	20.48
4	0.59853	0.2999	0.67522	20.43
5	0.6263	0.32386	0.68253	15.68
6	0.66155	0.35523	0.72668	17.53
Mean				19.20
Standard Deviation				2.13
Standard Error				0.87

Appendix

Table H-7 Apparent density of sintered specimens made from PB7 (Binder = zb[®]60)

Specimens	Mass (g)	V (cm ³)	D (g/cm ³)
1	1.32	0.80	1.65
2	1.26	0.80	1.58
3	1.3	0.74	1.75
4	1.23	0.74	1.66
5	1.31	0.85	1.54
6	1.31	0.81	1.62
7	1.29	0.76	1.70
8	1.28	0.84	1.52
9	1.31	0.80	1.64
10	1.29	0.76	1.69
Mean			1.64
Standard Deviation			0.07
Standard Error			0.02

Appendix I. Infiltration of sintered parts with phosphate glass

Table I-1 Three-point bending results for beams printed from PB5 with(Binder = zb[®]60) after infiltration with phosphate glass at 900 °C for 30 min at a heating rate of 10 °C /min (method A)

Beam	Weight before infiltration	Weight after infiltration	Span (L) (mm)	Fracture Force (P) (N)	Width (b) (mm)	Height (h) (mm)	Bending Strength (f) (MPa)
1	0.96	0.96	30	32.00	4.01	3.28	33.38
2	0.91	0.92	30	28.61	3.84	3.52	27.06
3	0.89	0.92	30	28.93	3.85	3.58	26.38
4	0.91	0.94	30	23.34	4.21	3.58	19.47
5	0.91	0.95	30	30.32	3.86	3.38	30.94
6	0.89	0.93	30	24.77	4.03	3.5	22.58
7	0.95	0.99	30	32.54	4.09	3.34	32.09
8	0.97	1.01	30	33.93	4.15	3.29	33.99
9	0.92	0.96	30	33.82	3.88	3.47	32.57
10	0.97	1.02	30	35.84	4.26	3.47	31.44
11	0.96	1.01	30	38.67	4.18	3.34	37.32
12	0.92	0.97	30	34.17	4	3.15	38.75
13	0.93	0.99	30	11.46	4.14	3.18	12.32
14	0.92	1	30	36.97	3.95	3.17	41.92
15	0.9	1	30	29.10	4.02	3.24	31.03
16	0.93	1.03	30	29.64	3.99	3.16	33.48
17	0.92	1.03	30	25.24	4.11	3.24	26.32
18	0.88	0.99	30	23.87	4.11	3.17	26.01
19	0.9	1.02	30	28.27	3.98	3.26	30.07
20	0.87	0.99	30	25.96	4.2	3.14	28.22
21	0.91	1.04	30	24.03	4.12	3.27	24.55
22	0.87	1.01	30	24.23	4.2	3.21	25.19
23	0.88	1.02	30	20.05	4.23	3.18	21.10
24	0.92	1.07	30	22.188	4.39	3.35	20.26
25	0.89	1.05	30	23.77	4.36	3.18	24.26
26	0.87	1.09	30	22.50	4.2	3.15	24.30
27	0.88	1.12	30	17.22	4.19	3.22	17.84
28	0.89	1.13	30	22.09	4.04	3.33	22.19
Mean Bending Strength (MPa)							27.68
Standard Deviation (MPa)							6.69
Standard Error							1.26
95% Confidence Interval							25.08, 30.27
Maximum (MPa)							41.92
Minimum(MPa)							12.32

Appendix

Table I-2 Total porosity of beams printed from PB5 with (Binder = zb[®]60) after sintering and after phosphate glass infiltration (method A)

PB	Sintered Part			Porosity (%)		
	Beam	Length (mm)	Width (mm)	Height (mm)	After sintering	After infiltration
1	40.22	4.01	3.28	40.89	40.89	
2	40.3	3.84	3.52	45.58	44.88	
3	40.2	3.85	3.58	47.68	45.60	
4	40.35	4.21	3.58	51.26	49.36	
5	40.23	3.86	3.38	43.53	40.59	
6	40.01	4.03	3.5	48.63	45.90	
7	40.26	4.09	3.34	43.73	40.94	
8	40.62	4.15	3.29	43.03	40.26	
9	40.25	3.88	3.47	44.70	41.86	
10	40.27	4.26	3.47	46.92	43.69	
11	40.3	4.18	3.34	44.42	41.01	
12	40.03	4	3.15	40.59	36.77	
13	40.09	4.14	3.18	42.60	38.23	
14	40.22	3.95	3.17	40.50	34.39	
15	40.13	4.02	3.24	43.91	36.55	
16	40.43	3.99	3.16	40.57	33.03	
17	40.11	4.11	3.24	43.89	35.97	
18	40.03	4.11	3.17	45.04	36.93	
19	40.23	3.98	3.26	43.84	34.99	
20	40.37	4.2	3.14	46.77	38.10	
21	40.22	4.12	3.27	45.30	36.07	
22	40.15	4.2	3.21	47.65	37.70	
23	40.12	4.23	3.18	46.89	36.91	
24	40.38	4.39	3.35	49.54	39.82	
25	40.57	4.36	3.18	48.46	37.52	
26	40.28	4.2	3.15	46.82	30.94	
27	40.2	4.19	3.22	47.15	30.13	
28	40.13	4.04	3.33	46.30	29.20	
Mean					38.51	
Standard Deviation					4.82	
Standard Error					0.91	

Appendix

Table I-3 Open porosity of beams printed from PB5 with (Binder = zb[®]60) after phosphate glass infiltration (method A)

Specimens	Mass (dry) (g)	Mass (submerged) (g)	Mass (wet) (g)	Open Porosity (%)
1	0.53822	0.33515	0.55168	6.22
2	0.52242	0.32832	0.53211	4.75
3	0.71125	0.44533	0.72315	4.28
Mean				5.08
Standard Deviation				1.01
Standard Error				0.58

Table I-4 Three-point bending results for beams printed from PB5 with (Binder = zb[®]60) after infiltration with phosphate glass at 900 °C for 30 min with a heating rate of 10 °C /min (method B)

Beam	Weight before infiltration	Weight after infiltration	Span (L) (mm)	Fracture Force (P) (N)	Width (b) (mm)	Height (h) (mm)	Bending Strength (f) (MPa)
1	0.91	1.42	30	30.29	4.5	3.44	25.60
2	0.9	1.46	30	37.31	4.42	3.44	32.10
3	0.91	1.49	30	44.3	4.43	3.52	36.32
Mean Bending Strength (MPa)							31.34
Standard Deviation (MPa)							5.40
Standard Error							3.12
95% Confidence Interval							17.92, 44.75
Maximum (MPa)							36.32
Minimum(MPa)							25.60

Appendix

Table I-5 Young's modulus of sintered beams printed from PB5 with (Binder = zb[®]60) after phosphate glass infiltration (method B)

Beam	Span (L) (mm)	(F/δ)Slope (N/mm)	Width (b) (mm)	Height (h) (mm)	Young's modulus (GPa)
1	30	462.25	4.5	3.44	17.03
2	30	449.73	4.42	3.44	16.87
3	30	701.13	4.43	3.52	24.49
Mean Young's modulus (GPa)					19.46
Standard Deviation (GPa)					4.35
Standard Error					2.51
95% Confidence Interval					8.64, 30.27
Maximum (GPa)					24.49
Minimum(GPa)					16.87

Table I-6 Total porosity of beams made from PB5 with (Binder = zb[®]60) after sintering and after phosphate glass infiltration (method B)

PB	Sintered Part			Porosity (%)	
Beam	Length (mm)	Width (mm)	Height (mm)	After sintering	After infiltration
1	42.24	4.5	3.44	54.67	24.67
2	41.95	4.42	3.44	54.04	20.27
3	41.81	4.43	3.52	54.53	20.32
Mean					21.75
Standard Deviation					2.53
Standard Error					1.46

Appendix

Table I-7 Open porosity of beams made from PB5 with (Binder = zb[®]60) after phosphate glass infiltration (method B)

Specimens	Mass (dry) (g)	Mass (submerged) (g)	Mass (wet) (g)	Open Porosity (%)
1	0.74472	0.44411	0.76236	5.54
2	0.7351	0.44644	0.73901	1.34
3	0.74586	0.45215	0.74736	0.51
Mean				2.46
Standard Deviation				2.70
Standard Error				1.56

Table I-8 Three-point bending results for beams printed from PB6 with (Binder = zb[®]60) after phosphate glass infiltration at 900 °C for 30 min at a heating rate of 10 °C /min (method B)

Beam	Weight before infiltration	Weight after infiltration	Span (L) (mm)	Fracture Force (P) (N)	Width (b) (mm)	Height (h) (mm)	Bending Strength (f) (MPa)
1	0.57	0.69	30	13.86	3.57	3.21	16.95
2	0.60	0.7	30	12.96	3.57	3.43	13.89
3	0.60	0.65	30	18.6	3.61	3.37	20.42
4	0.58	0.65	30	13.35	3.44	3.38	15.29
5	0.57	0.72	30	18.19	3.53	3.18	22.93
Mean Bending Strength (MPa)							17.89
Standard Deviation (MPa)							3.72
Standard Error							1.66
95% Confidence Interval							13.27, 22.51
Maximum (MPa)							22.93
Minimum(MPa)							13.89

Appendix

Table I-9 Young's modulus of sintered beams printed from PB6 with (Binder = zb[®]60) after phosphate glass infiltration (method B)

Beam	Span (L) (mm)	(F/δ)Slope (N/mm)	Width (b) (mm)	Height (h) (mm)	Young's modulus (GPa)
1	30	159.55	3.57	3.21	9.12
2	30	223.65	3.57	3.43	10.48
3	30	147.93	3.61	3.37	7.23
Mean Young's modulus (GPa)					8.94
Standard Deviation (GPa)					1.63
Standard Error					0.94
Maximum (GPa)					10.48
Minimum(GPa)					7.23

Table I-10 Total porosity of beams made from PB6 with (Binder = zb[®]60) after sintering and after phosphate glass infiltration (method B)

PB	Sintered Part			Porosity (%)	
Beam	Length (mm)	Width (mm)	Height (mm)	After sintering	After infiltration
1	34.47	3.57	3.21	53.00	41.31
2	34.34	3.57	3.43	53.52	44.38
3	34.49	3.61	3.37	54.97	42.14
4	34.38	3.44	3.38	52.74	45.04
5	33.99	3.53	3.18	51.34	38.23
Mean					42.22
Standard Deviation					2.71
Standard Error					1.21

Appendix

Table I-11 Three-point bending results for beams printed from PB7 with (Binder = zb[®]60) after phosphate glass infiltration at 900 °C for 30 min at a heating rate of 10 °C /min (method B)

Beam	Weight before infiltration	Weight after infiltration	Span (L) (mm)	Fracture Force (P) (N)	Width (b) (mm)	Height (h) (mm)	Bending Strength (f)(MPa)
1	0.61	0.81	30	28.85	3.60	3.47	29.95
2	0.61	0.65	30	13.94	3.62	3.43	14.73
3	0.57	0.78	30	27.46	3.79	3.59	25.30
4	0.58	0.66	30	13.28	3.64	3.47	13.63
5	0.61	0.71	30	23.32	3.69	3.43	24.17
Mean Bending Strength (MPa)							21.56
Standard Deviation (MPa)							7.08
Standard Error							3.17
95% Confidence Interval							12.76, 30.35
Maximum (MPa)							29.95
Minimum(MPa)							13.63

Table I-12 Young's modulus of sintered beams printed from PB7 with (Binder = zb[®]60) after phosphate glass infiltration (method B)

Beam	Span (L) (mm)	(F/δ)Slope (N/mm)	Width (b) (mm)	Height (h) (mm)	Young's modulus (GPa)
1	30	381.89	3.60	3.47	17.14
2	30	225.55	3.62	3.43	10.42
3	30	303.41	3.79	3.59	11.68
Mean Young's modulus (GPa)					13.08
Standard Deviation (GPa)					3.57
Standard Error					2.06
Maximum (GPa)					17.14
Minimum(GPa)					10.42

Appendix

Table I-13 Total porosity of beams made from PB7 with (Binder = zb[®]60) after sintering and after phosphate glass infiltration (method B)

PB		Sintered Part			Porosity (%)	
Beam	Length (mm)	Width (mm)	Height (mm)	After sintering	After infiltration	
1	34.36	3.60	3.47	53.71	35.79	
2	33.97	3.62	3.43	52.89	49.24	
3	34.29	3.79	3.59	60.20	42.89	
4	34.30	3.64	3.47	56.39	49.29	
5	34.33	3.69	3.43	54.27	45.42	
Mean					44.53	
Standard Deviation					5.59	
Standard Error					2.50	

Appendix J. Accuracy of Printed Parts and Devices

Table J-1 Accuracy of green part and sintered parts made from PB1 (Binder = 98% distilled water/2% glycerol)

PB1	Green Part			Sintered Part		
	Length (mm)	Width (mm)	Height (mm)	Length (mm)	Width (mm)	Height (mm)
	X	Y	Z	X	Y	Z
n	10	10	10	10	10	10
Mean	49.66	5.81	4.04	40.39	4.91	3.86
SD	0.107	0.087	0.045	0.213	0.07	0.072
SE	0.03	0.03	0.01	0.07	0.02	0.02
maximum	49.8	5.9	4.12	40.74	4.98	3.96
minimum	49.5	5.6	4.00	40.16	4.79	3.75
95% CI	(49.5, 49.7)	(5.7, 5.8)	(4.01, 4.08)	(40.2, 40.5)	(4.8, 4.9)	(3.8, 3.9)

Table J-2 Accuracy of green part and sintered parts made from PB2 (Binder = 98% distilled water/2% glycerol)

PB2	Green Part			Sintered Part		
	Length (mm)	Width (mm)	Height (mm)	Length (mm)	Width (mm)	Height (mm)
	X	Y	Z	X	Y	Z
n	10	10	10	10	10	10
Mean	49.16	5.70	4.27	40.54	4.65	3.32
SD	0.105	0.206	0.059	0.321	0.188	0.111
SE	0.03	0.07	0.02	0.1	0.06	0.04
max	49.38	5.95	4.35	40.90	4.98	3.50
min	49.01	5.45	4.15	39.80	4.38	3.15
95% CI	(49.1, 49.2)	(5.5, 5.8)	(4.2, 4.3)	(40.3, 40.7)	(4.5, 4.7)	(3.2, 3.4)

Appendix

Table J-3 Accuracy of green part and sintered parts made from PB2 (Binder = zb®60)

PB2		Green Part			Sintered Part		
Beam	Length (mm)	Width (mm)	Height (mm)	Length (mm)	Width (mm)	Height (mm)	
	X	Y	Z	X	Y	Z	
n	10	10	10	10	10	10	
Mean	52.35	6.15	4.52	46.03	5.07	3.99	
SD	0.051	0.941	0.047	0.133	0.059	0.054	
SE	0.02	0.3	0.01	0.04	0.02	0.02	
max	52.46	5.85	4.59	46.27	5.18	4.09	
min	52.27	5.73	4.46	45.78	5.00	3.92	
95% CI	(52.3, 52.4)	(5.4, 6.8)	(4.4, 4.5)	(45.9, 46.1)	(5.02, 5.1)	(3.9, 4.03)	

Table J-4 Accuracy of green part and sintered parts made from PB3 (Binder = 98% distilled water/2% glycerol)

PB3		Green Part			Sintered Part		
Beam	Length (mm)	Width (mm)	Height (mm)	Length (mm)	Width (mm)	Height (mm)	
	X	Y	Z	X	Y	Z	
n	10	10	10	10	10	10	
Mean	49.77	6.65	4.26	38.97	5.41	3.32	
SD	0.241	0.188	0.041	0.201	0.188	0.048	
SE	0.08	0.06	0.01	0.06	0.06	0.02	
max	50.08	6.78	4.32	39.34	5.57	3.41	
min	49.36	6.14	4.20	38.70	4.92	3.26	
95% CI	(49.5, 49.9)	(6.5, 6.7)	(4.23, 4.29)	(38.8, 39.1)	(5.2, 5.5)	(3.29, 3.36)	

Appendix

Table J-5 Accuracy of green part and sintered parts made from PB3 (Binder = zb®60)

PB3	Green Part			Sintered Part		
	Length (mm)	Width (mm)	Height (mm)	Length (mm)	Width (mm)	Height (mm)
	X	Y	Z	X	Y	Z
n	10	10	10	10	10	10
Mean	51.6	5.35	4.40	47.20	5.04	4.36
SD	0.082	0.104	0.062	0.29	0.077	0.071
SE	0.03	0.03	0.02	0.09	0.02	0.02
max	51.81	5.56	4.50	47.76	5.14	4.43
min	51.55	5.21	4.33	46.74	4.91	4.20
95% CI	(51.5, 51.6)	(5.2, 5.4)	(4.3, 4.4)	(47.0, 47.4)	(4.9, 5.1)	(4.2, 4.3)

Table J-6 Accuracy of green part and sintered parts made from PB4 (Binder = zb®60)

PB4	Green Part			Sintered Part		
	Length (mm)	Width (mm)	Height (mm)	Length (mm)	Width (mm)	Height (mm)
	X	Y	Z	X	Y	Z
n	10	10	10	10	10	10
Mean	49.39	5.49	4.14	38.65	4.43	3.37
SD	0.92	0.38	0.076	0.722	0.34	0.143
SE	0.29	0.12	0.02	0.23	0.11	0.04
max	50.74	5.80	4.28	39.76	4.89	3.68
min	48.61	4.80	4.01	38.12	3.93	3.21
95% CI	(48.7, 50.0)	(5.2, 5.7)	(4.09, 4.2)	(38.1, 39.1)	(4.1, 4.6)	(3.2, 3.4)

Appendix

Table J-7 Accuracy of green part and sintered parts made from PB5 (Binder = zb®60)

PB5	Green Part			Sintered Part		
	Length (mm)	Width (mm)	Height (mm)	Length (mm)	Width (mm)	Height (mm)
	X	Y	Z	X	Y	Z
n	10	10	10	10	10	10
Mean	50.15	4.92	4.07	40.66	4.19	3.44
SD	0.09	0.19	0.17	0.18	0.17	0.11
SE	0.03	0.06	0.05	0.06	0.05	0.03
max	50.26	5.13	4.56	40.96	4.59	3.61
min	50.02	4.56	3.96	40.29	3.96	3.31
95% CI	(50.1, 50.2)	(4.7, 5.1)	(3.9, 4.1)	(40.5, 40.8)	(4.1, 4.3)	(3.4, 3.5)

Table J-8 Accuracy of green part and sintered parts made from PB6 (Binder = zb®60)

PB6	Green Part			Sintered Part		
	Length (mm)	Width (mm)	Height (mm)	Length (mm)	Width (mm)	Height (mm)
	X	Y	Z	X	Y	Z
n	10	10	10	10	10	10
Mean	52.40	5.20	4.29	44.86	4.75	4.30
SD	0.054	0.11	0.070	0.19	0.17	0.07
SE	0.02	0.03	0.02	0.06	0.05	0.02
max	52.47	5.42	4.45	45.11	4.96	4.47
min	52.32	5.09	4.23	44.51	4.41	4.18
95% CI	(52.3, 52.4)	(5.1, 5.2)	(4.2, 4.3)	(44.7, 45)	(4.6, 4.8)	(4.2, 4.3)

Appendix

Table J-9 Accuracy of green part and sintered parts made from PB7 (Binder = zb[®]60)

PB7 Beam	Green Part			Sintered Part		
	Length (mm)	Width (mm)	Height (mm)	Length (mm)	Width (mm)	Height (mm)
	X	Y	Z	X	Y	Z
n	10	10	10	10	10	10
Mean	51.98	5.32	4.35	45.00	4.52	3.87
SD	0.154	0.26	0.22	0.38	0.17	0.087
SE	0.02	0.03	0.02	0.06	0.05	0.02
max	52.21	5.88	4.80	45.60	4.78	3.99
min	51.71	4.98	4.03	44.31	4.35	3.74
95% CI	(51.8, 52.1)	(5.1, 5.5)	(4.1, 4.5)	(44.7, 45.2)	(4.4, 4.6)	(3.8, 3.9)

Table J-10 Accuracy of 8 mm (diameter) by 2 mm (height) printed discs after sintering

Disk	A (mm)	B (mm)
1	7.95	1.90
2	7.89	1.84
3	7.91	1.89
4	7.91	1.86
5	7.89	1.82
6	7.93	1.91
7	8.11	1.87
8	7.85	1.88
9	7.88	1.86
10	8.09	1.87
Mean	7.94	1.87
SD	0.09	0.030
SE	0.03	0.01
Maximum	8.11	1.91
Minimum	7.85	1.82
95% CI	(7.87, 8.00)	(1.85, 1.88)

Appendix

Table J-11 Accuracy of 8 mm (diameter) by 2 mm (height) printed disc with four pockets after sintering

	A	B	C₁	D₁	C₂	D₂	C₃	D₃	C₄	D₄
	(mm)	(mm)	(mm)	(mm)	(mm)	(mm)	(mm)	(mm)	(mm)	(mm)
1	8.09	2.02	0.99	0.60	1.01	0.45	0.99	0.50	1	0.45
2	7.99	2.00	0.95	0.40	.99	0.55	1	0.45	0.97	0.60
3	8.01	1.99	1	0.50	0.97	0.50	0.97	0.40	0.99	0.45
4	8.07	1.95	0.98	0.45	0.99	0.45	0.99	0.50	0.98	0.45
5	7.96	2.01	0.99	0.45	1.01	0.45	0.99	0.55	1.01	0.45
6	7.99	1.96	0.95	0.55	0.97	0.50	1.02	0.45	0.99	0.50
7	7.97	1.93	1.01	0.50	0.99	0.55	0.97	0.45	0.98	0.50
8	8.04	1.96	1.01	0.50	0.98	0.45	0.98	0.60	1.01	0.45
9	8.05	1.95	0.98	0.45	0.98	0.45	0.98	0.50	1	0.45
10	8.03	1.97	0.95	0.45	0.99	0.45	0.98	0.55	1	0.45
Mean	8.09	1.97	0.98	0.48	0.98	0.48	0.98	0.49	0.99	0.47
SD	0.430	0.020	0.023	0.050	0.139	0.042	0.014	0.059	0.013	0.048
SE	0.14	0.01	0.01	0.02	0.04	0.01	0.01	0.02	0.01	0.02
Maximum	8.09	2.02	1.01	0.60	1.01	0.55	1.02	0.60	1.01	0.60
Minimum	7.96	1.93	0.95	0.40	0.97	0.45	0.97	0.40	0.97	0.45

Table J-12 Accuracy of 6 mm (diameter) by 7 mm (height) printed plug with two through holes and one pocket hole after sintering

	A (mm)	B (mm)	C₁ (mm)	C₂ (mm)	D (mm)
1	6.10	7.07	0.99	0.99	2.20
2	5.99	6.98	0.96	0.96	2.10
3	6.02	7.01	0.96	0.98	2.10
4	6.03	7.04	0.99	0.99	2.20
5	5.98	6.99	0.99	1.01	2.22
6	5.96	7.00	0.99	0.99	2.05
7	5.97	7.05	0.99	1.01	2.24
8	6.10	7.05	1.00	0.99	1.98
9	6.05	6.99	1.01	0.99	2.14
10	6	6.99	0.99	0.99	2.11
Mean	6.02	7.01	0.98	0.99	2.13
SD	0.050	0.032	0.015	0.014	0.082
SE	0.02	0.01	0.01	0.01	0.03
Maximum	6.10	7.07	1.01	1.01	2.24
Minimum	5.96	6.98	0.96	0.96	1.98
95% CI	(5.98, 6.05)	(6.99, 7.04)	(0.97, 0.99)	(0.97, 1.00)	(2.07, 2.19)

Appendix

Table J-13 Accuracy of 6 mm (diameter) by 7 mm (height) printed hollow cylinder after sintering

	A (mm)	B (mm)	C (mm)
1	5.96	6.88	0.95
2	6.05	6.90	0.95
3	5.98	6.85	0.95
4	5.95	6.86	0.99
5	5.99	6.91	1.00
6	5.96	6.81	1.15
7	5.99	6.85	1.06
8	5.96	6.82	1.02
9	5.98	6.90	1.16
10	5.95	6.85	1.14
Mean	5.97	6.86	1.03
SD	0.029	0.034	0.085
SE	0.01	0.01	0.03
Maximum	6.05	6.91	1.16
Minimum	5.95	6.81	0.95
95% CI	(5.95, 5.99)	(6.83, 6.88)	(0.97, 1.09)

Table J-14 Accuracy of printed disk with lip after sintering

	A (mm)	B (mm)	C (mm)	D (mm)
1	8.33	3.97	1.11	2.40
2	8.12	4.11	1	2.41
3	8.42	3.96	1.20	2.42
4	8.08	3.95	1.12	2.39
5	8.25	3.90	1.15	2.43
6	8.39	4.15	1.12	2.40
7	8.33	4.09	1.08	2.42
8	8.20	4.03	1.08	2.40
9	8.33	4.16	1.11	2.41
10	8.33	4.11	1.16	2.41
Mean	8.27	4.04	1.11	2.40
SD	0.112	0.092	0.050	0.011
SE	0.04	0.03	0.02	0.01
Maximum	8.42	4.16	1.20	2.43
Minimum	8.08	3.90	1.00	2.39
95% CI	(8.19, 8.35)	(3.97, 4.10)	(1.07, 1.15)	(2.40, 2.41)

Appendix

Table J-15 Accuracy of 6 mm (diameter) by 8 mm (height) printed anchor plug after sintering

	A (mm)	B (mm)	C (mm)	D (mm)	E (mm)	F (mm)
1	6.20	8.01	2.10	0.96	2.00	2.20
2	6.15	7.97	2.06	0.95	1.95	2.30
3	6.07	7.90	2.08	0.96	1.90	2.20
4	6.00	7.89	2.15	0.96	2.10	2.40
5	6.06	7.99	2.19	0.95	1.99	2.38
6	6.00	8.00	2.10	0.92	2.05	2.30
7	6.00	7.98	2.10	0.94	1.95	2.25
8	6.10	7.90	2.08	0.96	2.05	2.30
9	6.10	7.98	2.15	0.97	2.00	2.35
10	6.11	7.89	2.12	0.94	1.95	2.20
Mean	6.07	7.95	2.11	0.95	1.99	2.28
SD	0.067	0.049	0.039	0.014	0.059	0.074
SE	0.02	0.02	0.01	0.01	0.02	0.02
Maximum	6.20	8.01	2.19	0.97	2.10	2.40
Minimum	6.00	7.89	2.06	0.92	1.90	2.20
95% CI	(6.03, 6.12)	(7.91, 7.98)	(2.08, 2.14)	(0.94, 0.96)	(1.95, 2.03)	(2.23, 2.34)

Appendix K. Academic Contribution

List of publications:

AlHarbi, N., Khan S.F., Bretcanu, O. and Dalgarno, K.W. Processing of apatite-wollastonite (AW) glass-ceramic for three-dimensional printing (3DP). *Applied Mechanics and Materials*, Switzerland, 2015, Trans Tech Publications Vols.754-755 (2015) pp 974-978, doi:10.4028/www.scientific.net/AMM.754-755.974.

AlHarbi, N., BRETCANU, O., AND DALGARNO, K.W. (2014) Indirect Three Dimensional Printing of Apatite-Wollastonite Scaffolds. *Tissue and Cell Engineering Society Conference*, Newcastle, UK, 2014, European Cells and Materials Vol. 28. Suppl. 4, 2014 (page 35), ISSN 1473-2262

Rodrigues, N., Alharbi, N., Benning, M., Mungia, J., and Kenneth Dalgarno. (2014) Materials processing for the manufacture of musculoskeletal medical devices at the point of need. *Tissue and Cell Engineering Society Conference*, Newcastle, UK, 2014, European Cells and Materials Vol. 28. Suppl. 4, 2014 (page 121), ISSN 1473-2262

List of Conferences and Poster presentations:

AlHarbi, N., Khan S.F., Bretcanu, O. and Dalgarno, K.W., (2014) ‘Processing of apatite-wollastonite (AW) glass-ceramic for three-dimensional printing (3DP)’, *3rd International Conference on Advanced Material Engineering & Technology*, Ho Chi Minh City, Vietnam.

AlHarbi, N., Bretcanu, O., Dalgarno, K.W., Tcancu, I. and Marshall, M., (2014) ‘Indirect three-dimensional printing of apatite-wollastonite scaffolds’, *European Materials Research Society Conference*, Warsaw, Poland.

AlHarbi, N., Bretcanu, O. and Dalgarno, K.W. (2014) Indirect three-dimensional printing of apatite-wollastonite scaffolds. *Tissue and Cell Engineering Society Conference*, Newcastle, UK.

Natacha Rodrigues, Naif Alharbi, Matthew Benning, Javier Mungia and Kenneth Dalgarno. (2014) Materials processing for the manufacture of musculoskeletal Medical devices at the point of need. *Tissue and Cell Engineering Society Conference*, Newcastle, UK.

AlHarbi, N. (2014) Indirect three-dimensional printing of apatite-wollastonite scaffolds. *Postgraduate Conference*, Newcastle, UK.

AlHarbi, N., Bretcanu, O. and Dalgarno, K.W. (2013) Indirect three-dimensional printing of apatite-wollastonite scaffolds. *ESB: 25th European Conference on Biomaterials*, Madrid, Spain.

AlHarbi, N. (2013) Indirect three-dimensional printing of apatite-wollastonite scaffolds. *Postgraduate Conference*, Newcastle, UK.

AlHarbi, N., Khan, S.F. and Dalgarno, K.W, (2012) ‘Indirect biofabrication of apatite-wollastonite (A-W) implantable devices by three-dimensional printing (3DP)’ *International Conference on Biofabrication*, Manchester, UK.

AlHarbi, N., (2012) Rapid manufacturing of bone tissue engineering scaffolds. *Postgraduate Conference*, Newcastle, UK.